

Strategies for the Design of Upconversion Nanoparticles with Enhanced Luminescence Properties in Biological Samples

Dissertation

zur Erlangung des

Doktorgrades der Naturwissenschaften

(Dr. rer. nat.)

an der Fakultät Chemie und Pharmazie

der Universität Regensburg

Deutschland



vorgelegt von

Lisa Marie Wiesholler

aus Ottobrunn

im Jahr 2019

Die vorliegende Dissertation entstand in der Zeit von November 2015 bis April 2019 am Institut für Analytische Chemie, Chemo- und Biosensorik der Universität Regensburg.

Die Arbeit wurde angeleitet von Prof. Dr. Antje J. Bäumner und Dr. Thomas Hirsch.

Promotionsgesuch eingereicht am: 17. April 2019

Kolloquiumstermin: 21. Juni 2019

Prüfungsausschuss

Vorsitzender: Prof. Dr. Oliver Tepner

Erstgutachterin: Prof. Dr. Antje J. Bäumner

Zweitgutachter: Prof. Dr. Arno Pfitzner

Drittprüfer: PD Dr. Hans-Heiner Gorris

Danksagung

Ich möchte mich zuallererst herzlichst bei **Prof. Dr. Antje Bäumner** und **Dr. Thomas Hirsch** bedanken, dass sie mir die Möglichkeit gegeben haben meine Promotion, zu diesem spannenden Thema anzufertigen. Vielen Dank für die stets verfügbare Betreuung, Unterstützung und Hilfe bei Problemstellungen aller Art.

Vielen Dank auch an **Prof. Dr. Arno Pfitzner** für die Übernahme des Zweitgutachtens. Mein herzlicher Dank gilt **PD Dr. Hans-Heiner Gorris** für die Übernahme der Aufgabe des Drittprüfers und **Prof. Dr. Oliver Tepner** für das Ausüben der Funktion des Prüfungsvorsitzenden.

Den Arbeitsgruppen um **Dr. Ute Resch-Genger** an der BAM und an allen voran **Florian Frenzel** danke ich herzlichst für die kontinuierliche erfolgreiche Zusammenarbeit über die ganzen Jahre. Des Weiteren danke ich **Prof. KiBum Lee** und **Yixiao Zhang** von der Rutgers Universität in New Jersey für die spannende und erfolgreiche Kooperation.

Beim **Upcon-Team**, allen voran bei **Dr. Thomas Hirsch**, bedanke ich mich für die unzähligen hilfreichen wissenschaftlichen und auch nicht-wissenschaftlichen Anregungen und Diskussionen.

Ich bedanke mich bei **Alexandra Schroter** und **Franziska Beck**, die im Rahmen ihrer Bachelorarbeiten kleine Teilprojekte übernommen haben, sowie bei **allen Kollegen** die einen Teil zu dieser Arbeit beigetragen haben. An dieser Stelle möchte ich besonders **Dr. Christa Genslein** und **Eva-Maria Kirchner** erwähnen, die mir immer mit Rat und Tat zur Seite standen.

Vielen, vielen lieben Dank auch an die gesamte aktuelle und ehemalige Arbeitsgruppe „**4. Stock**“ und an **alle Kollegen und Mitarbeitern am Institut** für die ausgezeichnete Arbeitsatmosphäre und vielen lieben Dank an die gute Seele des „4. Stocks“ **Rosi Walter** für die aufmunternden Worte.

Ein ganz besonderer Dank geht an meine **Eltern**, meinen Bruder **Max** und an meinen Freund **Nico** für die fortwährende Unterstützung und den Beistand über die gesamte Zeit.

Table of Contents

Scientific Original Publications and Peer Reviewed Review Articles	1
Declaration of Collaborations	2
Abstract	4
Deutsche Zusammenfassung	6
1. Strategies for the Design of Bright Upconversion Nanoparticles for Sensing Applications	9
1.1 Abstract	9
1.2 Introduction	10
1.3 Enhancement Strategies of the Upconversion Luminescence	13
1.3.1 Antenna Coupling.....	14
1.3.2 Plasmonic and Photonic Engineering for Enhanced Upconversion Luminescence	15
1.3.2.1 Surface Plasmon Coupling	15
1.3.2.2 Photonic Crystal Engineering	20
1.3.3 Concepts for Reduced Non-Radiative Decay.....	23
1.3.3.1 Lattice Manipulation	24
1.3.3.2 Doping Ratio	25
1.3.3.3 Surface Passivation	26
1.3.3.4 Energy Migration.....	28
1.3.4 Change of Excitation Wavelength.....	29
1.4 Conclusion and Perspective.....	32
1.5 References.....	34
2. Aim of the Work	42
3. Plasmonic Enhancement of NIR to UV Upconversion by a Nanoengineered Interface Consisting of NaYF₄:Yb,Tm Nanoparticles and a Gold Nanotriangle Array for Optical Detection of Vitamin B12 in Serum	44
3.1 Abstract	44
3.2 Introduction	46
3.3 Materials and Methods.....	48
3.3.1 Chemicals and Characterization Methods	48
3.3.2 Synthesis and Surface Modification of Upconversion Nanoparticles.....	49
3.3.2.1 Synthesis of Hexagonal NaYF ₄ :25%Yb,0.3%Tm	49

3.3.2.2 Surface Modification of NaYF ₄ :Yb,Tm.....	50
3.3.3 Functionalization of Glass Slides	51
3.3.4 Preparation of a Particle Layer <i>via</i> Self-Assembly	51
3.3.5 Stability Measurements of the Particles Attached to a Continuous Gold Film.....	52
3.3.6 Measurement of Vitamin B12	52
3.4 Results and Discussion.....	52
3.4.1 Substrate Fabrication and Functionalization with NaYF ₄ :Yb,Tm Upconversion Nanoparticles	52
3.4.2 Luminescence Properties	60
3.4.3 Luminescence Detection of Vitamin B12 at Nanoengineered Interfaces.....	64
3.5 Conclusion	69
3.6 References.....	70
4. NIR-mediated Spatiotemporal Control of Stem Cell Behavior Using Multifunctional Upconversion Nanoparticle	74
4.1 Abstract	74
4.2 Introduction	76
4.2.1 Materials	78
4.2.2 Methods.....	79
4.2.2.1 Synthesis.....	79
4.2.2.2 Silica Shell Growing	81
4.2.2.3 hiPSC-NSC Culture and Differentiations.....	81
4.2.2.4 Immunocytochemistry and Fluorescence Imaging	82
4.3 Results and Discussion.....	82
4.4 Conclusion	98
4.5 References.....	98
5. Yb,Nd,Er-Doped Upconversion Nanoparticles: 980 nm versus 808 nm Excitation	102
5.1 Abstract	102
5.2 Introduction	104
5.3 Materials and Methods.....	106
5.3.1 Chemicals and Characterization Methods	106
5.3.2 Synthesis and Surface Modifcation of UCNPs	107
5.3.2.1 Synthesis of hexagonal Core Particles NaYF ₄ :20%Yb,2%Er.....	107
5.3.2.2 Synthesis of Pre-cursor Nanoparticles.....	108

5.3.2.3 Synthesis of Core – shell Nanoparticles.....	108
5.3.2.4 Surface Modification.....	108
5.3.3 Determination of the Absorption Cross-Section	109
5.3.4 Penetration Depth Measurements.....	109
5.4 Results and Discussion.....	110
5.4.1 Particle Design, Synthesis and Characterization.....	111
5.4.2 Comparison of (Yb@Yb,Nd) ^{is} and (Yb@Yb) ^{is}	118
5.4.3 Comparison of Nd- and Yb- Excitation of (Yb@Yb,Nd) ^{is}	119
5.4.4 Influence of Particle Architecture.....	126
5.4.5 Penetration Depth in Phantom Tissue	128
5.5 Conclusion	132
5.6 References.....	133
6. Conclusion and Future Perspectives	138
6.1 References.....	146
Curriculum Vitae	148
Eidesstattliche Erklärung	152

Scientific Original Publications and Peer Reviewed Review Articles

4. **Lisa Marie Wiesholler**, Florian Frenzel, Bettina Grauel, Christian Würth, Ute Resch-Genger, Thomas Hirsch, Yb,Nd,Er-Doped Upconversion Nanoparticles: 980 nm versus 808 nm Excitation, *published in Nanoscale, July 1th, 2019*, doi:10.1039/C9NR03127H.
3. Yixiao Zhang, **Lisa Marie Wiesholler**, Pengfei Jiang, Jinping Lai, Hudifah Rabie, Thomas Hirsch, KiBum Lee, NIR-mediated Spatiotemporal Control of Stem Cell Behavior Using Multifunctional Upconversion Nanoparticles, *submitted to Nature Nanotechnology, July 4th, 2019*.
2. **Lisa Marie Wiesholler**, Christa Genslein, Alexandra Schroter, Thomas Hirsch, Plasmonic Enhancement of NIR to UV Upconversion by a Nanoengineered Interface Consisting of NaYF₄: Yb, Tm Nanoparticles and a Gold Nanotriangle Array for Optical Detection of Vitamin B12 in Serum. *Analytical Chemistry*. **2018**; 90(24):14247-54, doi:10.1021/acs.analchem.8b03279, published November 15, 2018.
1. **Lisa Marie Wiesholler**, Thomas Hirsch, Strategies for the design of bright upconversion nanoparticles for bioanalytical applications. *Optical Materials*. **2018**; 80:253-64, doi:10.1016/j.optmat.2018.04.015, published June 30, 2018.

Declaration of Collaborations

Most of the experimental and theoretical work presented in this thesis was carried out solely by the author. However, some of the results were obtained together with other researchers. In accordance with § 8 Abs. 1 Satz 2 Punkt 7 of the „Ordnung zum Erwerb des akademischen Grades eines Doktors der Naturwissenschaften (Dr. rer. nat.) an der Universität Regensburg vom 18. Juni 2009“, this section gives information about these collaborations.

Chapter 1: Strategies for the Design of Bright Upconversion Nanoparticles for Sensing Applications

This chapter is published as a review article. The literature survey was performed by the author. The concept and structure of the manuscript was planned together with Thomas Hirsch. The author wrote the manuscript. Thomas Hirsch revised the manuscript and is corresponding author. The schemes presented in Figures 1.2 and 1.14 are taken from the master's thesis of the author.

Chapter 3: Plasmonic Enhancement of NIR to UV Upconversion by a Nanoengineered Interface Consisting of NaYF₄:Yb,Tm Nanoparticles and a Gold Nanotriangle Array for Optical Detection of Vitamin B12 in Serum

This chapter is published. The author and Christa Genslein contributed equally to this publication. The author designed and synthesized the upconverting nanoparticle while Christa Genslein fabricated the nanotriangle array. First preliminary tests to fabricate the nanoengineered interface were conducted by Alexandra Schroter supervised by Christa Genslein and the author. The author performed the luminescence measurements, carried out the vitamin B12 measurements in water and serum and investigated the cross-sensitivity. The Raman measurements were performed by the author and Christa Genslein and the surface plasmon measurements were carried out by the author. The manuscript was written by the author and Christa Genslein. Throughout the publishing revision process the finalization of the manuscript was implemented by the author. The article was revised by the author, Christa Genslein, and Thomas Hirsch. Thomas Hirsch is corresponding author.

Chapter 4: NIR-mediated Spatiotemporal Control of Stem Cell Behavior Using Multifunctional Upconversion Nanoparticle

This work is a collaboration with the group of Professor KiBum Lee from Rutgers University, NJ. The author designed the particle architecture. The author synthesized the $\text{NaYF}_4:\text{Yb,Tm}@ \text{NaYF}_4:\text{Yb,Nd}@ \text{NaYF}_4$ upconversion nanoparticles and studied different doping ratios of Yb^{3+} and Nd^{3+} to receive particles with efficient luminescence allowing deep tissue penetration investigations. Yixiao Zhang functionalized the particles with a silica shell and the drug loading system. During the whole process the author and Yixiao Zhang discussed the obtained results. The article was written by Yixiao Zhang excluding the sections on synthesis and characterization of the 808 nm excitable particles. Regarding the other parts the author supported Yixiao Zhang with input and corrections. Thomas Hirsch and KiBum Lee revised the manuscript. KiBum Lee is the corresponding author.

Chapter 5: Yb,Nd,Er-Doped Upconversion Nanoparticles: 980 nm versus 808 nm Excitation

This work is a collaboration with the group of Ute Resch-Genger from the Federal Institute for Materials Research and Testing (BAM), Berlin. This chapter is submitted, and the author and Florian Frenzel contributed equally to this publication. The author designed, synthesized the $\text{NaYF}_4:\text{Yb,Er,Nd}$ particle systems and performed the surface modification. $\text{NaYF}_4:20\%\text{Yb},2\%\text{Er}@ \text{NaYF}_4:x\%\text{Yb},x\%\text{Nd}$ nanoparticles with $x = 5, 10$ and 15% , shown in Fig. 5.4, have been prepared during the master's study of LMW. Characterization and luminescence data of these particles have been obtained during PhD study. Additionally all other characterization including luminescence spectra of all systems were performed by the author. The absorption cross-section of the sensitizers within the particle were measured by the author. The experimental set-up was designed and realized together with Thomas Hirsch. The quantum yield measurements and brightness calculation were carried out by Florian Frenzel with input by Christian Würth while the decay data were measured together with Bettina Grauel during a research visit of the author at the BAM. During the whole process, the author and Thomas Hirsch discussed consequently results with the group of the BAM and planned further steps. All experiments with phantom tissue were carried out by the author. The author wrote the manuscript excluding the photophysical part. Thomas Hirsch and Ute Resch-Genger revised the manuscript and are both corresponding authors.

Abstract

This thesis addresses enhancement strategies for increasing the brightness of the upconversion nanoparticles to be used in biological samples or for bioanalytical applications.

Chapter 1 critically reviews the state of the art for enhancement strategies of the upconversion luminescence in nanoparticle systems as reported in literature. The enhancement strategies are classified in three main directions: a) the improvement of the energy absorption of the particles *via* coupling to plasmonic or photonic structures or *via* attachment of ligands for light harvesting, b) minimizing the non-radiative deactivation by varying the architecture of upconversion nanoparticles (UCNPs), and c) the shift of the excitation wavelength from 980 nm to 808 nm. Furthermore, current limitations and future perspectives of efficient UCNPs for sensing application in biological samples or cells are discussed.

Chapter 2 summarizes the motivation and the aim of the work by four main tasks: a) to get a better understanding of the photophysics of lanthanide-doped NaYF₄ upconversion nanoparticles, b) to search for possibilities to change the spectral properties of UCNPs for better sensing abilities, c) to prevent sample heating when exciting UCNPs by NIR light in aqueous systems, and d) to investigate the deep tissue penetration, which will be the key for future theranostic applications of these probes.

Chapter 3 presents the enhancement strategy of Tm³⁺-doped NaYF₄ nanoparticles coupled to a gold nanotriangle array, in the following named nanoengineered interface. Hot spots of the gold assembly generate a local enhancement of the electromagnetic-field, favoring the four-photon upconversion process at the low-power excitation of approximately 13 W·cm⁻². An improvement by about six times of the intensity for the emission peaking at 345 nm was achieved. Due to this enhancement it was possible to apply the nanoengineered interface in a simple intensity-based optical readout for vitamin B12, which is known as marker for the risk of cancer; Alzheimer disease; or, during pregnancy for neurological abnormalities in newborn babies. In this proof-of-concept study, vitamin B12 was detected in serum down to 3.0 nmol·L⁻¹ without any sample pretreatment.

Chapter 4 focusses on the enhancement of upconversion luminescence by shifting the excitation wavelength from classical 980 nm to 808 nm to minimize the absorbance by water at the excitation wavelength to avoid sample heating for applications of stem cell differentiation into neurons. For this aim the doping-ratio of the sensitizer neodymium confined in an active shell was studied. Particles with core – active shell – inert shell architecture showed increased emission in the UV. After coating with a mesoporous silica shell as a molecular cage was generated, modified by spiropyran, that works as a photo-activatable gate, which switches between open and closed form upon stimulating by the UV-emission of the UCNPs. An encapsulation of the drug retinoic acid into this advanced multifunctional nanoparticle system was used to stimulate the differentiation of pluripotent stem cells into neurons in a controlled manner.

Chapter 5 reports on a systematic study of Nd^{3+} -sensitized UCNPs in comparison to Yb^{3+} -sensitization in terms of deep tissue penetration. A set of similarly sized Yb^{3+} , Nd^{3+} , Er^{3+} -doped core- and core – shell particles of different architecture colloidally stable in water was investigated at broadly varied excitation power densities with steady state and time-resolved fluorometry for excitation at 980 nm and 808 nm. For the UCNPs performance, the power dependent upconversion quantum yield (Φ_{UC}) and its saturation behaviour were used as well as a new measure particle brightness (B_{UC}) was introduced. Spectroscopic measurements at both excitation wavelengths in water and in a phantom tissue, together with B_{UC} calculations suggests that for this particle architecture at relative low excitation power a penetration depth of approx. 6 cm is necessary to gain advantage in brightness by 808 nm excitation.

Chapter 6 discusses the state of the art in UCNPs synthesis under the aspect of getting bright luminescent nanoparticles, including the main results of this thesis in terms of applying UCNPs in biological samples. Future perspectives in the field are envisioned.

Deutsche Zusammenfassung

Die vorliegende Arbeit beschreibt Strategien zur Verbesserung der Helligkeit von aufkonvertierenden Nanopartikel (englisch: upconversion nanoparticles, UCNPs) mit dem Ziel diese in biologischen Proben oder für bioanalytische Anwendungen einzusetzen.

Kapitel 1 bietet eine kritische Übersicht bekannter Strategien zur Verstärkung der Lumineszenz aufkonvertierender Nanopartikel an Hand der zu diesem Thema publizierten Arbeiten. Es werden drei Prinzipien unterschieden: a) verbesserte Energieaufnahme der Partikel durch Kopplung mit plasmonischen oder photonischen Strukturen, sowie der Funktionalisierung mit Farbstoffen die als Lichtsampler dienen, b) Minimierung von Prozessen zur strahlungslosen Deaktivierung angeregter Zustände durch gezielte Veränderung der Partikelarchitektur, und c) Verschiebung der klassischen Anregung bei 980 nm zu niedrigerer Wellenlänge (808 nm). Zudem werden Limitierungen dieser Konzepte, sowie mögliche zukünftige Entwicklungen zur Erzeugung von effizienten UCNPs, insbesondere für die Anwendung in der Sensorik und für biologische Proben und Zellen, vorgestellt.

Kapitel 2 stellt die Motivation und die Ziele der Arbeit, gegliedert in vier Punkte, zusammen: a) die systematische Untersuchung photophysikalischer Fragestellungen in lanthanoid-dotierter NaYF_4 Nanopartikeln, b) die Modulation der spektralen Eigenschaften von UCNPs hinsichtlich dem Ziel eine sensorischen Anwendung unter Ausnutzung effizienter Aufkonvertierung von Nahinfrarotlicht in UV-Strahlung zu ermöglichen, c) die Aufheizung wässriger Proben als Folge der nahinfrarot Anregung von aufkonvertierenden Nanopartikel zu minimieren, und d) eine für theranostische Anwendungen entscheidende hohe Eindringtiefe ins Gewebe mittels maßgeschneiderten UCNPs, anregbar bei zwei verschiedenen Wellenlängen, zu erzielen.

Kapitel 3 beschreibt eine Verstärkungsstrategie der UV-Lumineszenz von Tm^{3+} -dotierten NaYF_4 Nanopartikel durch deren Kopplung an eine nanostrukturierte Goldoberfläche. Die Gold-Nanostrukturen generieren dabei lokale Zonen mit verstärktem elektromagnetischem Feld, welches den sonst nur äußerst schwach ausgeprägten vier-Photonen-Aufkonvertierungs-Prozess bei niedriger Laseranregungsleistung bevorzugt und zu einer bis zu 6-fachen Verstärkung der Emission bei 345 nm führt. Hiermit ist es erstmals gelungen einen

einfachen intensitäts-basierten optischen Sensor für Vitamin B12 mit hoher Nachweisgrenze zu realisieren. Vitamin B12, bekannt als Marker für Krebsrisiko, Alzheimer Erkrankungen oder während einer Schwangerschaft auftretenden neurologische Anomalien von Neugeborenen, konnte im Serum im physiologisch relevanten Konzentrationsbereich mit einer Nachweisgrenze von $3.0 \text{ nmol}\cdot\text{L}^{-1}$ ohne Probenvorbereitung detektiert werden.

Kapitel 4 befasst sich mit dem Design und der Realisierung von Kern-Hülle UCNPs zur Anregung bei 808 nm, mit dem Ziel, die ungewollte Begleiterscheinung der Probenaufheizung durch die relativ hohe Absorbanz von Wasser bei 980 nm zu minimieren. Hierfür wurden verschiedene Dotierungsverhältnisse von Neodym und Ytterbium in der Partikelhülle untersucht. Eine zusätzliche inerte Hülle ergab eine Partikelarchitektur, die in Wasser ohne die Probe zu erwärmen, eine außergewöhnlich helle und zudem eine verstärkte Emission im UV-Bereich zeigt. Der praktische Nutzen dieser Partikel wurde durch eine Anwendung in der Stammzellen Differenzierung in Neuronen demonstriert. Mittels nahinfrarot-Anregung gelang es durch Aufkonvertierung UV-Licht lokal für eine gezielte, photoinduzierte Freisetzung eines in einer mesoporösen Silikathülle eingeschlossenen Wirkstoffs zu nutzen und so die kontrollierte Differenzierung von pluripotenten Stammzellen in Neuronen zu stimulieren.

Kapitel 5 beschreibt die systematische Studie von Nd^{3+} -dotierten UCNPs im Vergleich zu Yb^{3+} Anregung, in Bezug auf eine hohe Eindringtiefe ins Gewebe. Eine Zusammenstellung von identisch großen ($\text{Yb}^{3+}, \text{Nd}^{3+}, \text{Er}^{3+}$)-dotierten Kern-Hülle Partikeln mit verschiedenen Architekturen, wurde über einen großen Anregungsdichtebereich für Anregung bei 980 nm und 808 nm fluoreszenzspektroskopisch untersucht. Erstmals wurden die leistungsabhängigen Quantenausbeuten Nd-dotierter UCNPs in Wasser bestimmt und zur besseren Vergleichbarkeit von UCNPs mit unterschiedlicher Anregungswellenlänge die Partikel-Helligkeit als neues Maß definiert. Die spektroskopischen Daten für beide Anregungswellenlängen in Wasser und Phantom-Gewebe, zusammen mit der Berechnung der Partikel Helligkeit ergeben, dass für multi-dotierte UCNPs mit Kern-Hülle Architektur ab einer Eindringtiefe von ungefähr 6 cm die 808 nm gegenüber der 980 nm Anregung bei relativ schwacher Laser Leistung zur effizienteren Aufkonvertierung führt.

Kapitel 6 diskutiert die wichtigsten Ergebnisse und Erkenntnisse, welcher in dieser Arbeit erlangt wurden unter Einbeziehung des Stands der Technik zur Verbesserung der

Lumineszenzeigenschaften von UCNPs, um diese in biologischen Proben erfolgreich anwenden zu können. Zudem werden mögliche zukünftige Entwicklungen in diesem Forschungsgebiet beleuchtet.

1. Strategies for the Design of Bright Upconversion Nanoparticles for Sensing Applications

1.1 Abstract

In recent years upconversion nanoparticles (UCNPs) received great attention because of their outstanding optical properties. Especially in bioanalytical applications this class of materials can overcome limitations of common probes, like high background fluorescence or blinking. Nevertheless, the requirements for UCNPs to be applicable in biological samples, *e.g.* small size, water-dispersibility, excitation at low power density are in contradiction with the demand of high brightness. Therefore, a lot of attention is paid to the enhancement of the upconversion luminescence. This review discusses the recent trends and strategies to boost the brightness of UCNPs, classified in three main directions: a) improving the efficiency of energy absorption by the sensitizer *via* coupling to plasmonic or photonic structures or *via* attachment of ligands for light harvesting; b) minimizing non-radiative deactivation by variations in the architecture of UCNPs; and c) changing the excitation wavelength to get bright particles at low excitation power density for applications in aqueous systems. These strategies are critically reviewed including current limitations as well as future perspectives for the design of efficient UCNPs especially for sensing application in biological samples or cells.

This chapter has been published.

Lisa Marie Wiesholler, Thomas Hirsch. *Optical Materials*, **2018**, 80, 253-64.

Author contributions: This review article was published after peer reviewing. The authors have been invited to make this contribution. The literature survey was performed by LMW. The concept and structure of the manuscript was planned together with TH. LMW wrote the manuscript. TH revised the manuscript and is corresponding author. The schemes presented in Figures 1.2 and 1.14 are taken from the master's thesis of the author.

1.2 Introduction

Upconversion nanoparticles became very popular in recent years. The number of publications almost doubled in the last five years and exceed more than 25,000 paper in 2017 (Fig. 1.1). These fascinating class of luminescent nanomaterials with its unique properties to convert low energy excitation light in high energy emitting photons attracted research from many directions such as for chemistry, photophysics, biology and medicine. Applications ranging from bio(sensors) to photovoltaic applications, from bioimaging to theranostic applications [1-5].

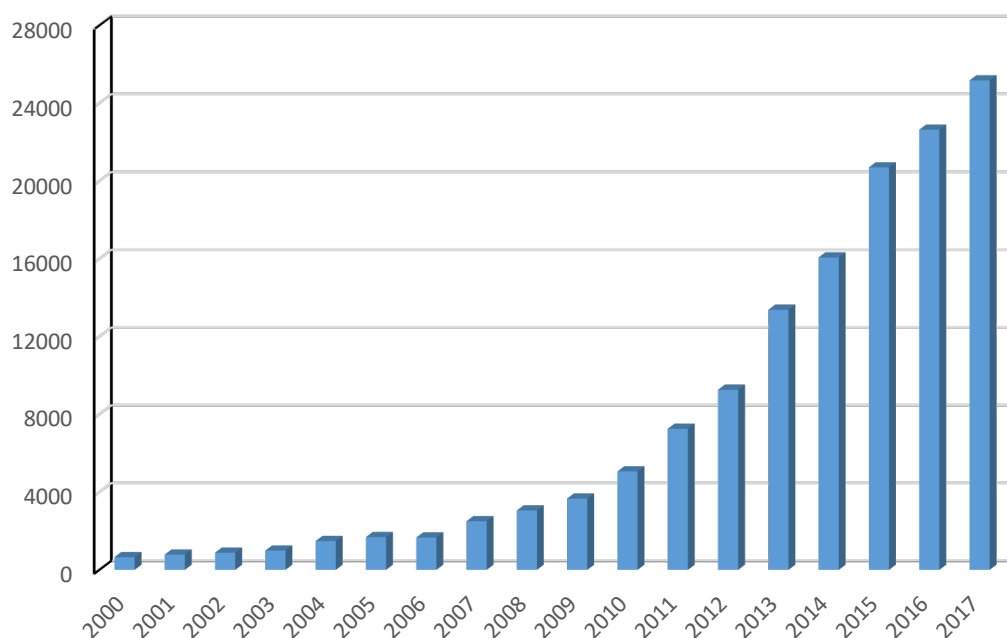


Figure 1.1 | Number of publications on the topic “upconversion nanoparticle” from the year 2000 to 2017 indexed in Web of Science.

Photon upconverting nanomaterials are characterized by many remarkable properties especially for biological applications like narrow emission bands, high chemical stability, minimized auto-fluorescence, deep tissue penetration and low toxicity [6-9]. Therefore, UCNPs have become an attractive alternative to organic fluorophores and quantum dots in (bio)sensors [1,2].

The upconversion phenomenon, leading to the emission of light at a shorter wavelength compared to the excitation light, which was first described in year 1959 [10], is called anti-

Stokes emission and is triggered in UCNPs by a sequential absorption of photons. In order to observe upconversion luminescence, a crystalline host material needs to be doped by two types of lanthanide ions as dopants (one type acting as sensitizer, the other one as activator). For high upconversion efficiency host materials of low lattice phonon energy, such as β -NaYF₄ are favored [11,12]. Such nanocrystals doped with 20% ytterbium and 2% erbium represent the most frequently used UCNPs in literature [13]. The sensitizer ions Yb³⁺ are excited by a continuous wave (cw) laser at a wavelength of 980 nm and the Er³⁺ activator ions show predominately green and red emissions. Other possible activator ions are thulium (blue and near infrared emissions) [14] or holmium (blue and green emissions) [15]. The mechanism, design, synthesis, chemical modification as well as the applications of upconversion nanoparticles have been described in excellent reviews recently and will not be discussed in detail here [4,16-21]. The efficiency of the upconversion process, especially nanoparticles dispersions, is rather low and is affected by several parameters such as size [8], the type of host material [22], crystal phase [23], composition of lanthanide ions [24], surface chemistry and solvents [21,25]. For the design of effective upconversion materials for bioanalytical applications one has to fulfil certain demands which are in contradiction to high upconversion efficiency as illustrated in Figure 1.2.

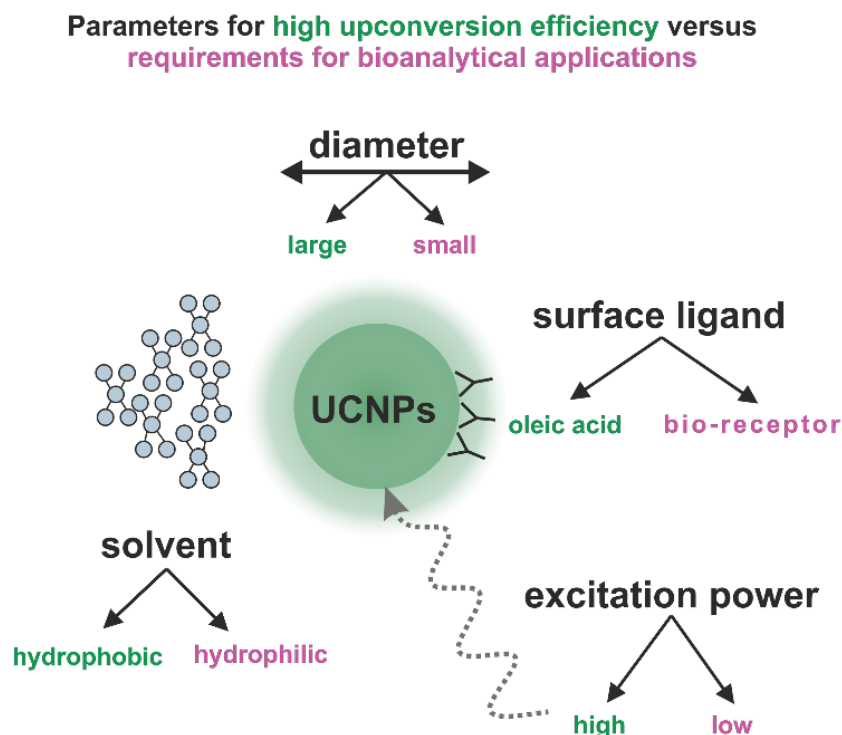


Figure 1.2 | Contradicting parameters to achieve high upconversion efficiency (green) and requirements for using UCNPs in bioanalytical applications (pink). Adapted from the authors master's thesis.

The efficiency of the upconversion luminescence depends – as a non-linear photo-physical process – on the power density of the excitation light [26]. Nevertheless, the irradiation power density of the near-infrared light needs to be lower than $4 \text{ W} \cdot \text{cm}^{-2}$ [27] to prevent tissue and cell damages. It is also well known, that the efficiency of UCNPs increases with the diameter of the particles. Particles applied in diagnostics, need to be completely discarded from the body after examination. The body distribution and metabolism of UCNPs revealed the excretion of about 20 nm sized particles previously introduced into lymph [28]. Therefore, small particles with high brightness at low excitation power density are highly desired. So far, various approaches have been tried to design UCNPs for bioanalytical applications with enhanced luminescence properties. The strategies can be divided in three main routes: a) coupling of UCNPs to materials boosting the luminescence by light harvesting, photonic or plasmonic effects; b) optimization of the particle architecture by minimizing non-radiative decay; c) shift of the excitation wavelength to overcome the water absorbance overlapping with the classical 980 nm excitation (Fig. 1.3). In the following recent advances regarding these strategies are critically reviewed for the design of efficient UCNPs especially for sensing application in biological samples or cells.

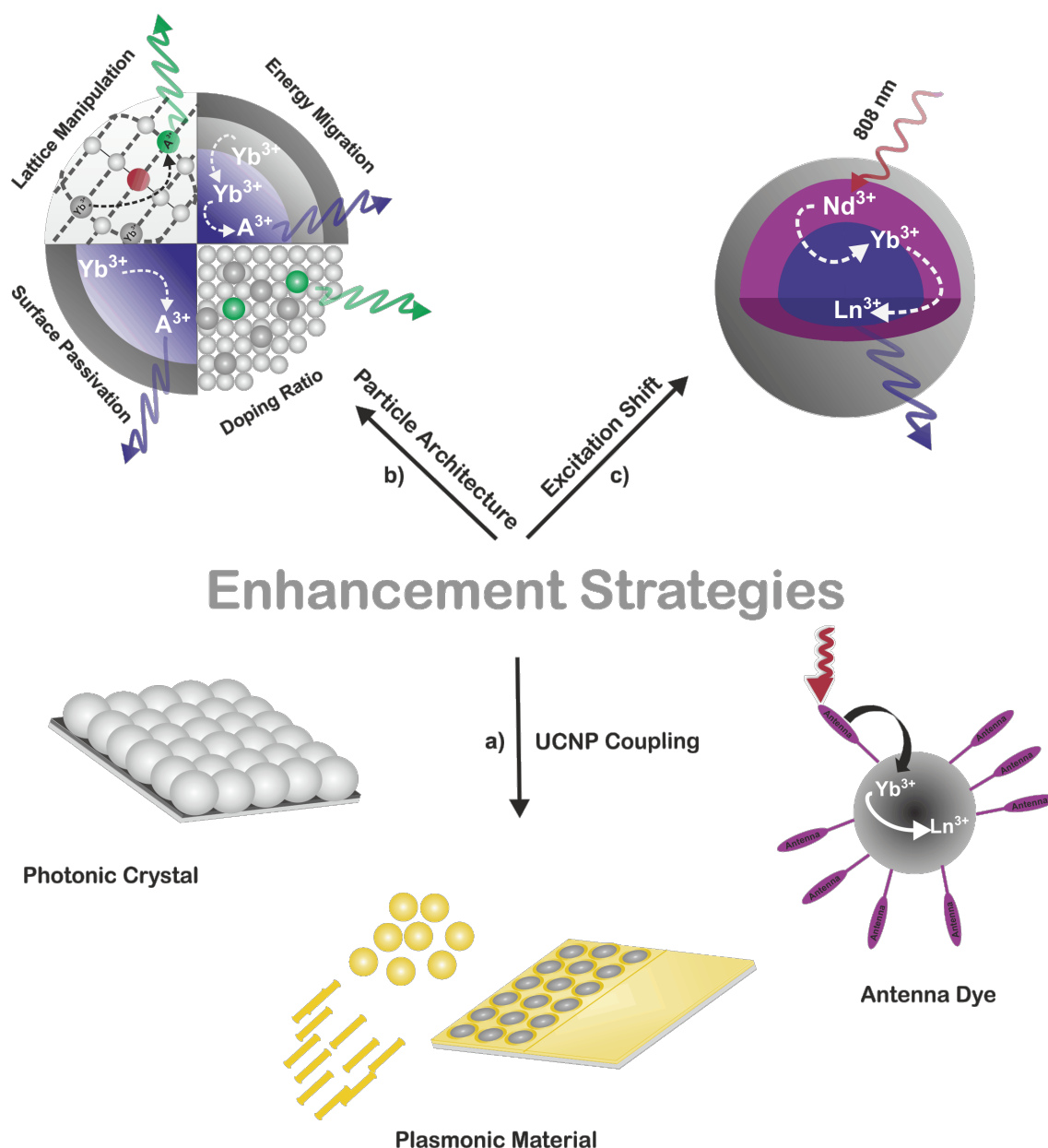


Figure 1.3 | Three main strategies to enhance the upconversion luminescence: a) improve the efficiency of energy absorption by the sensitizer via coupling to plasmonic or photonic structures or to attach ligands for light harvesting; b) minimizing non-radiative deactivation by changing the architecture of UCNPs; and c) changing the excitation wavelength to get bright particles at low excitation power density for applications in aqueous systems.

1.3 Enhancement Strategies of the Upconversion Luminescence

The poor quantum efficiency of UCNPs can be attributed to a low absorption coefficient of the sensitizer Yb^{3+} ($\sim 10 \text{ M}^{-1} \cdot \text{cm}^{-1}$) [29]. Several strategies have been investigated to enhance the upconversion luminescence. By a closer look to the spectral properties of Yb^{3+} , Er^{3+} -doped UCNPs one can see a large gap between the absorption and anti-stokes emission spectra

(Fig. 1.4). This spectral range can be used for enhancing the upconversion efficiency by light harvesting *via* antenna molecules, plasmonic or photonic features, which will be reviewed in the following in detail.

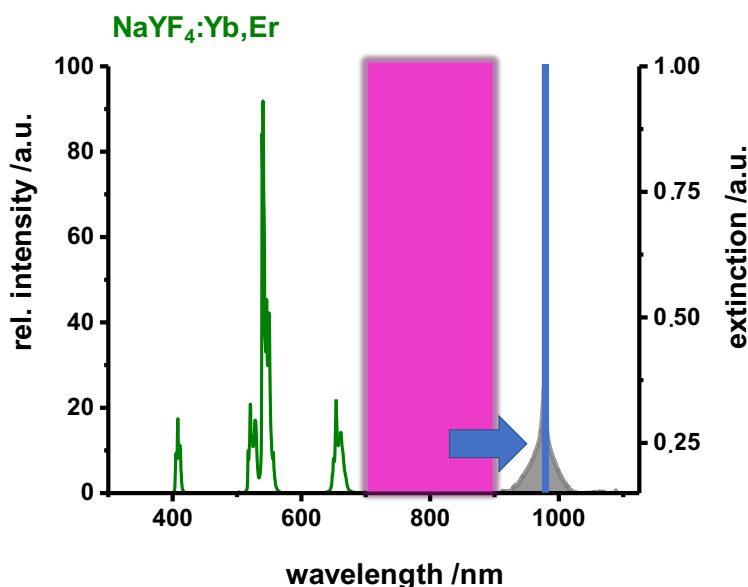


Figure 1.4 | Spectral properties of NaYF₄:Yb,Er. The absorbance of Yb³⁺ is shown in grey, the anti-stokes emission of Er³⁺ is displayed in green. The blue line symbolizes the typical laser irradiation at 980 nm. In purple one can see the large gap between excitation and emission which can be utilized by several techniques to enhance the weak absorbance of the Yb³⁺ ions.

1.3.1 Antenna Coupling

One of the first approaches to enhance the luminescence properties of UCNPs was described by attaching light harvesting molecules on the particle surface [30-35]. This dye-sensitizing concept increased the upconversion luminescence because of the comparable large absorption cross-section (typically in the range of 10^{-14} cm² [30]) and the broad absorption range of organic dye molecules (700 - 900 nm). The emission of these dyes is in the range of 750 – 1150 nm. Coupling the dye IR-806 to NaYF₄:Yb,Er particles (16 nm) enhances the efficiency about 3,300 times by using a 2 mW calibrated wavelength-tunable continuous wave laser [35]. A promising approach for anti-counterfeiting or security applications is reported by using dye modified NaYF₄:Yb,Er particles of 20 nm size. A series of particles modified with different near-infrared (NIR) dyes (IR-783, IR-820, IR-808, IR-845) *via* surface ligand exchange were blended in poly(methyl methacrylate) (PMMA) and used as inks for printing applications. When such printings will be illuminated by different wavelengths only those parts of the image printed by dye modified particles excitable at this wavelength show the

green emission [32]. Unfortunately, such strategies have not been established for bioanalytical applications so far. Reasons might be found in the limited photostability of NIR dyes and the poor colloidal stability of dye-modified particles in aqueous solutions [36,37]. Nevertheless, for the design of lateral flow assays such concepts seem to be promising in reaching lower limits of detection, broadening of the dynamic range or making the readout simpler by decreasing the power of the illumination source.

1.3.2 Plasmonic and Photonic Engineering for Enhanced Upconversion Luminescence

Plasmonic metallic structures [38,39] or photonic dielectric structures can increase the absorption of lanthanide-doped NaYF_4 . Especially dielectric plasmonic structures seems to be advantageous as they do not suffer from parasitic absorption [40]. In the following examples are shown for strategies including the coupling of UCNPs to a) metals (surface attached as well as core/shell architecture) and b) photonic crystals (PCs), fabricated as an artificial periodic pattern of materials with different permittivity, as depicted in Figure 1.5.

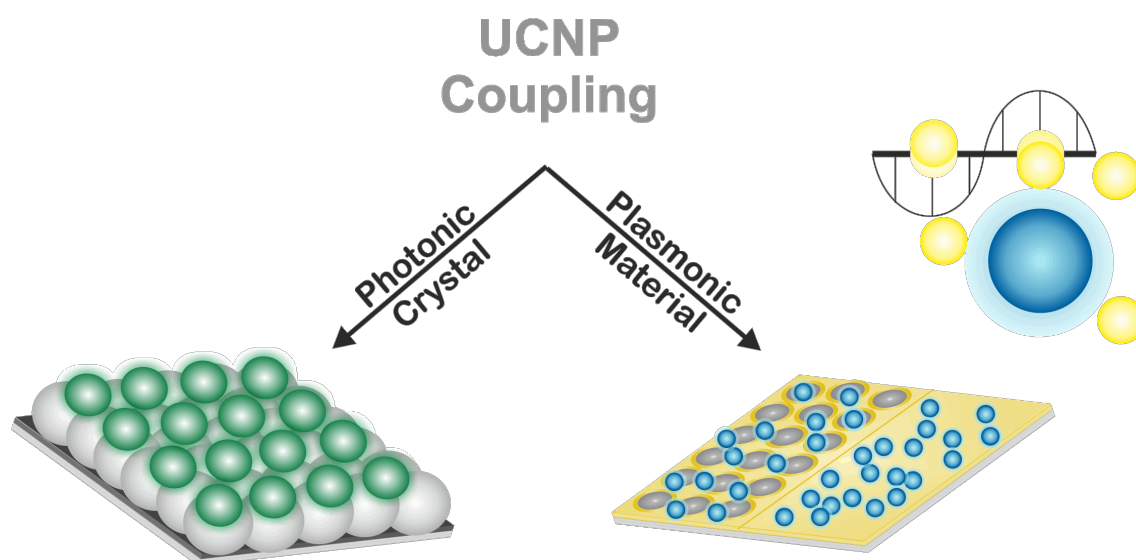


Figure 1.5 | Upconversion luminescence can be enhanced by coupling of UCNPs (green spheres in the left, blue spheres in the right) to photonic crystals or metallic plasmonic structures. For the latter approach, propagating surface plasmons on a continuous metal film or localized surface plasmons of either individual gold particles (yellow spheres) or nanostructured metal films can be exploited.

1.3.2.1 Surface Plasmon Coupling

Metallic nanomaterials, known as effective light-trapping components, can be coupled with UCNPs to boost the efficiency of the energy conversion processes. The electric field of the surface plasmons, which propagate along the metallic surface lead to an increase of the

upconversion luminescence [41]. Parameters which have the largest impact on this enhancement strategy are the geometry of the surface plasmon generating nanostructure and the dielectric property of the surrounding media [42].

The attachment of UCNPs directly to a noble metal surface has been utilized for enhancing the upconversion luminescence efficiency by taking benefit of the surface plasmons, excited at the metal surface interacting with the UCNPs. Stanley May *et al.* reported on a gold surface modified by a thin PMMA film with NaYF₄:Yb,Er nanocrystals (NCs) embedded in a monolayer assembly. Here the green and red emission were enhanced by similar factors of about three, explained by the intensification of the excitation by 980 nm. This is especially useful for low power excitation, as it was found that an increase of the excitation power from 3 mW to 24 mW results in a lower enhancement [43]. When using discontinuous gold islands of 20 nm instead of a continuous gold film, enhancements of even up to 12 times have been reported [44]. The difference in the brightness is ascribed to localized surface plasmons in the cavity of the periodic structure of the substrate. A change in the relative emission intensities at certain wavelengths is described [44]. Also, nanostructures with other geometries have been reported in literature: Hole arrays, pillar arrays, or waveguides [39]. Kagan *et al.* fabricated a 30 nm thin gold film structured by an array of holes with diameters of 110 nm (Fig. 1.6). NaYF₄:Yb,Er particles of 70 nm diameter were chosen to fill every hole with only one particle by a squeegee process. The upconversion luminescence intensity measured at 543 nm revealed an enhancement of 35 times for such nanostructured supports consisting of a thin gold film compared to identical nanostructures consisting of glass only [45].

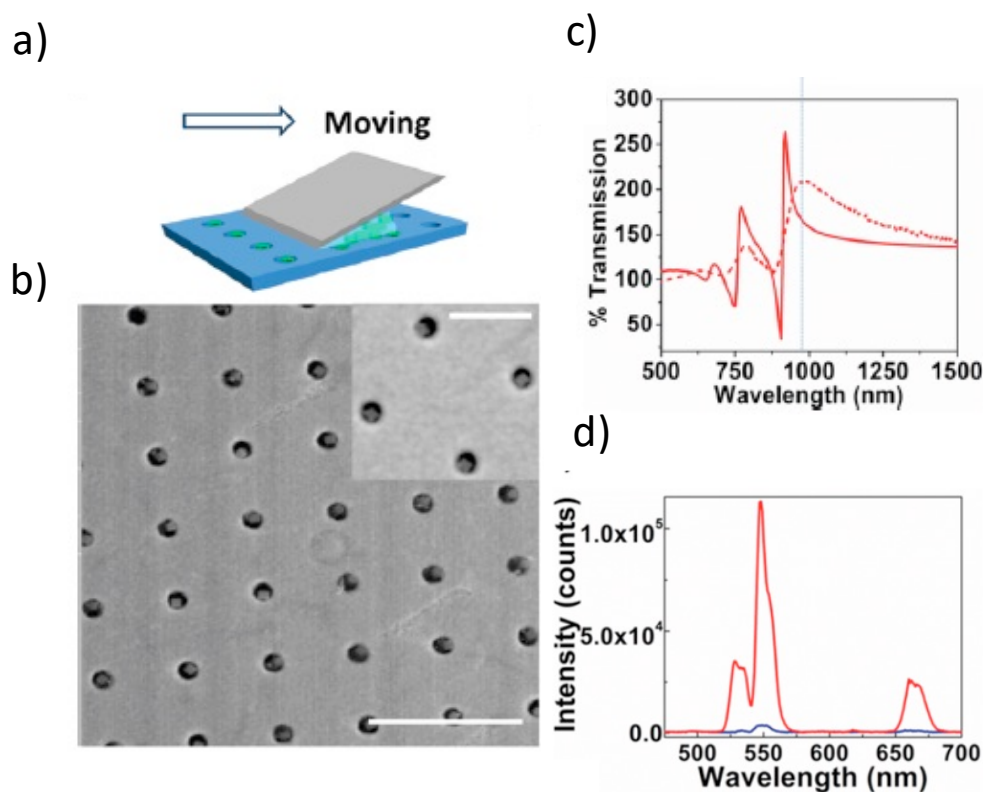


Figure 1.6 | Scheme of the squeegee method used to fill the nanohole array with UCNPs (a) and SEM images (scale bar: 500 nm) of the particle filled nanohole array (b). Transmission spectra of the filled nanohole arrays based on experimental measurements (solid red) and the theoretical simulation results (dashed red) with respect to the transmission from a 30 nm layer of Au deposited on a glass substrate. Upconversion luminescence spectra of NaYF₄:Yb,Er UCNPs in a glass nanohole array (blue line) and in Au nanohole array (red line) under 980 nm excitation. Picture adapted with permission from Ref [45] © 2016 American Chemical Society.

Smith and May investigated a gold nanopillar system with NaYF₄:Yb,Tm particles embedded in PMMA. At optimized geometry of the metallic nanostructures and at ideal proximity of the UCNPs to the metallic surface an upconversion enhancement of five times compared to a continuous gold film was found. This effect is attributed to the collective modes of the nanopillar array which enhances the near-infrared absorption and simultaneously exploits the localized surface plasmons generated from the individual pillars [38]. For the design of such nanostructured substrates it is important to excite a surface plasmon mode at 980 nm. Park *et al.* achieved a surface plasmon mode at 980 nm by a silver nanograting layer and the deposition of the three monolayers of the UCNPs on a 30 nm thick spacer of Si₃N₄. Compared to a flat metal film a 16× and 39× enhancement in the green and red peak intensities was obtained [46]. A three-layer structure containing plasmonic Cu_{2-x}S NCs layer, a MoO₃ spacer on top a layer of NaYF₄:Yb,Er nanoparticles was fabricated by Song *et al.* to study the upconversion enhancement. The energy matching of the band gap of Cu_{2-x}S and the green emission of the UCNPs leads to stronger green than red emission at an excitation power density of 123 W·cm⁻² with an enhancement factor of almost 100 [47]. Moreover, in most of the publications the brightness of the particles coupled to the metallic nanostructures according

to the excitation power density was investigated. Nearly all results demonstrate the highest enhancement by using significant low excitation power densities like $70 \text{ mW}\cdot\text{cm}^{-2}$ [38,43-45]. By high laser power (e.g. $10 \text{ kW}\cdot\text{cm}^{-2}$) a saturation of the excited states takes place and non-radiative decay is encouraged [44,46]. Even when those approaches demonstrate an enhancement of the upconversion luminescence by using nano-engineered surfaces, the fabrication of those substrates is often time consuming or expensive equipment is needed, which clearly limits their application so far. Up to now there are no reports of the usage of such systems in sensing applications. Nevertheless, for the design of chip-based sensing applications the approach of coupling UCNPs to metal surfaces seems to be promising, especially when the fabrication can be performed by printing technologies.

The enhancement of the upconversion luminescence by direct coupling of UCNPs to nanoparticles consisting of noble metals has also been studied, as such an approach will be easily adaptable for liquid-based assays performed in cuvettes or micro-titer plates. First reports explained the enhancement process by a more efficient population of the energy states by a local field enhancement [48,49]. Duan *et al.* synthesized $\text{NaYF}_4:\text{Yb,Tm}$ particles of 180 nm size. For the attachment of negatively charged gold nanoparticles of 5 nm the UCNPs were modified with poly(acrylic acid) *via* ligand exchange and then an additional layer of poly(allylamine hydrochloride) was grown on the surface to render the surface of the particles positively charged. By introducing additional gold precursors together with reducing agents into the solution with the UCNPs, a continuous shell of Au of 7 nm thickness was formed on the UCNP surface. First, during the seeding steps of the 5 nm sized gold particles, the emission intensity at 452 nm of the UCNPs was doubled while the formation of a continuous shell of Au on the nanoparticles resulted in four times decreased emission intensity due to scattering effects [48]. $\text{NaYF}_4:\text{Yb,Er}$ nanoflowers (UCNFs) decorated with Au particles have been utilized for selective 2,4,6-trinitrotoluene TNT detection (Fig. 1.7). In presence of TNT the distance of the gold nanoparticles to the UCNFs gets minimized, accompanied by an enhancement of the upconversion luminescence. UCNFs (106 – 142 nm) with negatively charged surfaces were fabricated through encapsulating of hydrophobic NaYF_4 UCNPs with oleylamine functionalized polysuccinimide. The positively charged gold NPs coated with cysteine were attached onto the negatively charged UCNFs *via* electrostatic interactions, while the luminescence of nanoflowers is enhanced by the plasmon resonance properties of the gold nanoparticles. TNT can bind to the amino groups and cause the aggregation which

influences the luminescence spectra in respect to the analyte concentration by enhanced green and red emission [50].

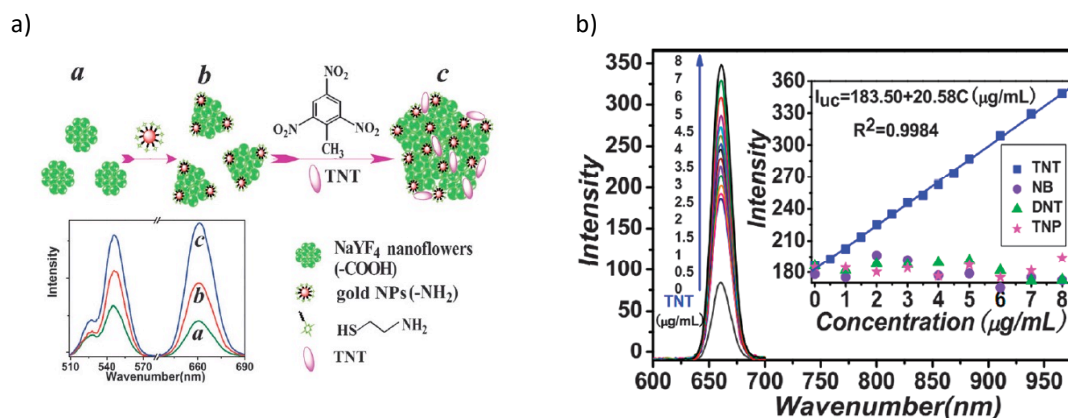


Figure 1.7 | Illustration of TNT sensing based on the interaction among the NaYF₄ nanoflowers, gold nanoparticles (NPs) and TNT. With the addition of gold particles and TNT, the upconversion luminescence gets enhanced (a). The upconversion emission spectra of the mixture of NaYF₄ UCNFs (0.1 mg mL⁻¹) and gold NPs (38 mg mL⁻¹) in the presence of various concentrations of TNT are shown in (b). The inset displays the calibration plot of upconversion emission intensity versus the nitroaromatic concentrations. Picture adapted with permission from Ref [50] ©2013, Royal Society of Chemistry.

Beside gold, also silver nanoparticles can promote the upconversion luminescence by utilizing plasmonic effects. The brightness of NaYF₄:Yb,Er particles modified with 100 nm sized Ag particles was doubled, whereas smaller Ag particles lead to a quenching of the upconversion luminescence [51]. In order to obtain an enhancement of the upconversion luminescence metal particle size and the geometry have to be carefully adjusted to optimize the spectral overlap of the localized surface plasmon resonance (LSPR) with the absorption or rather emission of the UCNPs. Other geometries of noble metal nanostructures described for luminescence enhancement are nanowires [52] or nanorods [53]. UCNPs decorated with gold nanorods of 90 nm and under a NIR pumping power of 2 W result in an enhancement up to 27-fold of the 800 nm emission. These particle assemblies were used in a simple dual-mode (UV-vis and fluorescence) optical based sensor for the sensitive and selective detection of uric acid [53]. Using Ag nanowires which have a broader extinction coefficient compared to gold also lead to a 2.3× increased green or 3.7× higher red emission intensity [52]. Beside the dimensions of UCNPs and noble metal nanomaterials, the choice of the distance between both nanomaterials is very critical. A distance of 10 nm between Ag particles and the UCNPs is found to result in the largest enhancement (14.4-fold for 543 nm and 12.5-fold for 656 nm) [54]. The distance dependency was studied for systems consisting of spin-casted layers of Ag or Au particles and a monolayer of UCNPs separated by an Al₂O₃ layer of varying thicknesses ranging from 2 to 15 nm. For the Au particles a layer Al₂O₃ thickness of 5 nm is favored while

by using Ag particles the thickness should be 10 nm [55]. For 110 nm thick gold nanorods a spacer of 8 nm thickness revealed the best enhancement of about 10-fold for the green emission [56]. These studies clearly indicate the potential of luminescence enhancement but so far these strategies suffer from experimental difficulties in fabricating not only monodisperse UCNPs but also noble metal nanostructures of defined size and geometry with a nanometer precise distance between both materials.

1.3.2.2 Photonic Crystal Engineering

Photonic crystals (PCs), fabricated as a three-dimensional packed periodic alignment of materials with different permittivity, can be used as a substrate to enhance the upconversion luminescence of coupled UCNPs. Such crystals are known to modulate the emission wavelength, direction, and intensity of light [57,58]. Several concepts of photonic crystals used in sensing application have been reviewed by Fenzl *et al.* [59]. Upconversion emissions can be modulated within and on top of the photonic crystals. Upon deposition of UCNPs on the surface of photonic crystals a significant enhanced luminescence can be stimulated by the Bragg reflection of photonic band gap effects. In contrast, the spontaneous emission of lanthanide ions within the photonic crystals can be affected regarding the photonic band gap which can be tuned to meet distinct radiative transitions of the respective lanthanide ion [60]. An enhancement factor of 32 of the overall upconversion luminescence was reported by coupling 20 nm big NaYF₄:Yb,Tm nanoparticles to a three-dimensional PMMA opal photonic crystal (OPC) with a lattice constant of 320 nm, upon low power excitation at 980 nm using a 5 mW laser diode [61]. The enhanced brightness of UCNPs were applied for cellular imaging using the PMMA OPC as reflection substrates. The feasibility in sensing was demonstrated by Sai *et al.* by an application of a composite film of NaYF₄:Yb,Er / TiO₂ inverse opal in the energy transfer-based detection of Hg²⁺ in serum with a remarkable low limit of detection of 70.5 nmol·L⁻¹ [62]. A strong relation of the particle size and the excitation power density but not to any variation in the inverse opal photonic crystal was found. Enhancement factors of 32 are found for the upconversion luminescence of 6 nm sized NaYF₄:Yb,Er particles excited at 980 nm with a power density of 0.03 W·mm⁻². The enhancement factors increase for smaller particles and lower excitation power densities. Other opals used for luminescence enhancement of NaYF₄:Yb,Er nanoparticles were made from LaPO₄ [63], a material which can also be directly doped by Yb³⁺ and Tm³⁺ as shown by Ghosh *et al.* [64] and might offer the possibility of spontaneous upconversion emission. A notable increase in the luminescence intensity for large UCNPs of 65 to 80 nm diameters doped with Er³⁺ or Tm³⁺ as activator ions

was also reported when deposited on opals of different band gaps [65]. The authors ascribed the enhancement to the coupling between the upconversion emission light and surface states due to the efficient and selective Bragg reflection of the photonic crystal. Gold or silver nanoparticles embedded in inverse opals of SiO_2 have been used as substrates for ~ 8 nm big $\alpha\text{-NaYF}_4\text{:Yb,Er}$ nanoparticles. A luminescence enhancement of ~ 10 for gold and ~ 6 for silver was explained by the combination of the photonic band gap by the plasmon absorption of the metal nanoparticles [66,67]. Nevertheless, information on the excitation power density was not provided. Depending on the engineering of the Au modified inverse opals by using differently sized polystyrene templates, the enhancement of the green or the red emission of the UCNPs can be tuned independently [66]. By assembling a hybrid structure of Er-doped UCNPs upon silver nanoparticles attached to the surface of a polystyrene PC an enhancement of the upconversion luminescence of $\sim 10\times$ is reported [68]. For even more enhancement, the shape of the metal particles can be changed. Here gold nanorods were implanted into the periodic structure of three-dimensional PMMA OPC and the $\text{NaYF}_4\text{:Yb,Er}$ particles were assembled on the surface leading to a 1200-fold enhancement by the combination of photonic effects together with surface plasmon resonance [69].

Bringing the UCNPs in direct contact to a noble metal, does not result in a significant enhancement as non-radiative transitions from UCNPs to the metal is expected. This can be suppressed by an additional dielectric layer between the metal and the particle as shown by Wang *et al.* [70]. They used Ta_2O_5 as spacer because of the high refractive index of 2.1 which closely matches the refractive index of NaYF_4 of 1.95. An overall upconversion intensity of the Er^{3+} emission was 145-fold enhanced by excitation at 980 nm with a power density of $73 \text{ W}\cdot\text{cm}^{-2}$. It is reported that this complex hybrid system can easily be assembled on flexible substrates by inkjet printing and therefore this method might become of importance for future bioanalytical applications. Hu *et al.* have developed a biochip-based application for bare eye detection of mRNA in patient samples for early diagnosis of cancer, presented in Figure 1.8 [71].

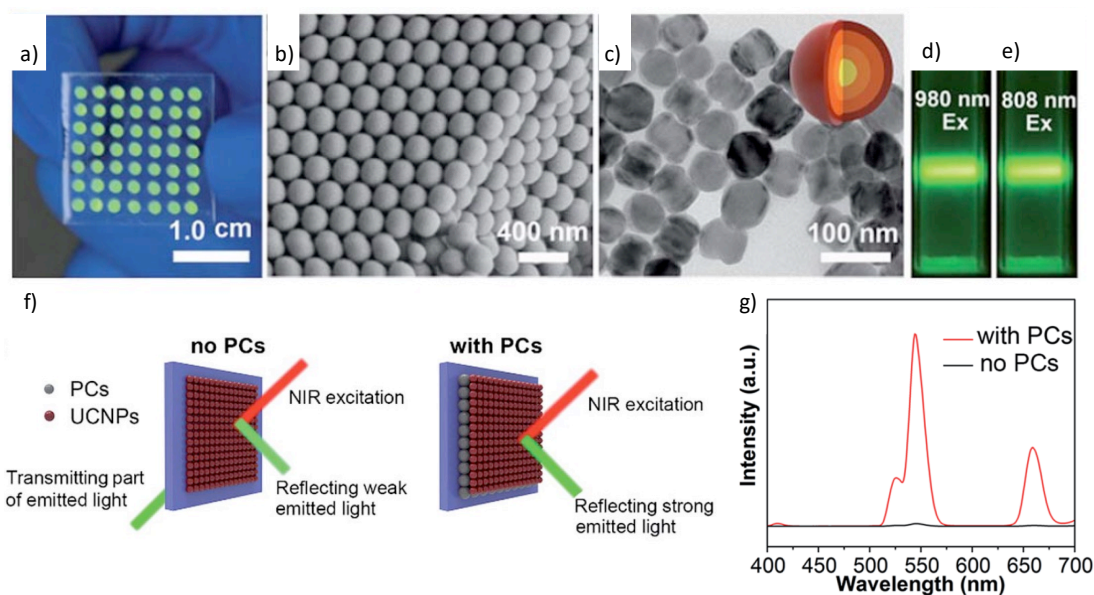


Figure 1.8 | (a) Photograph of the PC-based substrate. (b) Scanning electron microscope image of the PC dots. (c) Transmission electron microscopy image of the Er-doped UCNP. Luminescence photographs of the Er-doped UCNP using 980 nm (d) and 808 nm (e) illumination of an aqueous dispersion of the UCNP with an excitation power density of $1.00 \text{ W}\cdot\text{cm}^{-2}$. (f) Optical pathway diagrams of the upconversion emitted light when Er-doped UCNP are deposited on the substrate without (left) and with (right) PCs under NIR excitation. (g) Upconversion luminescence (UCL) spectra of the Er-doped UCNP on the substrate with and without PCs. Picture adapted with permission from Ref [71] ©2017 The Royal Society of Chemistry (RSC).

High sensitivity was achieved by the enhanced upconversion luminescence arisen from the combination of a photonic crystal functionalized with dual-wavelength excitable UCNP. The photonic crystal was assembled from monodisperse polystyrene spheres (215 nm in size) and core-shell $\beta\text{-NaYF}_4\text{:Yb,Er@NaYF}_4\text{:Yb@NaNbF}_4\text{:Yb@NaYF}_4\text{:Yb}$ (diameter of $\sim 60 \text{ nm}$). Excitation at 808 nm with a power density of $0.50 \text{ W}\cdot\text{cm}^{-2}$ enhances the luminescence intensity recorded at 544 nm more than 300 times. By such an enhancement it was possible to design a Förster resonance energy transfer (FRET)-based diagnosis tool suitable for smartphone camera read out at low excitation power. Niu *et al.* reports a 30 \times increased upconversion intensity due to the enhanced absorption by coupling opal photonic crystals with 40 nm sized UCNP doped with Tm^{3+} or Er^{3+} . The layer of nanoparticles is densely packed on the surface of the PC assembled from polystyrene and has been excited with a power density of $4 \text{ W}\cdot\text{cm}^{-2}$ [72]. A change in the refractive index of the photonic crystal provides an additional option to enhance the upconversion efficiency. This was shown by Su *et al.* when comparing PCs of polystyrene or SiO_2 spheres with relatively low refractive indices (< 1.6) to a PC made of CdS (with a bulk refractive index of 2.51) [73]. For $\text{NaYF}_4\text{:Yb,Er}$ particles assembled in a composite CdS PC film, the upconversion characteristics changed: The luminescence lifetimes get significantly shortened and red emission gets enhanced. These effects are explained by a redistribution of the density of optical states by the large refractive

index of the PC. The group of Goldschmidt studied one-dimensional photonic crystals based on Bragg stacks consisting of alternating layers of PMMA containing β -NaYF₄:Er nanoparticles and TiO₂. In a theoretically optimized assembly upconversion luminescence enhancement factors of up to 480 can be reached at 100 W·cm⁻². Such a strong enhancement can be achieved because of the modulation of the local density of photon states, while unwanted spontaneous emission processes can be suppressed [74]. The biggest enhancement so far has been reported by Lin *et al.* as a 10⁴-fold enhancement of the upconversion emissions at 450, 480 and 650 nm by embedding NaYF₄:Yb,Tm nanocrystals in PMMA resonant waveguide grating *via* excitation at 976 nm with a power density of 66 W·cm⁻² [75]. This tremendous enhancement is attributed to coupling both, excitation and upconversion emission. For sensing applications, still it is very difficult to transfer UCNPs in a well-ordered assembly on a solid-phase. Even if in literature many examples are shown bioanalytical applications of this concept are only sparsely demonstrated. Establishing suitable surface modification protocols for the particles would help to overcome this limitation [61,65].

1.3.3 Concepts for Reduced Non-Radiative Decay

Except the enhancement strategies which are still in its infancy, and therefore not so popular in bioanalytical and sensor applications yet, a lot of research was attributed on another possibility to enhance the brightness, by optimizing the particle architecture and the interface between particle and surrounding by minimizing the non-radiative deactivation of the excited states of Ln³⁺ ions in UCNPs. Strategies in modifying the particle architecture for getting brighter upconversion luminescence are a) symmetry changing of the crystal lattice with the consequence of higher energy transfers rates of the dopants in the crystal lattice; b) variations of the doping ratio, taking into account that for small particles < 50 nm surface-to-volume effects become more important, c) surface passivation preventing the non-radiative decay due to surface defects, ligands or solvent molecules, and d) energy migration by core – shell architecture promoting the energy transfer towards the core of the particle (Fig. 1.9) [16].

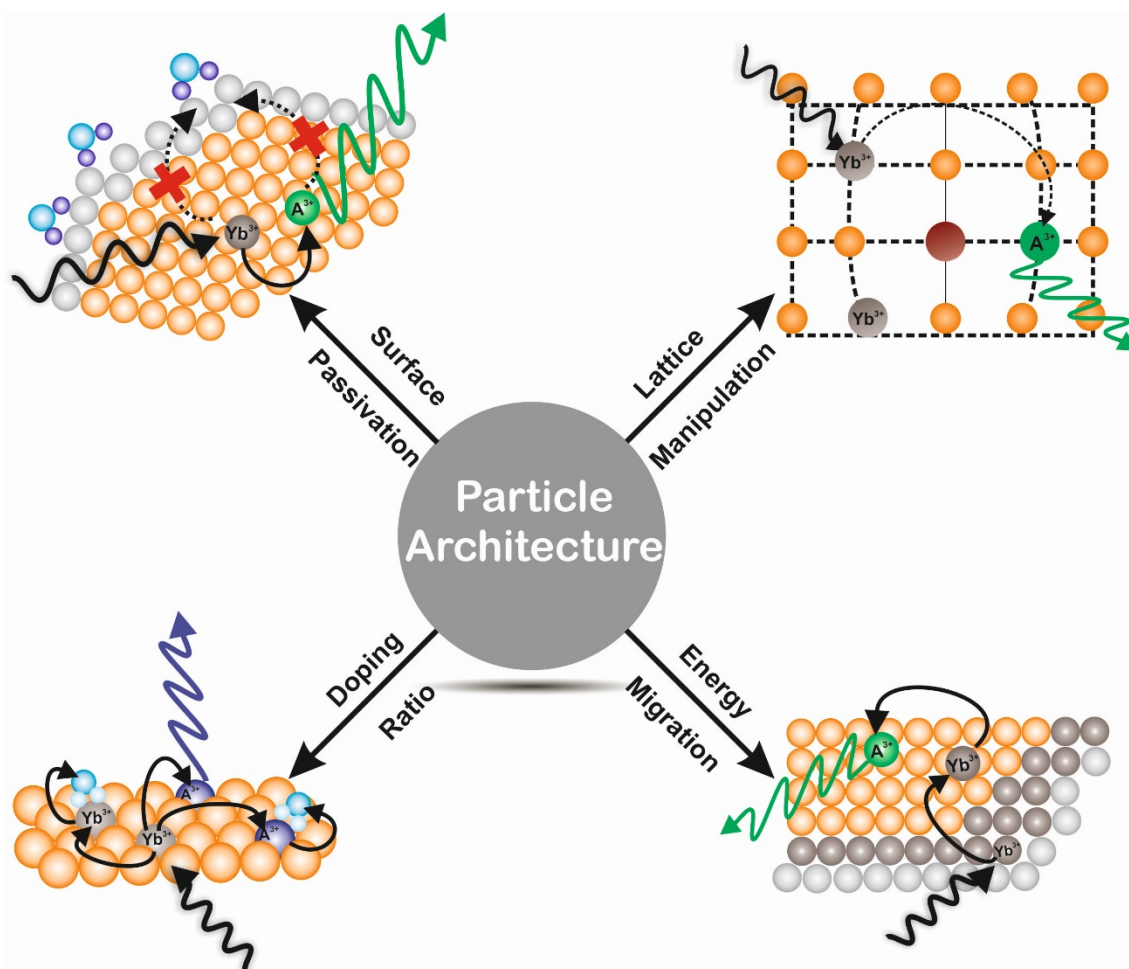


Figure 1.9 | Schemes for the various concepts to reduce non-radiative decay by changing the architecture of the upconversion nanoparticle. A³⁺ demonstrate the activator ions, in green the Er³⁺-ions and in blue the Tm³⁺-ions.

1.3.3.1 Lattice Manipulation

The most promising improvement by host lattice manipulation can be realized by replacing the Na⁺ ions of the host material by Li⁺ or K⁺, in order to optimize the distance between the lanthanide ions within the crystal. It is established that the upconversion emission of rare earth ions doped material is dependent of the 4f-transition probabilities, which are significantly affected by the local crystal field symmetry of the rare earth ions [18]. An exchange of ions can result in a less symmetric crystal lattice, with a distortion of the local field symmetry and lower energy transitions [76]. In total an enhanced luminescence intensity is expected. A significant luminescence enhancement was found by partially replacing the sodium ions in NaYF₄ crystal lattice (ionic radii: 0.97 Å) by smaller lithium ions (0.68 Å). As a consequence, Li⁺ incorporation slightly shrinks the size of the unit cell in the crystal, influencing the luminescence properties [77]. Selective enhancement of the green emission was observed. Nevertheless, by a 60% amount of lithium ions a change from the hexagonal phase to the cubic one occurs, which shows lower upconversion efficiency. By increasing the lithium

concentration to 80% the crystal lattice changes again to the tetragonal LiYF_4 phase [78]. Zhang *et al.* report on $\text{NaYF}_4:\text{Yb,Tm}$ with lithium doping of 7%, which enhances the luminescence intensity five to eight times. By increasing the doping ratio of Li^+ to 15% the luminescence intensity decreased [79]. In 2009, Nann and Wang described a luminescence enhancement of 30 times by co-doping the NaYF_4 host lattice with 80% lithium ions, which was achieved by a microwave-assisted synthesis during the heating process according to the La Mer-mechanism [80]. The X-ray powder diffraction (XRD)-measurements of the particles doped with 80% lithium ions confirmed the tetragonal phase [81]. Moreover, also the opposite case was studied by doping of NaYF_4 with an alkali ion with larger ionic radius. An exchange of up to 60% of sodium ions by potassium ions favors the hexagonal crystal lattice. Higher K^+ -content leads to the formation of K_2NaYF_6 , which lacks the stability of the hexagonal phase. Regarding to the luminescence intensity only a change in the red-to-green-ratio was observed, but no significant enhancement of the luminescence properties was found [78]. Other dopants investigated so far are Ca^{2+} , Sr^{2+} , or Ba^{2+} . A cubic phase was reported for high content (20 mol%) of M^{2+} . A 15 times higher emission (475 nm and 795 nm) by using Tm^{3+} as activator in 5 nm sized particles was obtained [82]. Wang *et al.* studied the influence of strontium respectively calcium doping ratio in dependence of the crystal growth. Sr^{2+} or Ca^{2+} dopants can significantly modify the crystal phase and the particle size of $\text{NaYF}_4:\text{Yb,Er}$ [83]. In 2017, Dionne *et al.* reported the exchange of Y^{3+} by the larger Gd^{3+} and the smaller Lu^{3+} ions. Identical particle morphology and similar unit cells were confirmed by Transmission electron microscopy (TEM), XRD and inductively coupled plasma optical emission spectrometer (ICP-OES). In summary, a 1.6× enhancement of the upconversion quantum yield was achieved by local symmetry distortion [84]. The enhancement strategy of crystal lattice manipulation is still very promising, nevertheless for practical bioanalytical applications it is mandatory to investigate the stability of such nanocrystals in aqueous systems. Recently several publications report on the leaching of ions in the presence of phosphate buffered solutions which will have massive impact on the brightness as well as on the toxicity of UCNPs [85].

1.3.3.2 Doping Ratio

To design bright particles, an effective energy transfer from the sensitizer to the activator must be ensured. The efficiency of the energy transfer can be controlled by parameters like the combination of the dopants, the distance and therefore the concentration between the sensitizer and activator ions [86]. In 2003, Krämer *et al.* optimized the doping ratio for the bulk phase of $\text{NaYF}_4:\text{Yb,Er}$ and $\text{NaYF}_4:\text{Yb,Tm}$ to 18:2 for Yb:Er and 25:0.3 Yb:Tm [14]. Many

research groups adapted these doping ratios for the design of bio(analytical) application of UCNPs [87-89], neglecting the fact that for small nanoparticles the increased surface-to-volume-ratio gets more prominent. Especially for particles in the size-regime of 10 to 50 nm different doping ratios [90] together with variations in the excitation power [91] affects the brightness of the upconversion luminescence. Jin *et al.* synthesized NaYbF₄ particles with a doping ratio of 4% Tm³⁺ (14 nm in diameter) and compared the brightness of these particles with the classical NaYF₄:20%Yb,0.3%Tm particles. The blue emission was increased about three times by low laser power excitation [92]. For NaYF₄:Yb,Er (8 nm) [93] and also NaYF₄:Yb,Tm (25 nm and 40 nm) [94,95] particles an increase in the activator concentration results in an improved upconversion efficiency. In both cases high laser power densities of 10⁵ W·cm⁻² and 10⁶ W·cm⁻² were used, which complicates the situation as saturation of individual excited states need to be taken into account. Cohen *et al.* developed a systematic model based on a robotic particle synthesis of the interactions between Ln³⁺ dopants for the ideal design of the UCNPs, resulting in bright particles for tracking biological processes [96]. All particle designs presented so far, show a heterogeneous doping which can induce cross-relaxation and energy transfer barrier between dopant ions because of the local relative enrichment of the dopants. For avoiding this, a homogenous doping by a layer by layer particle architecture might be attractive. The quantum yield of the homogenous Er³⁺,Yb³⁺-doped particle was two times higher than the same heterogenous doped particles under a laser power density of 50 W·cm⁻² [97]. For bioanalytical applications where the size of the particles is critical and cannot be varied or when the excitation power needs to be low and fixed the degree of freedom in enhancing the luminescence by variations of the dopants is low. So, in detail, having a model for calculating the ideal doping ratios of the lanthanides in UCNPs of a desired size would be advantageous for receiving bright particles. Such a model only can be established when the photophysical properties of UCNPs in dependence of the doping and the size are fully described.

1.3.3.3 Surface Passivation

The luminescence of surface dopants can be readily quenched by high oscillators arising from surface defects, ligands and solvent molecules [98], therefore surface passivation will lead to an enhancement of the brightness of UCNPs [13]. Wang *et al.* studied in detail the influence of an inert shell on differently sized particles. Particles of 15 nm in diameter consisting of a 2.5 nm thick shell show a comparable brightness like core particles with a size of 25 nm (Fig. 1.10). A comparison of the intensity loss of core particles and the core – shell particles

confirmed the quenching of the upconversion luminescence by water molecules in close proximity to the particle surface [99]. A coating with a thin non-doped NaYF_4 -shell of less than 1.5 nm thickness on the core particles $\text{NaYF}_4:\text{Yb},\text{Er}$ of ~ 8.5 nm results in a 7.4-fold enhancement of the upconversion luminescence [100]. Also Rinkel *et al.* synthesized 5 nm sized core particles $\text{NaYF}_4:\text{Yb},\text{Er}$ and enhanced the upconversion efficiency about 16 times by growing a 2 nm inert shell on the particles [101]. A shell of only 2 nm thickness is sufficient for reaching the maximal luminescence increase. This was demonstrated by Gargas *et al.* by studying the luminescence properties of single particles [93]. Through the increased upconversion efficiency by a core – shell design, Drees *et al.* applied $\text{NaYF}_4:\text{Yb},\text{Er}@\text{NaYF}_4$ particles modified with a nanobody recognizing the green fluorescent protein (GFP) inside living cells for resolving protein interactions [102].

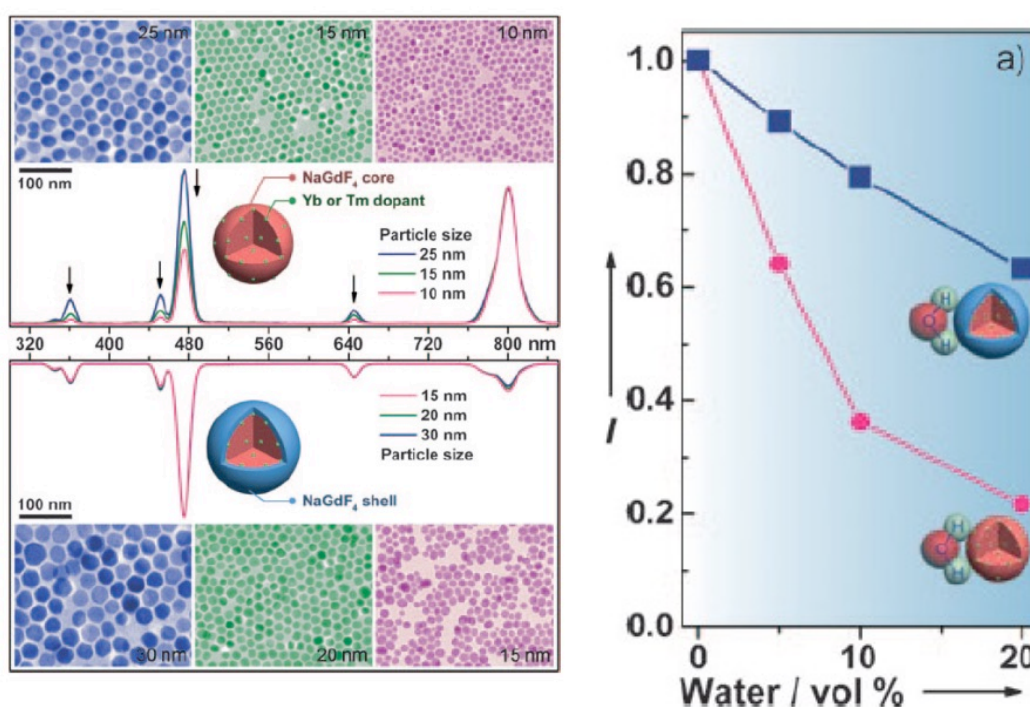


Figure 1.10 | Upconversion emission spectra of $\text{NaGdF}_4:\text{Yb},\text{Tm}$ with different sizes with and without a thin layer of NaGdF_4 . All spectra were recorded under excitation of a 980 nm cw diode laser at a power density of $10 \text{ W}\cdot\text{cm}^{-2}$ (left). Comparison of emission intensity loss for 15 nm core particles and corresponding 20 nm core/shell particles in ethanol with different amounts of water (right). Picture adapted with permission from Ref [99] © 2014 Wiley-VCH GmbH, Weinheim.

Core – shell structures with different host materials in one particle are also presented in the literature. Capping of 26 nm sized cubic NaYF_4 UCNPs with a 2 nm thick shell of CaF_2 has been shown to produce nanocrystals with an unusually high quantum yield of $\sim 3\%$ for the red emission at low excitation power densities of $10 \text{ W}\cdot\text{cm}^{-2}$. These particles, conjugated with aminolevulinic acid for application in photodynamic therapy, show 70% cell death after 20 min

of NIR irradiation [103]. Zhu *et al.* studied also particles with an inert shell of CaF_2 on the core particles of $\text{NaYbF}_4:\text{Tb}$, resulting in 12 nm sized particles showing a 690-fold increased emission intensity due to the shell growing and have comparable upconversion intensities like the well-known $\text{NaYF}_4:\text{Yb,Er}$ particles. These core – shell particles were applied to lymph node imaging in vivo [104]. The inert shell has to be critically investigated for sensor applications based on an efficient FRET as the efficiency decreases by the power of six with increasing distance between donor and acceptor. Nevertheless, this strategy will be a simple method of choice when applying UCNPs as luminescent probes in theranostic and bioimaging applications.

1.3.3.4 Energy Migration

In contrast to inert shells one also can grow a shell doped with sensitizer ions on a core particle. It is expected that more photons get absorbed and migrate to the core which leads to an enhancement of the upconversion luminescence. In 2009, Capobianco *et al.* presented the strategy of a core – active shell architecture for enhancing the intensity of the upconversion: Particles with a diameter of 14 nm of the type $\text{NaGdF}_4:\text{Yb,Er}@\text{NaGdF}_4:\text{Yb}$ demonstrated a 10-times increase in the green or rather in the red emission compared with core only (11 nm) particles which were doped with an unusual high content of 40% Yb^{3+} for having equal amount of sensitizer ions [105]. Here the spatial separation of the sensitizer enables a higher energy input to the luminescence center in the core, which results in five times increase in the green and eight times increase in the red emission. The idea of active shell growing is very popular [94,98,104]. Ostwald ripening dynamics enables the growth of several shells which adjustable thickness on the core particle [106]. Chen *et al.* reported on NCs consisting of an active core-multi-shell $\text{NaGdF}_4:60\%\text{Yb}@\text{NaYF}_4:20\%\text{Yb},2\%\text{Er}@\text{NaGdF}_4:20\%\text{Yb}$ presenting a rod like structure with a length of ~30 nm and a width of ~17 nm. By such Yb^{3+} distribution in the core and shells no self-quenching was found and an efficient transfer of the absorbed NIR radiation to the luminescent shell layer through the Yb^{3+} doping in the active-core and active-shell was reached. The luminescence spectra for this particle architecture was compared with other core – shell – shell particles (Fig. 1.11) showed the highest intensity for the green and red emission [107].

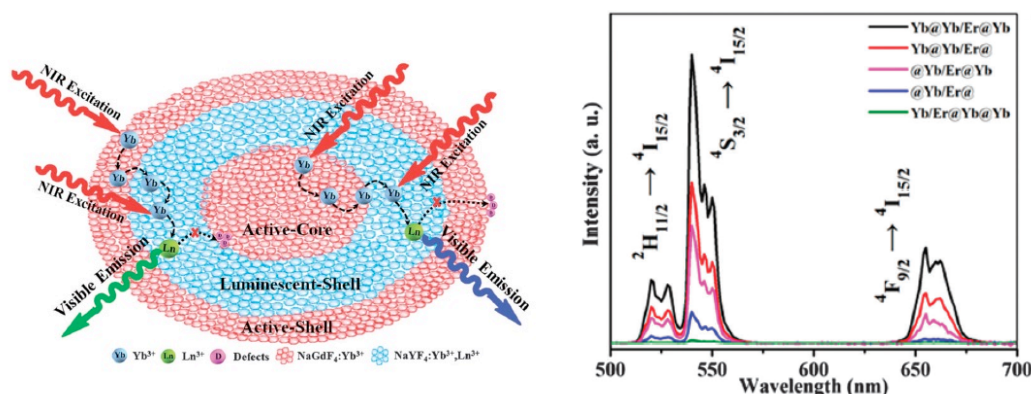


Figure 1.11 | Schematic design of the active-core - luminescent-shell - active-shell architecture to enhance the Ln³⁺ upconversion luminescence (left) and the luminescence spectra of the different particle designs upon NIR excitation. Picture adapted with permission from Ref © [107]. 2016 The Royal Society of Chemistry (RSC).

Zhang *et al.* presented a fundamental study (theoretical model and spectroscopic measurements) in which they can control the upconversion emission time behavior by tuning the energy migration paths in various specifically designed nanostructures [108]. For a further increase in the luminescence properties of these core-multi-shell particles a final inert shell is favored. The luminescence efficiency was tripled by growing a 3 nm thick inert shell of NaGdF₄ on 14 nm sized core/active shell particles from the type NaGdF₄:Yb,Er@NaGdF₄:Yb upon 980 nm illumination with a power density of 50 W·cm⁻² [98]. Haase *et al.* reported the intermixing of core and shell material of 14 nm sized NaEuF₄@NaGdF₄ particles during the shell formation [109], which indicate stability issues of such core-multi-shell particle architectures. Detailed studies on long-time stability and ion intermixing are still missing.

1.3.4 Change of Excitation Wavelength

Biological and sensor applications of UCNPs are predominately performed in aqueous systems. In such media, one can gain more upconversion luminescence by shifting the excitation wavelength by tandem sensitization. Water shows a local absorption maximum at 980 nm (Fig. 1.12), which implies that excitation light at this wavelength gets absorbed leading to a distance dependent decrease in the excitation power density. This is especially crucial in bioanalytical applications using the individual emission bands of UCNPs for self-referenced sensing. Another drawback is displayed by the fact that illumination by a 980 nm cw laser can lead to overheating effects. This is especially a problem when the UCNP sensing probe should be used in cells or tissue [110].

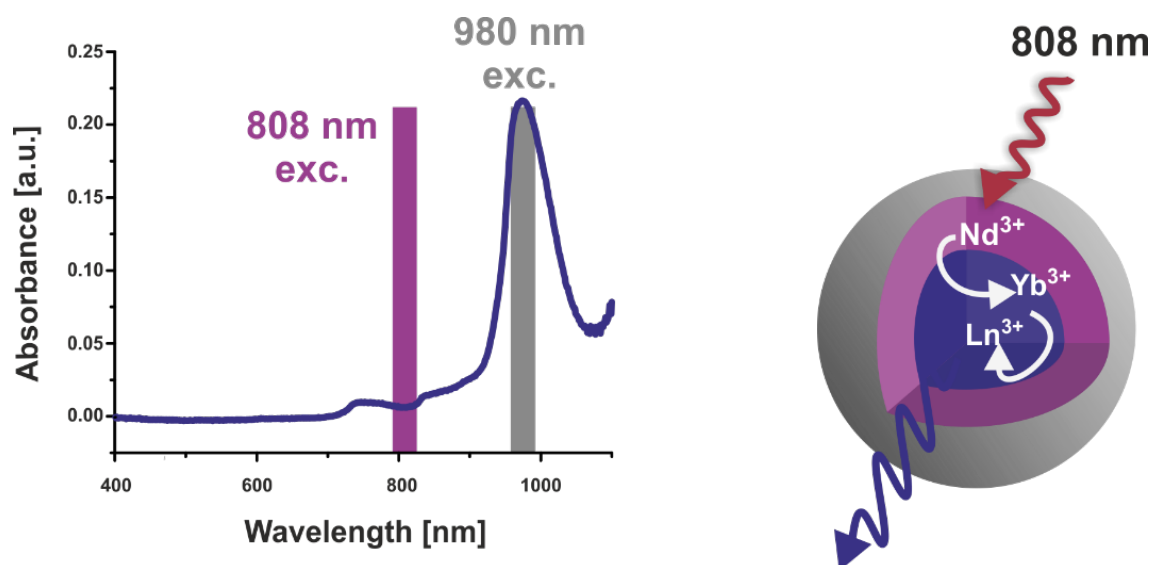


Figure 1.12 | Right: Absorbance spectra of water (blue line) showing the overlap to 980 nm excitation (grey) and almost no absorbance at 808 nm excitation (purple). Left: Core – shell particle architecture for 808 nm excitation with spatial separation of Nd^{3+} and activator ions Ln^{3+} preventing non-radiative energy back transfer to the sensitizer ion.

In 2011, Andersson-Engels and co-worker reported on this problem and present a solution by shifting the excitation wavelength to 915 nm for $\text{NaYbF}_4:\text{Tm},\text{Er},\text{Ho}$ particles. Overheating effects were significantly minimized, and deeper tissue penetration was achieved. But the excitation wavelength still overlaps partially with the absorption peak of H_2O [110]. These limitations can be fully overcome by the design of core – shell particles with Nd^{3+} , Yb^{3+} doping in the shell. Neodymium absorbs light at 808 nm and transfers the energy to Yb^{3+} which is also present in the core and acting as a bridge to excite Er^{3+} , Tm^{3+} , or Ho^{3+} ions doped in the core of the particle [34]. These architecture seems to be most promising so far, but a lot of other core – shell systems with huge variations in the doping ratios have been described in literature so far, e.g. tri-doped $\text{NaYF}_4:20\%\text{Yb},2\%\text{Er},2\%\text{Nd}@ \text{NaYF}_4$ core – shell particles excitable at 808 nm [111]. The excitation at 808 nm presents a lower overheating effect of water compared to the 980 nm excitation. But the concentration of neodymium ions has to be lower than 2% minimizing cross-relaxation between Nd^{3+} and the Er^{3+} ions if the ions are placed together in the core [112,113]. To overcome this Xie and co-workers synthesized $\text{NaYF}_4:30\%\text{Yb},2\%\text{Er},1\%\text{Nd}$ core particles with a NaYF_4 -shell doped with 20% Nd^{3+} enhancing the luminescence properties by a factor of seven compared to tri-doped $\text{NaYF}_4:\text{Yb},\text{Er},\text{Nd}@ \text{NaYF}_4$ core – shell particles. Here the sensitizer Nd^{3+} and the activator Er^{3+} are spatially separated. Gao *et al.* compared particles $\text{NaYF}_4:\text{Yb},\text{Tm},\text{Nd}@ \text{NaYF}_4:\text{Nd}$ excitable at 808 nm with particles having instead the Nd^{3+} -shell an inert shell. The particles excited at 808 nm show a seven times higher blue emission compared with $\text{NaYF}_4:\text{Yb},\text{Tm},\text{Nd}@ \text{NaYF}_4$ particles excited at 980 nm [114]. The importance of separating the Nd^{3+} ions from the

activator lead to particle architectures with an additional separating shell doped with Yb^{3+} between activator and the sensitizer layer. The transition layer doped with 10% Yb^{3+} of 1.45 nm thickness successfully blocked the non-radiative resonant energy transfer from the activator to the sensitizer [115]. The advantage of a transition layer is also reported by the workgroup of Bednarkiewicz for enhancing the brightness of Tb^{3+} -doped core – multi-shell particles, with emissions at 540 and 585 nm [116]. From all studies describing Nd^{3+} -sensitized UCNPs so far one can identify that there are numerous compositions of core-multi-shell architectures as well as doping ratios (Fig. 1.13). This clearly indicates that there is a lack of information about the exact interplay of parameters like core size, shell thickness and lanthanide compositions.

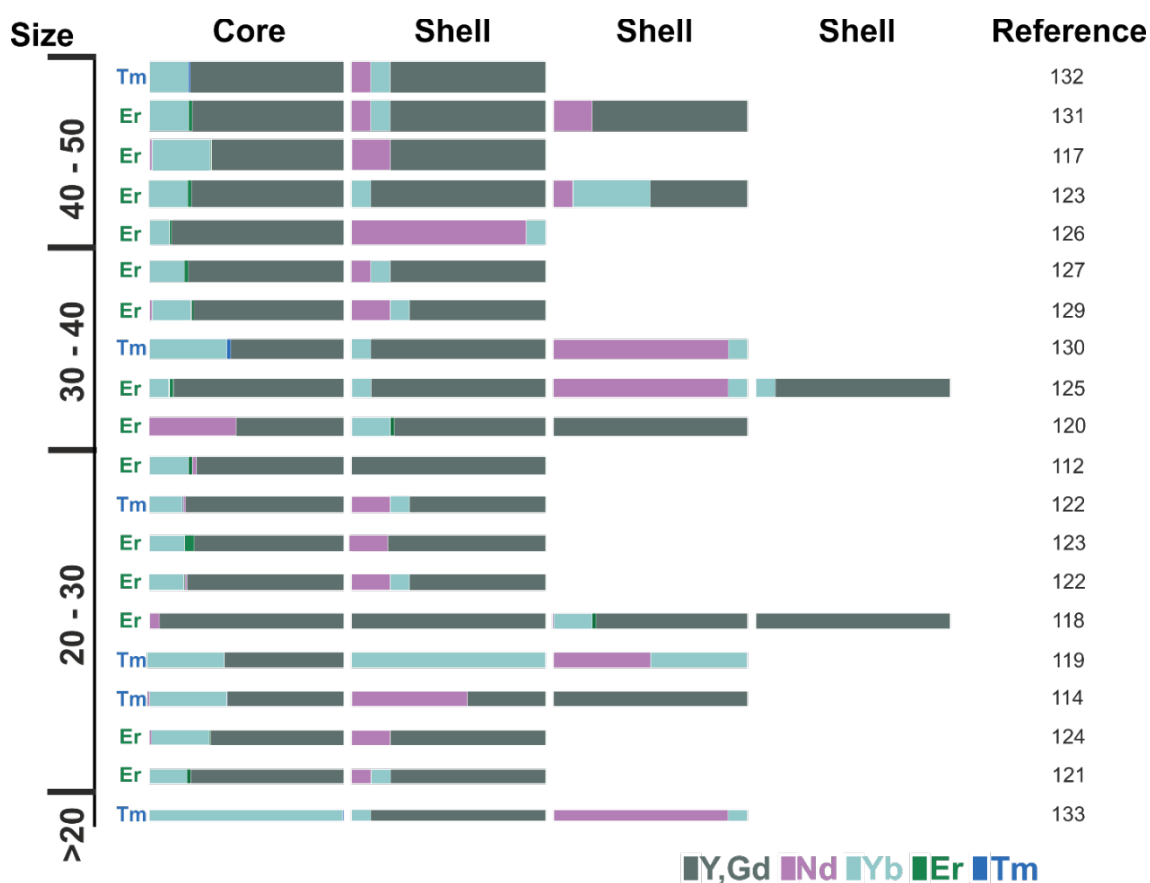


Figure 1.13 | Examples of combinations of Nd^{3+} -sensitized upconversion nanoparticle architectures. The systems are sorted according to the final particle size. The doping ratios are presented in different colors as explained in the legend. In case core or shells are doped by an activator ion it is given by the symbol of the chemical element [112, 114, 117-133].

First (bio)analytical applications of Nd^{3+} -sensitized UCNPs have been described recently. Cyanine dye (hCy3) modified core – shell nanoparticles consisting of $\text{NaYF}_4:\text{Yb},\text{Nd},\text{Er}@ \text{NaYF}_4:\text{Nd}$ were applied to detect ClO^- with a low detection limit of 27 ppb, high selectivity and rapid response in living cells of a mouse by ratiometric upconversion luminescence imaging [124]. Neodymium sensitized UCNPs are of high interest in theranostic

applications as for example in photodynamic therapy [126,128,133] because of deep tissue penetration. Figure 1.14 displays an aqueous dispersion of the Nd^{3+} -sensitized core – shell nanoparticles filled in a 10 cm long cuvette ($\sim 4 \text{ mg}\cdot\text{mL}^{-1}$) and excited simultaneously by an 808 nm and 980 nm laser module. A continuous green upconversion luminescence over the whole distance can be observed for 808 nm excitation, while for 980 nm excitation the luminescence intensity fades out with increasing distance due to the absorbance of the excitation light by water. A forensic application is presented by blood fingerprint imaging with UCNPs with tandem sensitization which subtly averts the laser-induced thermal effect [133]. Also $\text{NaGdF}_4:\text{Yb},\text{Er}@ \text{NaYF}_4:\text{Yb},\text{Nd}$ core shell particles were used as luminescent marker for water detection application. The ligand free Nd^{3+} -sensitized core – shell particles dispersed in DMF shows a linear dependence of the relative luminescence intensity as a function of the water content *via* 808 nm excitation ($0.5 \text{ W}\cdot\text{cm}^{-2}$) [134].

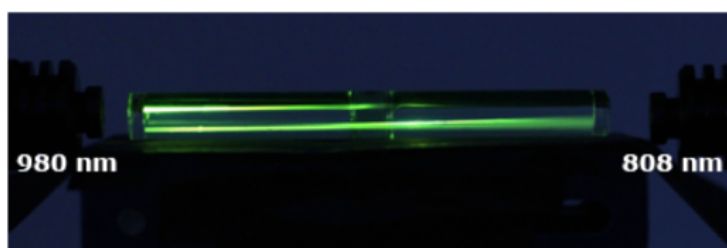


Figure 1.14 | Image of $\text{NaYF}_4:\text{Yb},\text{Er}@ \text{NaYF}_4:\text{Yb},\text{Nd}$ particles dispersed in water and excited by 980 nm (from the left) and 808 nm (from the right) at comparable low excitation power density. Adapted from the authors master's thesis.

The combination of the Nd^{3+} doping and antenna molecules has shown by Prasad's group. The concept describes a multistep cascade energy transfer from broadly infrared-harvesting organic dyes to the sensitizer Nd^{3+} in the shell followed by a sequential non-radiative energy transfer to the upconverting ion pairs in the core. Here a remarkable upconversion quantum efficiency of about 19% was obtained, which is nearly 100 times higher than quantum efficiencies reported by others [135,30]. The combination of the both strategies shows excellent temperature sensing properties due to enhanced brightness of the particles, but the transfer of these particles in aqueous solution has not been reported [33].

1.4 Conclusion and Perspective

In many publications, researcher demonstrated the proof of principle for the great potential of UCNPs in applications ranging from biology to medicine. The low quantum efficiency is still one of the main issues that impede the development of products like commercially available

bioassays based on UCNPs. Therefore, one of the main research directions in this field deals with improving the brightness of these type of luminescent nanomaterials. In this review the recent strategies for the enhancement of upconversion luminescence, classified in three main directions are highlighted: a) improve the efficiency of energy absorption by the sensitizer *via* coupling to plasmonic or photonic structures or to attach ligands for light harvesting; b) minimizing non-radiative deactivation by changing the architecture of UCNPs; and c) changing the excitation wavelength to get bright particles at low excitation power density for applications in aqueous systems. All strategies clearly lead to an improvement as displayed in Figure 1.15, but it is really difficult at the present stage to compare these enhancement factors or to make suggestions which direction is most promising.

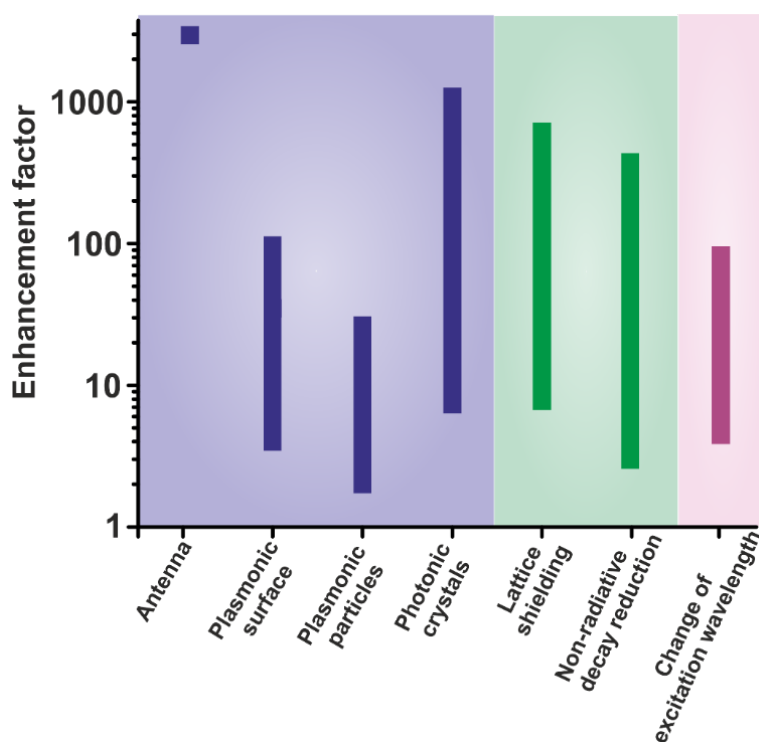


Figure 1.15 | Comparison of the ranges of enhancement factors achieved by several strategies to enhance the upconversion luminescence.

One has to keep in mind, that in general, it is much easier to achieve tremendous enhancement when the original efficiency is poor. For such reason enhancement factors are often misleading and should not be overestimated. As long as there are no standardized materials or standardized protocols for classifying the brightness of upconversion nanomaterials available, those numbers comparing relative emission intensities are only of limited usability. The research in enhancing the luminescence of UCNPs is still in its infancy and a better understanding of the photophysics, especially of complex core – shell systems or for complex

hybrid systems coupling different types of materials with UCNPs is mandatory. Furthermore, investigations on chemical stability, the composition of these materials at an atomic scale, the time-scale of processes happening at all interfaces in core – multi shell architectures are only in the early beginning. Up to now there is only little knowledge on the interaction of dispersed particles with the media itself or with adsorbates from the media, which also will affect the luminescence properties by quenching effects, or even by dissolution or by aggregation of particles, both of great importance for bioanalytical applications. By taking into account the manifold parameters which can be optimized on the way to design small but also bright UCNPs excitable at moderate laser power density, it is expected that fundamental studies will lead to a better understanding of the upconversion luminescence and have a huge impact to a bright future of UCNPs as probes in biosensors, healthcare and many other applications.

1.5 References

- [1] Liu X, Yan CH, Capobianco JA (2015) Photon upconversion nanomaterials. *Chem. Soc. Rev.* 44(6):1299-301.
- [2] Ali Y, Zohre R, Mostafa J, Samaneh R (2015) Applications of upconversion nanoparticles in molecular imaging: A review of recent advances and future opportunities. *Biosci., Biotechnol. Res. Asia* 12:131-40.
- [3] Wang F, Banerjee D, Liu Y, Chen X, Liu X (2010) Upconversion nanoparticles in biological labeling, imaging, and therapy. *Analyst* 135(8):1839-54.
- [4] Auzel F (2004) Upconversion and anti-stokes processes with f and d ions in solids. *Chem. Rev.* 104(1):139-74.
- [5] Scheeps R (1996) Upconversion laser processes. *Prog. Quant. Electr.* 20(4):271-358.
- [6] Zhou JC, Yang ZL, Dong W, Tang RJ, Sun LD, Yan CH (2011) Bioimaging and toxicity assessments of near-infrared upconversion luminescent NaYF₄:Yb,Tm nanocrystals. *Biomaterials* 32(34):9059-67.
- [7] Wilhelm S, Hirsch T, Patterson WM, Scheucher E, Mayr T, Wolfbeis OS (2013) Multicolor upconversion nanoparticles for protein conjugation. *Theranostics* 3(4):239-48.
- [8] Schietinger S, Menezes LD, Lauritzen B, Benson O (2009) Observation of size dependence in multicolor upconversion in single Yb³⁺, Er³⁺ codoped NaYF₄ nanocrystals. *Nano Lett.* 9(6):2477-81.
- [9] Zhou J, Liu Z, Li F (2012) Upconversion nanophosphors for small-animal imaging. *Chem. Soc. Rev.* 41(3):1323-49.
- [10] Bloembergen (1959) N. Solid state infrared quantum counters. *Phys. Rev. Lett.* 2(3):84.
- [11] Wang F, Liu X (2014) Multicolor tuning of lanthanide-doped nanoparticles by single wavelength excitation. *Acc. Chem. Res.* 47(4):1378-85.
- [12] Suyver JF, Grimm J, van Veen MK, Biner D, Krämer KW, Güdel HU (2006) Upconversion spectroscopy and properties of NaYF₄ doped with Er³⁺, Tm³⁺, and/or Yb³⁺. *J. Lumin.* 117:1–12.
- [13] Chen G, Qiu H, Prasad PN, Chen X (2014) Upconversion nanoparticles: Design, nanochemistry, and applications in theranostics. *Chem. Rev.* 114(10):5161-214.

- [14] Krämer KW, Biner D, Frei G, Güdel HU, Hehlen MP, Lüthi SR (2004) Hexagonal sodium yttrium fluoride based green and blue emitting upconversion phosphors. *Chem. Mater.* 16(7):1244-51.
- [15] Naccache R, Vetrone F, Mahalingam V, Cuccia LA, Capobianco JA (2009) Controlled synthesis and water dispersibility of hexagonal phase $\text{NaCdF}_4\text{:Ho}^{3+}/\text{Yb}^{3+}$ nanoparticles. *Chem. Mater.* 21(4):717-23.
- [16] Haase M, Schäfer H (2011) Upconverting nanoparticles. *Angew. Chem. Int. Ed.* 50(26):5808-29.
- [17] Resch-Genger U, Gorris HH (2017) Perspectives and challenges of photon-upconversion nanoparticles-Part I: Routes to brighter particles and quantitative spectroscopic studies. *Anal. Bioanal. Chem.* 409(25):5855-74.
- [18] Han S, Deng R, Xie X, Liu X (2014) Enhancing luminescence in lanthanide-doped upconversion nanoparticles. *Angew. Chem. Int. Ed.* 53(44):11702-15.
- [19] Wang F, Liu X (2009) Recent advances in the chemistry of lanthanide-doped upconversion nanocrystals. *Chem. Soc. Rev.* 38(4):976-89.
- [20] Gorris HH, Resch-Genger U (2017) Perspectives and challenges of photon-upconversion nanoparticles-Part II: Bioanalytical applications. *Anal. Bioanal. Chem.* 409(25):5875-90.
- [21] Muhr V, Wilhelm S, Hirsch T, Wolfbeis OS (2014) Upconversion nanoparticles: From hydrophobic to hydrophilic surfaces. *Acc. Chem. Res.* 47(12):3481-93.
- [22] Zhou J, Liu Q, Feng W, Sun Y, Li F (2014) Upconversion luminescent materials: Advances and applications. *Chem. Rev.* 115(1):395-465.
- [23] Lin M, Zhao Y, Wang S, Liu M, Duan Z, Chen Y, Li F, Xu F, Lu T (2012) Recent advances in synthesis and surface modification of lanthanide-doped upconversion nanoparticles for biomedical applications. *Biotechnol. Adv.* 30(6):1551-61.
- [24] Niu W, Wu S, Zhang S (2010) A facile and general approach for the multicolor tuning of lanthanide-ion doped NaYF_4 upconversion nanoparticles within a fixed composition. *J. Mater. Chem.* 20(41):9113-7.
- [25] Wilhelm S, Kaiser M, Würth C, Heiland J, Carrillo-Carrion C, Muhr V, Wolfbeis OS, Parak WJ, Resch-Genger U, Hirsch T (2015) Water dispersible upconverting nanoparticles: Effects of surface modification on their luminescence and colloidal stability. *Nanoscale* 7(4):1403-10.
- [26] Fischer S, Fröhlich B, Krämer KW, Goldschmidt JC (2014) Relation between excitation power density and Er^{3+} doping yielding the highest absolute upconversion quantum yield. *J. Phys. Chem. C.* 118(51):30106-14.
- [27] Chen G, Shen J, Ohulchanskyy TY, Patel NJ, Kutikov A, Li Z, Song J, Pandey RK, Ågren H, Prasad PN, Han G (2012) α - $\text{NaYbF}_4\text{:Tm}^{3+}/\text{CaF}_2$ core/shell nanoparticles with efficient near-infrared to near-infrared upconversion for high-contrast deep tissue bioimaging. *ACS Nano.* 6(9):8280-7.
- [28] Gnach A, Lipinski T, Bednarkiewicz A, Rybka J, Capobianco JA (2015) Upconverting nanoparticles: Assessing the toxicity. *Chem. Soc. Rev.* 44(6):1561-84.
- [29] van Veggel FC, Dong C, Johnson NJ, Pichaandi J (2012) Ln^{3+} -doped nanoparticles for upconversion and magnetic resonance imaging: Some critical notes on recent progress and some aspects to be considered. *Nanoscale* 4(23):7309-21.
- [30] Chen G, Damasco J, Qiu H, Shao W, Ohulchanskyy TY, Valiev RR, Wu X, Han G, Wang Y, Yang C, Ågren H (2015) Energy-cascaded upconversion in an organic dye-sensitized core/shell fluoride nanocrystal. *Nano Lett.* 15(11):7400-7.
- [31] Zhang J, Shade CM, Chengelis DA, Petoud S (2007) A strategy to protect and sensitize near-infrared luminescent Nd^{3+} and Yb^{3+} : Organic tropolonate ligands for the sensitization of Ln^{3+} -doped NaYF_4 nanocrystals. *J. Am. Chem. Soc.* 129(48):14834-5.

- [32] Wu X, Lee H, Bilsel O, Zhang Y, Li Z, Chen T, Liu Y, Duan C, Shen J, Punjabi A, Han G (2015) Tailoring dye-sensitized upconversion nanoparticle excitation bands towards excitation wavelength selective imaging. *Nanoscale* 7(44):18424-8.
- [33] Shao Q, Li X, Hua P, Zhang G, Dong Y, Jiang J (2017) Enhancing the upconversion luminescence and photothermal conversion properties of ~ 800 nm excitable core/shell nanoparticles by dye molecule sensitization. *J. Colloid Interface Sci.* 486:121-7.
- [34] Xie X, Liu X (2012) Photonics: Upconversion goes broadband. *Nat. Mater.* 11(10):842-3.
- [35] Zou W, Visser C, Maduro JA, Pshenichnikov MS, Hummelen JC (2012) Broadband dye-sensitized upconversion of near-infrared light. *Nat. Photonics* 6(8):560-4.
- [36] Wang X, Valiev RR, Ohulchanskyy TY, Ågren H, Yang C, Chen G (2017) Dye-sensitized lanthanide-doped upconversion nanoparticles. *Chem. Soc. Rev.* 46(14):4150-67.
- [37] Kastrop L, Hell SW (2004) Absolute optical cross section of individual fluorescent molecules. *Angew. Chem. Int. Ed.* 43(48):6646-9.
- [38] Luu Q, Hor A, Fisher J, Anderson RB, Liu S, Luk TS, Paudel HP, Farrokh Baroughi M, May PS, Smith S (2014) Two-color surface plasmon polariton enhanced upconversion in NaYF₄:Yb,Tm nanoparticles on Au nanopillar arrays. *J. Phys. Chem. C* 118(6):3251-7.
- [39] Wu DM, García-Etxarri A, Salleo A, Dionne JA (2014) Plasmon-enhanced upconversion. *J. Phys. Chem. Lett.* 25(22):4020-31.
- [40] Fischer S, Kumar D, Hallermann F, von Plessen G, Goldschmidt JC (2016) Enhanced upconversion quantum yield near spherical gold nanoparticles – a comprehensive simulation-based analysis. *Optics Express* 24(6):460-75.
- [41] Deng W, Xie F, Baltar HT, Goldys EM (2013) Metal-enhanced fluorescence in the life sciences: Here, now and beyond. *Phys. Chem. Chem. Phys.* 15(38):15695-708.
- [42] Lindquist NC, Nagpal P, McPeak KM, Norris DJ, Oh SH (2012) Engineering metallic nanostructures for plasmonics and nanophotonics. *Rep. Prog. Phys.* 75(3):036501.
- [43] Paudel HP, Zhong L, Bayat K, Baroughi MF, Smith S, Lin C, Jiang C, Berry MT, May PS (2011) Enhancement of near-infrared-to-visible upconversion luminescence using engineered plasmonic gold surfaces. *J. Phys. Chem. C* 115(39):19028-36.
- [44] Zhang H, Xu D, Huang Y, Duan X (2011) Highly spectral dependent enhancement of upconversion emission with sputtered gold island films. *Chem. Commun.* 47(3):979-81.
- [45] Saboktakin M, Ye X, Chettiar UK, Engheta N, Murray CB, Kagan CR (2013) Plasmonic enhancement of nanophosphor upconversion luminescence in Au nanohole arrays. *ACS Nano* 7(8):7186-92.
- [46] Lu D, Cho SK, Ahn S, Brun L, Summers CJ, Park W (2014) Plasmon enhancement mechanism for the upconversion processes in NaYF₄:Yb³⁺,Er³⁺ nanoparticles: Maxwell versus Förster. *ACS Nano* 8(8):7780-92.
- [47] Zhou D, Liu D, Xu W, Yin Z, Chen X, Zhou P, Cui S, Chen Z, Song H (2016) Observation of considerable upconversion enhancement induced by Cu_{2-x}S plasmon nanoparticles. *ACS Nano* 10(5):5169-79.
- [48] Zhang H, Li Y, Ivanov IA, Qu Y, Huang Y, Duan X (2010) Plasmonic modulation of the upconversion fluorescence in NaYF₄:Yb/Tm hexaplate nanocrystals using gold nanoparticles or nanoshells. *Angew. Chem. Int. Ed.* 49(16):2865-8.
- [49] Liu N, Qin W, Qin C, Jiang T, Zhao D (2011) Highly plasmon-enhanced upconversion emissions from Au@β-NaYF₄:Yb,Tm hybrid nanostructures. *Chem. Commun.* 47(27):7671-3.
- [50] Tu N, Wang L (2013) Surface plasmon resonance enhanced upconversion luminescence in aqueous media for TNT selective detection. *Chem. Commun.* 49(56):6319-21.

- [51] Wang Z, Wang C, Han Q, Wang G, Zhang M, Zhang J, Gao W, Zheng H (2017) Metal-enhanced upconversion luminescence of NaYF₄:Yb/Er with Ag nanoparticles. *Mater. Res. Bull.* 88:182-7.
- [52] Feng W, Sun LD, Yan CH (2009) Ag nanowires enhanced upconversion emission of NaYF₄:Yb,Er nanocrystals via a direct assembly method. *Chem. Commun.* 14(29):4393-5.
- [53] Kannan P, Abdul Rahim F, Chen R, Teng X, Huang L, Sun H, Kim DH (2013) Au nanorod decoration on NaYF₄:Yb/Tm nanoparticles for enhanced emission and wavelength-dependent biomolecular sensing. *ACS Appl. Mater. Interfaces* 5(9):3508-13.
- [54] Yuan P, Lee YH, Gnanasammandhan MK, Guan Z, Zhang Y, Xu QH (2012) Plasmon enhanced upconversion luminescence of NaYF₄:Yb,Er@SiO₂@Ag core-shell nanocomposites for cell imaging. *Nanoscale* 4(16):5132-7.
- [55] Saboktakin M, Ye X, Oh SJ, Hong SH, Fafarman AT, Chettiar UK, Engheta N, Murray CB, Kagan CR (2012) Metal-enhanced upconversion luminescence tunable through metal nanoparticle-nanophosphor separation. *ACS Nano* 6(10):8758-66.
- [56] Feng AL, You ML, Tian L, Singamaneni S, Liu M, Duan Z, Lu TJ, Xu F, Lin M (2015) Distance-dependent plasmon-enhanced fluorescence of upconversion nanoparticles using polyelectrolyte multilayers as tunable spacers. *Sci. Rep.* 5:7779.
- [57] Lodahl P, Van Driel AF, Nikolaev IS, Irman A, Overgaag K, Vanmaekelbergh D, Vos WL (2004) Controlling the dynamics of spontaneous emission from quantum dots by photonic crystals. *Nature* 430(7000):654-7.
- [58] Ródenas A, Zhou G, Jaque D, Gu M (2009) Rare-earth spontaneous emission control in three-dimensional lithium niobate photonic crystals. *Adv. Mater.* 21(34):3526-30.
- [59] Fenzl C, Hirsch T, Wolfbeis OS (2014) Photonic crystals for chemical sensing and biosensing. *Angew. Chem. Int. Ed.* 53(13):3318-35.
- [60] Ji Y, Chen Q, Wang C, Lu X, Mei Y, Xu P, Li L, Tan T, Wang J (2018) The modification of upconversion emissions by photonic band gap in β -NaYF₄:Yb³⁺,Tm³⁺ inverse opal structures. *J. Lumin.* 194:420-3.
- [61] Yin Z, Zhu Y, Xu W, Wang J, Xu S, Dong B, Xu L, Zhang S, Song H (2013). Remarkable enhancement of upconversion fluorescence and confocal imaging of PMMA Opal/NaYF₄:Yb³⁺,Tm³⁺/Er³⁺ nanocrystals. *Chem. Commun.* 49(36):3781-3.
- [62] Sai Xu, Zhang Y, Xiangping Li, Zhang J, Jiashi Su, Cheng L, Baojiu CH (2017) Remarkable fluorescence enhancement of upconversion composite film and its application on mercury sensing. *J. Rare Earths* 35(5):460-7.
- [63] Liao J, Yang Z, Wu H, Lai S, Qiu J, Song Z, Yang Y, Zhou D, Yin Z (2014) Upconversion luminescence enhancement of NaYF₄:Yb³⁺, Er³⁺ nanoparticles on inverse opal surface. *Surf. Rev. Lett.* 21(01):1450017.
- [64] Ghosh P, de la Rosa E, Oliva J, Solis D, Kar A, Patra A (2009) Influence of surface coating on the upconversion emission properties of LaPO₄:Yb/Tm core-shell nanorods. *J. Appl. Phys.* 105(11):113532.
- [65] Liao J, Yang Z, Wu H, Yan D, Qiu J, Song Z, Yang Y, Zhou D, Yin Z (2013) Enhancement of the up-conversion luminescence of Yb³⁺/Er³⁺ or Yb³⁺/Tm³⁺ co-doped NaYF₄ nanoparticles by photonic crystals. *J. Mater. Chem. C* 1(40):6541-6.
- [66] Shao B, Yang Z, Li J, Yang J, Wang Y, Qiu J, Song Z (2017) Au nanoparticles embedded inverse opal photonic crystals as substrates for upconversion emission enhancement. *Am. Ceram. Soc.* 100(3):988-97.
- [67] Shao B, Yang Z, Wang Y, Li J, Yang J, Qiu J, Song Z (2015) Coupling of Ag nanoparticle with inverse opal photonic crystals as a novel strategy for upconversion emission enhancement of NaYF₄:Yb³⁺,Er³⁺ nanoparticles. *ACS Appl. Mater. Interfaces* 7(45):25211-8.
- [68] Liao J, Yang Z, Lai S, Shao B, Li J, Qiu J, Song Z, Yang Y (2014) Upconversion emission enhancement of NaYF₄:Yb,Er nanoparticles by coupling silver nanoparticle plasmons and photonic crystal effects. *J. Phys. Chem. C* 118(31):17992-9.

- [69] Yin Z, Li H, Xu W, Cui S, Zhou D, Chen X, Zhu Y, Qin G, Song H (2016) Local field modulation induced three-order upconversion enhancement: combining surface plasmon effect and photonic crystal effect. *Adv. Mater.* 28(13):2518-25.
- [70] Wang H, Li M, Yin Z, Zhang T, Chen X, Zhou D, Zhu J, Xu W, Cui H, Song H (2017) Remarkable enhancement of upconversion luminescence on cap-Ag/PMMA ordered platform and trademark anticounterfeiting. *ACS Appl. Mater. Interfaces* 9(42):37128-35.
- [71] Hu X, Wang Y, Liu H, Wang J, Tan Y, Wang F, Yuan Q, Tan W (2017) Naked eye detection of multiple tumor-related mRNAs from patients with photonic-crystal micropattern supported dual-modal upconversion bioprobes. *Chem. Sci.* 8(1):466-72.
- [72] Niu W, Su LT, Chen R, Chen H, Wang Y, Palaniappan A, Sun H, Tok AI (2014) 3-Dimensional photonic crystal surface enhanced upconversion emission for improved near-infrared photoresponse. *Nanoscale* 6(2):817-24.
- [73] Su X, Sun X, Wu S, Zhang S (2017) Manipulating the emission intensity and lifetime of $\text{NaYF}_4:\text{Yb}^{3+}, \text{Er}^{3+}$ simultaneously by embedding it into CdS photonic crystals. *Nanoscale* 9(22):7666-73.
- [74] Hofmann CL, Herter B, Fischer S, Gutmann J, Goldschmidt JC (2016) Upconversion in a Bragg structure: photonic effects of a modified local density of states and irradiance on luminescence and upconversion quantum yield. *Optics Express* 24(13):14895-914.
- [75] Lin JH, Liou HY, Wang CD, Tseng CY, Lee CT, Ting CC, Kan HC, Hsu CC (2015) Giant enhancement of upconversion fluorescence of $\text{NaYF}_4:\text{Yb}^{3+}, \text{Tm}^{3+}$ nanocrystals with resonant waveguide grating substrate. *ACS Photonics* 2(4):530-6.
- [76] Hao J, Zhang Y, Wei X (2011) Electric-induced enhancement and modulation of upconversion photoluminescence in epitaxial $\text{BaTiO}_3:\text{Yb}/\text{Er}$ thin films. *Angew. Chem. Int. Ed.* 50(30):6876-80.
- [77] Shannon RT, Prewitt CT (1969) Effective ionic radii in oxides and fluorides. *Acta Cryst. Section B: Structural Crystallography and Crystal Chemistry.* 25(5):925-46.
- [78] Dou Q, Zhang Y (2011) Tuning of the structure and emission spectra of upconversion nanocrystals by alkali ion doping. *Langmuir* 27(21):13236-41.
- [79] Zhao C, Kong X, Liu X, Tu L, Wu F, Zhang Y, Liu K, Zeng Q, Zhang H (2013) Li^+ ion doping: An approach for improving the crystallinity and upconversion emissions of $\text{NaYF}_4:\text{Yb}^{3+}, \text{Tm}^{3+}$ nanoparticles. *Nanoscale* 5(17):8084-9.
- [80] Vreeland EC, Watt J, Schober GB, Hance BC, Austin MJ, Price AD, Fellows BD, Monson TC, Hudak NS, Maldonado-Camargo L, Bohorquez AC (2015) Enhanced nanoparticle size control by extending LaMer's mechanism. *Chem. Mater.* 27(17):6059-66.
- [81] Wang HQ, Nann T (2009) Monodisperse upconverting nanocrystals by microwave-assisted synthesis. *ACS Nano* 3(11):3804-8.
- [82] Chen D, Wang Y (2013) Impurity doping: a novel strategy for controllable synthesis of functional lanthanide nanomaterials. *Nanoscale* 5(11):4621-37.
- [83] Chen X, Peng D, Wang F (2013) Tuning NaYF_4 nanoparticles through alkaline earth doping. *Nanomaterials* 3(4):583-91.
- [84] Wisser MD, Fischer S, Maurer PC, Bronstein ND, Chu S, Alivisatos AP, Salleo A, Dionne JA (2016) Enhancing quantum yield via local symmetry distortion in lanthanide-based upconverting nanoparticles. *ACS Photonics* 3(8):1523-30.
- [85] Lahtinen S, Lyytikäinen A, Pääkkilä H, Hömppi E, Perälä N, Lastusaari M, Soukka T (2016) Disintegration of hexagonal $\text{NaYF}_4:\text{Yb}^{3+}, \text{Er}^{3+}$ upconverting nanoparticles in aqueous media: The role of fluoride in solubility equilibrium. *J. Phys. Chem. C* 121(1):656-65.
- [86] Chan EM, Levy ES, Cohen BE (2015) Rationally designed energy transfer in upconverting nanoparticles. *Adv. Mater.* 27(38):5753-61.

- [87] Mader HS, Kele P, Saleh SM, Wolfbeis OS (2010) Upconverting luminescent nanoparticles for use in bioconjugation and bioimaging. *Curr Opin Chem Bio* 14(5):582-96.
- [88] Mader HS, Wolfbeis OS (2010) Optical ammonia sensor based on upconverting luminescent nanoparticles. *Anal. Chem.* 82(12):5002-4.
- [89] Liu Y, Tu D, Zhu H, Chen X (2013) Lanthanide-doped luminescent nanoprobe: controlled synthesis, optical spectroscopy, and bioapplications. *Chem. Soc. Rev.* 42(16):6924-58.
- [90] Noculak A, Podhorodecki A (2017) Size and shape effects in β -NaGdF₄:Yb³⁺,Er³⁺ nanocrystals. *Nanotechnology* 28(17):175706.
- [91] Kaiser M, Würth C, Kraft M, Hyppänen I, Soukka T, Resch-Genger U (2017) Power-dependent upconversion quantum yield of NaYF₄:Yb³⁺,Er³⁺ nano- and micrometer-sized particles—measurements and simulations. *Nanoscale* 9(28):10051-8.
- [92] Ma C, Xu X, Wang F, Zhou Z, Liu D, Zhao J, Guan M, Lang CI, Jin D (2017) Optimal sensitizer concentration in single upconversion nanocrystals. *Nano Lett.* 17(5):2858-64.
- [93] Gargas DJ, Chan EM, Ostrowski AD, Aloni S, Altoe MV, Barnard ES, Sanii B, Urban JJ, Milliron DJ, Cohen BE, Schuck PJ (2014) Engineering bright sub-10-nm upconverting nanocrystals for single-molecule imaging. *Nat. Nanotechnol.* 9(4):300-5.
- [94] Yang D, Li C, Li G, Shang M, Kang X, Lin J (2011) Colloidal synthesis and remarkable enhancement of the upconversion luminescence of BaGdF₅:Yb³⁺/Er³⁺ nanoparticles by active-shell modification. *J. Mater. Chem.* 21(16):5923-7.
- [95] Zhao J, Jin D, Scharfner EP, Lu Y, Liu Y, Zvyagin AV, Zhang L, Dawes JM, Xi P, Piper JA, Goldys EM (2013) Single-nanocrystal sensitivity achieved by enhanced upconversion luminescence. *Nat. Nanotechnol.* 8(10):729-34.
- [96] Chan EM, Han G, Goldberg JD, Gargas DJ, Ostrowski AD, Schuck PJ, Cohen BE, Milliron DJ (2012) Combinatorial discovery of lanthanide-doped nanocrystals with spectrally pure upconverted emission. *Nano Lett.* 12(7):3839-45.
- [97] Li X, Wang R, Zhang F, Zhao D (2014) Engineering homogeneous doping in single nanoparticle to enhance upconversion efficiency. *Nano Lett.* 14(6):3634-9.
- [98] Qiu H, Yang C, Shao W, Damasco J, Wang X, Ågren H, Prasad P, Chen G (2014) Enhanced upconversion luminescence in Yb³⁺/Tm³⁺-codoped fluoride active core/active shell/inert shell nanoparticles through directed energy migration. *Nanomaterials* 4(1):55-68.
- [99] Wang F, Wang J, Liu X (2010) Direct evidence of a surface quenching effect on size-dependent luminescence of upconversion nanoparticles. *Angew. Chem. Int. Ed.* 49(41):7618-22.
- [100] Yi GS, Chow GM (2007) Water-soluble NaYF₄:Yb,Er(Tm)/NaYF₄/polymer core/shell/shell nanoparticles with significant enhancement of upconversion fluorescence. *Chem. Mater.* 19(3):341-3.
- [101] Rinkel T, Raj AN, Dühnen S, Haase M (2016) Synthesis of 10 nm β -NaYF₄:Yb,Er/NaYF₄ core/shell upconversion nanocrystals with 5 nm particle cores. *Angew. Chem. Int. Ed.* 55(3):1164-7.
- [102] Drees C, Raj AN, Kurre R, Busch KB, Haase M, Piehler J (2016) Engineered upconversion nanoparticles for resolving protein interactions inside living cells. *Angew. Chem. Int. Ed.* 55(38):11668-72.
- [103] Punjabi A, Wu X, Tokatli-Apollon A, El-Rifai M, Lee H, Zhang Y, Wang C, Liu Z, Chan EM, Duan C, Han G (2014) Amplifying the red-emission of upconverting nanoparticles for biocompatible clinically used prodrug-induced photodynamic therapy. *ACS Nano* 8(10):10621-30.
- [104] Xue M, Zhu X, Qiu X, Gu Y, Feng W, Li F (2016) Highly enhanced cooperative upconversion luminescence through energy transfer optimization and quenching protection. *ACS Appl. Mater. Interfaces* 8(28):17894-901.

- [105] Vetrone F, Naccache R, Mahalingam V, Morgan CG, Capobianco JA (2009) The active-core/active-shell approach: A strategy to enhance the upconversion luminescence in lanthanide-doped nanoparticles. *Adv. Funct. Mater.* 19(18):2924-9.
- [106] Johnson NJ, Korinek A, Dong C, van Veggel FC (2012) Self-focusing by Ostwald ripening: a strategy for layer-by-layer epitaxial growth on upconverting nanocrystals. *J. Am. Chem. Soc.* 134(27):11068-71.
- [107] Ding M, Chen D, Ma D, Dai J, Li Y, Ji Z (2016) Highly enhanced upconversion luminescence in lanthanide-doped active-core/luminescent-shell/active-shell nanoarchitectures. *J. Mater. Chem. C* 4(13):2432-7.
- [108] Zuo J, Sun D, Tu L, Wu Y, Cao Y, Xue B, Zhang Y, Chang Y, Liu X, Kong X, Buma WJ (2018) Precisely tailoring upconversion dynamics via energy migration in core-shell nanostructures. *Angew. Chem. Int. Ed.* 57(12):3108-12.
- [109] Dühnen S, Haase M (2015) Study on the intermixing of core and shell in NaEuF₄/NaGdF₄ core/shell nanocrystals. *Chem. Mater.* 27(24):8375-86.
- [110] Zhan Q, Qian J, Liang H, Somesfalean G, Wang D, He S, Zhang Z, Andersson-Engels S (2011) Using 915 nm laser excited Tm³⁺/Er³⁺/Ho³⁺-doped NaYbF₄ upconversion nanoparticles for in vitro and deeper in vivo bioimaging without overheating irradiation. *ACS Nano* 5(5):3744-57.
- [111] Dai H, Stafsudd OM, Dunn B (1991) Measurement of stimulated emission cross section and fluorescence branching ratio for Nd³⁺ in sodium-β alumina. *Appl. Opt.* 30(30):4330-6.
- [112] Shen J, Chen G, Vu AM, Fan W, Bilsel OS, Chang CC, Han G (2013) Engineering the upconversion nanoparticle excitation wavelength: Cascade sensitization of tri-doped upconversion colloidal nanoparticles at 800 nm. *Adv. Opt. Mater.* 1(9):644-50.
- [113] Söderlund H, Mousavi M, Liu H, Andersson-Engels S (2015) Increasing depth penetration in biological tissue imaging using 808-nm excited Nd³⁺/Yb³⁺/Er³⁺-doped upconverting nanoparticles. *J. Biomed. Opt.* 20(8):086008.
- [114] Xie X, Gao N, Deng R, Sun Q, Xu QH, Liu X (2013) Mechanistic investigation of photon upconversion in Nd³⁺-sensitized core-shell nanoparticles. *J. Am. Chem. Soc.* 135(34):12608-11.
- [115] Zhong Y, Tian G, Gu Z, Yang Y, Gu L, Zhao Y, Ma Y, Yao J (2014) Elimination of photon quenching by a transition layer to fabricate a quenching-shield sandwich structure for 800 nm excited upconversion luminescence of Nd³⁺-sensitized nanoparticles. *Adv. Mater.* 26(18):2831-7.
- [116] Prorok K, Pawlyta M, Stręk W, Bednarkiewicz A (2016) Energy migration up-conversion of Tb³⁺ in Yb³⁺ and Nd³⁺ codoped active-core/active-shell colloidal nanoparticles. *Chem. Mater.* 28(7):2295-300.
- [117] Chen Y, Liu B, Deng X, Huang S, Hou Z, Li C, Lin J (2015) Multifunctional Nd³⁺-sensitized upconversion nanomaterials for synchronous tumor diagnosis and treatment. *Nanoscale* 7(18):8574-83.
- [118] Li X, Wang R, Zhang F, Zhou L, Shen D, Yao C, Zhao D (2013) Nd³⁺-sensitized up/down converting dual-mode nanomaterials for efficient in-vitro and in-vivo bioimaging excited at 800 nm. *Sci. Rep.* 3:3536.
- [119] Wen H, Zhu H, Chen X, Hung TF, Wang B, Zhu G, Yu SF, Wang F (2013) Upconverting near-infrared light through energy management in core-shell-shell nanoparticles. *Angew. Chem. Int. Ed* 52(50):13661-5.
- [120] Ju Q, Chen X, Ai F, Peng D, Lin X, Kong W, Shi P, Zhu G, Wang F (2015) An upconversion nanoprobe operating in the first biological window. *J. Mater. Chem. B* 3(17):3548-55.
- [121] Wang YF, Liu GY, Sun LD, Xiao JW, Zhou JC, Yan CH. Nd³⁺-sensitized upconversion nanophosphors: efficient in vivo bioimaging probes with minimized heating effect. *ACS Nano* 7(8):7200-6.
- [122] Huang X, Lin J (2015) Active-core/active-shell nanostructured design: an effective strategy to enhance Nd³⁺/Yb³⁺ cascade sensitized upconversion luminescence in lanthanide-doped nanoparticles. *J. Mater. Chem. C* 3(29):7652-7.

- [123] Ma D, Meng L, Chen Y, Hu M, Chen Y, Huang C, Shang J, Wang R, Guo Y, Yang J (2015) NaGdF₄:Yb³⁺/Er³⁺@NaGdF₄:Nd³⁺@sodium-gluconate: multifunctional and biocompatible ultrasmall core-shell nanohybrids for UCL/MR/CT multimodal imaging. *ACS Appl. Mater. Interfaces* 7(30):16257-65.
- [124] Zou X, Liu Y, Zhu X, Chen M, Yao L, Feng W, Li F (2015) A Nd³⁺-sensitized upconversion nanophosphor modified with a cyanine dye for the ratiometric upconversion luminescence bioimaging of hypochlorite. *Nanoscale* 7(9):4105-13.
- [125] Liu B, Chen Y, Li C, He F, Hou Z, Huang S, Zhu H, Chen X, Lin J (2015) Poly(acrylic acid) modification of Nd³⁺-sensitized upconversion nanophosphors for highly efficient UCL imaging and pH-responsive drug delivery. *Adv. Funct. Mater.* 25(29):4717-29.
- [126] Xu B, Zhang X, Huang W, Yang Y, Ma Y, Gu Z, Zhai T, Zhao Y (2016) Nd³⁺ sensitized dumbbell-like upconversion nanoparticles for photodynamic therapy application. *J. Mater. Chem. B* 4(16):2776-84.
- [127] Jiang C, Zhou S, Wei X, Chen Y, Duan C, Yin M, Yang B, Cao W (2016) 794 nm excited core-shell upconversion nanoparticles for optical temperature sensing. *RSC Adv.* 6(14):11795-801.
- [128] Wang D, Xue B, Kong X, Tu L, Liu X, Zhang Y, Chang Y, Luo Y, Zhao H, Zhang H (2015) 808 nm driven Nd³⁺-sensitized upconversion nanostructures for photodynamic therapy and simultaneous fluorescence imaging. *Nanoscale* 7(1):190-7.
- [129] Liu J, Zhang T, Song X, Xing J (2018) Enhanced red emission of 808 nm excited upconversion nanoparticles by optimizing the composition of shell for efficient generation of singlet oxygen. *Opt. Mater.* 75:79-87.
- [130] Dai Y, Bi H, Deng X, Li C, He F, Yang P, Lin J (2017) 808 nm near-infrared light controlled dual-drug release and cancer therapy in vivo by upconversion mesoporous silica nanostructures. *J. Mater. Chem. B* 5(11):2086-95.
- [131] Ding X, Liu J, Liu D, Li J, Wang F, Li L, Wang Y, Song S, Zhang H (2017) Multifunctional core/satellite polydopamine@Nd³⁺-sensitized upconversion nanocomposite: A single 808 nm near-infrared light-triggered theranostic platform for in vivo imaging-guided photothermal therapy. *Nano Res.* 10(10):3434-46.
- [132] Chen W, Shi C, Tao T, Ji M, Zheng S, Sang X, Liu X, Qiu J (2016) Optical temperature sensing with minimized heating effect using core-shell upconversion nanoparticles. *RSC Adv.* 6(26):21540-5.
- [133] Li J, Zhu X, Xue M, Feng W, Ma R, Li F (2016) Nd³⁺-sensitized upconversion nanostructure as a dual-channel emitting optical probe for near infrared-to-near infrared fingerprint imaging. *Inorg. Chem.* 55(20):10278-83.
- [134] Chen D, Xu M, Huang P, Ma M, Ding M, Lei L (2017) Water detection through Nd³⁺-sensitized photon upconversion in core-shell nanoarchitecture. *J. Mater. Chem. C* 5(22):5434-43.
- [135] Wei W, Chen G, Baev A, He GS, Shao W, Damasco J, Prasad PN (2016) Alleviating luminescence concentration quenching in upconversion nanoparticles through organic dye sensitization. *J. Am. Chem. Soc.* 138(46):15130-3.

2. Aim of the Work

The low quantum yields and the poor brightness of upconversion nanoparticles (UCNPs) is one of the major limitations to bring this class of probes, with its unique features to a practical application. Motivated by this, the aim of this work was a) to get a better understanding in the photophysics of lanthanide doped upconversion nanoparticles of the NaYF₄ type, b) to search for possibilities to change the spectral properties for better sensing abilities, c) to prevent sample heating when exciting UCNPs by NIR light in aqueous systems, and d) to investigate deep tissue penetration which will be the key for future theranostic applications of this probes.

In sensing applications, it would be beneficial to use a probe with large anti Stokes shift. This will improve the sensitivity by a high signal-to-noise ratio due to minimizing the noise. It will be also very attractive to operate in a label-free manner and use intrinsic parameters of an analyte. This feature enables in-field or home-care application usable by non-trained persons in a reliable way. Upconversion nanoparticles, when used as so-called nanolamps can give an option to realize such an application, especially when using the four-photon process of these nanolamps generating UV light upon NIR excitation. Usually, UV emissions of UCNPs are extremely weak, and an enhancement strategy is necessary. It was the aim of this work to investigate the possibility to use a plasmonic enhancement to boost the UV-emission of Thulium-doped UCNPs for a photometric sensing application.

The main advantage of photo upconversion is ascribed to allow the generation of background free signals in biological medium like in cells, where no other component is able to be stimulated to send out light upon NIR excitation. This is important in imaging, diagnostics but also in drug delivery. If an emission is only generated at a desired location, it is possible to release a drug by a photochemical reaction. One limitation so far is the use of 980 nm light to excite UCNPs by sensitization via Yb³⁺ ions in the crystal. This light gets also absorbed from water and sample heating will become an issue for long-time irradiation of biological material. Therefore, it was the aim of this work to design and synthesize core – multi-shell particles with Nd³⁺, Yb³⁺ tandem sensitization for efficient upconversion in the blue region. Such particle

were fabricated to be used by our colleagues at Rutgers University, NJ for a NIR stimulated stem cell growth.

Another feature of UCNPs often discussed in literature is the ability of deep tissue penetration of UCNPs, as the excitation in the NIR is in the so-called first biological window where tissue shows low absorbance. Nevertheless, a thoroughly investigation of this feature is missing so far. Therefore, the aim of this work was to design a set of particles allowing together with our colleagues from the Federal Institute of Material Research and Testing (BAM) in Berlin to fully investigate the photophysical properties comparing 980 nm and 808 nm excitation in an excitation power dependent way. An answer to the question at which distance it makes sense to go for the more complex core – multi shell particles with Nd^{3+} sensitization to achieve a brighter upconversion luminescence is expected.

3. Plasmonic Enhancement of NIR to UV Upconversion by a Nanoengineered Interface Consisting of NaYF₄:Yb,Tm Nanoparticles and a Gold Nanotriangle Array for Optical Detection of Vitamin B12 in Serum

3.1 Abstract

A nanoengineered interface fabricated by self-assembly enables the online determination of vitamin B12 *via* a simple luminescence readout in serum without any pretreatment. The interplay of Tm³⁺-doped NaYF₄ nanoparticles (UCNPs) and a gold nanotriangle array prepared by nanosphere lithography on a glass slide is responsible for an efficient NIR to UV upconversion. Hot spots of the gold assembly generate local electromagnetic-field enhancement, favoring the four-photon upconversion process at the low-power excitation of approximately 13 W·cm⁻². An improvement by about six times of the intensity for the emission peaking at 345 nm is achieved. The nanoengineered interface has been applied in a proof-of-concept sensor for vitamin B12 in serum, which is known as a marker for the risk of cancer; Alzheimer disease; or, during pregnancy neurological abnormalities in newborn babies. Vitamin B12 can be detected in serum down to 3.0 nmol·L⁻¹ by a simple intensity-based optical readout, consuming only 200 µL of a sample, which qualifies as easy miniaturization for point-of-care diagnostics. Additionally, this label-free approach can be used for long-term monitoring because of the high photostability of the upconversion nanoparticles.

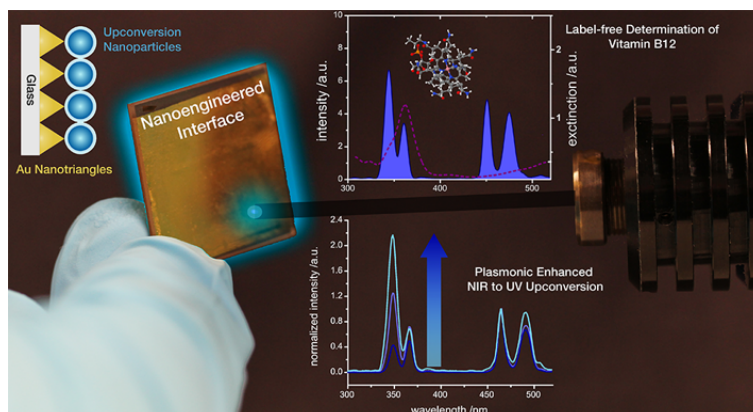


Figure 3.1 | Graphical abstract for plasmonic enhancement of NIR to UV upconversion by a nanoengineered interface consisting of NaYF₄:Yb,Tm nanoparticles and a gold nanotriangle array for optical detection of vitamin B12 in serum.

This chapter has been published. Lisa Marie Wiesholler, Christa Genslein, Alexandra Schroter, Thomas Hirsch. *Analytical Chemistry*, **2018**, 90(24), 14247-54.

Author contributions: This manuscript was published after peer reviewing. LMW and CG contributed equally in this publication. LMW designed and synthesized the upconverting nanoparticle while CG fabricated the nanotriangle array. First preliminary test to fabricate the nanoengineered interface were conducted by AS supervised by CG and LMW. LMW performed the luminescence measurements, carried out the vitamin B12 determination in water and serum and investigated the selectivity. The Raman measurements were performed by LMW and CG and the surface plasmon resonance studies were carried out by LMW. The manuscript was written by LMW and CG. The article was revised by the LMW, CG, and TH. TH is corresponding author.

3.2 Introduction

The increasing demand for sensors, especially in the field of health care and point-of-care diagnostics [1], motivates researchers to develop new concepts to overcome limitations in elaborative detection principles [2]. Online monitoring is highly desired in production lines in environment control, and in diagnostics, as it does not require periodic sampling and maximizes the information, which provides efficiency and safety [3]. Label-free approaches, especially those that monitor intrinsic features of an analyte, such as its absorption characteristics, are most suitable for long term usage [4]. Miniaturization and energy efficiency are also key players in sensor development as they enable easy integration in many systems. The tremendous progress in nanotechnology established a lot of new nanomaterials with outstanding properties, helping to advance sensor technologies. Upconversion nanoparticles (UCNPs) are one of these materials, as they efficiently convert NIR light to UV-vis emission [5]. In particular, the good biocompatibility of UCNPs and the reduction of the background fluorescence [6] make them attractive for applications like biosensing [7-9] and bioimaging [6,10]. Despite the progress in the last few years, for some applications, the quantum efficiency of these nanoparticles is still not sufficient, which is attributed to the generally low absorption coefficient of the Ln³⁺ ions caused by Laporte-forbidden 4f-4f-transitions [11,12]. Haase *et al.* have reported on the synthesis of erbium-doped core – shell nanoparticles of 45 nm in size, which exhibit almost the same brightness as the bulk material [13]. For biological applications, UCNPs doped with thulium are of interest as they are capable of emitting at 345 and 360 nm, which is realized by a four-photon process [14]. These emissions usually require a high laser power. Researchers have developed many strategies [15] for enhancing upconversion luminescence [16], such as optimizing the concentrations of the lanthanide ions [17], modulating the shapes and phases of the particles [18], and designing composite materials [19]. Spectral management in UCNPs can enhance a particular emission peak by redistribution of the excitation energy [20]. Another promising strategy is the assembly of the particles onto solid supports [21], like the combination of UCNPs with metallic nanostructured surfaces. Here, the key point is the occurrence of surface plasmons, appearing in the presence of conducting materials, defined as oscillations at the interface between a material with free electrons (*e.g.* gold) and a dielectric material [22]. The interaction of surface plasmons with UCNPs has been reported to enhance the upconversion efficiency [23,24]. These short-ranging, high-frequency electromagnetic resonances of electrons change the electromagnetic field (EMF) in close proximity to upconversion nanoparticles [24]. The

interplay of UCNPs and metallic nanostructured surfaces is influenced by the plasmonic properties of the material and the geometrical structures, such as shape and size [25]. Localized surface plasmons (LSPs) are favored for emission enhancement. They are characterized by a confined EMF rather than by propagating surface plasmons on a continuous metal film [26]. The optical phenomenon is generated by a light wave trapped in a structure smaller than its wavelength, called a hot spot [27]. Light interactions are strongly enhanced at the edges of such structures, and the energy is focused to a close vicinity at the metal surface [28]. For sensor applications, regular arrangements of these nanostructures need to be fabricated in large dimensions with sufficient reproducibility. Nanosphere lithography, based on the self-assembly of nanoparticles, covers these requirements. The use of different sphere sizes allows for facile hot-spot design, in particular nanotriangle arrays [29]. In this work a gold nanotriangle array is merged with UCNPs to result in a nanoengineered interface with the advantages of high UV luminescence and label-free, online monitoring. The increased upconversion emission in the UV range was selected for sensing vitamin B12 (vitB12) concentration in serum, which is in the range of 0.15 – 750 nmol·L⁻¹ for healthy people [30]. Recent studies have reported that vitB12 in blood serum can be used as a marker for Alzheimer's disease [31], and a low vitB12 content in serum during pregnancy enhances the risk of neurological abnormalities in newborn babies [32]. Table 3.1 compares different methods reported for the determination of vitB12. Some techniques, like Raman or mass spectroscopy, suffer from long assay times because of their intensive pretreatment steps or from poor specificity, as for the example of surface-plasmon resonance (SPR).

Table 3.1. Comparison of different techniques reported for the determination of vitaminB12 in real samples in order of their limit of detection (LOD).

technique	LOD (nM)	sample volume (μL)	assay time	pre-treatment	comments	refer-ences
mass spectrometry	0.63·10 ⁻⁸	n.r. ^{a)}	5 days	yes	cost intensive	33
immunoassays	0.001	50 - 100	20 h	yes	laborious	34
chemi-luminescence	0.016	30 - 50	3.6-6 s	yes	not label free	35
microbiological detection	0.13	50 - 100	20 h	yes	growth rate also influenced by antibiotics	36
nanoengineered interface	3	200	5 min	no	-	this work
high performance liquid chromatography	51	20	5 min	yes	no online monitoring	37
surface plasmon resonance	63	nr ^{a)}	5 min	yes	poor specificity	38
Raman spectroscopy	70	2.500	7 h	yes	interference by proteins	39
fluorescence	100	2.000	4 min	no	high background due to UV excitation	40

a) not reported

3.3 Materials and Methods

3.3.1 Chemicals and Characterization Methods

Lanthanide chloride hexahydrates (> 99.9%) were purchased from Sigma-Aldrich and Treibacher Industrie AG. Oleic acid and 1-octadecene (both technical grade, 90%) were obtained from Alfa Aesar. Nitrosonium tetrafluoroborate (95%) was purchased from Sigma-Aldrich. All other chemicals were of analytical grade and obtained from Sigma-Aldrich, Merck or Acros. All chemicals were used as received without further purification.

The sizes of the nanoparticles were determined by transmission electron microscopy (TEM) with a 120 kV Philips CM12 microscope on carbon-coated copper grids (400 mesh) from Plano. A small volume (10 μ L) of particles dispersed in cyclohexane (1 mg·mL⁻¹) was dropped on the grid and the solvent was allowed to evaporate. The elemental composition was verified by using a flame end on plasma (EOP) inductively coupled plasma optical-emission spectrometer (ICP-OES) from Spectro. Dynamic light scattering (DLS) was performed with a Malvern Zetasizer Nano ZS to characterize the particle-size distributions in the dispersions. Disposable semimicro poly(methyl methacrylate) cuvettes were used and the temperature was held at a constant level of 20 °C. To analyze the crystal structure, X-ray-powder-diffraction patterns (XRD) with a resolution of 0.005° (2 θ) were collected using a STOE STADI P diffractometer equipped with a Dectris Mythen 1K detector. Monochromatic Cu K α_1 radiation (λ = 1.54056 Å) was used. Luminescence measurements were carried out with an Aminco Bowman Series 2 luminescence spectrometer from the Thermo Electron Corporation equipped with a continuous wave (cw) 980 nm laser module (200 mW) from Picotronic for excitation. Absorbance measurements of the vitB12 solutions were obtained with a Varian Cary 50 spectrophotometer. SPR analysis was performed with a BioSuple SPR instrument (Mivitec GmbH) using an F1-65 glass prism installed on a swivel carriage. The substrate was placed on the top face with index-matching fluid between the chip and the prism. A flow cell with two channels was placed on the chip. The device operated with laser illumination at 650 nm. SPR slides covered with a continuous gold film of 45 nm in thickness were obtained from Mivitec GmbH. For Raman measurements (DXR Raman microscope, Thermo Fisher Scientific GmbH) 532 nm laser excitation (8 mW) and a 50 μ m slit were used. The Raman microscope was equipped with a 100x magnification MPlan N objective (100x/0.90 BD, Olympus SE & Company).

3.3.2 Synthesis and Surface Modification of Upconversion Nanoparticles

Particles were synthesized according to a general method reported by Wilhelm *et al.* [41] with modifications.

3.3.2.1 Synthesis of Hexagonal NaYF₄:25%Yb,0.3%Tm

A total of 5 mmol rare earth trichlorides of Y³⁺, Yb³⁺ and Tm³⁺ with the corresponding molar doping ratios as desired in the nanoparticle were dissolved in 40 mL methanol and transferred into a three necked round bottom flask under nitrogen flow. A mixture of 8 mL oleic acid and 15 mL 1-octadecene per 1 mmol of rare earth salts was added to the solution. The suspension

was heated to 160 °C and vacuum was applied for 30 min to form a clear solution. After this the solution was cooled to room temperature and 0.148 g (4.0 mmol) NH₄F and 0.1 g (2.5 mmol) NaOH dissolved in 20 mL methanol were added per 1 mmol of rare earth salts. Then the suspension was kept at 120 °C for 30 min and then heated to reflux (approx. 325 °C). The progress of the reaction was monitored with a 980 nm cw laser module. 10 min from the time on, when upconversion luminescence can be observed for the first time, the reaction mixture was cooled to room temperature. After the synthesis the particles were precipitated by the addition of ethanol in excess and collected by centrifugation at 1,000 g for 5 min. The precipitate was washed twice with chloroform/ethanol (1:10, v/v) and three times with cyclohexane/acetone (1:10, v/v) by repeated re-dispersion-precipitation-centrifugation cycles. Finally, the particles were dispersed in cyclohexane, centrifuged at 1,000 g for 3 min to remove aggregates, and the supernatant was collected and stored at 4 °C.

3.3.2.2 Surface Modification of NaYF₄:Yb,Tm

The ligand exchange strategy with tetrafluoroborate is based on the method described by Dong *et al.* [42]. In a two-phase system consisting of equal volumes of cyclohexane and dimethylformamide (DMF) the nanoparticles were dispersed. NOBF₄ (1 mg per 1 mg UCNPs) was added and the dispersion was stirred and slightly heated (~40 °C) for 10 min. During this time the oleate capped hydrophobic UCNPs were transferred from the cyclohexane phase into the DMF phase. The process can be easily monitored by control of the upconversion luminescence *via* excitation with a 980 nm cw laser module (200 mW). Surface modification is complete when only the DMF phase shows upconversion luminescence. The clear upper cyclohexane phase was discarded, and the particles were precipitated by excess of chloroform. The suspension is centrifuged at 1,000 g for 5 min. The jellylike precipitate is washed twice with chloroform. Finally, the BF₄⁻-stabilized particles are dispersed in DMF, and aggregates were removed by centrifugation at 1,000 g for 3 min. Poly(acrylic acid) (M_w ~2,100) was dissolved in water (2 mg·mL⁻¹) and added to the BF₄⁻-stabilized nanoparticles dispersed in DMF. The solution was stirred and also kept at a moderate temperature of 40 °C for 15 min. Afterwards the dispersion was centrifuged (13,600 g for 20 min) and washed twice for 20 min with water (13,600 g). The supernatants were finally collected after centrifugation at 1,000 g for 3 min.

3.3.3 Functionalization of Glass Slides

All substrates were based on glass slides (20 x 20 mm²) of F1 type with a refractive index of 1.61 (Mivitec GmbH). Glass slides were cleaned in a piranha solution (3:1 (v/v) mixture of conc. H₂SO₄ and 30% (w/w) H₂O₂) for 90 min and then in a 5:1:1 (v/v/v) mixture of water, ammonia, and hydrogen peroxide for 60 min. Triangle arrays were prepared according to a modified protocol described by Genslein *et al.* [43]. In brief, polystyrene particles were dispersed in a water/ethanol solution with a ratio of 87:13 (v/v), and a concentration of 13 mg·mL⁻¹. A spherical mask of particles with a diameter of $1.04 \pm 0.04 \mu\text{m}$ was formed on the glass substrate by drop-coating 40 μL of the particle dispersion. After evaporation of the solvent, the spherical mask was covered with a film of ~5 nm of titanium and ~50 nm of gold. The metal films were deposited by electron-beam vapor deposition consisting of a Leybold Univex 450 vacuum pump, a Ferro-Tec EVM-8 e-beam gun, and an Inficon oscillating quartz device. In the last step, the polystyrene spheres were removed from the surface by sonication in ethanol for 2 min, yielding triangle nanoarrays. Glass slides covered with a continuous gold film of ~50 nm in thickness on a 5 nm adhesion layer of chromium were obtained from Mivitec GmbH. Scanning electron microscopy (SEM) was used for characterization (JSM-6510 SEM-device, JEOL GmbH) with voltages of 15 and 30 kV.

3.3.4 Preparation of a Particle Layer via Self-Assembly

1-Mercaptohexadecane was used for monolayer formation on the continuous gold film and on the nanotriangle array, and hexadecyltrimethoxysilane was used for the glass slide. First, the gold was modified with an alkanethiol self-assembled monolayer (SAM). The gold modified glass slides (either with a continuous gold film or with a gold nanotriangle assembly) were washed with ethanol and dried with nitrogen. The monolayer on substrates with a continuous gold film or a triangle array was formed by immersion in a solution of 1-mercaptohexadecane in ethanol (200 $\mu\text{g}\cdot\text{mL}^{-1}$) overnight. For the SAM formation on a glass slide a solution of hexadecyltrimethoxysilane in ethanol (200 $\mu\text{g}\cdot\text{mL}^{-1}$) was used. After washing with ethanol, 200 μL of oleate capped NaYF₄:Yb,Tm nanoparticles in cyclohexane (22 mg·mL⁻¹) were deposited on the gold substrate. The solvent was evaporated at ambient air, and the slide was subsequently washed with cyclohexane. To achieve a complete coverage of the substrates by particles, the NaYF₄:Yb,Tm-solution was dropped on the surface for four times, after each deposition the substrate was washed thoroughly with cyclohexane. For characterization, SEM (SUPRA 55VP ZEISS, Carl Zeiss AG) at a voltage of 8 kV was used.

3.3.5 Stability Measurements of the Particles Attached to a Continuous Gold Film

The surface coverage as well as the stability of the nanoparticles on continuous gold films was investigated by surface plasmon resonance spectroscopy (SPR). The SPR angle is determined by the refractive index next to the gold surface. The refractive index for water ($n_D = 1.33$) and NaYF₄:Yb,Tm ($n_D = 1.47$) [44] differ a lot, which allows to detect the assembly of the particles on the alkanethiol modified gold by measuring the SPR angle. The SPR setup creates two measurement spots on one gold slide. Only that region of the gold which belongs to one measurement spot is covered by NaYF₄:Yb,Tm particles *via* drop-casting, the second measurement spot acts as reference. The chip is covered by a flow cell, separated in two channels, one for each measurement spot. By a flow of water ($1 \text{ mL} \cdot \text{min}^{-1}$) the change of the SPR angle was followed for 30 min. The theoretical curves were performed by the software WinSpall [45]. For stability measurements by Raman spectroscopy, UCNPs were attached to a 1-mercaptohexadecane-modified continuous gold film by the drop-casting method. The substrate was immersed in 20 mL of water. Spectra were measured before the first immersion in water (day 0) and on consecutive days. No variation in the intensity can be found, which is indicating a good stability of the assembly.

3.3.6 Measurement of Vitamin B12

A homemade measurement cell was used for detection. On the nanoengineered interface, a polydimethylsiloxane (PDMS) gasket was mounted and sealed with a glass slide. The cell held a total volume of 200 μL of analyte solution and was fixed in the spectrometer. A 980 nm laser (200 mW, cw) illuminated the nanoengineered interface *via* the glass cell. The upconversion luminescence was detected in a reflectometric configuration with a constant angle to avoid any excitation light at the detector.

3.4 Results and Discussion

3.4.1 Substrate Fabrication and Functionalization with NaYF₄:Yb,Tm Upconversion Nanoparticles

The nanoengineered interface is formed by an assembly of a nanostructured gold array with UCNPs on top, as outlined in Figure 3.2. An interaction between the plasmonic features of the

gold and the UCNPs is expected to enhance the luminescence properties of the anti-Stokes emission of the nanoparticles [46].

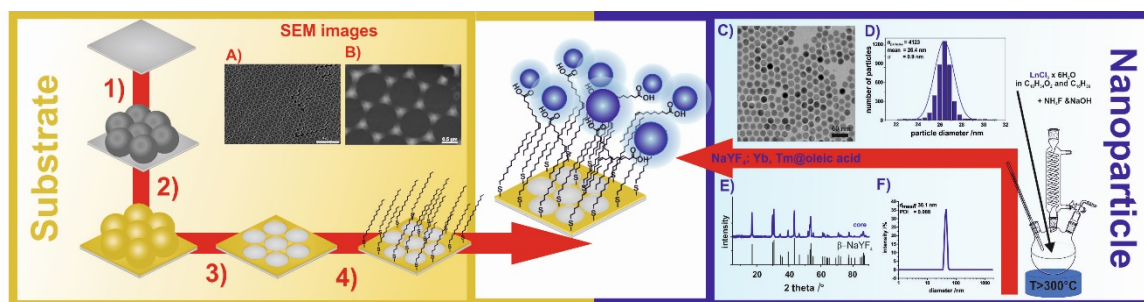


Figure 3.2 | Schema of the fabrication of the nanoengineered interface. The left part illustrates the assembly and functionalization of the nanotriangle array. Starting with a glass slide, polystyrene spheres are drop-coated (1), and then gold is deposited by evaporation (2). After the slide is sonicating to remove the polystyrene spheres (3), a nanotriangle array is obtained. This array is further functionalized with a self-assembled monolayer of a thiol for coupling of the particles (4). **(A)** SEM image showing the polystyrene mask with gold on top and **(B)** SEM image of the resulting nanotriangle array. On the right, the synthesis of the NaYF₄:Yb,Tm UCNPs (NaYF₄:25%Yb,0.3%Tm) by a bottom-up method is displayed. **(C)** TEM image and **(D)** corresponding size distribution of monodisperse particles of about 26 nm in diameter. In the middle, the nanoengineered interface is displayed, with the self-assembly of the UCNPs on the surface-functionalized gold nanotriangle array.

The structured gold on the glass was fabricated by nanosphere lithography, outlined in Figure 3.3 [47]. This method offers outstanding and convenient possibilities in terms of (a) the variability in the dimensions and periodicity of the metallic nanostructures; (b) its fast and precise patterning of large-scaled surfaces in the square-centimeter regime; and (c) the easy and cheap fabrication, which does not need any expensive instrumentation. In a first step, an ethanolic solution consisting of polystyrene spheres (PSS) of a diameter of 1.0 μm was drop-casted on a clean glass slide. The concentration of the spheres was set to allow the formation of a self-assembled, hexagonal closely packed monolayer arrangement. After slow evaporation of the solvent, an adhesive layer of ~ 5 nm of titanium followed by ~ 50 nm of gold was evaporated on top of the assembly. In the last step, the particles were removed by sonication for 2 min. The PSS act as mask that defines the area where no gold film is deposited on the glass. Scanning electron microscopy confirmed the hexagonal arrangement of the PSS as well as the formation of the gold nanotriangle array.

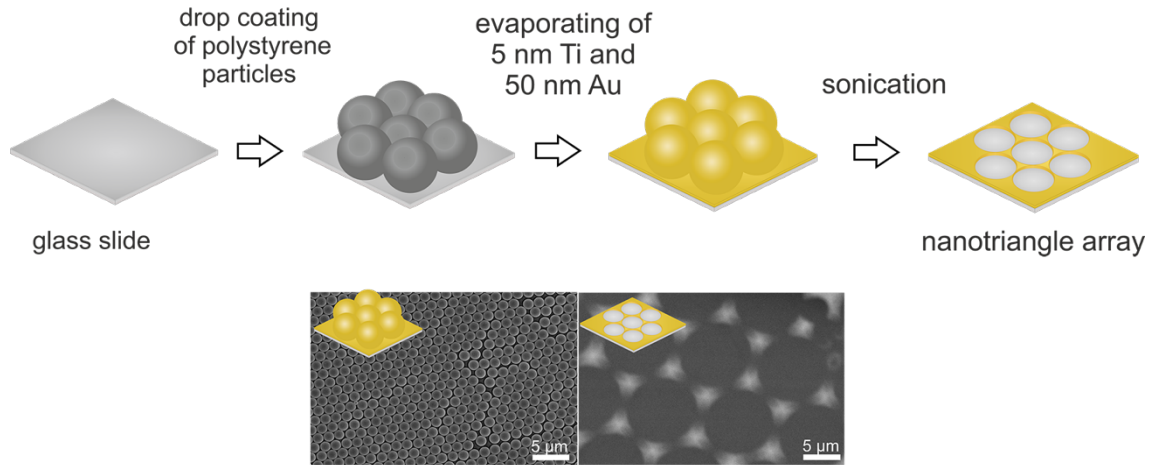


Figure 3.3 | Outline of the fabrication steps to form a triangle array with a modified nanosphere lithography technique. Polystyrene particles of ~1 μm in diameter were used for mask formation. Gold (~50 nm) was deposited on a ~5 nm Ti adhesion layer by thermal vacuum deposition. In a last step the particles were removed by sonication in a water bath. The scanning electron microscope (SEM) images of the polystyrene sphere mask (left) and the triangle array (right) show the highly ordered hexagonal arrangement of the polystyrene spheres after the deposition of the gold layer and resulting array of the nanotriangles with a center to center distance of 1 μm and a gold nanotriangle area of 0.04 μm².

An area on the glass slide of only 9% is covered by the gold (Fig. 3.4 and calculation presented in the following), which concentrates the electro-magnetic field (EMF) generated by free electrons in the metal in so-called hot spots at the corners of the triangle. By changing the diameter of the PSS, the density and the size of the gold nanotriangles can be easily adjusted.

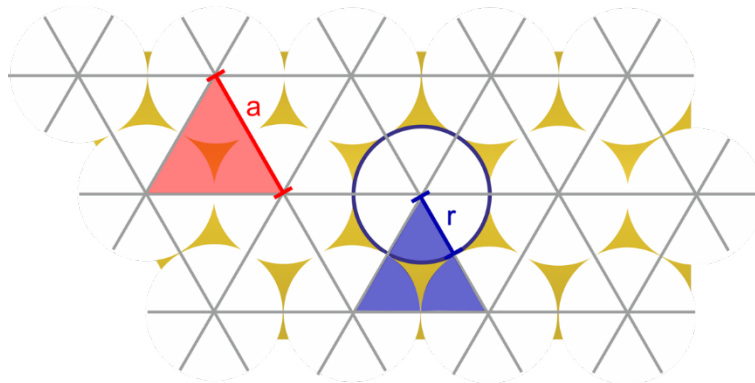


Figure 3.4 | Scheme of the hexagonal arrangement of the polystyrene sphere mask and the gold nanotriangle array.

Calculation of the area covered by gold the nanotriangle array:

$$a = 2 \cdot r = 1 \mu m$$

$$A(\text{Triangle Array}) = A(\text{Triangle, red}) - 3 \cdot A(\text{Circular Segment, blue})$$

$$A(\text{Triangle, red}) = \frac{a^2 \cdot \sqrt{3}}{4} = 0.43 \mu m^2$$

$$\begin{aligned}
 3 \cdot A(\text{Circular Segment, blue}) &= \frac{\pi \cdot r^2}{2} = 0.39 \mu\text{m}^2 \\
 \text{Surface Coverage} &= \frac{A(\text{Triangle, red}) - 3 \cdot A(\text{Circular Segment, blue})}{A(\text{Triangle, red})} \\
 &= \frac{0.43 \mu\text{m}^2 - 0.39 \mu\text{m}^2}{0.43 \mu\text{m}^2} = 9.3 \cdot 10^{-2}
 \end{aligned}$$

Therefore, it is expected that the plasmonic features, especially the EMF enhancement, can be tuned. Upconversion nanoparticles of the composition NaYF₄: 25%Yb,3%Tm with oleic acid as the capping ligand were prepared *via* a bottom-up synthesis by a well-established method [41]. Ytterbium ions act as a sensitizer excitable at 980 nm that transfers the energy in a multiphoton process sequentially to the Tm³⁺-ions. Upon relaxation, anti-Stokes emissions of narrow bandwidth at 800, 475, 450, 360, and 345 nm can be recorded [48]. In dispersion, at low-power irradiation, the emissions at higher energy become less bright compared with those at longer wavelengths. The emission intensity and the quantum efficiency depend not only on the excitation-power density but also on the size and the crystallinity. A favorable low phonon energy of 305 cm⁻¹ of NaYF₄ was the reason we chose this material as the host [49]. Monodisperse particles with a diameter of 26 ± 0.9 nm, estimated from TEM-images (Figs. 3.5A and 3.5B) were synthesized with pure hexagonal crystallinity, as demonstrated by XRD measurements (Fig. 3.5D). Such a crystal structure is known for its one order of magnitude brighter upconversion luminescence compared with that of cubic form [50]. No tendency for agglomeration in cyclohexane was found, and this was verified by dynamic light scattering (Fig. 3.5C).

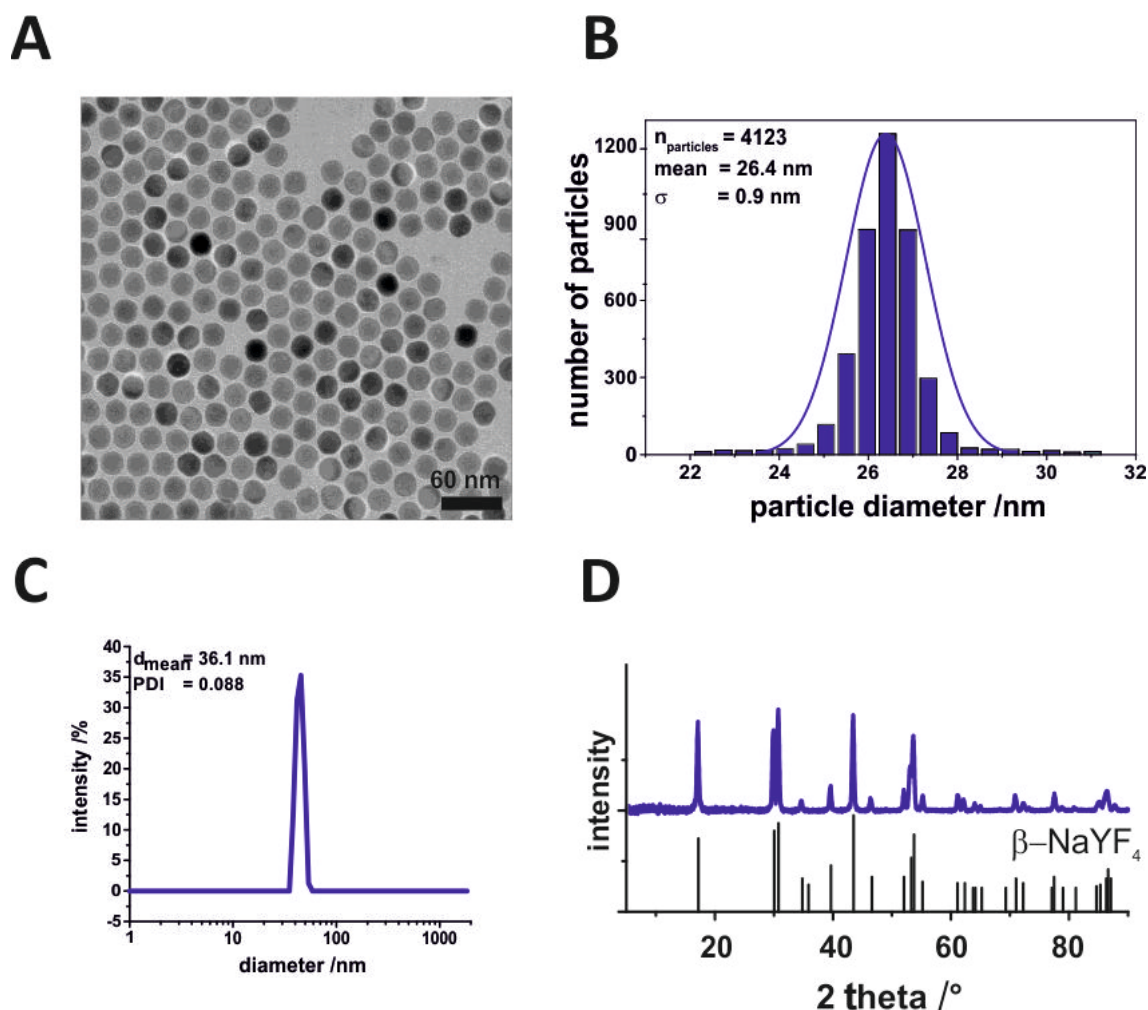


Figure 3.5 | TEM-image (A) and corresponding size distribution (B) of NaYF₄:Yb,Tm particles. The diameter averaged from 4,123 particles is $26.4 \pm 0.9 \text{ nm}$. The monodispersity of the particles was confirmed by a solvodynamic diameter of 33 nm with a polydispersity index of 0.086, measured by dynamic light scattering of the particle dispersion in cyclohexane ($3 \text{ mg} \cdot \text{L}^{-1}$) (C). No agglomeration of the particles in dispersion can be observed. The diffraction pattern (blue) reveals a hexagonal crystal phase as the reflexes of the nanocrystals match the standard reference pattern of $\beta\text{-NaYF}_4$ (ICDD PDF #16-334) (black) (D).

ICP-OES measurements were performed to determine the exact composition and concentration of the UCNPs (Table 3.2). The contents of Yb³⁺ ($25\% \pm 0.2\%$, w/w) and Tm³⁺ ($0.4\% \pm 0.1\%$, w/w) are in good accordance with the ratio of the rare-earth chlorides used during the synthesis.

Table 3.2. The composition of the UCNPs was verified by ICP-OES measurements. The content of each rare earth ion in the particles is in accordance to the theoretical calculated amount of rare earth salts used in for the synthesis of NaYF₄:25%Yb,0.3%Tm.

ion	Y ³⁺	Yb ³⁺	Tm ³⁺	diameter
mole percentage /%	74.6 ± 0.2	25 ± 0.2	0.4 ± 0.1	26 ± 0.9 nm

Finally, the nanoengineered interface is obtained by the linkage of the UCNPs to the gold nanotriangle array by self-assembly. The glass slides with the nanotriangle array were immersed overnight in an ethanolic solution of a long-chained alkanethiol (HS-(CH₂)₁₅-CH₃) in order to form a self-assembled monolayer on gold, which was needed to warrant the stable binding of the UCNPs *via* intercalation of the long-chained oleate capping ligands. After subsequently dropping a total amount of 800 µL of a dispersion of the oleate-capped UCNPs in cyclohexane (22 mg·mL⁻¹) onto the glass slide with the thiol-modified gold nanotriangle array, a stable arrangement of the particles on the surface was achieved. Even after several washing steps a blue upconversion of the nanoengineered interface can be seen upon 980 nm excitation which proves the stable binding of the UCNPs covering the whole surface. This was confirmed by SEM studies (Fig. 3.6) which showed stacks of particles caused by van der Waals and hydrophobic interactions on top of the modified glass slide.

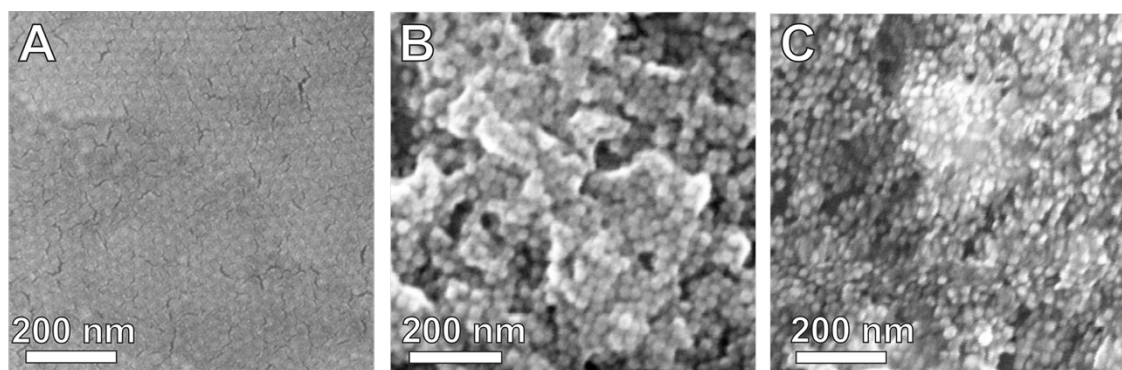


Figure 3.6 | SEM images of the three substrates blank substrate (glass slide) (A), a continuous gold film (B) and a nanoengineered interface (triangle array) (C) functionalized with NaYF₄:Yb,Tm particles.

The stable binding of the UCNPs on the gold chip due to the van der Waals interactions was confirmed by SPR measurements, pictured in Figure 3.7. The blue curves show SPR angle of 69.6° for an assembly identically to the one used for the detection of vitB12. The angle does not change over time, which indicates that no particles get washed away. When comparing this curve to theoretical calculations [45], the SPR angle of a monolayer of particles should be in the range of 67.6°, for a double layer at 72.5°. According to the value obtained by

measurement, it becomes obvious that in average there is more than a monolayer of particles assembled to the surface. When calculating the theoretical amount of particles which is needed to assemble a monolayer, drop-casting of exactly this amount of dispersed particles on the thiol coated gold slide results in an SPR angle of 63.1°, which is in accordance to the theoretical calculation of the SPR curve of a surface covered by 10% of particles only. Again, no loss of particles under flow conditions in water is found. The Figures 3.7E to 3.7G indicate that oleate coated UCNPs do not stick at the gold surface. Even after 1 min of flow all particles are washed away, as the resonance angel is almost the same than for bare gold. The same is found for the control experiment with particles, where the oleate was removed by a ligand exchange to BF₄⁻, when drop casted on a blank gold or on a thiol modified gold. On the blank gold, the particles tend to bind, resulting the same coverage as found for the oleate-coated particles on the thiol modified gold. Nevertheless, despite no effective binding, these particles get easily washed away over time. As expected, UCNPs@BF₄⁻ show no tendency to bind at all on thiol coated gold films.

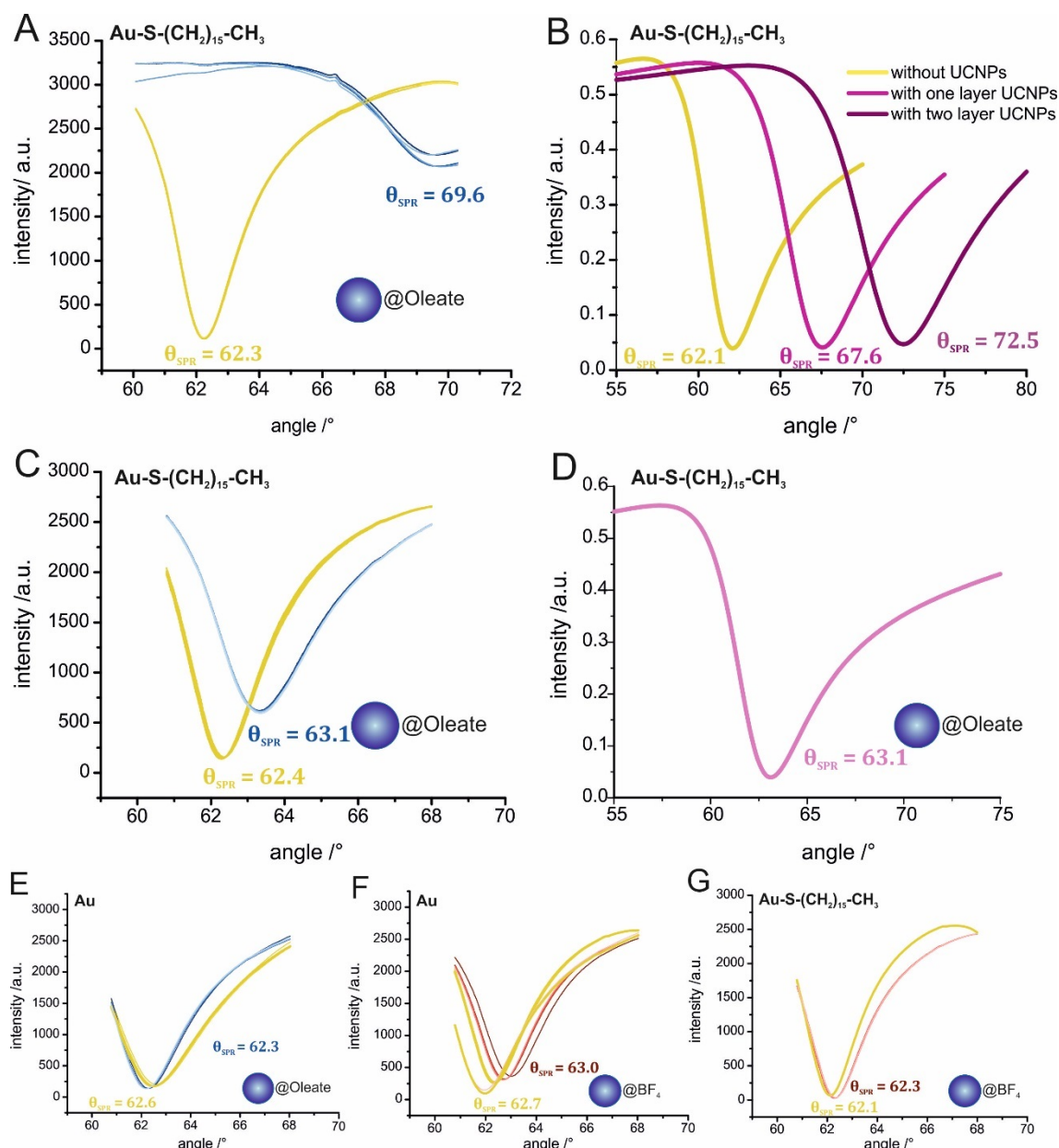


Figure 3.7 | SPR curves of particle attachment on blank and 1-mercaptohexadecane modified gold films (A, C, E-G) and theoretical calculations of SPR curves (B, D). The surface modification of the gold is given in the upper left corner and the particle modification is symbolized at the right bottom of each figure. In A, C, E-G curves were recorded after 1, 5, 10, 15 and 30 min under constant flow of 1 mL·min⁻¹, indicated by blurring of the curves. The blue curves represent the measurement channel where the particles have been immobilized, the yellow curves show the reference channel without any particles. Theoretical calculations of SPR curves of particle assemblies on gold are indicated in purple, without particles in yellow. The difference in A and C is the amount of particles which have been assembled: in A, it was the same amount as used for the chip assembly used in the luminescence studies; in C only an amount of particles was drop-casted which theoretically will be needed to form a monolayer arrangement. All curves were recorded at room temperature and in water.

The stability of the particles assembled on nanotriangles was additionally confirmed by Raman spectroscopy, showing no significant change in the intensity of the characteristic phonon band of the NaYF₄ lattice at 305 cm⁻¹ over 10 days (Fig. 3.8) [51].

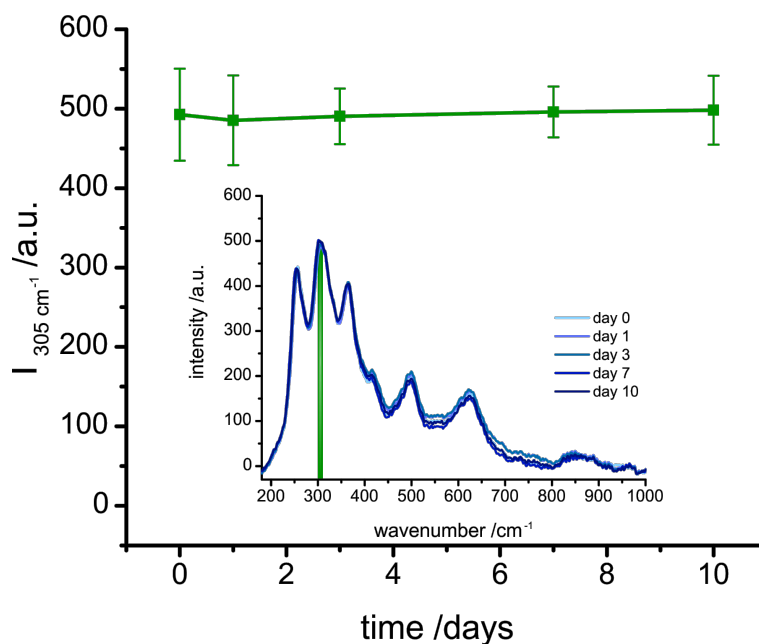


Figure 3.8 | Change in the intensity of the phonon band of the NaYF₄ lattice over time, measured by Raman spectroscopy of UCNPs on a continuous gold film modified with 1-mercaptopentadecane. The individual spectra are shown in the inset, the position of the phonon band at 305 cm⁻¹ which is marked in green. One spectrum represents an average over 30 spectra, recorded for each of the 10 different measurement spots randomly distributed over the whole gold surface with an acquisition time of 5 s. All experimental settings for acquiring the spectra were kept constant.

3.4.2 Luminescence Properties

The NaYF₄:Yb,Tm nanoparticles were assembled on three different types of glass slides: (a) a blank slide, (b) a modified with a continuous gold film, and (c) a slide modified with a gold nanotriangle array. The thickness of the gold was identically on both types. The enhancement of the NIR to UV upconversion caused by the gold and especially by the nanotriangle array can be seen from the normalization of the spectra to the 450 nm emission (Fig. 3.9).

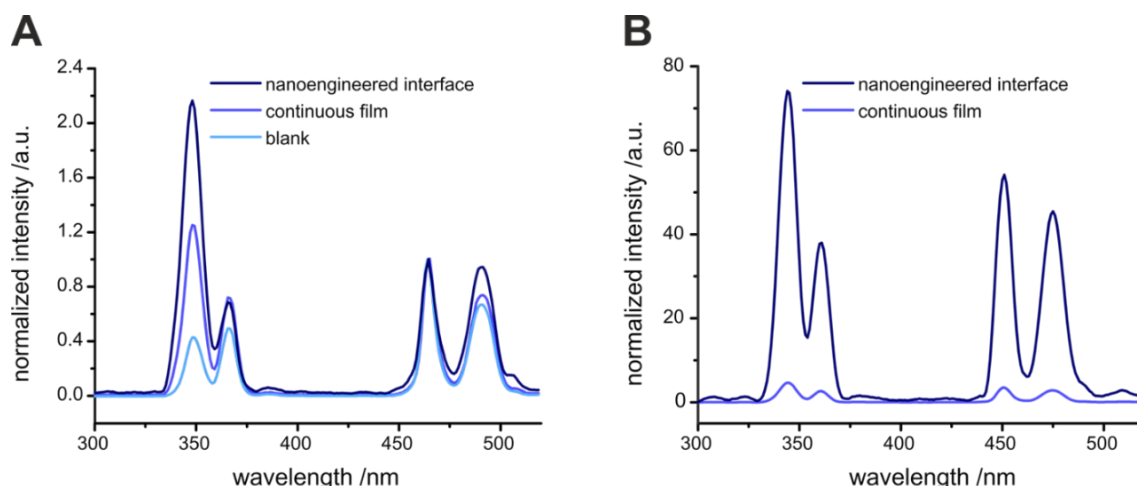


Figure 3.9 | Luminescence spectra of UCNPs attached on a blank substrate (glass slide, light blue), a continuous gold film (blue), and a nanoengineered interface (gold triangle array, dark blue). (A) Spectra normalized to 450 nm emission and (B) spectra normalized on the gold area. Nanoparticles were excited by a 980 nm laser module (200 mW, cw).

For the emission at 344 and 360 nm, peak inversion can be observed when gold is in close proximity to the UCNPs. The peak ratio of $I_{344\text{ nm}}/I_{360\text{ nm}}$ of 0.8 in the case of a blank glass substrate changes to 1.7 for the continuous gold film and increase to 3.2 for the nanotriangle array. On both gold surfaces, plasmonic features are responsible for the higher efficiency of the 1I_6 to 3H_6 transition. The EMF is supposed to interact with the UCNPs to improve the upconversion efficiency, as demonstrated by the peak inversion in the UV range. Jin *et al.* [52] reported recently that the four-photon process of the upconversion luminescence becomes more likely, compared with the three-photon process, when the excitation-power density increases, which results in peak ratios of >1 . Under relatively low-power excitation of approximately $13\text{ W}\cdot\text{cm}^{-2}$, as was used throughout these studies, the probability of the 1I_6 to 3H_6 transition for particles is very unlikely. This is demonstrated by the spectrum of the dispersion of these particles in water, showing a peak ratio $I_{344\text{ nm}}/I_{360\text{ nm}}$ of about 0.8 (Fig. 3.10A), which is very similar to the ratio measured for the UCNPs-modified glass slide.

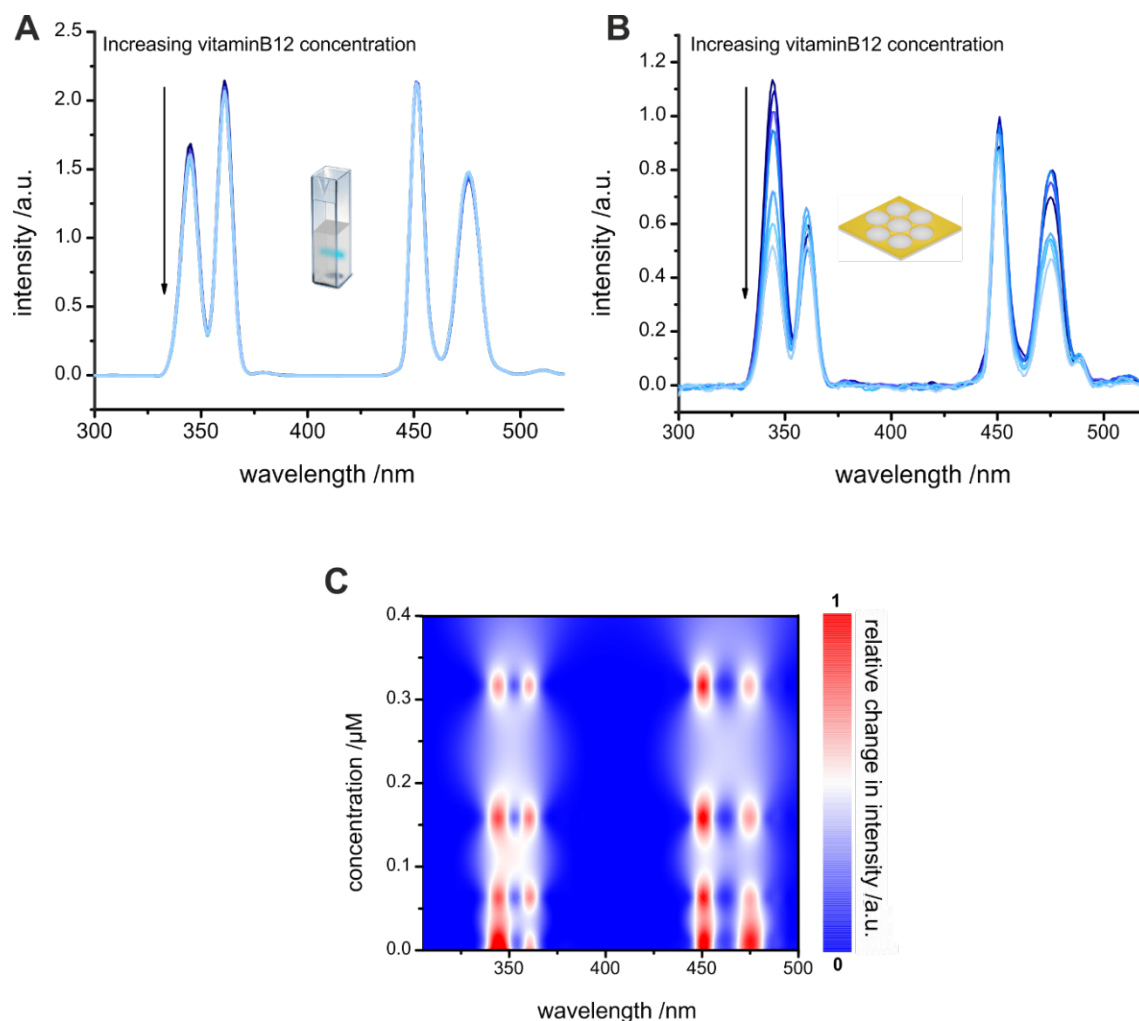


Figure 3.10 | (A) Luminescence spectra of NaYF₄:Yb,Tm@PAA particles in aqueous solution (10 mg·mL⁻¹) and (B) luminescence spectra of NaYF₄:Yb,Tm@oleate particles attached on a gold triangle array (nanoengineered interface) in the presence of an increasing amount of vitB12 ranging from 3 to 634 nM. (C) Color map of the relative changes of the emission spectra of the nanoengineered interface as a function of the vitB12. All spectra were excited by a 980 nm laser module at ~13 W·cm⁻².

An explanation for the enhancement might be given by the hot spots, which generate localized surface plasmons (LSP) at nanometer dimensions, in contrast to the propagating surface plasmons on a continuous gold film [53]. The EMF at the hot spots will confine the excitation-power density, and therefore the brightness of the 345 nm peak will be enhanced. In the study of Jin *et al.* [52] the excitation-power-dependent change of the emission-peak ratio was shown for larger NaYF₄:Yb,Tm@NaYF₄ nanorods with a length of ~46 nm and a width of ~25 nm. The highest value they report for $I_{344\text{ nm}}/I_{360\text{ nm}}$ was ~1.5, recorded at an excitation power density of ~60 W·cm⁻². This clearly shows that a massive enhancement takes place because of the small UCNPs of 26 nm diameter on the nanoengineered surfaces at the low excitation-power density of ~13 W·cm⁻². Unfortunately, with the equipment in our lab, we were not able to perform an excitation-power-dependent study. As a control experiment, extinction measurements with the three different types of substrates were carried out. For nanotriangle

arrays, the gold area is significantly smaller than that in a continuous gold film; therefore, a lower absorbance at 980 nm is expected. This is not the case, as the extinction is increased in a similar way for both gold surfaces, indicating the presence of an additional plasmonic effect (Fig. 3.11).

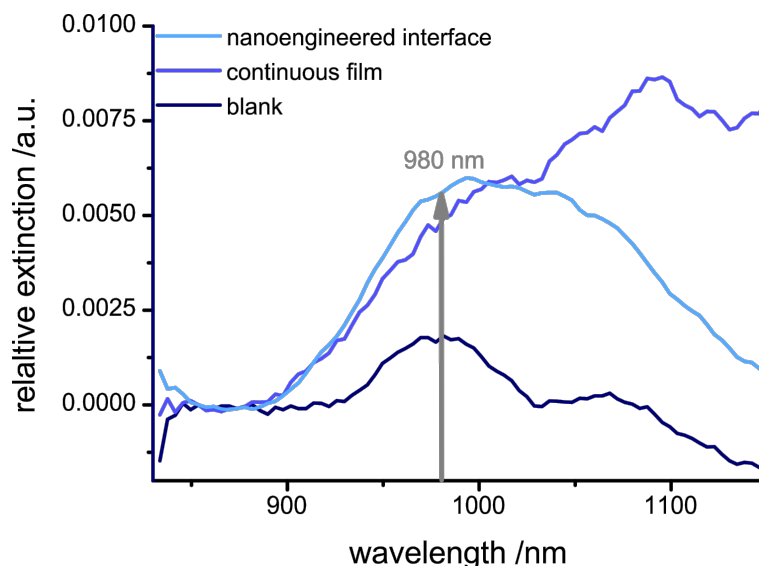


Figure 3.11 | Extinction spectra of the UCNPs on a glass slide (blank), a continuous gold film and a gold nanotriangle array (nanoengineered interface). Spectra were normalized for illustration of the peak variation and the excitation wavelength of 980 nm of the UCNPs is shown. Substrates were covered by ~50 nm Au with a ~5 nm Ti adhesion layer.

Furthermore, luminescence measurements with increased distance between the gold and the UCNPs, realized by depositing the UCNPs on the side opposite to the nanotriangle array on a glass slide of ~1 mm in thickness, showed no enhancement of the NIR to UV upconversion, confirming the effect of the plasmonic features on the UCNPs (Fig. 3.12).

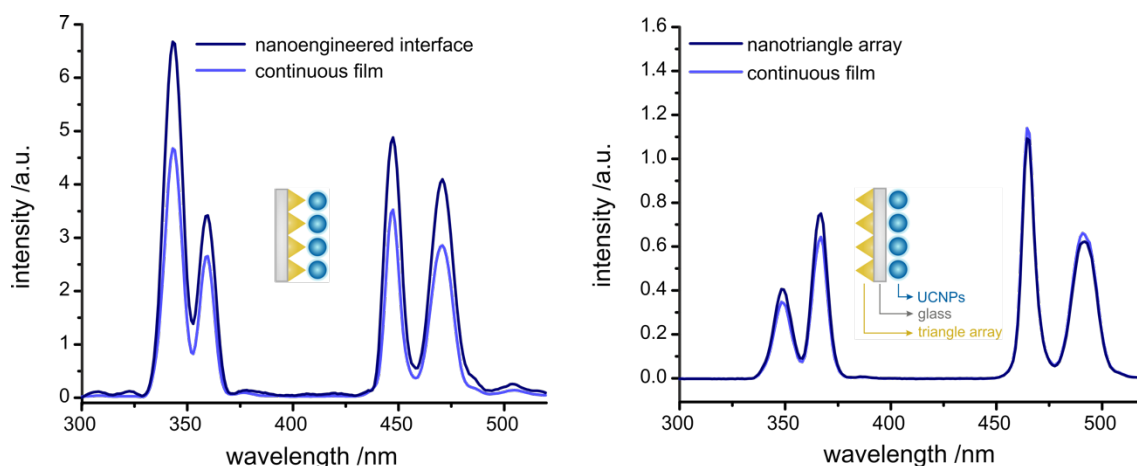


Figure 3.12 | Luminescence spectra of the NaYF₄:Yb,Tm particles assembled on a continuous gold film and a gold nanotriangle array upon 980 nm excitation at approx. 13 W·cm⁻². In (A), the UCNPs were placed on the gold, in (B) the UCNPs were attached to the glass with the gold on the other side as symbolized by the schema in the inserts. The spectra were not normalized to any peak. The inversion of the intensity ratio of the two emission peaks in the UV range as well as the increased emission intensity for both peaks shows the impact of the gold to the NIR to UV upconversion for the nanoengineered interface.

In Figure 3.9B, the spectra were normalized by the respective gold areas. In such cases, a ~16 times higher upconversion efficiency for the emission in the UV was found for the nanoengineered interface compared with that of the continuous gold film.

3.4.3 Luminescence Detection of Vitamin B12 at Nanoengineered Interfaces

The outstanding enhancement of the UV emission of the UCNPs by the nanoengineered interface enables a novel kind of sensing application based on luminescence measurements. One of the biggest advantages can be attributed to the fact that the UV region of the electromagnetic spectrum becomes accessible for a simple, label-free, intensity-based readout of changes in analyte concentrations caused by reabsorption processes. This is attributed to the excitation in the NIR range, which minimizes background caused by the fluorescence of organic molecules, proteins, or tissues. Vitamin B12, as a model analyte, exhibits an absorption peak at 361 nm, overlapping the anti-Stokes emissions of the ¹I₆ to ³H₆ and ¹D₂ to ³H₆ transitions and peaking at 345 and 360 nm (Fig. 3.13).

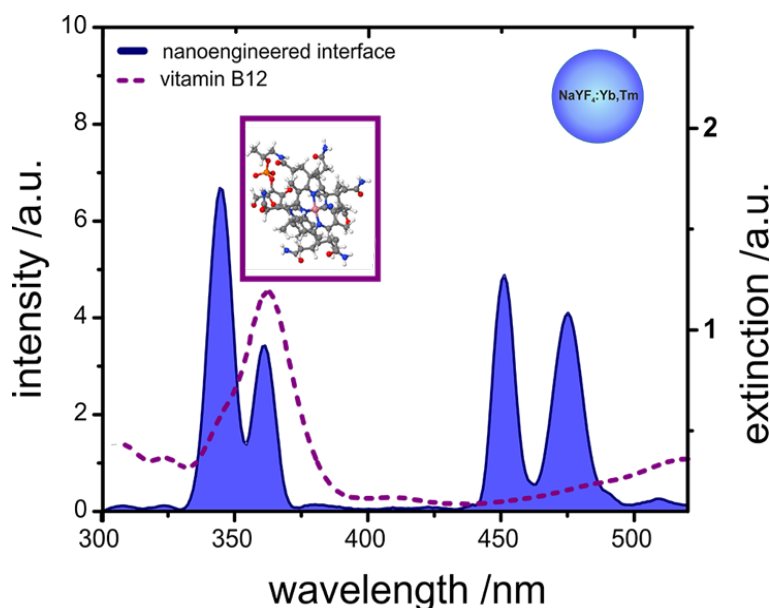


Figure 3.13 | Upconversion luminescence of a nanoengineered interface (blue) showing spectral overlap with the absorbance of vitB12 (purple).

Therefore, it is expected that the luminescence of the UCNPs in the UV range will decrease in the presence of vitB12. The determination of vitB12 by the same principle but in a classical cuvette assay with dispersed particles highlights the capabilities of the nanoengineered interface. Here, the same UCNPs have been used with the exception that the ligand oleate was replaced with poly(acrylic acid) *via* a ligand-exchange protocol [54]. For the determination of vitB12 using the nanoengineered interface, a homemade measurement cell consisting of two glass slides, one of which was modified with the nanoengineered interface separated by a ~3 mm PDMS gasket and holding a total volume of 200 μ L of the analyte, was used. Figure 3.10 compares the spectra for the different vitB12 concentrations. When the concentration of vitB12 increases from ~3 to ~630 nM, the luminescence of the UCNPs in the cuvette is almost not affected. Therefore, this method cannot be used with low-power NIR laser excitation in a complex media and high-power excitation at 980 nm suffers from the drawback that aqueous samples will be heated because of the local absorption maximum of water at this wavelength [55]. In contrast, the NIR to UV upconverted luminescence of the nanoengineered interface leads to a strong decrease of the signal in the UV range (Fig. 3.10B) for small analyte concentrations and low-excitation power density. All upconversion peaks in the UV and blue regions of the spectrum are influenced by the vitB12 concentration in terms of their intensity. For evaluation of the greatest peak change, a 2D color map of the relative changes in the luminescence intensity in the spectral range from 300 to 500 nm upon increasing vitB12 concentrations is shown (Fig. 3.10C). For the emissions at 360 and 450 nm, no significant change in the relative intensity is observed. The peak at 475 nm decreases at low

concentrations, similar to the one at 345 nm, but for the latter one, the dynamic range is larger. From Figure 3.13, it can be seen that there is no significant spectral overlap for the peak at 450 nm; therefore, one explanation of the decrease may be attributed to the fact that the excited states in the UCNPs might not be fully independent, as they both get fed by energy transfer from Yb³⁺ ions. Another possible explanation might be that the gold also interacts with the deactivation pathway of the excited states of Tm³⁺ (Fig. 3.14).

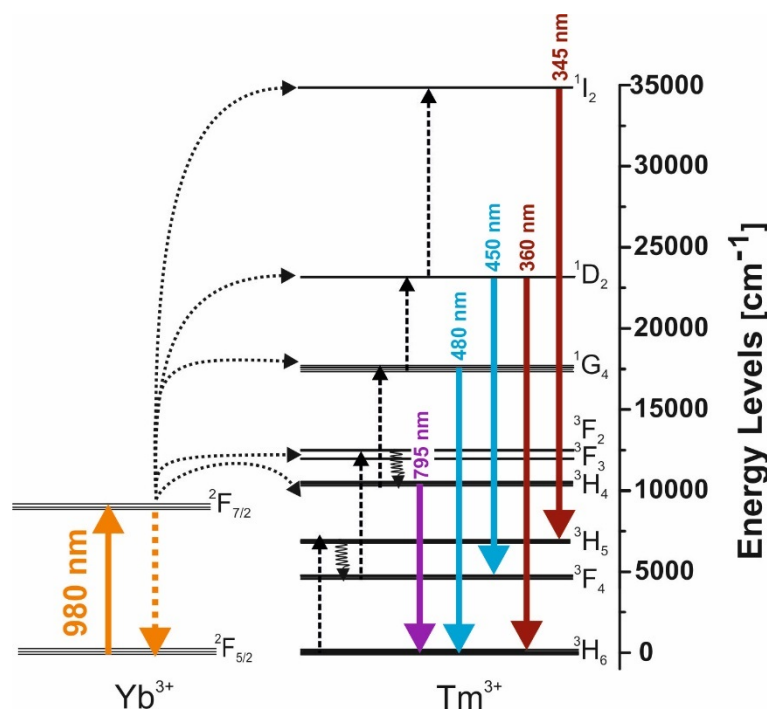


Figure 3.14 | Energy levels of Tm³⁺ and Yb³⁺ showing the transitions for 980 nm excitation of Yb³⁺ and the sequential energy transfer to Tm³⁺ to populate the states ¹I₂, ¹D₂, ¹G₄ and ³H₅, resulting in emissions at 345 nm, 360 nm, 450 nm, 480 nm and 785 nm. Non-radiative transitions are colored in black.

Both postulations will be investigated in a future study describing the detailed photophysics of such nanoengineered interfaces. As a consequence, a wavelength of 400 nm is suggested as a reference signal, as it shows no dependence on the vitB12 concentration (Fig. 3.10C). For the emissions at 360 and 450 nm, nearly no change in the relative intensity is observed. The peak at 475 nm decreases at low concentrations, similar to the one at 345 nm, but for the latter one, the dynamic range is larger.

Serum spiked with vitB12 at concentrations from 3 to 634 nM, without the need for any pretreatment and with a low consumption of sample volume (200 μ L), demonstrates the performance of the nanoengineered interface in sensing *via* the plasmonic enhancement of the NIR to UV upconversion. Two methods for data evaluation were compared. The spectral overlap of the analyte with both upconversion emissions in the UV range and the change in

the peak area, integrated from 334 to 395 nm, were monitored as functions of the vitB12 concentration. These results were compared with the change in the ratio $I_{345\text{ nm}}$ to $I_{400\text{ nm}}$ (Fig. 3.15A).

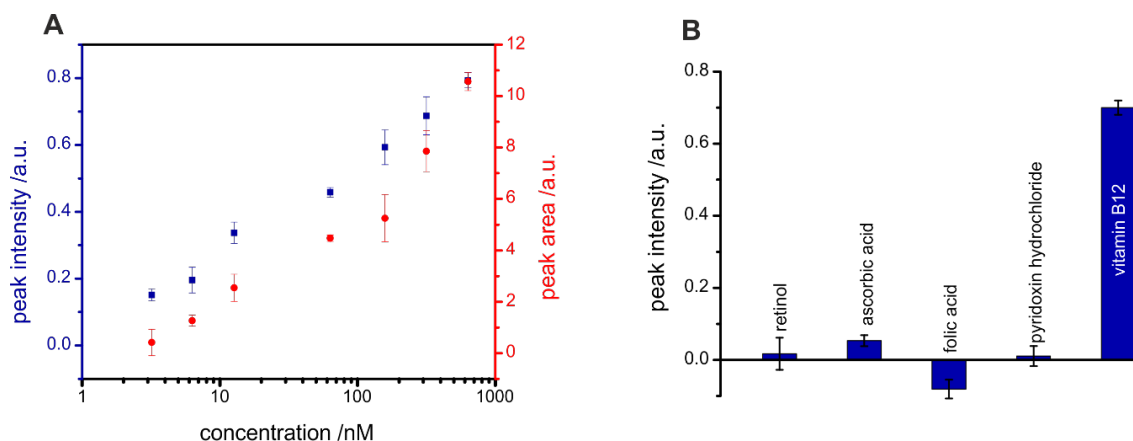


Figure 3.15 | (A) Calibration plots of the upconversion luminescence for peak intensity (blue) at 345 nm or peak area (red) integrated from 334 to 395 nm in serum spiked with different amounts of vitB12. The luminescence spectra for both methods were normalized to the luminescence intensity recorded at 400 nm. Excitation was performed by a 980 nm laser module of $\sim 13\text{ W}\cdot\text{cm}^{-2}$ power density. (B) Cross sensitivity evaluated by the peak-intensity readout at 345 nm at concentrations of 634 nM for all molecules. The light-blue bars represent the changes in the intensity of the possible interfering substance, and the dark-blue bars show the impact of these substances on the vitB12 determination.

Both methods of data evaluation correlated very well, as can be seen the almost identical sensitivities, and allowed the detection of vitB12 in the nanomolar range, which includes physiologically relevant levels in serum [30]. The analytical figures of merit are summarized in Figure 3.16 and Table 3.3.

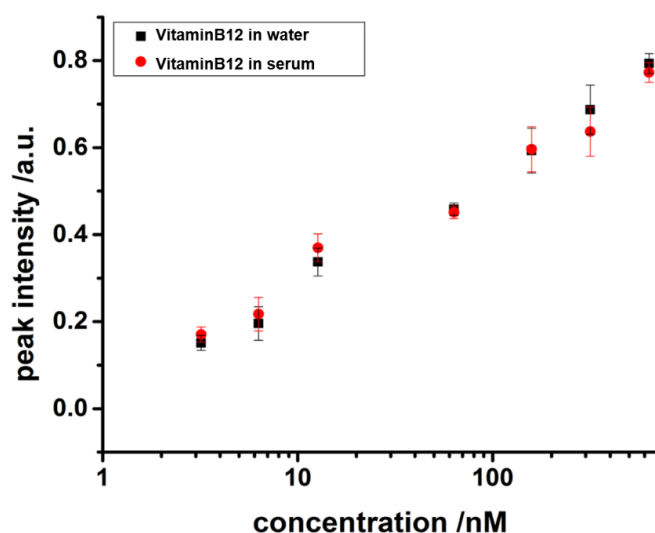


Figure 3.16 | Calibration plots of the upconversion luminescence for peak intensity (blue) at 345 nm in water and in serum, spiked with different amounts of vitB12. The luminescence spectra for both methods were normalized to the luminescence intensity recorded at 400 nm. Excitation was performed by a 980 nm laser module of $\sim 13\text{ W}\cdot\text{cm}^{-2}$ power density.

Table 3.3. Recovery rates for different amounts of vitB12 spiked into serum.

	added /nM	found /nM	recovery rate /%
sample1	3.20	3.18 ± 0.2	99.4
sample2	63.30	62.9 ± 1.3	99.3
sample3	158.3	158.0 ± 2.3	99.8
sample4	633.1	631.5 ± 2.9	99.7

The method has good selectivity toward molecules commonly present in serum that are known for their interference of classical fluorescence assays based on the Stokes shift (Fig. 3.17).

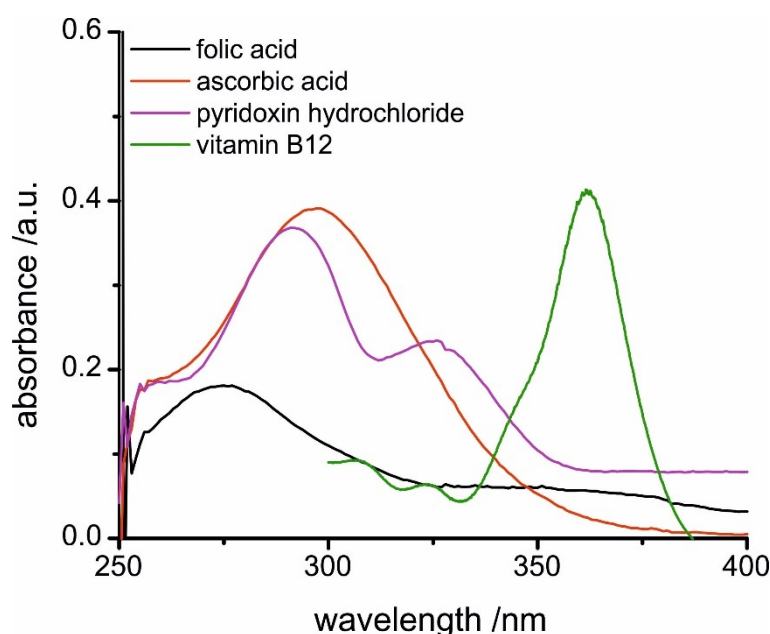


Figure 3.17 | Absorption spectra of folic acid, ascorbic acid, pyridoxin hydrochloride and vitaminB12. These molecules are commonly indicated as possible interfering substances for assays for vitB12 based on fluorescence read-out.

No cross-sensitivity was found for retinol, ascorbic acid, folic acid, or pyridoxin hydrochloride (Fig. 3.15B). The LOD for vitB12 determination with the nanoengineered interface was approximately one order of magnitude lower than those of established analytical technique like HPLC, Raman spectroscopy, fluorescence, and surface-plasmon resonance (Table 3.1). Immunoassays and mass spectrometry demonstrate the lowest LODs, with a remarkably low value of 0.063 fM for mass spectrometry. Those techniques suffer from costly instruments, numerous processing steps, and lengthy assay times. A microbiological assay already requires 25 h exposure time, which is needed for the detection of vitB12 by HPLC [36]. Here, the nanoengineered interface with assay times of a few minutes and a LOD sufficient for biosensor applications is beneficial. The most important characteristic, which emphasizes the

capabilities of our system, is its label-free nature. Chemiluminescence (CL) and radioimmunoassay enable similar LODs, but they depend on labeling and high trained operators.

The detection of vitB12 via CL relies on the presence of Co²⁺. Without a label, discrimination between free and unbound cobalt is not possible [35,56]. In contrast, the method presented in this work can also be used for online monitoring, as it does not require any label or sample pretreatment. Because of to the low-power excitation, cheap, small laser modules combined with microfluidics and a standard spectrometer the size of a match box can be used both of which make this approach attractive for sensing applications. In contrast to surface-plasmon resonance, the nanoengineered interface can be assembled on all optically transparent materials, and no need of high-refractive-index glass for coupling of surface plasmons is required.

3.5 Conclusion

In conclusion, an enhancement strategy of the NIR to UV upconversion of NaYF₄:Yb,Tm is presented by the construction of an nanoengineered interface consisting of a glass slide modified with gold nanotriangle arrays with UCNPs on top. It was demonstrated that such an assembly enhances the emission peak at 344 nm by a factor of ~6 upon excitation at 980 nm with an excitation-power density of only 13 W·cm⁻². Such low-power excitation makes this concept highly attractive for sensing applications based on luminescence detection in the UV region, especially in biological samples, as the NIR excitation avoids autofluorescence. This proof of concept can be used for an early readout of vitB12 in serum, where upregulated concentrations of vitB12 indicate the early stage of breast and liver cancer [57,58]. These results indicate that nanoengineered interfaces based on UCNPs deposited on nanotriangle arrays are promising for label-free, online monitoring of biomolecules.

Acknowledgement

The authors thank Sandy Franziska Himmelstoß for the transmission electron micrographs and Prof. Reinhard Rachel for his support. Furthermore, Joachim Rewitzer and Vanessa Tomanek are acknowledged for their assistance during the ICP-OES measurements. Prof. Arno Pfitzner is acknowledged for his support with the XRD measurements. Christian Bäuml

and Peter Hausler is thanked for the assistance with the SEM images. Christa Genslein has been supported by the DFG Research Training Group 1570.

3.6 References

- [1] Nayak S, Blumenfeld NR, Laksanasopin T, Sia SK (2017) Point-of-care diagnostics: Recent developments in a connected age. *Anal. Chem.* 89(1):102-23.
- [2] Griss R, Schena A, Reymond L, Patiny L, Werner D, Tinberg CE, Baker D, Johnsson K (2014) Bioluminescent sensor proteins for point-of-care therapeutic drug monitoring. *Nat. Chem. Biol.* 10(7):598-603.
- [3] Fan R, Ebrahimi M, Quitmann H, Aden M, Czermak P (2016) An innovative optical sensor for the online monitoring and control of biomass concentration in a membrane bioreactor system for lactic acid production. *Sensors* 16(3):411
- [4] Tu L, Li X, Bian S, Yu Y, Li J, Huang L, Liu P, Wu Q, Wang W (2017) Label-free and real-time monitoring of single cell attachment on template-stripped plasmonic nano-holes. *Sci Rep* 7(1):11020.
- [5] Hinamoto T, Takashina H, Sugimoto H, Fujii M (2017) Controlling surface plasmon resonance of metal nanocap for upconversion enhancement. *J. Phys. Chem. C* 121(14):8077-83.
- [6] Wang F, Banerjee D, Liu Y, Chen X, Liu X (2010) Upconversion nanoparticles in biological labeling, imaging, and therapy. *Analyst* 135(8):1839-54.
- [7] Wang F, Liu X (2009) Recent advances in the chemistry of lanthanide-doped upconversion nanocrystals. *Chem. Soc. Rev.* 38(4):976-89.
- [8] Gao R, Hao C, Xu L, Xu C, Kuang H (2018) Spiny nanorod and upconversion nanoparticle satellite assemblies for ultrasensitive detection of messenger RNA in living cells. *Anal. Chem.* 90(8):5414-21.
- [9] Buchner M, Ngoensawat U, Schenck M, Fenzl C, Wongkaew N, Matlock-Colangelo L, Hirsch T, Duerkop A, Baeumner A (2017) Embedded nanolamps in electrospun nanofibers enabling online monitoring and ratiometric measurements. *J. Mater. Chem. C* 5(37):9712-20.
- [10] Mader HS, Kele P, Saleh SM, Wolfbeis OS (2010) Upconverting luminescent nanoparticles for use in bioconjugation and bioimaging. *Curr. Opin. Chem. Biol.* 14(5):582-96.
- [11] Feng AL, You ML, Tian L, Singamaneni S, Liu M, Duan Z, Lu TJ, Xu F, Lin M (2015) Distance-dependent plasmon-enhanced fluorescence of upconversion nanoparticles using polyelectrolyte multilayers as tunable spacers. *Sci. Rep.* 5:7779.
- [12] Luu Q, Hor A, Fisher J, Anderson RB, Liu S, Luk T, Paudel HP, Farrokh Baroughi M, May PS, Smith S (2014) Two-Color surface plasmon polariton enhanced upconversion in NaYF₄:Yb,Tm nanoparticles on Au nanopillar arrays. *J. Phys. Chem. C* 118(6):3251-7.
- [13] Homann C, Krukewitt L, Frenzel F, Grauel B, Würth C, Resch-Genger U, Haase M (2018) NaYF₄:Yb,Er/NaYF₄ Core/Shell nanocrystals with high upconversion luminescence quantum yield. *Angew. Chem. Int. Ed.* 57(28):8765-9.
- [14] Suyver JF, Grimm J, van Veen MK, Biner D, Krämer KW, Güdel HU (2006) Upconversion spectroscopy and properties of NaYF₄ doped with and/or Er³⁺, Tm³⁺ and/or Yb³⁺. *J. Lumin.* 117(1):1-12.
- [15] Wiesholler LM, Hirsch T (2018) Strategies for the design of bright upconversion nanoparticles for bioanalytical applications. *Opt. Mat.* 80:253-64.

- [16] Lu D, Mao C, Cho SK, Ahn S, Park W (2016) Experimental demonstration of plasmon enhanced energy transfer rate in NaYF₄:Yb³⁺,Er³⁺upconversion nanoparticles. *Sci. Rep.* 6:18894.
- [17] Chen G, Ohulchanskyy TY, Kumar R, Agren H, Prasad PN (2010) Ultrasmall monodisperse NaYF₄:Yb³⁺/Tm³⁺ nanocrystals with enhanced near-infrared to near-infrared upconversion photoluminescence. *ACS Nano* 4(6):3163-8.
- [18] Lin M, Zhao Y, Liu M, Qiu M, Dong Y, Duan Z, Li YH, Pingguan-Murphy B, Lu TJ, Xu F (2014) Synthesis of upconversion NaYF₄:Yb³⁺,Er³⁺ particles with enhanced luminescent intensity through control of morphology and phase. *J. Mater. Chem. C* 2(19):3671-6.
- [19] Qiu Z, Shu J, Tang D (2018) Near-infrared-to-ultraviolet light-mediated photoelectrochemical aptasensing platform for cancer biomarker based on core – shell NaYF₄:Yb,Tm@TiO₂ upconversion microrods. *Anal. Chem.* 90(1):1021-8.
- [20] Wang Y, Zheng K, Song S, Fan D, Zhang H, Liu X (2018) Remote manipulation of upconversion luminescence. *Chem. Soc. Rev.* 47(17):6473-85.
- [21] Yi G, Chow G (2007) Water-soluble NaYF₄:Yb,Er(Tm)/NaYF₄/polymer core/shell/shell nanoparticles with significant enhancement of upconversion fluorescence. *Chem. Mater.* 19(3):341-3.
- [22] Brolo AG (2012) Plasmonics for future biosensors. *Nat. Photonics* 6(11):709-13.
- [23] Saboktakin M, Ye X, Oh SJ, Hong S, Fafarman AT, Chettiar UK, Engheta N, Murray CB, Kagan CR (2012) Metal-enhanced upconversion luminescence tunable through metal nanoparticle-nanophosphor separation. *ACS Nano* 6(10):8758-66.
- [24] Di Wu M, García-Etxarri A, Salleo A, Dionne JA (2014) Plasmon-enhanced upconversion. *J. Phys. Chem. Lett.* 5(22):4020-31.
- [25] Xiong K, Emilsson G, Dahlin AB (2016) Biosensing using plasmonic nanohole arrays with small, homogenous and tunable aperture diameters. *Analyst* 141(12):3803-10.
- [26] Aćimović SS, Šípová H, Emilsson G, Dahlin AB, Antosiewicz TJ, Käll M (2017) Superior LSPR substrates based on electromagnetic decoupling for on-a-chip high-throughput label-free biosensing. *Light. Sci. Appl.* 6(8):e17042.
- [27] Petryayeva E, Krull UJ (2011) Localized surface plasmon resonance: Nanostructures, bioassays and biosensing-a review. *Anal. Chim. Acta.* 706(1):8-24.
- [28] Fang Y, Jiao Y, Xiong K, Ogier R, Yang Z, Gao S, Dahlin AB, Käll M (2015) Plasmon enhanced internal photoemission in antenna-spacer-mirror based Au/TiO₂ Nanostructures. *Nano Lett.* 15(6):4059-65.
- [29] Masson J, Murray-Méthot M, Live LS (2010) Nanohole arrays in chemical analysis: manufacturing methods and applications. *Analyst* 135(7):1483-9.
- [30] Hitzhusen JC, Taplin ME, Ansell JE (1986) Vitamin B12 levels and age. *Am. J. Clin. Pathol.* 85(1):32-6.
- [31] Clarke R, Smith AD, Jobst KA, Refsum H, Sutton L, Ueland PM (1998) Folate, Vitamin B12, and serum total homocysteine levels in confirmed Alzheimer disease. *Arch. Neurol.* 55(11):1449-55.
- [32] Guerra-Shinohara EM, Paiva AA, Rondó PH, Yamasa-ki K, Terzi CA, D'Almeida V (2002) Relationship between total homocysteine and folate levels in pregnant women and their newborn babies according to maternal serum levels of vitamin B12. *BJOG* 109(7):784-91.
- [33] Carkeet C, Dueker SR, Lango J, Buchholz BA, Miller JW, Green R, Hammock BD, Roth JR, Anderson PJ (2006) Human vitamin B12 absorption measurement by accelerator mass spectrometry using specifically labeled ¹⁴C-cobalamin. *Proc. Natl. Acad. Sci.* 103(15):5694-9.
- [34] Kumar LS, Thakur MS (2011) Competitive immunoassay for analysis of vitamin B12. *Anal. Biochem.* 418(2):238-46.

- [35] Lok KS, Lee PP, Kwok YC, Nguyen NT. Rapid determination of vitamin B12 concentration with a chemiluminescence lab on a chip. *Lab Chip* 2012;12(13):2353-61.
- [36] Kelleher BP, Broin SD (1991) Microbiological assay for vitamin B12 performed in 96-well microtitre plates. *J. Clin. Pathol.* 44(7):592-5.
- [37] Heudi O, Kilinc T, Fontannaz P, Marley E (2006) Determination of vitamin B12 in food products and in premixes by reversed-phase high performance liquid chromatography and immunoaffinity extraction. *J. Chromatogr. A* 1101(1-2):63-8.
- [38] Cannon MJ, Myszka DG, Bagnato JD, Alpers DH, West FC, Grissom CB (2002) Equilibrium and kinetic analyses of the interactions between vitamin B12 binding proteins and cobalamins by surface plasmon resonance. *Anal. Biochem.* 305(1):1-9.
- [39] Radu AI, Kuellmer M, Giese B, Huebner U, Weber K, Cialla-May D, Popp J (2016) Surface-Enhanced Raman Spectroscopy (SERS) in food analytics: Detection of vitamins B2 and B12 in cereals. *Talanta* 160:289-97.
- [40] Gholami J, Manteghian M, Badii A, Javanbakht M, Ueda H (2015) Label free detection of vitamin B12 based on fluorescence quenching of graphene oxide nanolayer. *Fuller. Nanotub. Car. N.* 23(10):878-84.
- [41] Wilhelm S, Kaiser M, Würth C, Heiland J, Carrillo-Carrion C, Muhr V, Wolfbeis OS, Parak WJ, Resch-Genger U, Hirsch T (2015) Water dispersible upconverting nanoparticles: effects of surface modification on their luminescence and colloidal stability. *Nanoscale* 7(4):1403-10.
- [42] Dong A, Ye X, Chen J, Kang Y, Gordon T, Kikkawa JM, Murray CB (2011) A generalized ligand-exchange strategy enabling sequential surface functionalization of colloidal nanocrystals. *J. Am. Chem. Soc.* 133(4):998-1006.
- [43] Genslein C, Hausler P, Kirchner E, Bierl R, Baeumner AJ, Hirsch T (2017) Detection of small molecules with surface plasmon resonance by synergistic plasmonic effects of nanostructured surfaces and graphene. *SPIE BiOS.* 10080:100800F.
- [44] Sokolov VI, Zvyagin AV, Igumnov SM, Molchanova SI, Nazarov MM, Nechaev AV, Savelyev AG, Tyutyunov AA, Khaydukov EV, Panchenko VY (2015) Determination of the refractive index of β -NaYF₄:Yb³⁺,Er³⁺,Tm³⁺ nanocrystals using spectroscopic refractometry. *Opt. Spectrosc.* 118(4):609-13.
- [45] WinSpall, Version 3.01; Max-Planck Institute for Polymer Research: Mainz, Germany; Reflectivity simulation program solving Fresnel Equations.
- [46] Paudel HP, Zhong L, Bayat K, Baroughi MF, Smith S, Lin C, Jiang C, Berry MT, May PS (2011) Enhancement of near-infrared-to-visible upconversion luminescence using engineered plasmonic gold surfaces. *J. Phys. Chem. C* 115(39):19028-36.
- [47] Correia-Ledo D, Gibson KF, Dhawan A, Couture M, Vo-Dinh T, Graham D, Masson J (2012) Assessing the location of surface plasmons over nanotriangle and nanohole arrays of different size and periodicity. *J. Phys. Chem. C* 116(12):6884-92.
- [48] Kumar R, Nyk M, Ohulchanskyy TY, Flask CA, Prasad PN (2009) Combined optical and MR bioimaging using rare earth ion doped NaYF₄ nanocrystals. *Adv. Funct. Mater.* 19(6):853-9.
- [49] Haase M, Schäfer H (2011) Upconverting nanoparticles. *Angew. Chem. Int. Ed.* 50(26):5808-29.
- [50] Xu CT, Zhan Q, Liu H, Somesfalean G, Qian J, He S, Andersson-Engels S (2013) Upconverting nanoparticles for pre-clinical diffuse optical imaging, microscopy and sensing: Current trends and future challenges. *Laser Photon Rev.* 7(5):663-97.

- [51] Liu Q, Tian Y, Tang W, Huang F, Jing X, Zhang J, Xu S (2018) Broadening and enhancing 2.7 μm emission spectra in Er/Ho co-doped oxyfluoride germanosilicate glass ceramics by imparting multiple local structures to rare earth ions. *Photonics Research* 6(4):339-45.
- [52] Jin LM, Chen X, Siu CK, Wang F, Yu SF (2017) Enhancing multiphoton upconversion from NaYF₄:Yb/Tm@NaYF₄ core – shell nanoparticles via the use of laser cavity. *ACS Nano* 11(1):843–9.
- [53] Jackman JA, Rahim Ferhan A, Cho N (2017) Nanoplasmonic sensors for biointerfacial science. *Chem. Soc. Rev.* 46(12):3615-60.
- [54] Naccache R, Vetrone F, Mahalingam V, Cuccia LA, Capobianco JA (2009) Controlled synthesis and water dispersibility of hexagonal phase NaGdF₄:Ho³⁺Yb³⁺ nanoparticles. *Chem. Mater.* 21(4):717-23.
- [55] Li Y, Tang J, Pan D, Sun L, Chen C, Liu Y, Wang Y, Shi S, Yan C (2016) A versatile imaging and therapeutic platform based on dual-band luminescent lanthanide nanoparticles toward tumor metastasis inhibition. *ACS Nano* 10:2766-73.
- [56] Ovalle M, Arroyo E, Stoytcheva M, Zlatev R, Enriquez L, Olivas A (2015) An amperometric microbial biosensor for the determination of vitamin B12. *Anal. Methods* 7(19):8185-89.
- [57] Arendt JFB, Pedersen L, Nexø E, Sørensen HT (2013) Elevated plasma vitamin B12 levels as a marker for cancer: a population-based cohort study. *JNCI* 105:1799-805.
- [58] Matejcic M, Batlle J de, Ricci C, Biessy C, Perrier F, Huybrechts I, Weiderpass E, Boutron-Ruault MC, Cadeau C, His M, Cox DG, Boeing H, Fortner RT, Kaaks R, Lagiou P, Trichopoulou A, Benetou V, Tumino R, Panico S, Sieri S, Palli D, Ricceri F, Bueno-de-Mesquita HBA, Skeie G, Amiano P, Sánchez MJ, Chirlaque MD, Barricarte A, Quirós JR, Buckland G, van Gils CH, Peeters PH, Key TJ, Riboli E, Gylling B, Zeleniuch-Jacquotte A, Gunter MJ, Romieu I, Chajès V (2017) Biomarkers of folate and vitaminB12 and breast cancer risk: report from the EPIC cohort. *Int. J. Cancer* 140(6):1246-59.

4. NIR-mediated Spatiotemporal Control of Stem Cell Behavior Using Multifunctional Upconversion Nanoparticle

4.1 Abstract

Spatial and temporal modulation of stem cell behaviors are of great significance in the field of stem cell biology and regenerative medicine. Due to intrinsic spatial and temporal resolution, light has been vastly involved to achieve stem cell behavioral control. Current UV-Vis based approaches are highly limited, due to non-specific absorption, poor tissue penetration and photo-toxicity. On the contrary, upconversion nanoparticles (UCNPs) have gathered growing attention for vast applications due to minimal tissue absorption, high penetration depth, and minimal photo-toxicity from near-infrared (NIR) excitations. Moreover, 808 nm NIR mediated upconversion nanomaterials have shown greater potentials for biomedical applications comparing to 980 nm NIR based systems concerning fewer heating effects from water absorption and deeper tissue penetration. Herein, we developed an 808 nm NIR mediated stem cell differentiation modulation method based on controlled release of differentiation factors from multi-shell upconversion nanoparticles capable of 808 nm NIR to UV upconversion which further toggles photo-switching polymer coatings to achieve spatial temporal resolution. Moreover, with 808 nm NIR excitation, small molecule differentiation factors can be released to guide neural stem cell differentiation in a highly controlled manner. Given the challenges in spatial and temporal stem cell behavior modulation, our developed 808 nm NIR upconversion nanoparticle based neural stem cell differentiation control approach can represent a novel tool for studying single molecule roles in stem cell differentiation as well as developmental biology.

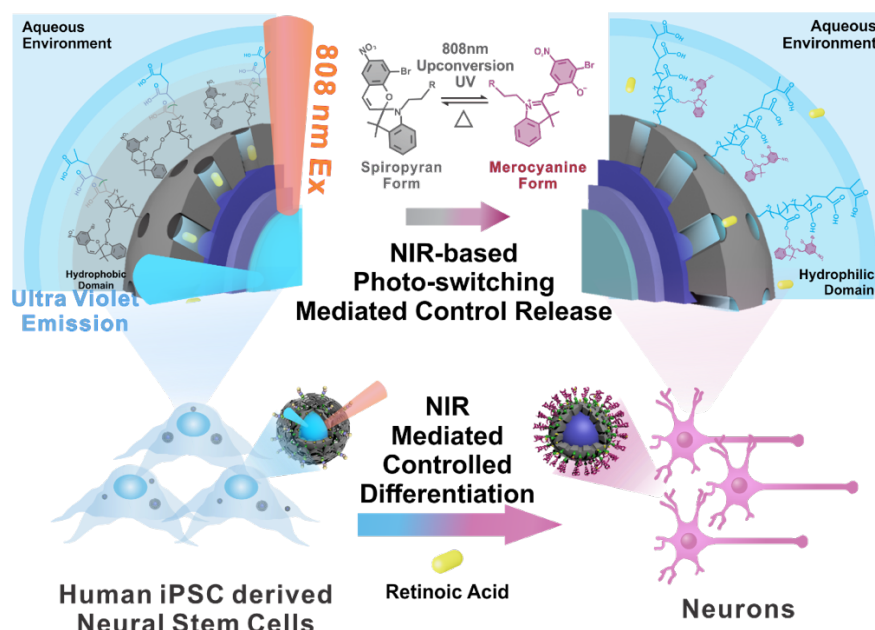


Figure 4.1 | Graphical abstract for NIR-mediated spatiotemporal control of stem cell behavior using multifunctional upconversion nanoparticles.

This chapter was submitted to Nature Nanotechnology at 04.07.2019.

Author contributions:

This work is a cooperation between Rutgers University, NJ and University of Regensburg. LMW and TH designed the particle architecture. LMW synthesized the $\text{NaYF}_4:\text{Yb},\text{Tm}@\text{NaYF}_4:\text{Yb},\text{Nd}@\text{NaYF}_4$ upconversion nanoparticles and studied different doping ratios of Yb^{3+} and Nd^{3+} to receive particles with efficient luminescence enabling deep tissue penetration without sample heating. YZ functionalized the particles with a silica shell and the drug loading system. During the whole process LMW and YZ discussed the results. The article was mostly written by YZ excluding the sections on synthesis and characterization of the 808 nm excitable particles, which was done by LMW. Regarding all other parts LMW supported YZ with input and corrections. The experiments and data shown in Figs 4.11 – 4.17 have been conducted and evaluated by the group at Rutgers University. The artwork in Figs. 4.1, 4.2 and 4.5 was performed by YZ. TH and KBL revised the manuscript. KBL is the corresponding author.

4.2 Introduction

Stem cell functions and fate are dynamically orchestrated by various biomolecular as well as physical signals in a spatially and temporally controlled manner [1-3]. Achieving precise control of stem cell fate and functions is of great significance for studying physiological mechanisms, identifying pathogenic pathways, and developing enhanced treatments of devastating diseases [4]. For instance, neurogenesis is a complicated biological process that incorporates several cellular behaviors such as proliferation, differentiation, migration, axon growth and synapse formation [5-6]. To better investigate and further regulate the complex process of neurogenesis, light, especially NIR, would be an ideal probe and stimulus for modulating the spatiotemporal dynamics of signals in living cells and organisms with high resolution [7,8]. In this regard, the optogenetic research field has provided several tools for light-controlled genome editing and gene transfection [9-14]. Other alternative approaches are based on photo-caged small molecules [15] and photo-switching molecules [16,17] for light-dependent biological regulations [18-20]. Photo-responsive nanomaterials have gained increasing research interests for achieving cell behavior control due to their exceptional photo-physical properties [21-23]. However, current applications of light-mediated biological manipulation are heavily dependent on the need for UV/Vis wavelengths light as the major excitation source, which is limited by its phototoxicity, its low tissue penetration depth due to phenomena including light scattering, and autofluorescence [24-27]. Regarding the intrinsic limitations of UV/Vis spectrophotometric applications, a promising alternative strategy is the use of low energy NIR light as an excitation source and its conversion into UV or Vis light, a process known as photon upconversion. A NIR-controlled drug delivery systems (DDSs) can be an ideal approach with significantly reduced cytotoxicity and better tissue penetration capability [28-30]. Lanthanide-doped upconversion nanoparticles (UCNPs) are renowned for their remarkable ability to sequentially absorb multiple long wavelength photons to generate single short wavelength photons in an anti-Stokes fashion [31]. However, current UCNP systems majorly utilize 980 nm excitation, which causes severe heating effect due to the local water absorption at this wavelength with an absorption coefficient of 0.48 cm^{-1} , thereby incurring thermal damages [32].

Recently, neodymium and ytterbium co-doped UCNPs have been demonstrated to have an 808 nm sensitization capability; subsequently, they have gained tremendous attention due to their minimized heating effect [33-36]. Moreover, comparing to conventional 980 nm excitation ($\sim 2.0 \text{ cm}$), 808 nm excitation demonstrates at least 50% deeper tissue penetration

depth (~3.4 cm) [37-39]. Nevertheless, one of the major restraints on utilizing 808 nm excitation for wide bio-applications falls on the detrimental cross-relaxation from activators to Nd^{3+} , leading to lower overall emission output as well as lower ultraviolet emission ratio [36]. The main strategy to mitigate this process is to utilize core – shell structure engineering to separate the Nd^{3+} from the activators [36,40-41]. Even though there is a clear need for various improvements on visible range emissions, which could be achieved with these 808 nm excitable core – shell architectures and their applications for neuroscience and stem cell biology, in the literature are only a small amount of systematic studies optimizing the UV upconversion emission yields for the development of such applications presented.

To address the challenges above, herein, we developed a unique stem cell differentiation control system (UCNP@mSi@polyspiropyran) using a core – shell – shell 808 nm NIR-excited upconversion nanoparticles (UCNPs) that can generate UV emissions to trigger photo-isomerization of polyspiropyran and achieve spatial and temporal control of small molecule factor release. Specifically, our unique 808 nm NIR-excited UCNPs were designed to be a multi-shell structure with compositional optimization for 808 nm NIR to UV upconversion (Fig. 4.1A). Subsequently, this UCNPs was coated with a mesoporous silica shell as a small molecule reservoir and further functionalized with a photo-responsive polymeric shell containing spiropyran groups (UCNP@mSi@polyspiropyran) (Fig. 4.1B). In conjunction with the UCNPs@mSi@polyspiropyran system, a small molecule named retinoic acid (RA), which is highly involved in various developmental processes including neurogenesis, was delivered to human induced pluripotent stem cell derived neural stem cells (hiPSC-NSCs) to promote neuronal differentiation in a controlled manner (Fig. 4.1C). The hiPSC-NSCs were selected for the stem cell neuronal differentiation, since the hiPSC-NSCs has been well established for their differentiation processes and translational potentials. While we used RA as a proof-of-concept drug for neuronal differentiation, other differentiation factors can potentially be incorporated into the UCNPs@mSi@polyspiropyran platform to regulate a broad range of stem cell lineage commitments as well. Thus, this 808 nm NIR-mediated differentiation control system can provide a variety of potential applications in stem cell therapy, neuroscience, and regenerative medicine.

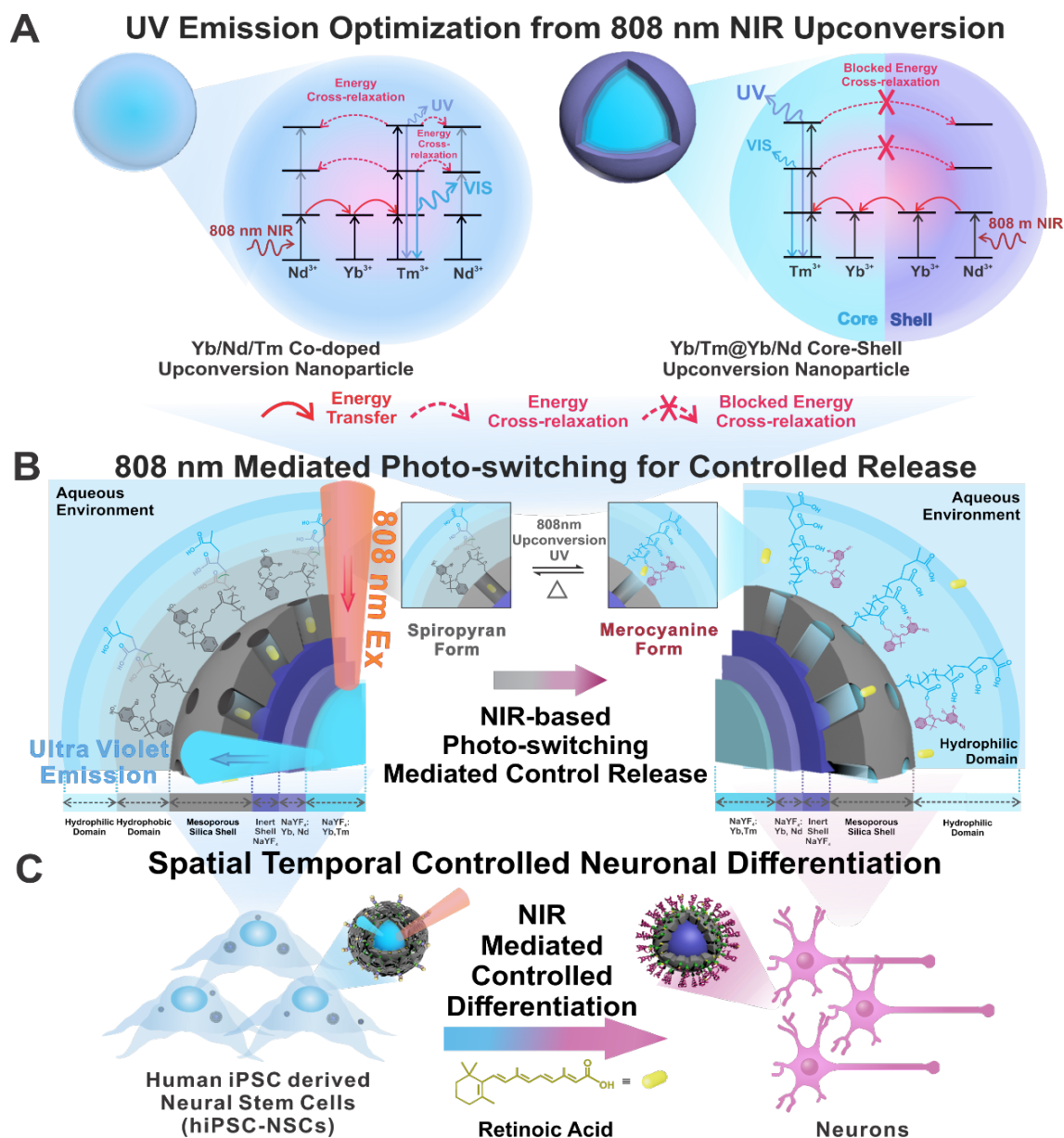


Figure 4.2 | Scheme of controlled stem cell differentiation using 808 nm upconversion nanoparticles: Schematic diagram for energy migration mechanism comparison among Yb,Nd,Tm doped UCNPs and NaYF₄:Yb,Tm@NaYF₄:Yb,Nd structured UCNPs. Left: Yb,Nd,Tm doped UCNPs, cross-relaxations (red arrows) from Tm³⁺ to Nd³⁺ exists throughout the nanoparticle. Right: the NaYF₄:Yb,Tm@NaYF₄:Yb,Nd@NaYF₄ UCNPs, cross-relaxation is blocked (red arrows with cross) due to spatial separation of the Tm³⁺ and Nd³⁺(A). Schematic diagram of the NIR mediated photoswitching on the constructed spiropyran polymer coated the NaYF₄:Yb,Tm@NaYF₄:Yb,Nd@NaYF₄ UCNPs@mesoporous silica for small molecule on-demand release. (B) Proof of concept demonstration for NIR-based neural stem cell differentiation using the aforementioned spiropyran polymer coated upconversion nanoparticle system (C).

4.2.1 Materials

Lanthanide chloride hexahydrates (>99.9%) were purchased from Sigma Aldrich and Treibacher Industrie AG. Oleic acid and 1-octadecene (both technical grade, 90%) were obtained from Alfa Aesar. Ammonium fluoride, 2,3,3-trimethyl-3H-indole, 1-iodopropane and 2-hydroxy-5-nitrobenzaldehyde, these chemicals were purchased from Sigma-Aldrich. All

chemicals were used as received, without any further purification. Solvents for NMR analysis (Cambridge Isotope Laboratories) were used as received.

4.2.2 Methods

Transmission electron microscopy (TEM) was implemented with a 120 kV Philips CM12 microscope. A Malvern Zetasizer was used for dynamic light scattering (DLS). X-ray powder diffraction (XRD) patterns with a resolution of 0.005° (2θ) were collected using a Huber Guinier G670 diffractometer (www.xhuber.com) with a Cu source ($K\alpha$ radiation, $\lambda=1.54060 \text{ \AA}$) operating at 40 kV and 30 mA. For the determination of the composition and concentration of the UCNPs a flame-EOP inductively coupled plasma optical emission spectrometer (ICP-OES) from Spectro (www.spectro.com) was used. Luminescence spectra of UCNPs were measured with an Aminco Bowman Series 2 luminescence spectrometer (Thermo Electron Corporation). The spectrometer was equipped with an external continuous wave 808 nm laser module (300 mW, $\sim 15 \text{ mW}\cdot\text{cm}^{-2}$), obtained from Picotronic. The luminescence lifetime was measured by a homemade lifetime measurement setup consisting of 808 nm laser cw laser module (300 mW, $\sim 15 \text{ mW}\cdot\text{cm}^{-2}$), optical chopper, temperature-controlled cuvette holder with integrated magnetic stirrer, collection lens filter wheel and mount for optical fiber. UV-vis absorption spectra were recorded on a Varian Cary 50 spectrophotometer. Fluorescence spectra were recorded on a Varian Cary Eclipse fluorescence spectrophotometer with external NIR lasers with a wavelength at 808 nm or 980 nm as excitation light source (CNI high power fiber coupled diode laser system, FC-W-980 and FC-W-808). The total output powers for the lasers are tunable from 1 mW to 10 W. The power density was detected by 1916-R handheld optical power meter with 818P thermophile detector (purchased from Newport corporation, USA) Unless otherwise stated, all spectra were obtained from hexane dispersion of nanoparticles (1 wt%). Fluorescence emission decays of UCNPs were collected on an Edinburgh FLS920 fluorescence spectrometer with an external continuous 980 nm NIR LED laser diode (1.5 W), which was coupled with a chopper to modulate the excitation into pulse mode. ^1H NMR and ^{13}C NMR was acquired on Varian 300 MHz NMR spectrometer.

4.2.2.1 Synthesis

Synthesis of core particles $\text{NaYF}_4\text{:X\%Yb,0.3\%Tm}$. The synthesis of Ln^{3+} -doped NaYF_4 nanocrystals was performed by a modified procedure based on a protocol reported by Wilhelm *et al.* [42]. For the synthesis of 1 mmol $\beta\text{-NaYF}_4\text{:Yb,Tm}$ particles the corresponding

molar ratios of the lanthanide chlorides were dissolved in methanol (5 mL). Under nitrogen flow, oleic acid (8 mL) and 1-octadecene (15 mL) was added into a 50 mL three necked round bottom flask. This solution was heated to 160 °C and vacuum was applied for 30 min unless a clear solution was obtained. The solution was cooled to room temperature and 4.00 mmol NH_4F and 2.5 mmol NaOH in 10 mL methanol were added and then the suspension was kept at 120 °C for 30 min before heating to reflux (ca. 320 °C). The heating-time was controlled by the appearance of upconversion luminescence in the synthesis flask *via* continuous excitation with a 980 nm cw laser module (200 mW). As soon as the upconversion luminescence can be identified by the bare eye, the solution is kept at reflux for additional 8 min. To obtain the fully transformation of the nanocrystals from the α - to the β -form and to receive monodisperse particles a heating time of 15 min turned out to be best.

The particles were precipitated by the addition of excess of ethanol and collected by centrifugation at 1,000 g for 5 min. The precipitate was washed with chloroform/ethanol (1:10 v/v) two times, and five times with cyclohexane/acetone (1:10 v/v) by repeated redispersion-precipitation-centrifugation cycles. In the end, for removing aggregates, the particles were dispersed in 10 mL cyclohexane, centrifuged at 1,000 g for 3 min and the supernatant was collected.

Synthesis of core – shell $\text{NaYF}_4\text{:Yb,Tm@NaYF}_4\text{:Yb,Nd}$ and core – shell – shell $\text{NaYF}_4\text{:Yb,Tm@NaYF}_4\text{:Yb,Nd@NaYF}_4$. Synthesis of shell-precursor material $\alpha\text{-NaYF}_4\text{:Yb,Nd}$ and $\alpha\text{-NaYF}_4$. The synthesis procedure is identical to the synthesis of hexagonal $\text{NaYF}_4\text{:Yb,Tm}$ particles except the composition of the lanthanide chlorides and the last heating step under reflux. Here, the solution is kept for 30 minutes at 240 °C for receiving the cubic crystal lattice. Moreover, the purification protocol is the same as described above. Under nitrogen flow the core material $\text{NaYF}_4\text{:25%Yb,0.3%Tm}$ such as the shell precursor $\text{NaYF}_4\text{:10%Yb,10%Nd}$ were filled in a 1:3 ratio into 50 mL three necked round bottom flasks. Per 1 mmol total content of NaYF_4 -particles, 5 mL oleic acid and 5 mL 1-octadecene were added. After this the $\beta\text{-NaYF}_4$ -particles and also the precursor material for the shell-formation were heated to 100 °C and vacuum was applied for 1 h unless a clear solution was obtained. After this the $\beta\text{-NaYF}_4$ -particles were heated to reflux and the shell precursor was kept under nitrogen flow at 100 °C. Every 10 minutes an addition of the shell precursor to the $\alpha\text{-NaYF}_4\text{:Yb,Nd}$ -particles was made to form the shell. When the precursor material was consumed, the solution was kept for another 10 min at reflux. Then the solution was cooled to room temperature. The same protocol was used for growing a second inert shell of NaYF_4

around the $\text{NaYF}_4\text{:Yb,Tm@NaYF}_4\text{:Yb,Nd}$ particles. The precipitation and purification of the core – shell nanoparticles was performed according to the protocol described for redispersion-precipitation cycles of $\text{NaYF}_4\text{:25%Yb,0.3%Tm}$.

4.2.2.2 Silica Shell Growing

The silica shell was coated *via* the surfactant-assistant sol–gel coating method. UCNPs (100 mg) were added to 20 mL of Triton X-100 solution and 80 mL deionized (DI) water was added before the solution was treated with sonication for 10 min. The solution was allowed to stir for 6 h and the nanoparticles were collected after centrifugation. The UCNPs were washed with water and then dispersed into a mixture of ethanol (160 mL), DI water (40 mL) and 2 mL of 28 wt% ammonia aqueous solution. The mixture was stirred for 30 min and then 0.06 g of TEOS was added. After 6 h, the product was collected by centrifugation.

4.2.2.3 hiPSC-NSC Culture and Differentiations

To culture hiPSC-NSC ($p = 3$), cell culture dish was first coated with laminin ($0.65 \mu\text{g}\cdot\text{cm}^{-2}$) dissolved in hank's balanced salt solution the incubator for 2 h. TrypLE (reagent which replaces trypsin) was used to detach hiPSC-NSCs from the cell culture dish. Approximately 45,000 cells were seeded in the 12-well cell culture dish containing the presterilized substrates bearing nanosized graphene oxide (NGO) patterns. After two days of cultivation to promote cell attachment and alignment, 0.5% fetal bovine serum (FBS) of human adipose stromal cells (ASC) medium was changed to osteogenic medium containing 100 nM dexamethasone, 50 μM ascorbic acid and 10 mM β -glycerol phosphate to start osteogenic differentiation of hiPSC-NSCs. The medium was changed every 5 days during the differentiation. In the case of neurogenesis, the hiPSC-NSCs were first induced toward an ectodermal (neural) lineage using a modified media formulation. Briefly, the hiPSC-NSCs were first grown to >90% confluence in 0.5% FBS ASC medium. Half of the cell culture media was the exchanged with neural induction media (NIM) (Dulbecco's modified eagle medium/nutrient mixture F-12 (DMEM-F12), 2% B27 (neuronal cell culture), 1% penicillin/streptomycin) supplemented with 20 $\text{ng}\cdot\text{mL}^{-1}$ epidermal growth factor (EGF), 20 $\text{ng}\cdot\text{mL}^{-1}$ basic fibroblast growth factor (bFGF) and 10 $\text{ng}\cdot\text{mL}^{-1}$ brain-derived neurotrophic factor (BDNF). The media was then completely exchanged with the growth factor supplemented NIM. After a total of 10 days, the neural-induced hiPSC-NSCs were detached using accutase and seeded on the laminin-coated ($10 \mu\text{g}\cdot\text{mL}^{-1}$) substrates. Cells were then cultured in NIM supplemented with bFGF and BDNF, and the media was exchanged every 4-5 days.

4.2.2.4 Immunocytochemistry and Fluorescence Imaging

For actin staining of hiPSC-NSC, cells were washed with Dulbecco's phosphate-buffered saline (DPBS) (pH 7.4) and fixed with 4% formaldehyde solution for 10 min at room temperature (RT), followed by three times of washing with DPBS. Cells were then treated with 0.1% Triton X-100 in Phosphate-buffered saline (PBS) for 5 min, washed with DPBS and stained with Alexa Fluor 546 phalloidin-containing solution for 20 min at RT. After washing cells with DPBS for two times, actin-stained cells were placed on the slide glass using ProLong Gold Antifade Mountant as mounting solution for fluorescence imaging. For immunofluorescence staining, cell fixation was same as actin staining described as above. After cell fixation, cells were treated with 0.3% Triton X-100 solution containing 10% normal goat serum for 1 h in cell culture hood. Solution containing primary antibody specifically binds to neuron-specific class III β -tubulin (TuJ1) was applied and kept for 1 h, followed by washing with DPBS. Secondary antibody (anti-mouse IgG) was further applied to tag primary antibody, kept for 1 h and washed with DPBS. Finally, Hoechst ($3\mu\text{g}\cdot\text{mL}^{-1}$) was used to stain nucleus for immunofluorescence imaging (Eclipse TiU, Nikon, Japan).

4.3 Results and Discussion

To utilize NIR as an excitation source for the spiropyran photo-switching reaction, an efficient NIR to ultraviolet-visible light converter is an essential prerequisite (Fig. 4.2B). We achieved this goal by designing and synthesizing core – shell – shell UCNPs possessing tandem-sensitization based on Nd^{3+} and Yb^{3+} ions [26,27]. Neodymium ions are known for a 10 times higher absorption cross-section of about 10^{-19} cm^2 compared to Yb^{3+} [42]. Specifically, this approach shifts the excitation wavelength from 980 nm to 808 nm which, thereby, it prevents sample heating (Fig. 4.3) as water shows a significant lower absorption at 808 nm compared to 980 nm-excitation conditions [42].

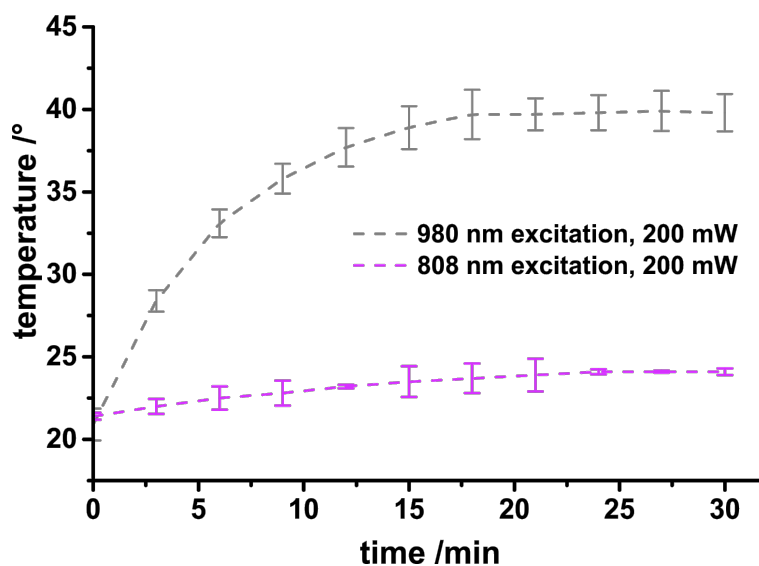


Figure 4.3 | Core – shell particles $\text{NaYF}_4:\text{Yb,Tm}@\text{NaYF}_4:\text{Yb,Nd}@PAA$ colloidal stable in aqueous solution and excited by a 980 nm (200 mW, cw) and 808 nm (200 mW, cw) laser module ($n = 3$). It needs to be mentioned that only 4% of the sample volume is excited by the low power laser of 200 mW. The 808 nm excitation shows only a slight increase in temperature while the 980 nm excitation shows an increase up to 40°C within 20 min illumination.

Furthermore, typically 808 nm excitation is known for a deeper tissue-penetration capability, which is favorable for the desired application [43]. In our experiment presented in Figure 4.4, we also demonstrated this phenomenon by a comparison 980 nm and 808 nm excitation in a 10 cm glass cuvette filled with aqueous solution containing $2 \text{ mg} \cdot \text{mL}^{-1}$ $\text{NaYF}_4:\text{Yb,Tm}@\text{NaYF}_4:\text{Nd,Yb}@\text{NaYF}_4$ UCNPs.

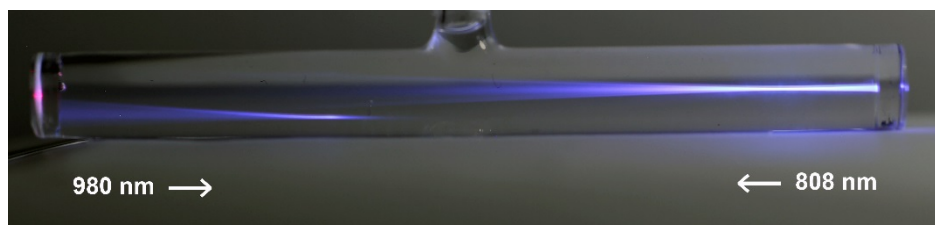


Figure 4.4 | A 10 cm long glass tube was filled by an aqueous dispersion ($2 \text{ mg} \cdot \text{mL}^{-1}$) of core – shell particles from the type $\text{NaYF}_4:\text{Yb,Tm}@\text{NaYF}_4:\text{Yb,Nd}@PAA$ and illuminated by 980 nm (from the left) and 808 nm (from the right) laser excitation (200 mW, cw) to demonstrate the deeper penetration by 808 nm excitation.

NaYF_4 was selected as host material due to its low lattice phonon energy of about 350 cm^{-1} [44]. The general design consist of a $\text{NaYF}_4:\text{Yb,Tm}$ core and two shells with different functions: the first shell ($\text{NaYF}_4:\text{Yb,Nd}$) as an 808 nm photon-absorbing shell and the second inert shell (NaYF_4), to protect Yb^{3+} ions against surface quenching (Fig. 4.5, top panel).

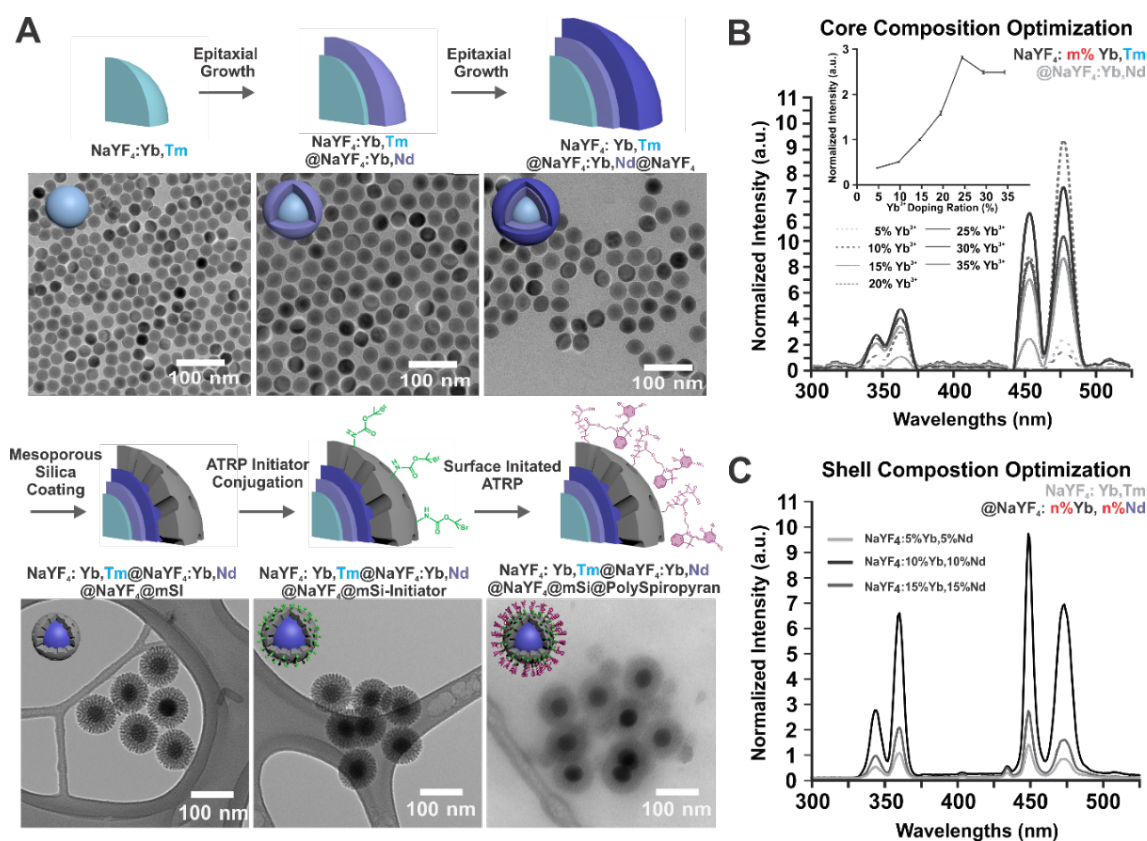


Figure 4.5 | Nanoparticle synthesis, surface functionalization and photophysical characterizations. Top: TEM characterization showing size and morphology evolution of the NaYF₄:Yb,Tm@NaYF₄:Yb,Nd@NaYF₄ core – shell – shell structured UCNPs. Bottom: TEM characterization showing the subsequent surface coating (mSi), functionalization (initiator), and surface initiated atomic transfer radical polymerization (poly(4-vinylpyridine)) (A). Upconversion luminescence comparison of different sensitizer Yb³⁺ in the core (0 – 35 mol%). Inset: quantitative comparison of UV emission (360 nm) peak intensity of different Yb³⁺ concentration (B). Upconversion luminescence comparison of different co-sensitizer concentration in the sensitizing shell (C).

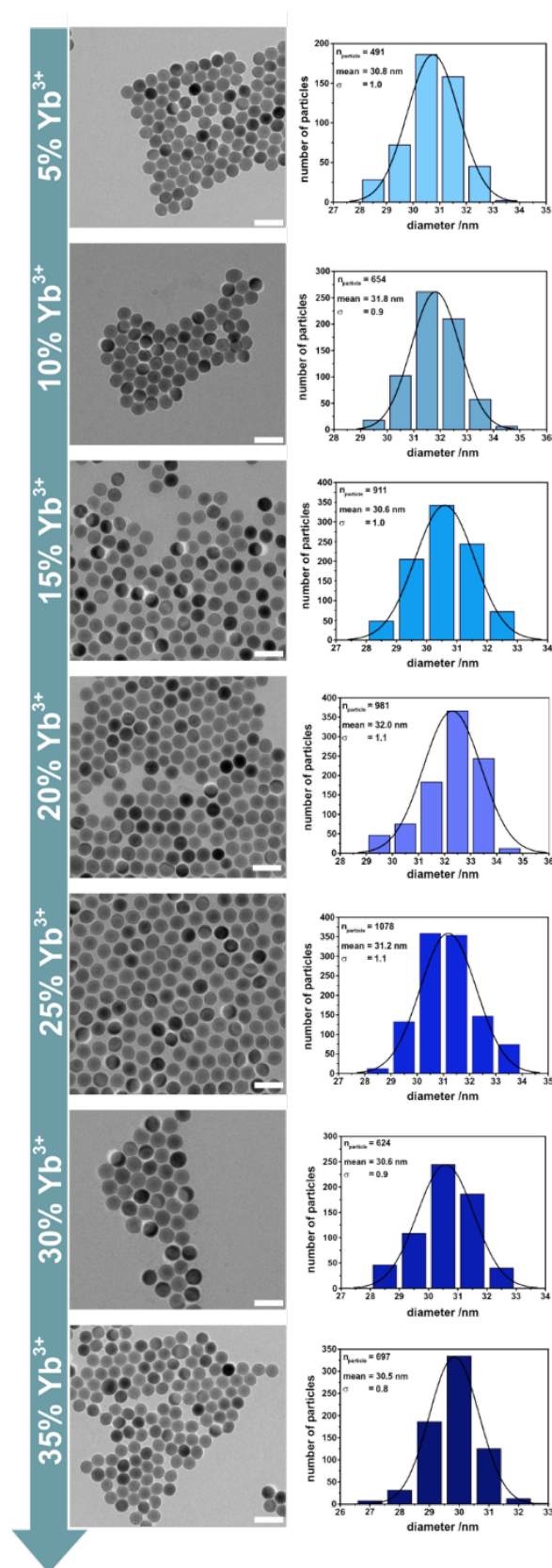


Figure 4.6 | TEM-images and particle size distribution of core shell particles with increasing Yb^{3+} content from 5% to 35% in the core ($\text{NaYF}_4:\text{X}\%, 0.03\%\text{Tm}@ \text{NaYF}_4:10\%\text{Yb}, 10\%\text{Nd}$).

Detailed luminescence studies regarding size and doping-ratio of the core and the shells were performed to achieve the best efficiency for 360 nm emissions, which triggers the drug release. Core – shell nanoparticles ($\text{NaYF}_4\text{:X\%Yb,0.3\%Tm@NaYF}_4\text{:10\%Nd,10\%Yb}$) of a core diameter of ~ 24 nm with variations in Yb^{3+} doping from 5-35% and a shell thickness of ~ 4 nm (estimated from TEM images, Fig. 4.6) were synthesized for the following experiments and applications.

Here the highest emission at 360 nm, verified by luminescence intensity (Fig. 4.5B) and lifetime measurements (Fig. 4.7), was obtained by a doping ratio of 25% for Yb^{3+} in the core.

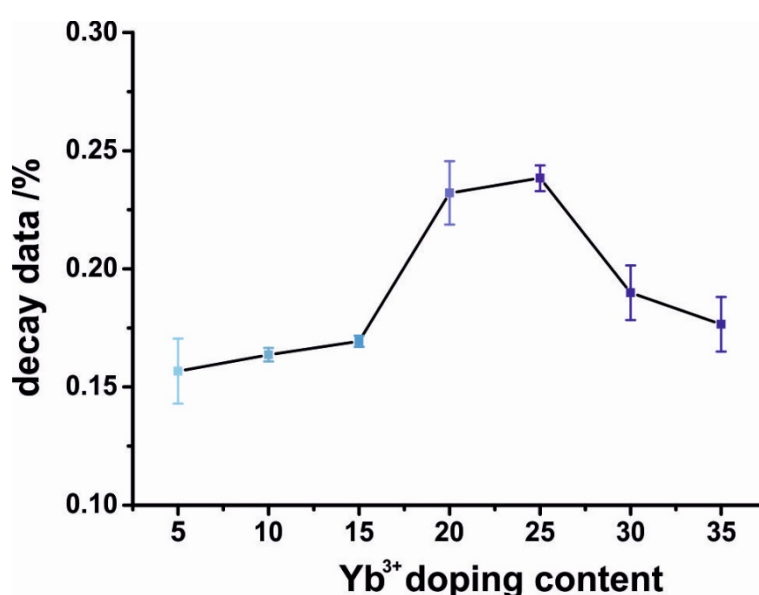


Figure 4.7 | Luminescence decay data of core – shell nanoparticles ($\text{NaYF}_4\text{:X\%Yb,0.03\%Tm@NaYF}_4\text{:10\%Yb,10\%Nd}$) dispersed in cyclohexane. All data ($n = 3$) were collected with an 808 nm (200 mW) laser module.

An additional study of variations in the doping ratio of Yb^{3+} (5 - 15%) and Nd^{3+} (5 - 15%) in the shell revealed that for both lanthanide ions a content of 10% showed the optimal upconversion efficiency (Figs. 4.5C and 4.8).

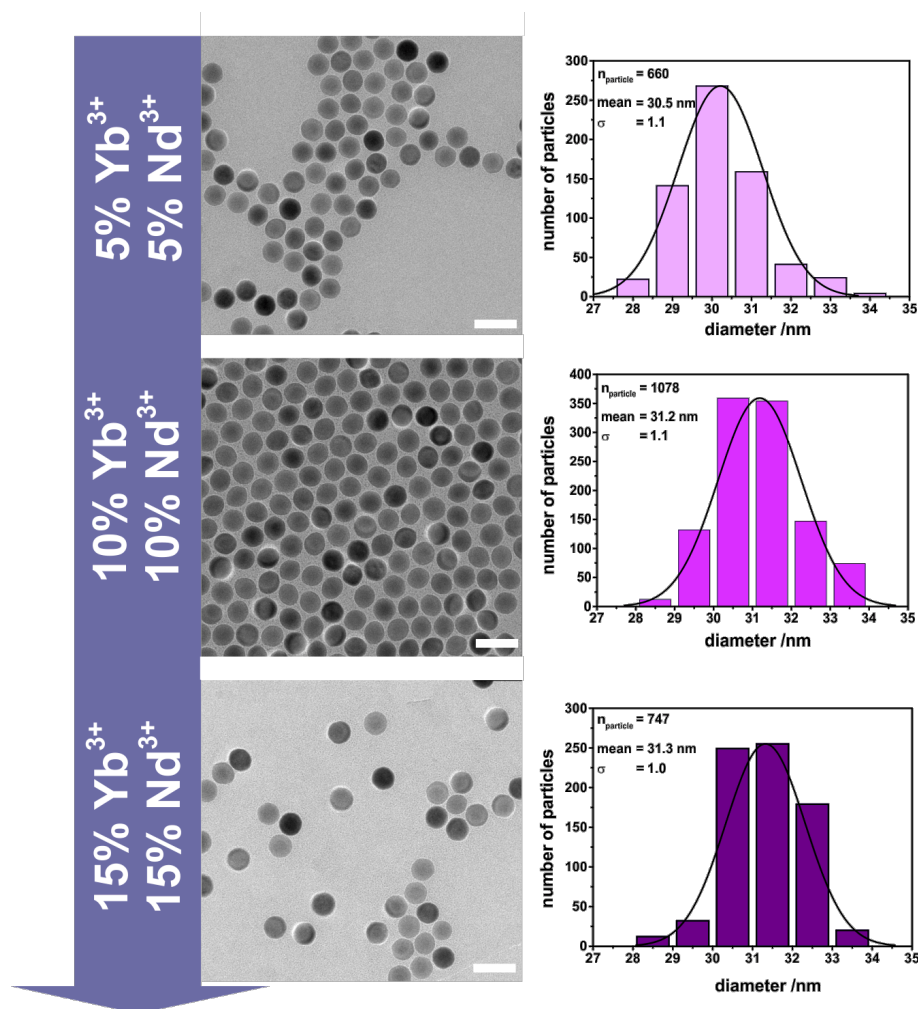


Figure 4.8 | TEM-images and particle-size distribution of core – shell particles with varied Nd³⁺ and Yb³⁺ content in the shell (NaYF₄:25%,0.03%Tm@NaYF₄:X%Yb,X%Nd).

A second additional inert shell of less than 2 nm thickness was grown on the optimized core – shell particles (NaYF₄:25%Yb,0.3%Tm@NaYF₄:10%Nd,10%Yb) to reduce quenching by surface defects and therefore additionally increasing the upconversion emission at 360 nm by 33% (Fig. 4.9).

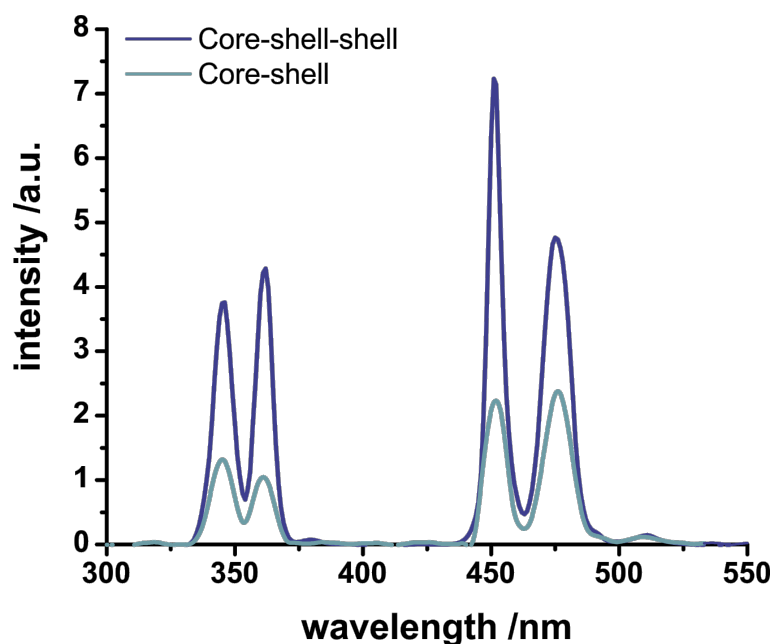


Figure 4.9 | Luminescence spectra of the core-shell particles ($\text{NaYF}_4:25\%,0.03\%\text{Tm}@ \text{NaYF}_4:10\%\text{Yb},10\%\text{Nd}$) and the core-shell-shell particles ($\text{NaYF}_4:25\%,0.03\%\text{Tm}@ \text{NaYF}_4:10\%\text{Yb},10\%\text{Nd}@ \text{NaYF}_4$) colloidal stable in aqueous solution and excited by an 808 nm laser module (200 mW, cw).

As a result, 808 nm excitable, monodisperse, pure hexagonal, core-shell-shell upconversion nanoparticles ($\text{NaYF}_4:24.5\%\text{Yb},0.27\%\text{Tm}@ \text{NaYF}_4:9.9\%\text{Nd},10.5\%\text{Yb}@ \text{NaYF}_4$) with a size of 36 ± 0.9 nm was obtained. The mono-dispersity was verified TEM image measurements (Figs. 4.10A and 3.10B) as well as DLS (Fig. 4.10C). In addition, the hexagonal crystal lattice was confirmed by XRD measurements (Fig. 4.10D). The final core-shell-shell UCNPs structural and compositional information was calculated (Table 4.1) and measured with an inductive coupled plasma optical emission spectrometry.

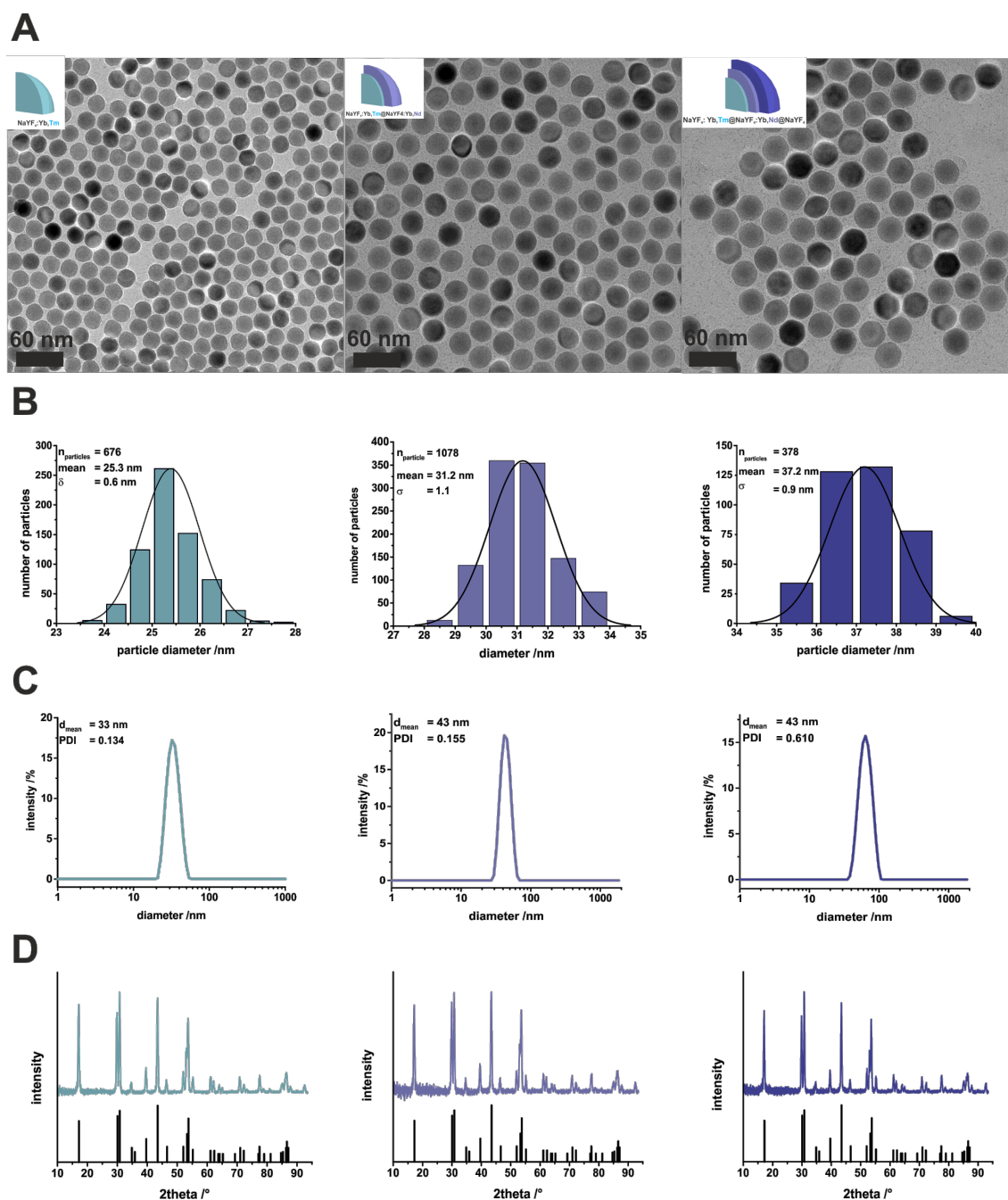


Figure 4.10 | Transmission electron micrographs (A), corresponding particle-size distributions (B), dynamic light scattering analysis (C) and XRD-patterns (D) of hexagonal-phase, oleate-capped NaYF₄:25%Yb,0.3%Tm, NaYF₄:25%Yb,0.3%Tm@NaYF₄:10%Yb,10%Nd and NaYF₄:25%Yb,0.3%Tm@NaYF₄:10%Yb,10%Nd@NaYF₄ nanocrystals (from left to right). The scale bars represent 60 nm. The standard reference pattern of hexagonal NaYF₄ is presented in black for all XRD-measurements β-NaYF₄ (ICDD PDF #16-334).

Table 4.1. Overview of the lanthanide contents in the core, core – shell and core – shell – shell particles determined by inductively coupled plasma optical emission spectroscopy ($n = 3$). The radius of the particles was determined by the size distribution calculated by the TEM images.

	theoretical composition	radius / nm	lanthanide content / %			
			Y ³⁺	Tm ³⁺	Yb ³⁺	Nd ³⁺
core	NaYF ₄ (25%Yb,0.3%Tm)	12.65 ± 0.3	75.0 ± 0.12	0.27 ± 0.01	24.5 ± 0.09	
active shell	NaYF ₄ (10%Yb,10%Nd)	4.15 ± 0.4	79.6 ± 0.22		10.5 ± 0.11	9.9 ± 0.07
inert shell	NaYF ₄	1.80 ± 0.5	101 ± 0.05			

As a result, the 808 nm sensitizing core – shell – shell particles show a higher efficiency for 360 nm emission, resulting in a peak ratio ($I_{360\text{ nm}}/I_{475\text{ nm}}$) of 0.53 compared to the classical 980 nm sensitizing particles (NaYF₄:25%Yb,0.3%Tm), having a peak ratio of 0.3, therefore making them attractive for a controlled drug release application.

To efficiently deliver RA as the neurogenic factor, a mesoporous silica (mSi) layer was further coated on the NaYF₄:Yb,Tm@NaYF₄:Nd,Yb@NaYF₄ particles, as demonstrated by a representative TEM image in Figure 4.3A (bottom panel). Furthermore, a photoresponsive polymer containing spiropyran-based moieties was synthesized through surface-initiated atomic transfer radical polymerization (ATRP). The ¹H-NMR spectroscopy results confirm the photoresponsive monomer. Spiropyran methacrylate (SPMA) was successfully prepared (Fig. 4.11).

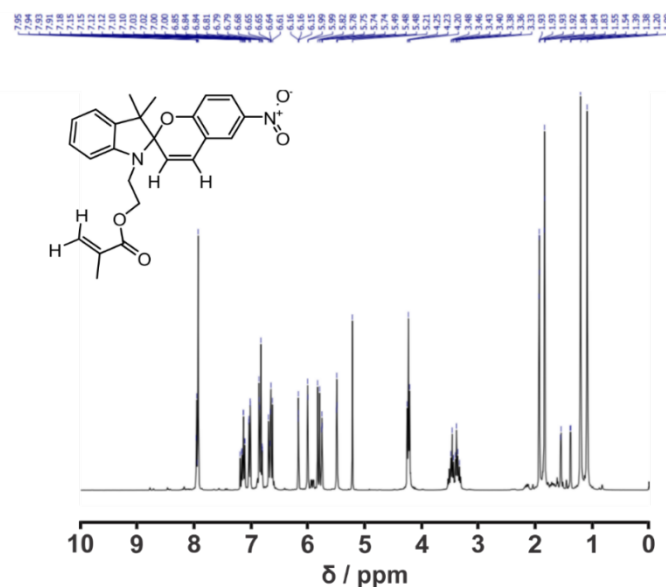


Figure 4.11 | ^1H -NMR spectrum (300 MHz) of spiropyran methacrylate (SPMA).

The UCNP@mSi-PSPMA particles were prepared by ATRP from an UCNP@mSi-Br initiator. The resulting UCNP@mSi-PSPMA particles were characterized by TEM. In Figure 4.3A, the characteristic TEM images of the mesoporous silica coating (left), ATRP initiator functionalization (middle), SPMA and acrylic acid (AA) functionalization (right) is shown. The multi-shell UCNPs show a diameter of 37 nm and the total size including mesoporous silica shell reach up to a particle diameter of 83 nm. With the functionalization of the 2-bromoisobutyryl bromide onto the amine coated mesoporous silica surface, a thin layer of initiator corona can be found (Fig. 4.3A, middle panel). The final polymer coating was grafted in a sequential manner. Firstly, a functional polymer of polyspiropyran methacrylate was grafted onto the initiator modified mesoporous silica surface. Due to the active initiator site on the polyspiropyran methacrylate, a colloidal stable polymer layer poly(acrylic acid) was further grafted onto the spiropyran polymer coated UCNPs. The final UCNP@mSi@poly-spiropyran nanoparticles presents a hydrodynamic size of 144 nm (PDI = 0.204).

To assess the efficiency of the nanoparticle's cellular uptake and its ability to deliver a neurogenic factor (RA) in spatiotemporally controlled manner, we performed a fluorescence imaging analysis on hiPSC-NSCs that were transfected with UCNP@mSi@polyspiropyran. To improve the cellular uptake efficiency of the UCNP@mSi@polyspiropyran, an arginylglycylaspartic acid (RGD) peptide was conjugated on to the nanoparticle surface, promoting the cellular uptake of UCNPs *via* RGD-mediated integrin binding to the cell membrane receptors which further facilitates receptor-mediated uptake processes (Fig. 4.12A). As shown in Figure 4.12B, upconversion luminescence and fluorescence

microscope images confirm that the different hiPSC-NSCs uptake behaviors after 24 h incubation with UCNP@mSi@polyspiropyran (control) and RGD-modified UCNP@mSi@polyspiropyran (experiment).

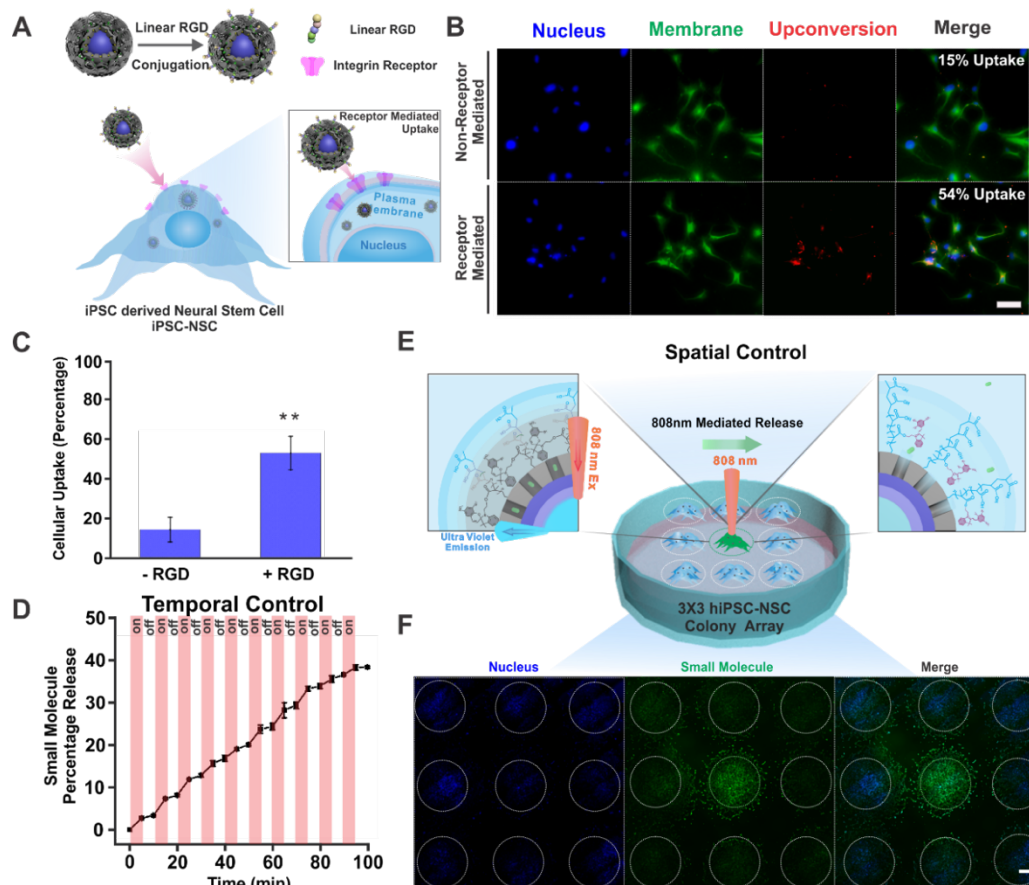


Figure 4.12 | Intracellular localization and temporal spatial control of UCNP@mSi@polyspiropyran: Schematic illustration of uptake process of the constructed spiropyran polymer coated upconversion nanoparticle (**A**). Fluorescence microscopy images of iPSC-NSCs stained with 3,3'-diiododipropylcarbocyanine perchlorate (DiI) (membrane: green) and NucBlue® (nucleus: blue) after 24 h incubation with RGD modified UCNP@mSi@polyspiropyran and UCNP@mSi@polyspiropyran (scale bar: 50 μ m) (**B**). Percentage of UCNP@mSi@polyspiropyran in iPSC-NSCs (**C**). 808 nm mediated temporal controlled release of fluorescein as model drug (**D**). Schematic diagram showing spatial and temporal control of small molecule release in neural stem cell colony culture (**E**). Fluorescence microscopy characterization of fluorescein spatial controlled release in induced pluripotent stem cell-derived neural stem cell colony culture (scale bar: 1000 μ m) (**F**).

The data from Figure 4.12C, on the other hand, shows quantification for the percentage of hiPSC-NSCs with UCL positive signal, therefore supporting our hypothesis that RGD-modified UCNP@mSi@polyspiropyran can have significantly more efficient cellular uptake in hiPSC-NSCs compared with non-RGD-modified constructs (UCNP@mSi@polyspiropyran). Meanwhile, the cell viability under 808 nm laser irradiation and UCNP@mSi@polyspiropyran transfection conditions were fully characterized for further formulation of NIR mediated neurogenesis. As shown in Figure 4.13A, a general decreasing trend in cellular viability corresponding to increasing 808 nm laser power densities was observed. For our experimental

conditions, a low power density of $1.05 \text{ W}\cdot\text{cm}^{-2}$ was chosen, due to the minimal toxicity at this setting. Minimal toxicity was also observed from the nanoparticle constructs up to a $100 \mu\text{g}\cdot\text{mL}^{-1}$ concentration (Fig. 4.13).

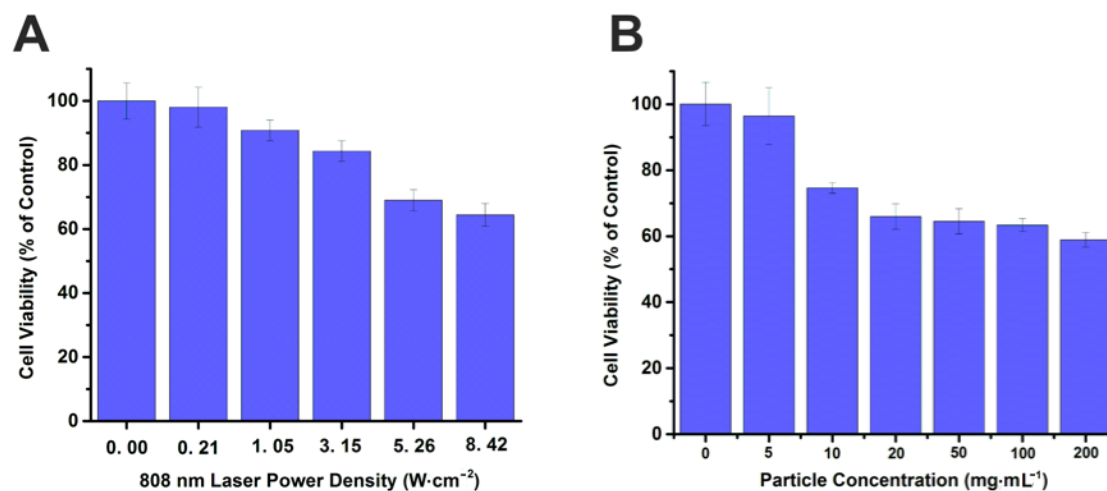


Figure 4.13 | 808 nm laser iPSC-NSC cell viability with different power densities (5 min exposure time) (A). UCNP@mSi@polyspiropyran nanoparticle cytotoxicity with different concentration (0 – 200 $\text{mg}\cdot\text{mL}^{-1}$) (Error bars represent mean \pm s.d.; n = 3) (B).

An 808 nm irradiation of the UCNP@mSi@polyspiropyran suspension in PBS (pH 7.4) showed the release of RA, as confirmed by UV absorption analysis on the collected supernatant buffer. Additionally, the temporal control of drug delivery with an innovative NIR-triggering on-off switchable drug release ability from UCNP@mSi@polyspiropyran was demonstrated (Fig. 4.12D). This result clearly demonstrates the spatial controlled release of the drug by the UCNP@mSi@polyspiropyran particles in response to the 808 nm NIR stimulation in a dose dependent manner. In addition, to demonstrate the spatial small molecule control capability, as shown in Figures 4.12E and 4.12F, a localized small molecule release in the center colony within a 3×3 array of hiPSC-NSCs colonies was observed from the fluorescence microscopy with 808 nm NIR irradiation. The details are presented in Figures 4.14 - 4.16.

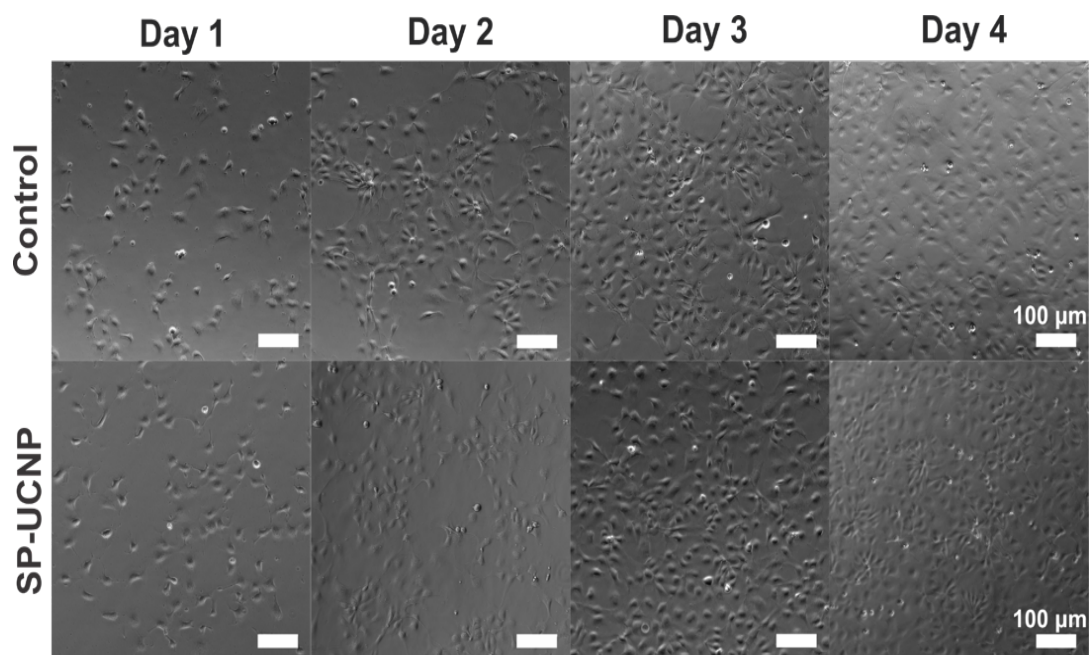


Figure 4.14 | Phase contrast microscope images of hiPSC-NSC proliferation under normal condition and SP-UCNP(UCNP@mSi@polyspiropyran) treatments. Minimal difference in hiPSC-NSC cell morphology and proliferation rate is observed during the culture period.

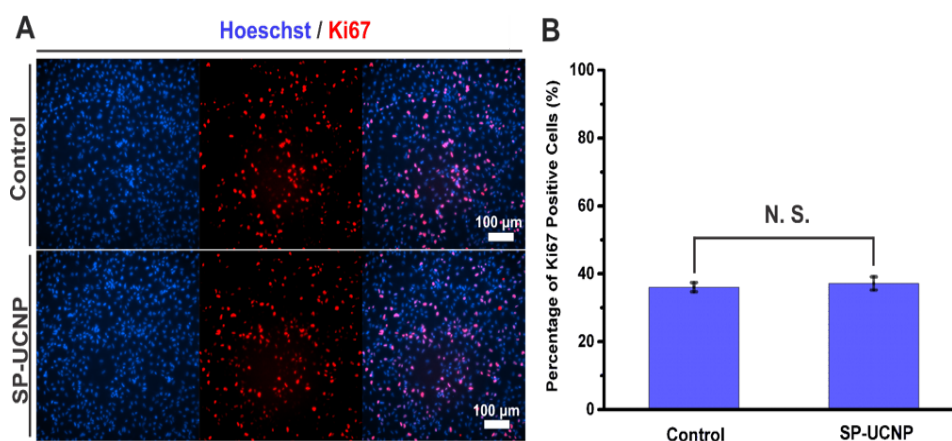


Figure 4.15 | Immunofluorescence microscope images of hiPSC-NSCs proliferation marker Ki67 under normal condition and SP-UCNP (UCNP@mSi@polyspiropyran) treatments (A). Quantitative analysis of percentage of Ki67 positive cells between the two groups. No significant difference was found showing minimal effect of the SP-UCNP on the proliferation of hiPSC-NSCs (B).

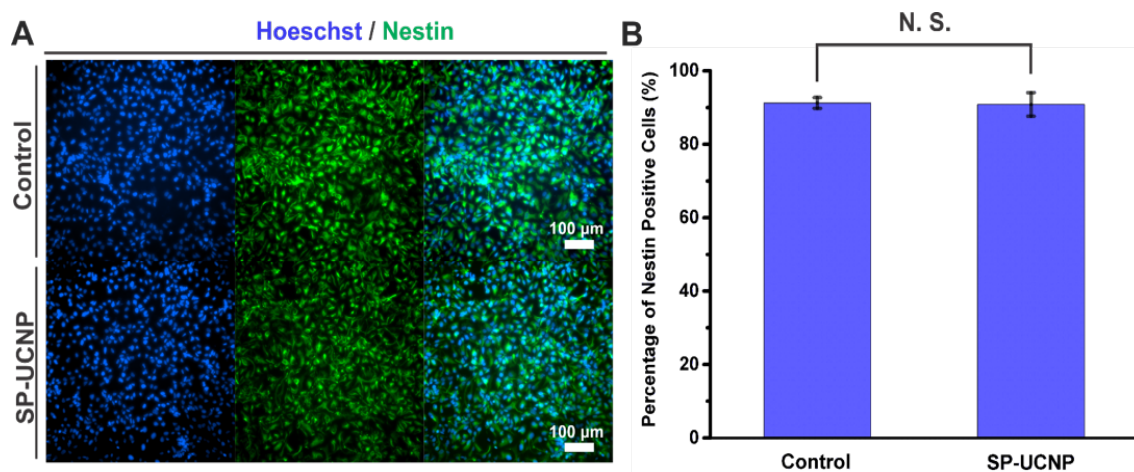


Figure 4.16 | Immunofluorescence microscope images of iPSC-NSCs marker Nestin (Neural Stem Cell marker) under normal condition and SP-UCNP (UCNP@mSi@polyspiropyran) treatments (A). Quantitative analysis of percentage of Ki67 positive cells between the two groups. No significant difference was found for the SP-UCNP and the control measurement on the multipotency of hiPSC-NSCs (B).

Recent advances in stem cell biology hold great potential in developing new approaches for the treatment of many devastating neuro-generative diseases and genetic disorders. Stem cell-based therapies for regenerating functional neurons and restoring neuronal functions to damage central nervous system areas can be much beneficial for realizing stem cell therapy for neurodegenerative diseases. Such approaches, however, require the generation of engraftable cell sources of functional neural cells and better control of stem cell neuronal differentiation in a spatiotemporally controlled and safe manner. Upon construction of the small molecule delivery system, we evaluated the ability of RGD-modified UCNP@mSi@polyspiropyran for the release of RA under 808 nm excitation to induce neuronal differentiation of hiPSC-NSCs in vitro. As can be seen in Figure 4.17A, hiPSC-NSCs were treated with RGD-modified UCNP@mSi@polyspiropyran containing RA molecules and exposed to 808 nm light ($1 \text{ W} \cdot \text{cm}^{-2}$) for 15 min (5-minute exposure intervals) prior to further culturing and stem cell as saying. After 5 days of culturing, an immunofluorescence assay (Fig. 4.17B) and a real-time polymerase chain reaction (qPCR) (Fig. 4.17D) were conducted to evaluate the hiPSC-NSCs neuronal differentiation. Specifically, as shown in Figure 4.17B, the negative controls (“control”: no NP treatment; “dark control”: NP treatment without 808 nm exposure) present a significant lower expression of early neuronal markers such as neuron-specific class III β -tubulin (TuJ1) compared to the experimental group (NP treatment with 808 nm exposure). As depicted in Figure 4.17C, cells treated with nanoparticles and 808 nm laser exposure displayed a dramatic morphological change compared to the control group and the dark control group, demonstrating a typical neurite outgrowth morphology indicating neuronal lineage commitment. Such morphological change was measured by quantifying neurite length

according to the TuJ1 immunofluorescence staining, with the experimental group showing significantly more and longer neurite outgrowths compared to the other two control groups (Fig. 4.17C). Furthermore, the experimental group showed an elevated TuJ1 mRNA expression level, confirmed through qPCR (Fig. 4.17D).

To further evaluate the maturity and functionality of the differentiated neurons, the experimental group was further differentiated to 14 days for mature neuronal marker and neuronal activity characterizations. As shown in Figures 4.17E and 4.17F, the immunostaining results showed that the UCNP@mSi@polyspiropyran based RA delivery system were a robust and effective method for the induction of neural differentiation in hiPSC-NSCs, displaying highly elevated neuronal mature markers, microtubule-associated protein 2 (MAP2) and synapsin. In order to further characterize the differentiated neurons' functionality, we performed calcium imaging to test the differentiated neurons response to cellular potential differences. Functionally active neurons spontaneously fire action potentials that allow for the influx in the concentration of cations including calcium. Using a commercially available calcium indicator dye, Fluo-4, changes in intracellular calcium concentrations were visualized (Fig. 4.17G). Furthermore, the fluorescence changes were quantified and observed for spontaneous fluctuations of calcium ions in the active neuron over a 250 second period while the control inactive neuron did not show any changes in fluorescence intensity (Fig. 4.17H).

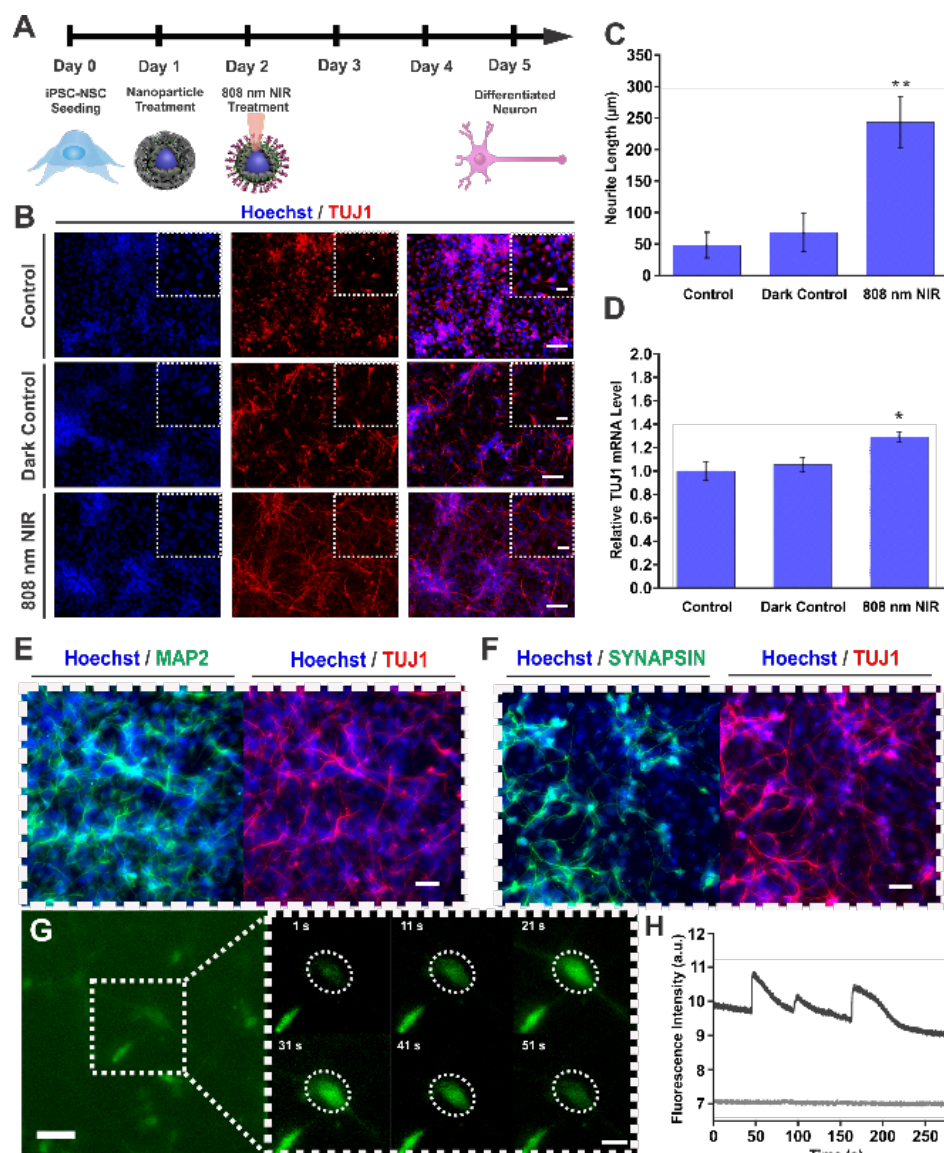


Figure 4.17 | NIR-mediated control of neural stem cell neurogenesis and maturation. **(A)** Schematic diagram of the *in vitro* differentiation control of hiPSC-NSCs. **(B)** Immunofluorescence microscope images of hiPSC-NSCs staining against key neuronal marker (TuJ1) red fluorescence; λ_{Ex} = 594 nm, λ_{Em} = 615 nm) after treatment with UCNP@mSi@polyspiropyran (scale bar = 100 μ m). **(C)** Quantification comparison of the morphological change (neurite growth) during the NIR mediated iPSC-NSCs differentiation process. **(D)** Gene expression analysis using qPCR in hiPSC-NSCs reveals that the NIR mediated iPSC-NSC differentiation correlates with an up-regulation of TuJ1. (Percent fold up-regulation of TuJ1 was calculated by normalizing to the housekeep gene, GAPDH, from the control) (Error bars represent mean \pm s.d.; n = 3, * p < 0.05, by one-way ANOVA with Tukey post-hoc test). **(E)** Immunofluorescence microscope characterization of the differentiated neurons staining against key late neuronal marker MAP2 (green fluorescence) along with TuJ1 staining after treatment with UCNP@mSi@polyspiropyran (scale bar = 50 μ m). **(F)** Immunofluorescence microscope characterization of the differentiated neurons staining against key late neuronal marker synapsin (green fluorescence) along with TuJ1 staining after treatment with UCNP@mSi@polyspiropyran (scale bar = 50 μ m). **(G)** Fluorescence microscope image of NIR mediated differentiated neurons stained with a commercially available calcium indicator dye, Fluo-4 (scale bar = 25 μ m). Inset: Spontaneous calcium fluctuations determined by Fluo-4 fluorescence (green) for an active neuron (white circle) (scale bar = 20 μ m). Traces for the fluorescence change representing spontaneous calcium ion influx for an active neuron (dark grey line) and an inactive neuron (light grey line) (H).

4.4 Conclusion

In summary, we have demonstrated an application of 808 nm NIR-mediated spatiotemporal control of stem cell fate using UCNPs having the capability of targeted and on-off switchable drug release responding to external stimuli. Our NIR-triggering DDSs could be used for the development of novel *ex vivo* and *in vivo* control of stem cell behaviors such as differentiation, proliferation, and migration. These novel methods complement recent advances in the principle, design, and synthesis of photonic nanomaterials with various bio applications. While the ability to delivery nanoparticle constructs to the targeted cells as well as release soluble cues under internal/externa stimuli in a spatiotemporally controlled manner is critical for the advanced nanoparticle-based drug delivery. This method could also provide a unique extension of nanotechnology to stem cell biology and neuro-regenerative medicine. In addition, the application of NIR-medicated drug delivery to modulate the key signaling pathways is important not only for selective stem cell fate control but also for dissecting signaling cascades affected by other stem cell microenvironments such as cell-cell interactions and biophysical/mechanical cues. Collectively, our strategy for NIR-mediated spatiotemporal control of stem cell differentiation using multifunctional UCNPs has significant potential for stem cell biology, *in vivo* drug delivery, and therapy.

Acknowledgement

KBL acknowledges partial financial support from the NIH R21 (1R21NS085569 and R21AR071101), NIH R01 (1R01DC016612-01 and 3R01DC016612-01S1), New Jersey Commission on Spinal Cord Research [CSCR17IRG010 and CSCR16ERG019], NSF [CHE-1429062 and CBET-1803517], and ACS New Directions Award (PRF# 55869-ND10). TH and LMW acknowledge Sandy Himmelstoß for the TEM studies.

4.5 References

- [1] Sasai Y (2013) Cytosystems dynamics in self-organization of tissue architecture. *Nature* 493(7432):318-26.
- [2] McGuigan AP, Javaherian S (2016) Tissue patterning: Translating design principles from *in vivo* to *in vitro*. *Annu. Rev. of Biomed. Eng.* 18:1-24.
- [3] Kinney MA, McDevitt TC (2013) Emerging strategies for spatiotemporal control of stem cell fate and morphogenesis. *Trends in Biotechnol.* 31(2):78-84.
- [4] Gitler AD, Dhillon P, Shorter J (2017) Neurodegenerative disease: Models, mechanisms, and a new hope. *The Company of Biologists* 10:499-502.

- [5] Yu S, Levi L, Siegel R, Noy N (2012) Retinoic acid induces neurogenesis by activating both retinoic acid receptors (RARs) and peroxisome proliferator-activated receptor β/δ (PPAR β/δ). *J. Biol. Chem.* 287(50):42195-205.
- [6] Ming GL, Song H (2011) Adult neurogenesis in the mammalian brain: Significant answers and significant questions. *Neuron* 70(4):687-702.
- [7] Guillemot F (2007) Spatial and temporal specification of neural fates by transcription factor codes. *The Company of Biologists* 134(21):3771-80.
- [8] Kohwi M, Doe CQ (2013) Temporal fate specification and neural progenitor competence during development. *Nature Rev. Neurosci.* 14(12):823-38.
- [9] Zhou W, Deiters A (2016) Conditional control of CRISPR/Cas9 function. *Angew. Chem. Int. Ed.* 55(18):5394-9.
- [10] Polstein LR, Gersbach CA (2012) Light-inducible spatiotemporal control of gene activation by customizable zinc finger transcription factors. *J. Am. Chem. Soc.* 134(40):16480-3.
- [11] Hemphill J, Borchardt EK, Brown K, Asokan A, Deiters A (2015) Optical control of CRISPR/Cas9 gene editing. *J. Am. Chem. Soc.* 137(17):5642-5.
- [12] Polstein LR, Gersbach CA (2015) A light-inducible CRISPR-Cas9 system for control of endogenous gene activation. *Nat. Chem. Biol.* 11(3):198-201.
- [13] Nihongaki Y, Kawano F, Nakajima T, Sato M (2015) Photoactivatable CRISPR-Cas9 for optogenetic genome editing. *Nat. Biotechnol.* 33(7):755-63.
- [14] Gomez EJ, Gerhardt K, Judd J, Tabor JJ, Suh J (2015) Light-activated nuclear translocation of adeno-associated virus nanoparticles using phytochrome B for enhanced, tunable, and spatially programmable gene delivery. *ACS Nano.* 10(1):225-37.
- [15] Chen X, Wu YW (2018) Tunable and photoswitchable chemically induced dimerization for chemo-optogenetic control of protein and organelle positioning. *Angew. Chem. Int. Ed.* 57(23):6796-9.
- [16] Zhou XX, Fan LZ, Li P, Shen K, Lin MZ (2017) Optical control of cell signalling by single-chain photoswitchable kinases. *Science* 355(6327):836-42.
- [17] Kienzler MA, Isacoff EY (2017) Precise modulation of neuronal activity with synthetic photoswitchable ligands. *Curr. Opin. Neurobiol.* 45:202-9.
- [18] Ruskowitz ER, DeForest CA (2018) Photoresponsive biomaterials for targeted drug delivery and 4D cell culture. *Nat. Rev. Mater.* 3(2):17087-104.
- [19] Ankenbruck N, Courtney T, Naro Y, Deiters A (2018) Optochemical control of biological processes in cells and animals. *Angew. Chem. Int. Ed.* 57(11):2768-98.
- [20] Li M, Zhao J, Chu H, Mi Y, Zhou Z, Di Z, Zhao M, Li L (2018) Light-activated nanoprobe for biosensing and imaging. *Adv. Mater.* 47(45):1804745-51.
- [21] Ferreira L, Karp JM, Nobre L, Langer R (2008) New opportunities: The use of nanotechnologies to manipulate and track stem cells. *Cell stem cell* 3(2):136-46.
- [22] Carradori D, Eyer J, Saulnier P, Pr  at V, des Rieux A (2017) The therapeutic contribution of nanomedicine to treat neurodegenerative diseases via neural stem cell differentiation. *Biomater.* 123:77-91.
- [23] Li J, Leung CW, Wong DS, Xu J, Li R, Zhao Y, Yung CY, Zhao E, Tang BZ, Bian L (2017) Photocontrolled SiRNA delivery and biomarker-triggered luminogens of aggregation-induced emission by up-conversion NaYF₄: Yb³⁺ Tm³⁺@ SiO₂ nanoparticles for inducing and monitoring stem-cell differentiation. *ACS Appl. Mater. Interfaces*, published ASAP, doi:10.1021/acsami.7b00845

- [24] Bryant SJ, Nuttelman CR, Anseth KS (2000) Cytocompatibility of UV and visible light photoinitiating systems on cultured NIH/3T3 fibroblasts in vitro. *J Biomater Sci Polym Ed.* 11(5):439-57.
- [25] Lai J, Yu A, Yang L, Zhang Y, Shah BP, Lee KB (2016) Development of photoactivated fluorescent N-Hydroxyoxindoles and their application for cell-selective imaging. *Chem. Eur. J.* 22(18):6361-7.
- [26] Liu D, Xu X, Wang F, Zhou J, Mi C, Zhang L, Lu Y, Ma C, Goldys E, Lin J, Jin D (2016) Emission stability and reversibility of upconversion nanocrystals. *J. Mater. Chem. C* 4(39):9227-34.
- [27] Han S, Deng R, Xie X, Liu X (2014) Enhancing luminescence in lanthanide-doped upconversion nanoparticles. *Angew. Chem. Int. Ed.* 53(44):11702-15.
- [28] Lai J; Shah BP, Zhang Y, Yang L, Lee K.-B (2019) Real-time monitoring of ATP-responsive drug release using mesoporous-silica-coated multicolor upconversion Nanoparticles. *ACS Nano* 9(5):5234-45.
- [29] Carling CJ, Boyer JC, Branda NR (2009) Remote-control photoswitching using NIR light. *J. Am. Chem. Soc.* 131(31):10838-9.
- [30] Wen S, Zhou J, Zheng K, Bednarkiewicz A, Liu X, Jin D (2018) Advances in highly doped upconversion nanoparticles. *Nat. Commun.* 9(1):2415-27.
- [31] Zhou B, Shi B, Jin D, Liu X (2015) Controlling upconversion nanocrystals for emerging applications. *Nat. Nanotechnol.* 10(11): 924-36.
- [32] Wang D, Xue B, Kong X, Tu L, Liu X, Zhang Y, Chang Y, Luo Y, Zhao H, Zhang H (2015) 808 nm driven Nd³⁺-sensitized upconversion nanostructures for photodynamic therapy and simultaneous fluorescence imaging. *Nanoscale* 7(1):190-7.
- [33] Vetrone F, Naccache R, Mahalingam V, Morgan CG, Capobianco JA (2009) The active-core/active-shell approach: A strategy to enhance the upconversion luminescence in lanthanide-doped nanoparticles. *Adv. Funct. Mater.* 19(18):2924-9.
- [34] Tuchinda C, Lim HW, Strickland FM, Guzmán EA, Wong HK (2007) Comparison of broadband UVB, narrowband UVB, broadband UVA and UVA1 on activation of apoptotic pathways in human peripheral blood mononuclear cells. *Photodermatol. Photoimmunol. Photomed.* 23(1):2-9.
- [35] Place ES, Evans ND, Stevens MM (2009) Complexity in biomaterials for tissue engineering. *Nat. Mater.* 8(6):457-70.
- [36] Bei L, Chunxia L, Piaoping Y, Zhiyao H, Jun L (2017) 808-nm-light-excited lanthanide-doped nanoparticles: Rational design, luminescence control and theranostic applications. *Adv. Mater.* 29(18):1605434.
- [37] Fan W, Huang P, Chen X (2016) Overcoming the Achilles' heel of photodynamic therapy. *Chem. Soc. Rev.* 45(23):6488-519.
- [38] Hudson DE, Hudson DO, Wininger JM, Richardson BD, (2013) Penetration of laser light at 808 and 980 nm in bovine tissue samples. *Photomedicine and laser surgery* 31(4):163-8.
- [39] Li T, Xue C, Wang P, Li Y, Wu L (2017) Photon penetration depth in human brain for light stimulation and treatment: A realistic Monte Carlo simulation study. *J. Innov. Opt. Health Sci.* 10(5):1743002-12.
- [40] Shen J, Chen G, Vu AM, Fan W, Bilsel OS, Chang CC, Han G (2013) Engineering the upconversion nanoparticle excitation wavelength: Cascade sensitization of tri-doped upconversion colloidal nanoparticles at 800 nm. *Adv. Opt. Mater.* 1(9):644-50.
- [41] Wang YF, Liu GY, Sun LD, Xiao JW, Zhou JC, Yan CH (2013) Nd³⁺-sensitized upconversion nanophosphors: Efficient in vivo bioimaging probes with minimized heating effect. *ACS Nano* 7(8):7200-6.

- [42] Wilhelm S, Kaiser M, Würth C, Heiland J, Carrillo-Carrion C, Muhr V, Wolfbeis OS, Parak WJ, Resch-Genger U, Hirsch T (2015) Water dispersible upconverting nanoparticles: effects of surface modification on their luminescence and colloidal stability. *Nanoscale* 7(4):1403-10.
- [43] Wiesholler LM, Hirsch T (2018) Strategies for the design of bright upconversion nanoparticles for bioanalytical applications. *Opt. Mater.* 80:253-64.
- [44] Wang F, Deng R, Wang J, Wang Q, Han Y, Zhu H, Chen X, Liu X (2011) Tuning upconversion through energy migration in core-shell nanoparticles. *Nat. Mater.* 10(12):968-73.

5. Yb,Nd,Er-Doped Upconversion Nanoparticles: 980 nm versus 808 nm Excitation

5.1 Abstract

Yb,Nd,Er-doped upconversion nanoparticles (UCNPs) have attracted considerable interest as luminescent reporters for bioimaging, sensing, energy conversion/shaping, and anticounterfeiting due to their capability to convert multiple near-infrared (NIR) photons into shorter wavelength ultraviolet, visible or NIR luminescence by successive absorption of two or more NIR photons. This enables optical measurements in complex media with very little background and high penetration depths for bioimaging. The use of Nd^{3+} as substitute for the commonly employed sensitizer Yb^{3+} or in combination with Yb^{3+} shifts the excitation wavelength from about 980 nm, where the absorption of water can weaken upconversion luminescence, to about 800 nm, and laser-induced local overheating effects in cells, tissue, and live animal studies can be minimized. To systematically investigate the potential of Nd^{3+} doping, we assessed the performance of a set of similarly sized ($\text{Yb}^{3+},\text{Nd}^{3+},\text{Er}^{3+}$)-doped core and core – shell UCNPs of different particle architecture in water at broadly varied excitation power densities (P) with steady state and time-resolved fluorometry for excitation at 980 nm and 808 nm. As a measure for UCNPs performance, the P -dependent upconversion quantum yield (Φ_{UC}) and its saturation behavior were used as well as particle brightness (B_{UC}). Based upon spectroscopic measurements at both excitation wavelengths in water and in a lipid phantom and B_{UC} -based calculations of signal size at different penetration depths, conditions under which excitation at 808 nm is advantageous are derived and parameters for the further optimization of triple-doped UCNPs are given.

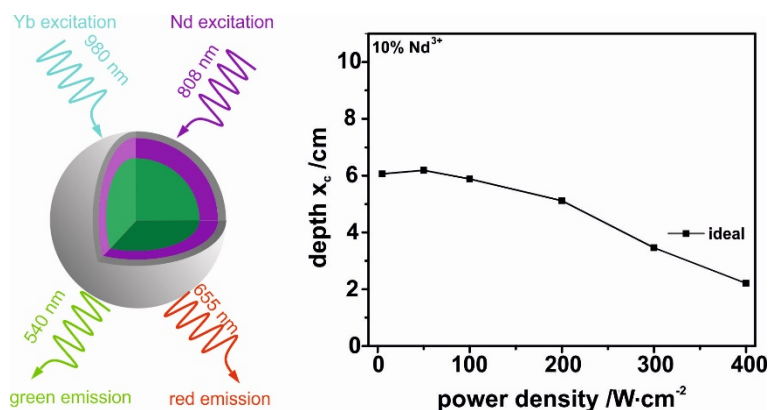


Figure 5.1 | Graphical abstract for (Yb³⁺,Nd³⁺,Er³⁺)-doped upconversion nanoparticles: 980 nm versus 808 nm excitation.

This chapter has been published. Lisa Marie Wiesholler, Florian Frenzel, Bettina Grauel, Christian Würth, Ute Resch-Genger, Thomas Hirsch. *Nanoscale*, 2019, doi:10.1039/C9NR03127H.

Author contributions: This chapter is submitted for peer reviewing, and LMW and FF contributed equally to this publication. LMW designed, synthesized the NaYF₄:Yb,Er,Nd particle systems and performed the surface modification. The characterization including luminescence spectra of all systems were performed by LMW. The absorption cross-section of the sensitizers within the particle were measured by LMW. The experimental set-up was designed and realized together with TH. The quantum yield measurements and brightness calculation were carried out by FF with input by CG while the decay data were measured together with BG during a research visit of LMW at Federal Institute for Materials Research and Testing (BAM). During the whole process, LMW and TH discussed consequently results with the group of the BAM and planned further steps. All experiments with phantom tissue were carried out LMW. LMW wrote the manuscript excluding the photophysical part. TH and URG revised the manuscript and are both corresponding authors.

5.2 Introduction

Lanthanide (Ln^{3+})-doped upconversion (UC) nanoparticles (UCNPs) with their high (photo)chemical stability and low biological toxicity have attracted considerable interest as luminescent reporters for bioimaging, sensing, energy conversion/shaping, and anticounterfeiting due to their capability to convert multiple near-infrared (NIR) photons into shorter wavelength ultraviolet (UV), visible (vis) or NIR UC luminescence (UCL; NIR-to-UV/vis/ (shorter) NIR conversion) by successive absorption of two or more NIR photons in a system of real energy levels of Ln^{3+} ions [1-11]. This enables *e.g.* optical measurements with zero background fluorescence and high penetration depths for imaging [12,13] in tissue and can be exploited for the intracellular conversion of NIR into vis light for photoactivation in optogenetics [14-18]. Other unique properties of UCNPs are a multitude of largely anti-Stokes shifted sharp and characteristic emission lines in the UV/vis/NIR, defined by the Ln^{3+} -dopants, microsecond lifetimes ideal for lifetime multiplexing and time-gated emissions [19,20], and lack of intermittence/blinking [21]. UCNPs have been recently used also for super-resolution nanoscopy [22]. Additionally, the downshifted or often termed downconverted luminescence (DCL; *e.g.*, NIR-to-(longer wavelength) NIR conversion) of Ln^{3+} ions at $\lambda_{\text{em}} > 1,000$ nm (*e.g.*, Nd^{3+} , Er^{3+}) [23] makes them attractive multiple emitters for the emerging short wavelength infrared (SWIR; ca. 1,000 to 1,700 nm) spectral region [11,23-25]. Much effort has been dedicated in the last years to gain better insights into the UC mechanisms of Ln^{3+} -doped hexagonal NaYF_4 nanoparticles and other UCNPs to derive structural and morphological requirements for high UC efficiencies and signal intensities. Crucial for UCL can be size, *i.e.*, surface-to-volume ratio, due to luminescence quenching by surface defects and high energy vibrations from ligands and water molecules [26-30]. As for some applications like *in vivo* bioimaging, UCNPs with sizes ≤ 20 nm or even ≤ 5 nm are desired, several systematic studies on UCNPs photophysics have been performed to make very small particles brighter, to derive models for surface quenching, and to estimate upper size limits for the so-called “nanoscale effect” [29,31-35]. As UCNPs photophysics are largely controlled by energy transfer (ET) processes, the efficiencies of which depend on inter-ion distance R (ET efficiency $\sim R^{-6}$ for dipole-dipole mechanism, and $\sim \exp[-R/R_0]$ for exchange coupling) and on the population of the energy levels of the sensitizer and activator ions, different factors affecting these quantities have been assessed.⁷ This includes approaches to optimize Ln^{3+} dopant concentrations and tuning of Ln^{3+} - Ln^{3+} distances, [21,36-38] tight surface passivation and protection shells with thicknesses of about 5 nm [39,40]. Other parameters studied are the lattice and crystal phase

of the host, which determine the local symmetry and crystal field faced by the Ln^{3+} ions, the controlled spatial arrangement of dopants in separated layers of sophisticated core – shell structures, [41,42] and high excitation power densities (P) to compensate for quenching effects [43]. These studies revealed also the importance to adjust and optimize dopant concentrations to application-relevant P ranges [44].

One approach to boost UCL in aqueous environments is the use of Nd^{3+} , known for a relatively large absorption cross-section for Ln^{3+} ions, as substitute for the commonly employed sensitizer Yb^{3+} or in combination with Yb^{3+} [21]. Thereby, also the excitation wavelength is shifted from 980 nm, where absorption of water can weaken UCL, to about 800 nm, and laser-induced local overheating effects in cells, tissue, and live animal studies can be minimized. This led to the introduction of Nd^{3+} as sensitizer and to an increasing number of Nd^{3+} -co-doped UCNPs varying in core and shell design and host matrix [4,5,8-13]. Nevertheless, the UCL of simple $\text{Nd}^{3+}, \text{Yb}^{3+}$ -doped UCNPs is often less efficient than that of their Yb^{3+} -based counterparts, particularly in simple Nd^{3+} -based systems, as the Nd^{3+} ion has a much more complicated energy level diagram than Yb^{3+} . Higher doping concentrations of Nd^{3+} can induce deleterious cross-reaction (CR) ET between Ln^{3+} activators and Nd^{3+} ions, leading to a reduction in UCL efficiency. Consequently, the Nd^{3+} doping concentration is commonly kept either below 1 mol-% e.g., in $(\text{Nd}^{3+}, \text{Yb}^{3+}, \text{Ln}^{3+})$ -triple-doped UCNPs or cascade ET processes together with higher Nd^{3+} concentrations are utilized to enhance UCL in $(\text{Nd}^{3+}, \text{Yb}^{3+})$ -co-doped UCNPs. This is realized in core – shell structures built to ensure successive $\text{Nd}^{3+} \rightarrow \text{Yb}^{3+} \rightarrow (\text{Er}^{3+}, \text{Ho}^{3+}, \text{Tm}^{3+})$ ET [45]. Recently, the need for onion-layered structures with Nd^{3+} confined within a layer, has been, however, questioned by demonstrating efficient UCL in $\text{NaYF}_4:\text{Yb}, \text{Er}(\text{Tm})@ \text{NaYF}_4$ UCNPs with Nd^{3+} coordinated to cucurbituril used as organic surface capping [46].

To shed more light on the potential of Nd^{3+} doping, we systematically assessed the performance of a set of similarly sized $(\text{Yb}^{3+}, \text{Nd}^{3+}, \text{Er}^{3+})$ -doped core and core – shell UCNP of different particle architecture in water at broadly varied P with steady state and time-resolved fluorometry at excitation wavelengths of 980 nm (Yb-excitation) and 808 nm (Nd-excitation). As a measure for UCNP performance, the P -dependent UC quantum yield (Φ_{UC}) and its saturation behavior were used as well as particle brightness (B_{UC}). The latter equals the product of the absorption cross-section of a UCNP at the chosen excitation wavelength, which is controlled by the (average) particle size and (average) number of absorbing Ln^{3+} ions, and Φ_{UC} . Based upon spectroscopic measurements at both excitation wavelengths in water and in a lipid

phantom and B_{UC} -based calculations of signal size at different penetration depths, conditions under which excitation at ~808 nm is advantageous are derived and parameters for the further optimization of triple-doped UCNPs are given.

5.3 Materials and Methods

5.3.1 Chemicals and Characterization Methods

Lanthanide chloride hexahydrates (>99.9%) were purchased from Sigma Aldrich and Treibacher Industrie AG. Intralipid, a phospholipid stabilized soybean oil, 20% emulsion was bought from Sigma Aldrich. All other chemicals were of technical grade and used as received. Oleic acid and 1-octadecene were obtained from Alfa Aesar. Nitrosonium tetrafluoroborate, poly(acrylic acid) ($M_w \sim 2,100$) was purchased from Sigma Aldrich and the Ln^{3+} multielement stock solution from Perkin Elmer. All other chemicals were obtained from Sigma Aldrich, Merck or Acros.

The size of the nanoparticles was determined by transmission electron microscopy (TEM) with a 120 kV Philips CM12 microscope on carbon coated copper grids (400 mesh) from Plano. For sample preparation, 10 μ L of a particle dispersion (cyclohexane; 1 mg·mL⁻¹) were dropped on the grid and the solvent was allowed to evaporate. For the determination of the elemental composition and the concentration of the dispersed UCNPs an inductively coupled plasma mass spectrometry (ICP-MS) ELAN 9000 from PerkinElmer was used. Several calibration samples were prepared with a commercial multielement stock solution (10,000 ppb; dilution: 1:100,000 – 1:50) and a rhodium standard solution (10,000 ppb) in 5% (w/v) HNO₃. For the measurement the nanoparticles had to be completely dissolved. UCNPs (0.3 mg) were dissolved in sulfuric acid (97%, w/v, 417 μ L). For achieving a complete decomposition this process was assisted by sonication. Afterwards 7.083 mL double-distilled water and 7.5 mL HNO₃ (1 M) were added. The solution was diluted in each case 1:50 with 5% (w/v) HNO₃ and rhodium standard was added (10,000 ppb, 1 μ L).

Dynamic light scattering (DLS) was performed with a Malvern Zetasizer Nano ZS to characterize the particle-size distribution in dispersion. Disposable semi-micro poly(methyl methacrylate) cuvettes were used and the temperature was kept constant at 20 °C. To analyze the crystal structure, X-ray powder diffraction patterns (XRD) with a resolution of 0.005° (2 θ) were collected using a STOE STADI P diffractometer equipped with a Dectris Mythen 1K

detector. Monochromatic Cu K α 1 radiation ($\lambda = 1.54056 \text{ \AA}$) was employed. Absorption spectra were collected on a Varian Cary 50 spectrophotometer. Luminescence measurements were carried out by a fibre-coupled spectrometer RGB photonics mini from RGB (Kehlheim, Germany) in a 90-degree measurement geometry (Cuvette Holder CVH100/M, Thorlabs) with two laser modules (808 nm (200 mW, continuous wave (cw)) and 980 nm (200 mW, cw)) from Picotronic for excitation. The spectra were recorded by the software Waves, developed by RGB. The excitation power density was adjusted and measured by a handheld optical power and power meter console PM400 from Thorlabs, equipped with a standard Si photodiode power sensor (400 – 1,100 nm, 500 mW). For the lifetime measurements the fluorescence spectrometer FLS980 from Edinburgh Instruments was used at 805 nm and 978 nm. P -dependent Φ_{UC} of the UCNP dispersions were measured absolutely at 805 nm and 978 nm using a custom-made integrating sphere setup equipped with two 8 W laser diodes covering power densities from 4 – 520 W·cm $^{-2}$ [47]. The exact profiles of all laser diodes are shown in Figure 5.10.

5.3.2 Synthesis and Surface Modification of UCNPs

5.3.2.1 Synthesis of hexagonal Core Particles NaYF $_4$:20%Yb,2%Er

Hexagonal core particles NaYF $_4$:Yb,Er were synthesized *via* a bottom-up strategy in a solvent mixture of oleic acid and 1-octadecene using the thermal decomposition method [48]. For the synthesis of 1 mmol β -NaYF $_4$:20%Yb,2%Er particles, the lanthanide chlorides were dissolved in methanol (5 mL) in the corresponding molar ratios. Oleic acid (8 mL) and 1-octadecene (15 mL) was added into a 50 mL three necked round bottom flask under nitrogen flow. This solution was heated to 160 °C and vacuum was applied for 30 min unless it appeared clear. This solution was cooled to room temperature and 4.00 mmol NH $_4$ F and 2.5 mmol NaOH in 10 mL methanol were added and then the suspension was kept at 120 °C for 30 min before heating to reflux (ca. 320 °C). The heating-time was controlled by the appearance of upconversion luminescence in the synthesis flask upon continuous excitation with a 980 nm laser module (200 mW, cw). When the upconversion luminescence can be identified by the bare eye, the solution is kept at reflux for additional 8 min. To achieve a complete transformation of the nanocrystals from the α - to the β -form and to receive monodisperse particles, a heating time of 15 min turned out to be best for the 25 nm sized particles. To obtain particles with bigger diameters the heating steps and the reflux time was adapted. The particles were precipitated by the addition of excess of ethanol and collected by centrifugation

at 1,000 g for 5 min. The precipitate was washed with chloroform/ethanol (1:10 v/v) two times and five times with cyclohexane/acetone (1:10 v/v) by repeated redispersion-precipitation-centrifugation cycles. In the end, for removing aggregates, the particles were dispersed in 10 mL cyclohexane, centrifuged at 1,000 g for 3 min and the supernatant was collected.

5.3.2.2 Synthesis of Pre-cursor Nanoparticles

Cubic shell-precursor materials (NaYF_4 :5%Yb,5%Nd; NaYF_4 :10%Yb,10%Nd; NaYF_4 :15%Yb,15%Nd; NaYF_4 :10%Yb and NaYF_4) were synthesized *via* a synthesis protocol almost identical to the synthesis of hexagonal NaYF_4 :Yb,Er particles, by using the respective molar ratios of the lanthanide chlorides. The suspension was not heating to reflux but kept for 30 min at 240 °C to receive the cubic crystal lattice. Moreover, the purification of the particles was performed as described above.

5.3.2.3 Synthesis of Core – shell Nanoparticles

Core-shell particles of the types NaYF_4 :20%Yb,2%Er@ NaYF_4 :5-15%Yb,5-15%Nd; NaYF_4 :20%Yb,2%Er@ NaYF_4 :10%Yb; $(\text{Yb}@\text{Yb,Nd})^{\text{is}}$; $(\text{Yb}@\text{Yb})^{\text{is}}$; $(\text{Yb})^{\text{is}2}$; $(\text{Yb})^{\text{is}5}$ have been synthesized by the following protocol: The shells were grown *via* Ostwald ripening using precursor particles of α - NaYF_4 :Yb,Nd, α - NaYF_4 :Yb and α - NaYF_4 [49]. The core particles (NaYF_4 :20%Yb,2%Er) together with the respective shell precursors were filled in different ratios according to the desired thickness of the shell into 50 mL three necked round bottom flasks and were kept under nitrogen flow. For the 4 nm shell a ratio core to precursor material of 1 to 3, while for the 2 nm shell a ratio of 1 to 1.5 was used. Per 1 mmol total content of core NaYF_4 -particles, 5 mL oleic acid and 5 mL 1-octadecene were added. After this the β - NaYF_4 -particles and the precursors were separately heated to 100 °C before vacuum was applied for 1 h unless a clear solution was obtained. After this the β - NaYF_4 -particles were heated to reflux and the shell precursor was kept under nitrogen flow at 100 °C. Every 10 minutes a small portion (approx. 1 - 3 mL) of the shell precursor was added to the mixture. When the precursor material was consumed, the solution was kept for another 10 min at reflux. The precipitation and purification of the core – shell nanoparticles was performed according to the protocol described for redispersion-precipitation cycles of NaYF_4 :20%Yb,2%Er.

5.3.2.4 Surface Modification

The ligand exchange strategy with nitrosyl tetrafluoroborate is based on a method described by Wiesholler *et al.* [50]. In a two-phase system consisting of equal volumes of cyclohexane

and DMF the nanoparticles were dispersed. NOBF_4 (1 mg per 1 mg UCNPs) was added and the dispersion was stirred at slightly elevated temperature ($\sim 40^\circ\text{C}$) for 10 min. During this time the oleate-capped hydrophobic UCNPs were transferred from the cyclohexane phase into the DMF phase. This phase transfer can be easily monitored by control of the upconversion luminescence *via* excitation with a 980 nm laser module (200 mW, cw). Surface modification is complete, when only the DMF phase exhibits upconversion luminescence. The clear upper cyclohexane phase was discarded, and the particles were precipitated by excess of chloroform. The suspension is centrifuged at 1,000 g for 5 min. The jellylike precipitate is washed twice with chloroform. Finally, the BF_4^- -stabilized particles are dispersed in DMF, and aggregates were removed by centrifugation at 1,000 g for 3 min. Poly(acrylic acid) ($M_w \sim 2,100$) was dissolved in water ($2 \text{ mg}\cdot\text{mL}^{-1}$) and added to the BF_4^- -stabilized nanoparticles dispersed in DMF. The solution was stirred and kept at a moderate temperature of 40°C for 15 min. Afterwards the dispersion was centrifuged (13,600 g for 20 min) and washed twice with water. Finally, the supernatants were collected after centrifugation at 1,000 g for 3 min.

5.3.3 Determination of the Absorption Cross-Section

For the measurement of P_λ^0 a quartz cuvette was filled with water and for the measurement of P_λ a similar quartz cuvette was filled with $(\text{Yb@Yb,Nd})_{\text{is}}$ in water ($6,34 \text{ mg}\cdot\text{mL}^{-1}$). The cuvettes were illuminated with a 980 nm laser diode (200 mW, cw, Picotronic) for the Yb-absorption cross-section (equation 1) and with an 808 nm laser diode (500 mW, cw, Picotronic) for the Nd-absorption cross-section (equation 1). The laser power was measured in 180° configuration with a handheld optical power meter console PM400 from Thorlabs, equipped with a standard Si photodiode power sensor (400 – 1,100 nm). When the signal became constant, the power values were recorded for a total illumination time of 1 min (600 data points). The average value was used for calculation of the P -values. From the ICP-measurements the Yb^{3+} - and Nd^{3+} - concentrations were calculated. C is the number concentration of molecular entities (number per volume) and l is the optical pathlength [51].

$$\sigma(\lambda) = \frac{\alpha(\lambda)}{C} = \frac{1}{Cl} \ln \left(\frac{P_\lambda^0}{P_\lambda} \right) \quad (1)$$

5.3.4 Penetration Depth Measurements

For the measurements mimicking UCNP performance in biological tissue, a glass cylinder (4.4 cm in diameter) was filled with phantom tissue (1% intralipid) [52] in different heights.

This cylinder was trans irradiated from the top by a laser module (808 nm or 980 nm, each 200 mW, cw from Picotronic) with a focused beam. The glass cylinder was placed on a standard Si photodiode power sensor (400 – 1100 nm, 500 mW), which was used to record the laser power. The transmission spectrum of intralipid (0.01%) in water was recorded on a Varian Cary 50 spectrophotometer.

5.4 Results and Discussion

There are vivid and sometimes controversial debates in the upconversion community regarding the choice of an optimum excitation wavelength, *i.e.*, 980 or 808 nm, and hence suitable doping ions and their combinations to enable a high signal-to-background ratio as a prerequisite for an ultralow detection sensitivity and a high spatial resolution and to avoid overheating. Common arguments are suppressing tissue autofluorescence, blurring-inducing scattering, and light absorption by other materials than the reporter as well as boosting sensitivity *via* enhanced absorption. The expected benefit of using Nd³⁺ as sensitizer ion together with 808 nm excitation arises from a) a higher absorption cross-section up to a factor of ~10 of Nd³⁺ compared to Yb³⁺ at the typical excitation wavelengths of 808 and 980 nm [53] and b) the considerably lower absorbance of water at 808 nm falling below the water absorbance at 980 nm by a factor of ~25 [45]. Nevertheless, a systematic comparison of the performance of differently doped UCNPs at different excitation wavelengths is still missing.

As UCL efficiency is affected by many different parameters such as UCNP size, crystal phase, architecture, surface chemistry, and *P*, this requires rationally designed and well-characterized UCNPs as well as quantitative measurements to derive comparable information.

To systematically compare 980 (Yb-) and 808 nm (Nd-) excitation, a set of core – active shell – inactive shell UCNPs was synthesized that match in size and contain the same amount of Nd³⁺, Yb³⁺, and Er³⁺ dopants, yet differ in particle architecture. This set is highlighted in Figure 5.2.

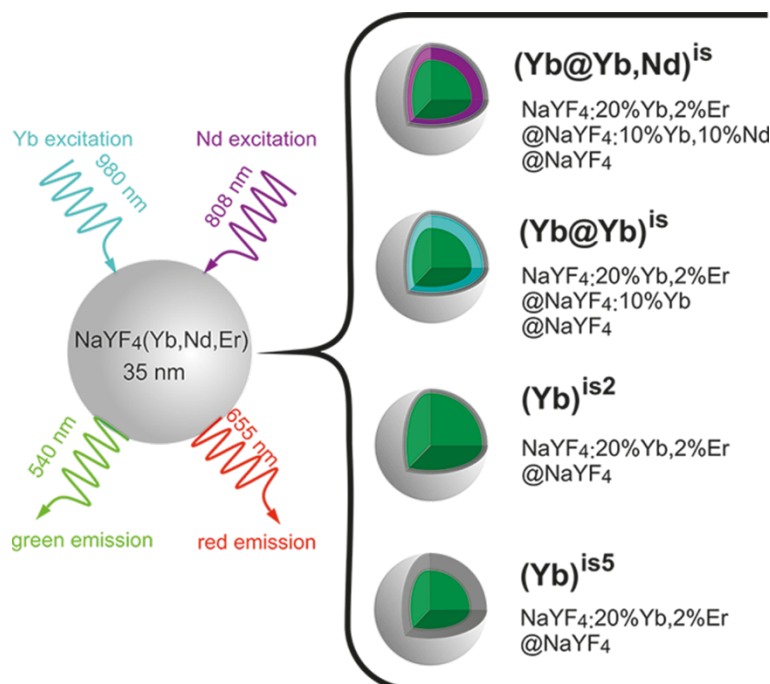


Figure 5.2 | Overview of the particle systems and the acronyms used in this study comparing different architectures of upconversion nanoparticles of one size for 808 and 980 nm excitation in terms of brightness and deep tissue penetration.

5.4.1 Particle Design, Synthesis and Characterization

NaYF₄-UCNPs were synthesized that consist of a core (diameter ~25 nm) doped with 20% Yb³⁺ and 2% Er³⁺ covered by an about 4 nm thick active shell doped with 10% Nd³⁺ and 10% Yb³⁺, protected by a ~2 nm thin inert shell, denoted NaYF₄:20%Yb,2%Er@NaYF₄:10%Yb,10%Nd@NaYF₄, or in short (Yb@Yb,Nd)^{is} (Figs. 5.2 and 5.3).

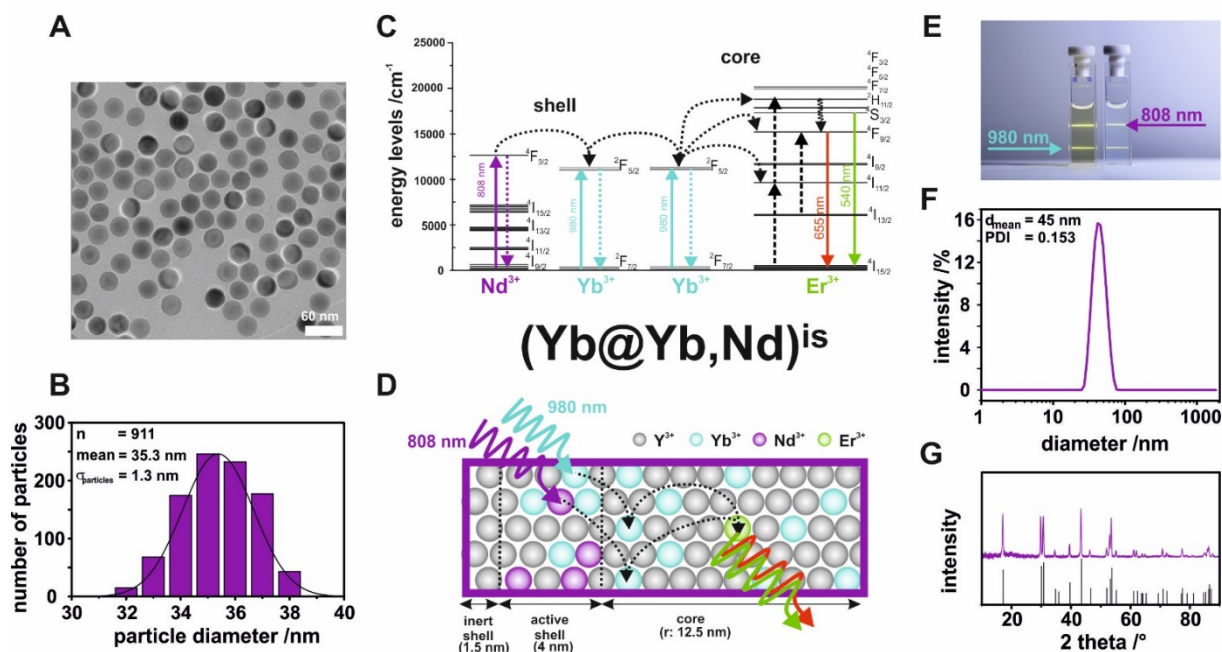


Figure 5.3 | Transmission electron microscopy (A), with corresponding particle size distribution (B) of $\text{NaYF}_4:20\%\text{Yb},2\%\text{Er}@ \text{NaYF}_4:10\%\text{Yb},10\%\text{Nd}@ \text{NaYF}_4$ ($(\text{Yb}@\text{Yb},\text{Nd})^{\text{is}}$) upconversion nanoparticles. Possible energy transfer processes (C) and lateral distribution of the lanthanide ions (Y^{3+} , Yb^{3+} , Nd^{3+} and Er^{3+}) in the different layers (core, active shell and inert shell) (D) are symbolized. A photo (E) of the particles colloidal stable in cyclohexane (left, $20 \text{ mg}\cdot\text{mL}^{-1}$) and water (right, $2 \text{ mg}\cdot\text{mL}^{-1}$) excited by an 808 (200 mW) and 980 nm (200 mW) laser module. The DLS-measurements (F) of particles ($2 \text{ mg}\cdot\text{mL}^{-1}$) underline the colloidal stability in aqueous solution. The diffraction pattern (purple) confirm a hexagonal crystal phase as indicated by the reflexes of the standard reference pattern of $\beta\text{-NaYF}_4$ (ICDD PDF #16-334) (black) (G).

We deliberately chose the most common Er^{3+} -doping ratio [54]. Monodisperse particles (PDI = 0.04) (Fig. 5.3B) with a pure hexagonal crystal lattice (Fig. 5.3G) have been obtained and the doping ratio was verified by ICP-MS (Table 5.1).

Table 5.1. ICP-MS-data showing the composition of all particle systems used in this study.

particle system	acronym	core			active-shell			inert-shell	total			
		Y ³⁺ /%	Yb ³⁺ /%	Er ³⁺ /%	Y ³⁺ /%	Yb ³⁺ /%	Nd ³⁺ /%	Y ³⁺ /%	Y ³⁺ /%	Yb ³⁺ /%	Nd ³⁺ /%	Er ³⁺ /%
NaYF ₄ :20%Yb,2%Er@ NaYF ₄ :5%Yb,5%Nd@NaYF ₄	-	77.6 ± 0.17	20.6 ± 0.21	1.8 ± 0.04	89.1 ± 0.17	5.9 ± 0.18	4.9 ± 0.01	-	74.1 ± 0.17	23.2 ± 0.12	2.0 ± 0.11	0.7 ± 0.01
NaYF ₄ :20%Yb,2%Er@ NaYF ₄ :10%Yb,10%Nd@NaYF ₄	(Yb@Yb,Nd) ^{is}	77.6 ± 0.17	20.6 ± 0.21	1.8 ± 0.04	80.2 ± 0.29	10.0 ± 0.16	9.8 ± 0.09	99.8 ± 0.20	78.5 ± 0.50	14.0 ± 0.14	6.5 ± 0.05	1.0 ± 0.02
NaYF ₄ :20%Yb,2%Er@ NaYF ₄ :15%Yb,15%Nd@NaYF ₄	-	77.6 ± 0.17	20.6 ± 0.21	1.8 ± 0.04	69.3 ± 0.10	15.1 ± 0.13	15.6 ± 0.10	-	68.6 ± 0.15	18.8 ± 0.07	12.0 ± 0.04	0.6 ± 0.02
NaYF ₄ :20%Yb,2%Er @NaYF ₄ :10%Yb@NaYF ₄	(Yb@Yb) ^{is}	77.6 ± 0.17	20.6 ± 0.21	1.8 ± 0.04	89.1 ± 0.75	10.9 ± 0.11	-	98.7 ± 0.13	84.2 ± 0.51	14.8 ± 0.06	-	1.0 ± 0.00
NaYF ₄ :20%Yb,2%Er@NaYF ₄	(Yb) ^{is5}	77.6 ± 0.17	20.6 ± 0.21	1.8 ± 0.04	-	-	-	99.0 ± 0.10	89.8 ± 0.8	9.2 ± 0.54	-	1.0 ± 0.01
NaYF ₄ :20%Yb,2%Er@NaYF ₄	(Yb) ^{is2}	77.6 ± 0.17	20.6 ± 0.21	1.8 ± 0.04	78.4 ± 0.57	19.4 ± 0.32	2.2 ± 0.00	100.0 ± 0.00	80.4 ± 0.32	17.5 ± 0.23	-	2.1 ± 0.01

These predominantly green emitting particles can be excited at 980 and 808 nm due to the presence of Yb³⁺ and Nd³⁺ ions (Figs. 5.3E and 5.3F). In Figure 5.3C the ET pathways of the individual Ln³⁺ ions upon both excitation at both wavelengths are depicted. The doping ratio of 10% Yb³⁺ and 10% Nd³⁺ of the 4 nm thick active shell was chosen after studying the luminescence intensity at Nd- and Yb-excitation of a series of similar particles with doping ratios of 5, 10 and 15% for both sensitizer ions. The same *P* was used for Nd- and Yb-excitation and the UCL intensities of the dispersed oleate-capped particles were normalized to the number of particles present in the cyclohexane dispersion, which was determined from ICP-MS and TEM measurements. An organic solvent was chosen for this comparison to exclude possible UCL quenching by —O-H vibrations [30,43]. For Nd-excitation, the highest luminescence intensity (*I*_{540 nm}) was observed for doping ratios of 10% Yb³⁺ and 10% Nd³⁺, equaling about 80% of the intensity reached for Yb-excitation (Fig. 5.4).

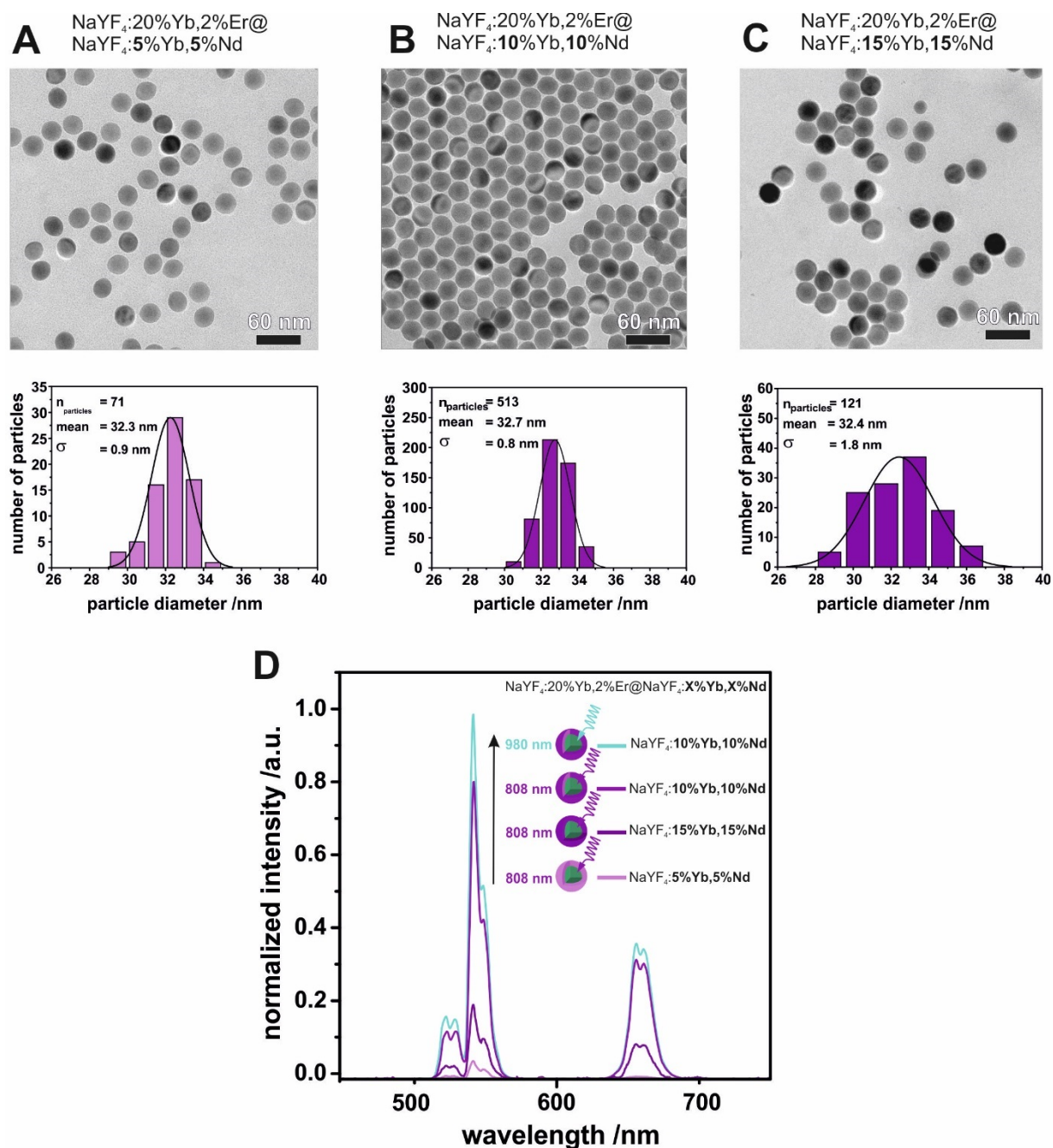


Figure 5.4 | TEM images and size distribution of core shell particles $\text{NaYF}_4\text{:}20\%\text{Yb},2\%\text{Er}@ \text{NaYF}_4\text{:}5\%\text{Yb},5\%\text{Nd}$ (A, light purple), $\text{NaYF}_4\text{:}20\%\text{Yb},2\%\text{Er}@ \text{NaYF}_4\text{:}10\%\text{Yb},10\%\text{Nd}$ (B, purple) and $\text{NaYF}_4\text{:}20\%\text{Yb},2\%\text{Er}@ \text{NaYF}_4\text{:}15\%\text{Yb},15\%\text{Nd}$ (C, dark purple). Luminescence spectra of core-shell particles $\text{NaYF}_4\text{:}20\%\text{Yb},2\%\text{Er}@ \text{NaYF}_4\text{:}5\%\text{Yb},5\%\text{Nd}$ (light purple), $\text{NaYF}_4\text{:}20\%\text{Yb},2\%\text{Er}@ \text{NaYF}_4\text{:}10\%\text{Yb},10\%\text{Nd}$ (purple) and $\text{NaYF}_4\text{:}20\%\text{Yb},2\%\text{Er}@ \text{NaYF}_4\text{:}15\%\text{Yb},15\%\text{Nd}$ (dark purple) excited by 808 nm and core shell particles $\text{NaYF}_4\text{:}20\%\text{Yb},2\%\text{Er}@ \text{NaYF}_4\text{:}10\%\text{Yb}$ (turquoise) excited by 980 nm (D). All particles are dispersed in cyclohexane. The spectra were acquired under same laser excitation power of $13 \text{ W}\cdot\text{cm}^{-2}$ and normalized to the particle concentration evaluated by ICP-MS. For the comparison the emission at 540 nm of the $\text{NaYF}_4\text{:}20\%\text{Yb},2\%\text{Er}@ \text{NaYF}_4\text{:}10\%\text{Yb},10\%\text{Nd}$ (turquoise) excited at 980 nm was set to one, and the spectra recorded at 808 nm excitation were corrected by the same factor.

This doping ratio was subsequently used for the $(\text{Yb}@\text{Yb},\text{Nd})^{\text{is}}$ system. In a last step, a thin inert shell was grown on the optimized core-shell particles to cure surface defects and prevent the presence of sensitizer ions at the particle surface. The latter minimizes the quenching of the excited states of the sensitizer ions by surface ligands and solvent molecules

[43]. Subsequently, the particles were transferred from the organic to the aqueous phase by exchanging the oleate for poly(acrylic acid) (PAA) ligands [50].

A comparison of the luminescence spectra and intensities of PAA-stabilized (Yb³⁺,Nd³⁺,Er³⁺)-doped UCNPs with and without inert shell in water confirmed the shielding of the sensitizer ions by the inactive shell as indicated by an increased green-to-red ratio of the Er³⁺ emission (Fig. 5.5).

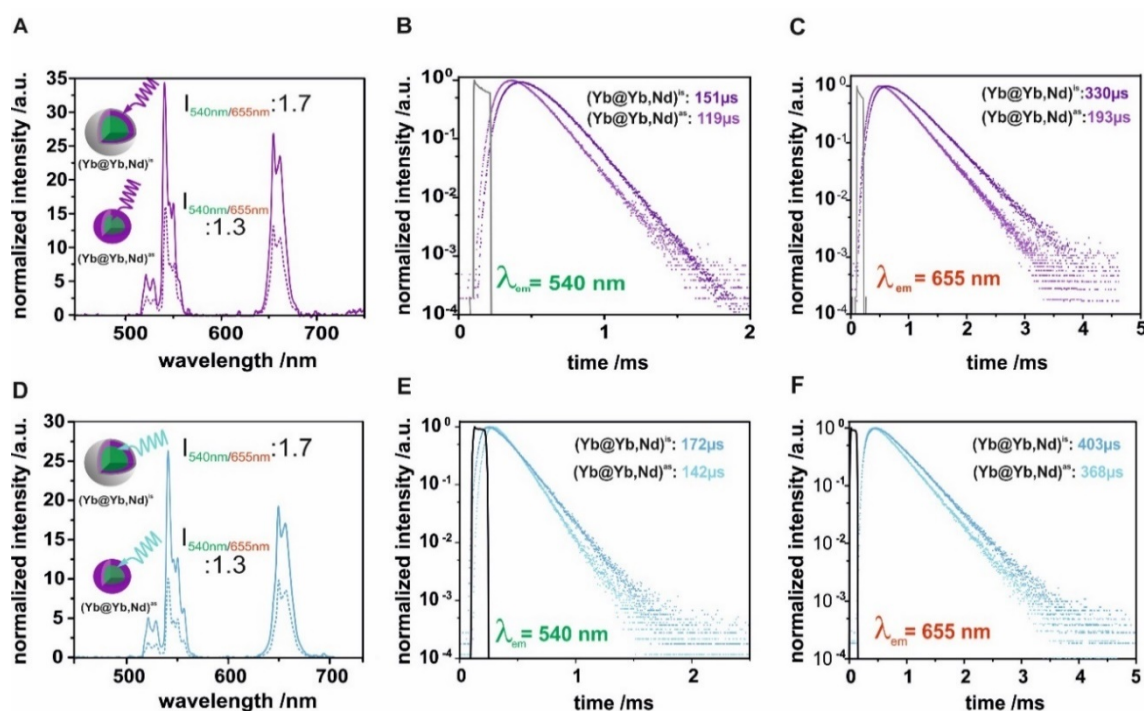


Figure 5.5 | Luminescence spectra (A) and decay times for the green (540 nm) (B) and red (655 nm) (C) emission of core – shell particles NaYF₄:Yb,Er@NaYF₄:Yb,Nd (Yb@Yb,Nd)^{as} (dashed line and bright purple) and core – shell – shell particles NaYF₄:Yb,Er@NaYF₄:Yb,Nd@NaYF₄ (Yb@Yb,Nd)^{is} (solid line and dark purple) in aqueous solutions, excited at 808 nm (purple). The luminescence spectra (D) for the 980 nm (turquoise) excitation and decay times for the green (540 nm) (E) and red (655 nm) (F) emission of core – shell particles NaYF₄:Yb,Er@NaYF₄:Yb,Nd (Yb@Yb,Nd)^{as} (dashed line and bright turquoise) and core – shell – shell particles NaYF₄:Yb,Er@NaYF₄:Yb,Nd@NaYF₄ (Yb@Yb,Nd)^{is} (solid line and dark turquoise) in aqueous solutions, excited at 980 nm (turquoise).

Core – shell – shell particles of identical size, but without Nd³⁺ doping of the active shell, were prepared in a similar way. These UCNP are referred to as (Yb@Yb)^{is} and presented in Figure 5.6.

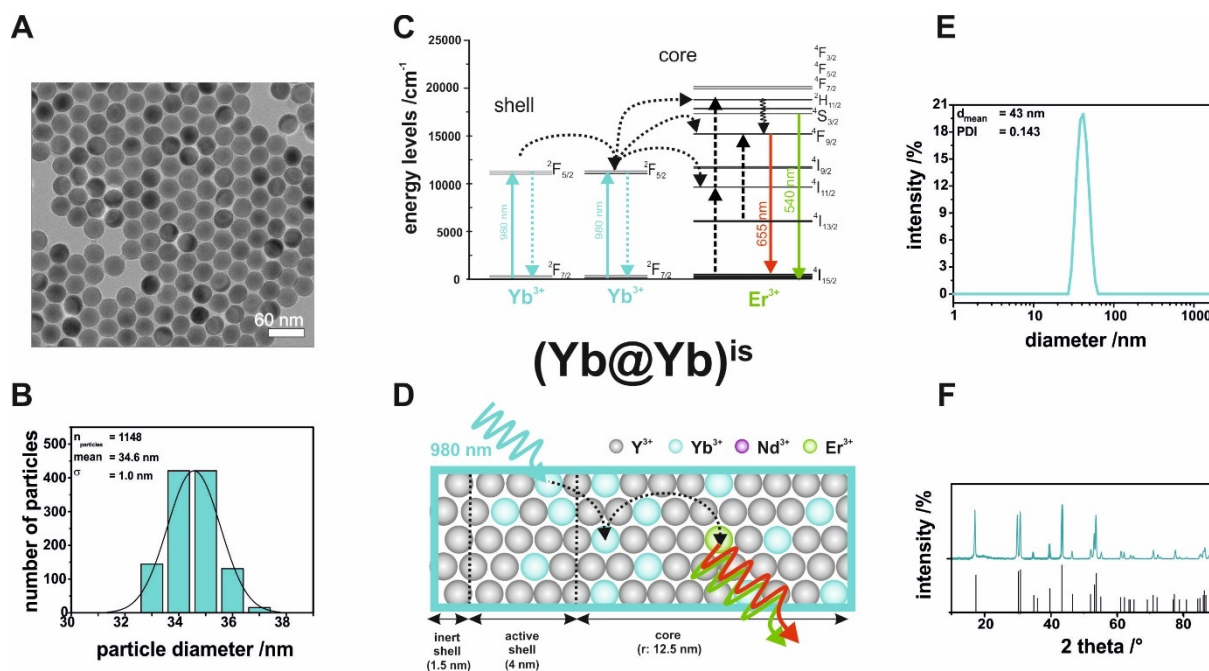


Figure 5.6 | TEM-image (A) and corresponding size distribution (B) of NaYF₄:Yb,Er@NaYF₄ particles ((Yb@Yb)^{is}). The diameter averaged from 1,148 particles is 34.6 ± 1.0 nm. Possible energy transfer processes (C) and lateral distribution of the lanthanide ions (Y³⁺, Yb³⁺, and Er³⁺) in the different layers (core, active and inert shell) (D) are symbolized. The near monodispersity of the particles in aqueous solutions was confirmed by a solvodynamic diameter of 43 nm with a polydispersity index of 0.143 measured by dynamic light scattering of the particle dispersion in water (1 mg·L⁻¹). No agglomeration of the particles over 3 months in dispersion can be observed (E). The diffraction patterns reveal a hexagonal crystal phase as the reflexes of the nanocrystals match the standard reference pattern of β-NaYF₄ (ICDD PDF #16-334) (black) (F).

To complete the picture on particles of identical size, core – shell particles without active shell, but with different thicknesses of the inert shell of 2 and 5 nm, labelled as (Yb)^{is2} (Fig. 5.7) and (Yb)^{is5} (Fig. 5.8), have been synthesized.

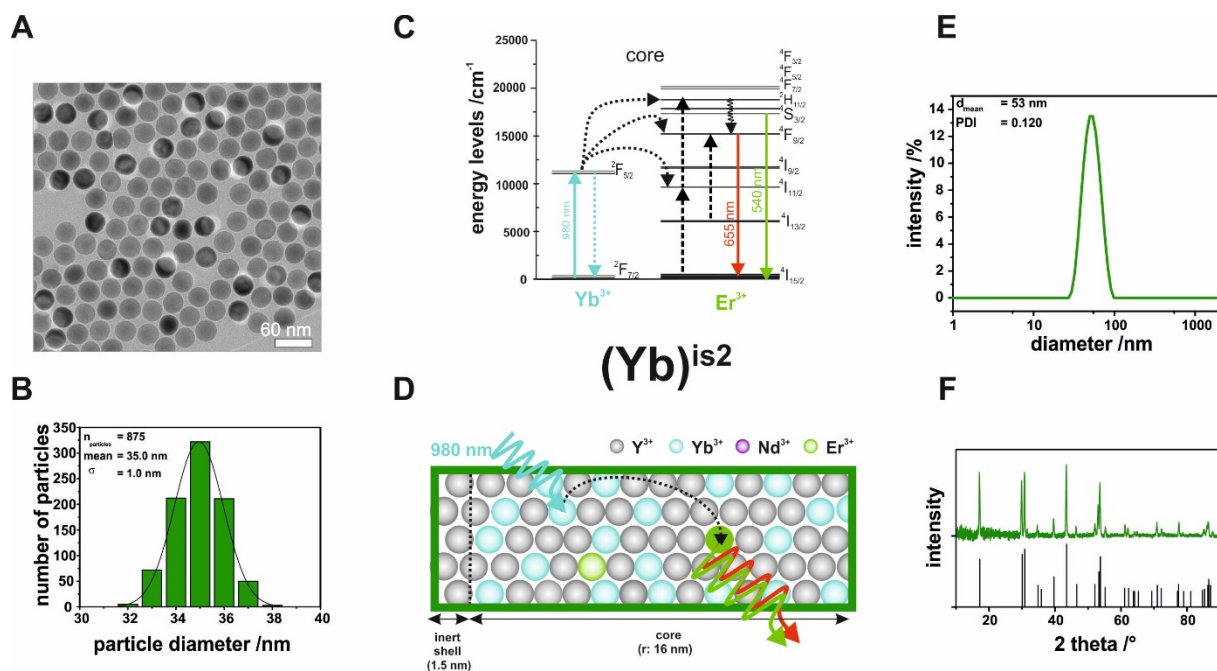


Figure 5.7 | TEM-image (A) and corresponding size distribution (B) of NaYF₄:Yb,Er@NaYF₄ particles ((Yb)^{is2}). The diameter averaged from 875 particles is 35.0 ± 1.0 nm. Possible energy transfer processes (C) and lateral distribution of the lanthanide ions (Y³⁺, Yb³⁺, and Er³⁺) in the different layers (core, active and inert shell) (D) are symbolized. The near monodispersity of the particles in aqueous solutions was confirmed by a solvodynamic diameter of 53 nm with a polydispersity index of 0.120 measured by dynamic light scattering of the particle dispersion in water (1 mg·L⁻¹). No agglomeration of the particles in dispersion over 3 months can be observed (E). The diffraction patterns reveal a hexagonal crystal phase as the reflexes of the nanocrystals match the standard reference pattern of β-NaYF₄ (ICDD PDF #16-334) (black) (F).

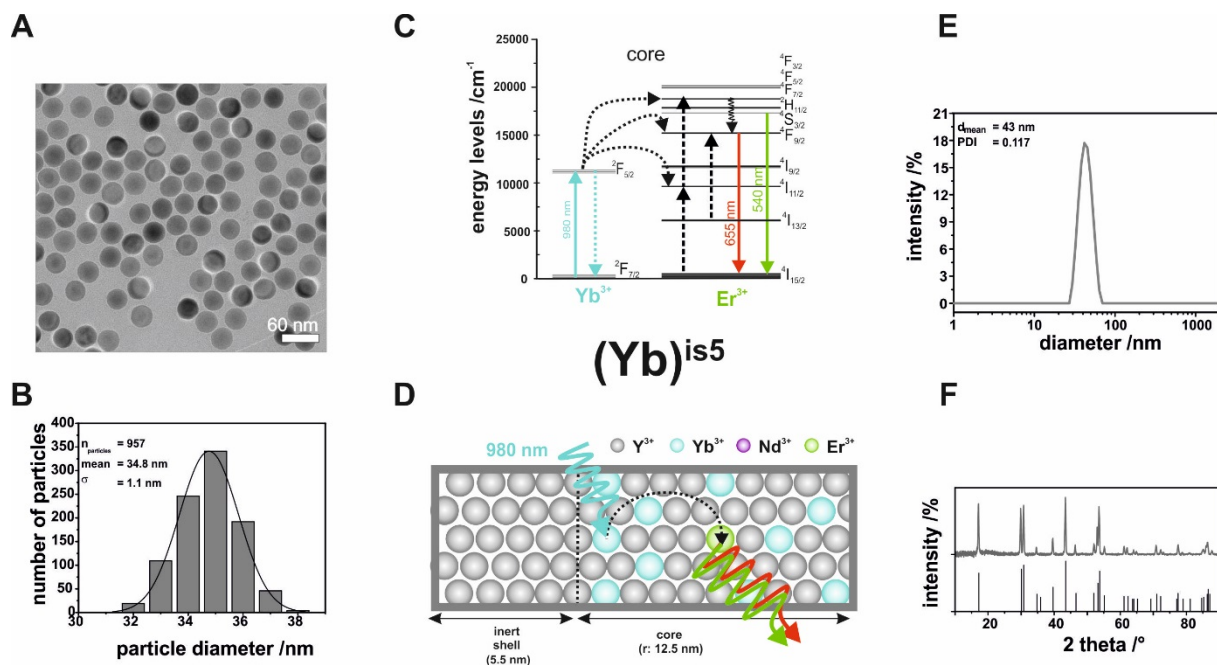


Figure 5.8 | TEM-image (A) and corresponding size distribution (B) of NaYF₄:Yb,Er@NaYF₄ particles ((Yb)^{is5}). The diameter averaged from 957 particles is 34.8 ± 1.1 nm. Possible energy transfer processes (C) and lateral distribution of the lanthanide ions (Y³⁺, Yb³⁺, and Er³⁺) in the different layers (core, active and inert shell) (D) are symbolized. The near monodispersity of the particles in aqueous solutions was confirmed by a solvodynamic diameter of 43 nm with a polydispersity index of 0.117 measured by dynamic light scattering of the particle dispersion in water (1 mg·L⁻¹). No agglomeration of the particles over 3 months in dispersion can be observed (E). The diffraction patterns reveal hexagonal crystal phases as the reflexes of the nanocrystals match the standard reference pattern of β-NaYF₄ (ICDD PDF #16-334) (black) (F).

5.4.2 Comparison of (Yb@Yb,Nd)^{is} and (Yb@Yb)^{is}

As a first step for the desired comparison, a possible influence of Nd³⁺ (Fig. 5.3D) with its complex energy scheme on the UCL resulting upon Yb-excitation at 980 nm was assessed. For this purpose, particles of identical architecture with and without Nd³⁺ ions in the active shell were studied. A comparison of the UCL spectra of both systems at normalized particle concentration in water revealed minimum effects (Fig. 5.9A; low P of 13 W·cm⁻²). In contrast, the luminescence lifetimes of the green and the red Er³⁺-emission of (Yb@Yb,Nd)^{is} show a longer decay for Yb-excitation compared to (Yb@Yb)^{is} (Figs. 5.9B and 5.9C). The differences in the rise behavior of the decay profiles of the green and red Er³⁺ emission observed in the time-resolved UCL measurements are attributed to an additional ET step from Yb³⁺ → Nd³⁺ in the ET processes involved in the population of the energy levels of the activator ions, namely the Yb³⁺ → Nd³⁺ → Yb³⁺ → Er³⁺ cascade. Contrarily, (Yb@Yb)^{is} UCNPs do not show UCL at Nd-excitation at the low P of 13 W·cm⁻². Therefore, the excited state absorption of the Er³⁺ ions can be neglected for the chosen experimental conditions. Consequently, (Yb@Yb,Nd)^{is} UCNPs are suitable for the subsequent direct comparison of Nd- and Yb-excitation.

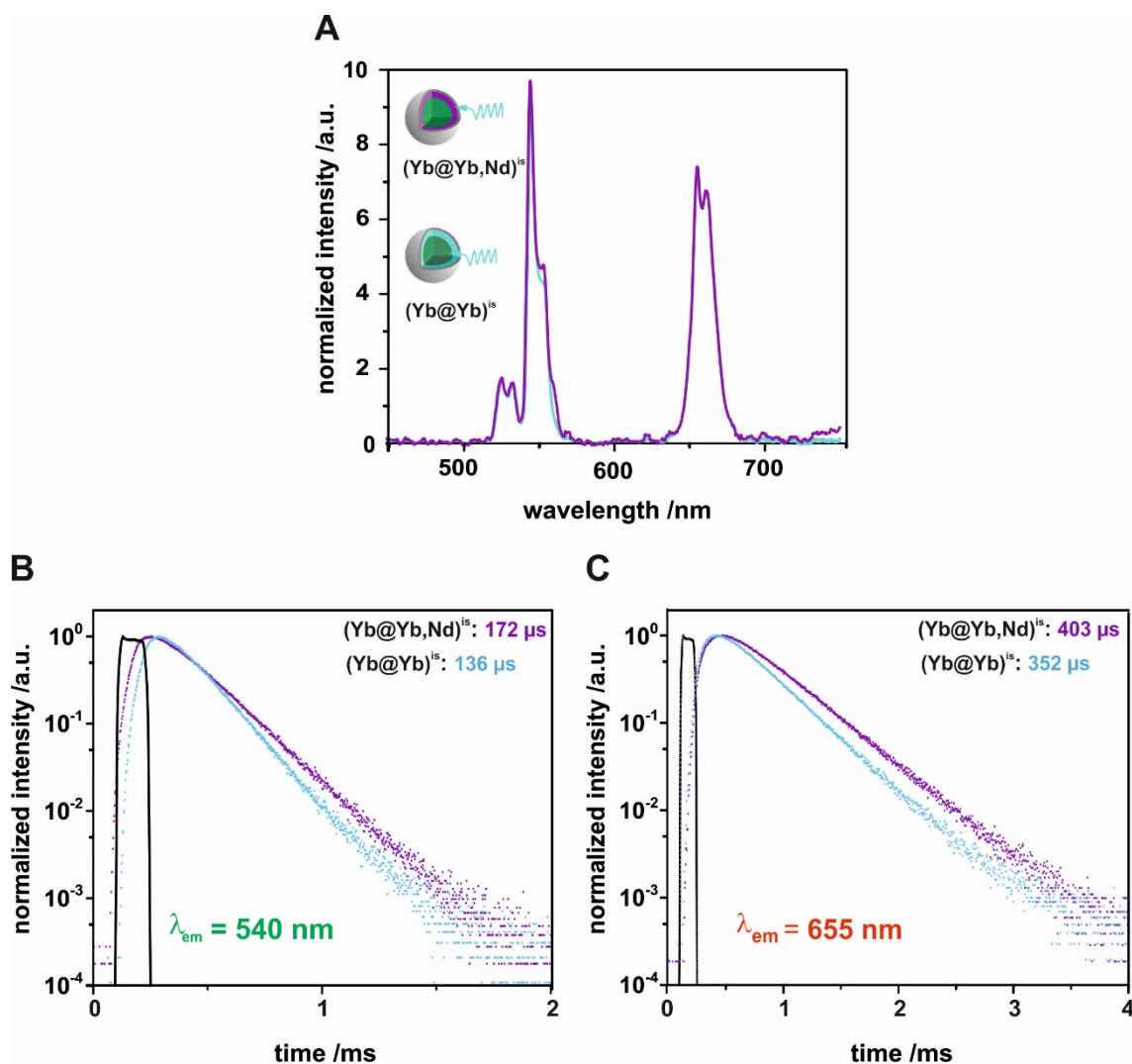


Figure 5.9 | The $NaYF_4:Yb,Er@NaYF_4:Yb,Nd@NaYF_4$ $(Yb@Yb,Nd)^{is}$ core-shell-shell particles (purple) were compared to $NaYF_4:Yb,Er@NaYF_4:Yb@NaYF_4$ $(Yb@Yb)^{is}$, turquoise) core-shell-shell particles in aqueous solution using (A) luminescence spectra and the lifetimes of the green (B) and red emission (C) at Yb-excitation in aqueous solution. All luminescence spectra were normalized to the particle concentration and measured with the same laser power conditions.

5.4.3 Comparison of Nd- and Yb- Excitation of $(Yb@Yb,Nd)^{is}$

The benefits of using Nd^{3+} as sensitizer and consequently 808 nm instead of 980 nm excitation as required for Yb^{3+} discussed in the literature are ascribed to the higher absorption cross-section of Nd^{3+} and the considerably lower absorbance of water at 808 nm. The former is assumed to exceed that of Yb^{3+} by a factor of ~ 10 and the latter to fall below the water absorbance at 980 nm by a factor of ~ 25 . The considerably lower water absorbance at 808 nm minimizes heating effects and may allow for a higher penetration depth, even though the scattering by tissue components is more pronounced at 808 nm. Subsequently, we assessed the parameters which contribute to signal size, thereby also simulating the influence of different penetration depths. These parameters can be separated in matrix-related properties

such as scattering and absorption and in particle related parameters summarized as the particle brightness ($B_{UC}(\lambda_{Ex})$). $B_{UC}(\lambda_{Ex})$ is defined as the product of the UCNP absorption cross-section ($\sigma_{UCNP}(\lambda_{Ex}) [cm^2]$) and $\Phi_{UC}(P_{Ex})$ (equation 2). Hence, this property is also P -dependent.

$$B_{UC}(\lambda_{Ex}) = \sigma_{UCNP}(\lambda_{Ex}) \times \Phi_{UC}(P_{Ex}) \quad (2)$$

Absorption cross-section of one UCNP. The absorption cross-section of one UCNP ($\sigma_{UCNP}(\lambda_{Ex}) [cm^2]$) is determined by the total number of Ln^{3+} absorbers per nanoparticle (N_{Ln}) and the absorption cross-section of a single absorbing Ln^{3+} ion at the chosen excitation wavelength λ_{Ex} ($\sigma_{Ln}(\lambda_{Ex}) [cm^2]$) (equation 3).

$$\sigma_{UCNP}(\lambda_{Ex}) = N_{Ln} \times \sigma_{Ln}(\lambda_{Ex}) \quad (3)$$

Thus, it depends on particle size and doping concentration. In many publications comparing the sensitizers Nd^{3+} and Yb^{3+} , $\sigma_{Ln}(\lambda_{Ex})$ values were taken from the literature, thereby assuming that the optical properties of Ln^{3+} ions are minimally affected by the host matrix. These data are typically not determined for the respective UCNPs as shown in Table 5.2 summarizing representative literature values. This is particularly the case for Nd^{3+} ions. The crystal field and symmetry of the UCNP matrix can, however, affect the Stark splitting and hence the intensity distribution of the absorption bands of the Ln^{3+} ions in a matrix-dependent manner. Therefore, we determined the $\sigma_{Ln}(\lambda_{Ex})$ values for $(Yb@Yb,Nd)^{is}$ dispersed in water ($6.34 \text{ mg} \cdot \text{mL}^{-1}$) at the wavelengths used for Nd- and Yb-excitation experimentally from transmission spectra and ICP-MS concentration measurements. The values obtained for $\sigma_{Nd}(808 \text{ nm})$ and $\sigma_{Yb}(983 \text{ nm})$ are $\sim 1.0 \cdot 10^{-19} \text{ cm}^2$ and $\sim 2.7 \cdot 10^{-20} \text{ cm}^2$. These data are included in Table 5.2. This table underlines the influence of the matrix on $\sigma_{Ln}(\lambda_{Ex})$.

Table 5.2. Composition of absorption cross section values for Nd³⁺ and Yb³⁺ ions found in the literature for different host materials and excitations wavelengths.

Ln ³⁺	host material	λ_{exc} /nm	absorption cross-section /cm ²	Ref.
Nd ³⁺	LaF ₃	790	$2.5 \cdot 10^{-20}$	55
Nd ³⁺	(Gd,Y)VO ₄	808	$2 \cdot 10^{-19}$	56
Nd ³⁺	Nd ³⁺	800	$1.2 \cdot 10^{-19}$	46
Nd ³⁺	Sc ₂ O ₃	825	$7.2 \cdot 10^{-20}$	57
Nd ³⁺	YAG*	808	$1.2 \cdot 10^{-19}$	45
Nd ³⁺	NaYF ₄	808	10^{-14} (calculated per NP)	58
Nd ³⁺	-	~800	$\sim 10^{-19}$	59
Nd ³⁺	NaYF ₄	808	$(1.015 \pm 0.004) \cdot 10^{-19}$	this work
Yb ³⁺	YAlO ₃	980	$2.1 \cdot 10^{-20}$	57
Yb ³⁺	YAG*	980	$2.5 \cdot 10^{-20}$	45
Yb ³⁺	Al ₂ O ₃	980	$1.2 \cdot 10^{-20}$	60
Yb ³⁺	-	~980	10^{-20}	58
Yb ³⁺	NaYF ₄	983	$(2.692 \pm 0.09) \cdot 10^{-20}$	this work

Another parameter affecting the efficiency with which UCNPs are excited is the match between the narrow absorption band of the Ln³⁺ ions and the spectral profile of the laser diode used as excitation light source. The diode profile can slightly vary amongst different laser diodes of similar specification and is affected by the operation conditions (Fig. 5.10).

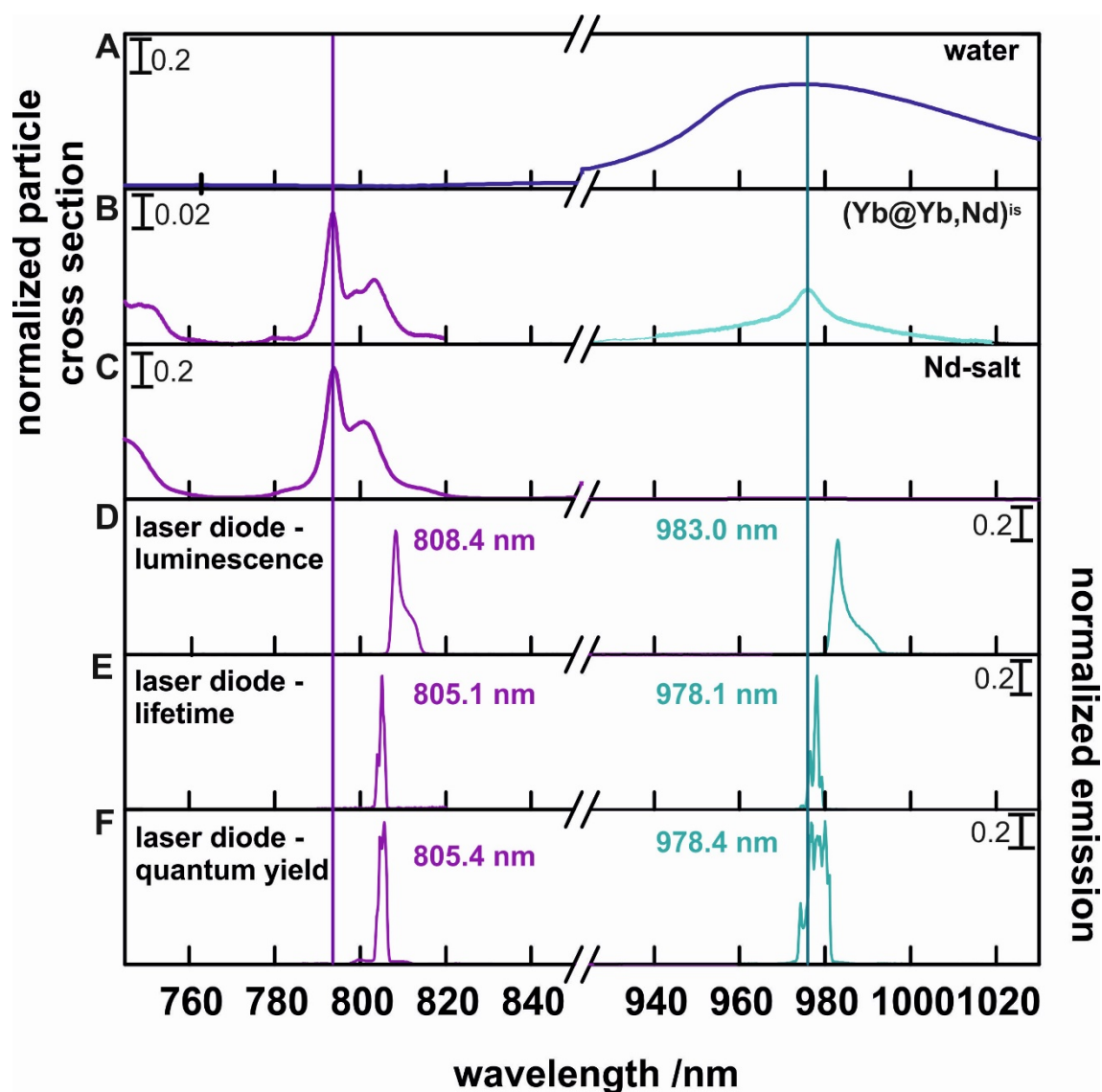


Figure 5.10 | Absorbance spectra of water (A), normalized particle cross-section of $\text{NaYF}_4:\text{Yb,Er}@\text{NaYF}_4:\text{Yb,Nd}@\text{NaYF}_4$ particles in cyclohexane (B) and normalized absorbance spectra of NdCl_3 salt (0.1 mol·L⁻¹) (C). The normalized emission of the laser modules 808 nm (purple) and 980 nm (turquoise) was also measured for the luminescence spectra (D), lifetimes (E) and quantum yield measurements (F). The exact values (real Nd- and Yb-excitation) for the laser excitation are listed in the Figure. The lines in purple and turquoise indicate the ideal excitation wavelengths.

The spectral profile of the laser diode used should therefore always be determined and provided. This is particularly important for Nd-excitation as the Nd^{3+} absorption band is narrower than that of Yb^{3+} . The influence of this effect is further highlighted in the sections on brightness values and influence of particle architecture. For all these reasons, for the desired comparison of the performance of the $(\text{Yb}@\text{Yb},\text{Nd})_{\text{is}}$ nanoparticle systems following Yb- and Nd-excitation, subsequently used relative particle brightness ($B_{\text{UC}}^{\text{rel}}$) values. Moreover, for $B_{\text{UC}}^{\text{rel}}$ values, neither the particle concentration in the solvent or matrix nor the actual absorption cross-sections of the particles need to be measured and considered, only the ratios of the latter. The $B_{\text{UC}}^{\text{rel}}$ values are calculated relative to an arbitrarily chosen particle cross-section, in

our case the maximum of the Yb³⁺ cross-section $\sigma_{Yb}(\lambda_{Ex,Yb}^{ideal})$, (Fig. 5.11A) using $\sigma_{UCNP}^{rel}(\lambda_{Ex}) = \sigma_{UCNP}(\lambda_{Ex})/\sigma_{Yb}(\lambda_{Ex,Yb}^{ideal})$. The relative absorption cross-sections for (Yb@Yb,Nd)^{is} at the actually used excitation laser wavelengths of 805 nm and 978 nm are 1.062 for Nd³⁺ and 0.808 for Yb³⁺. This results only in an absorption-related enhancement of ~1.3 for Nd-excitation.

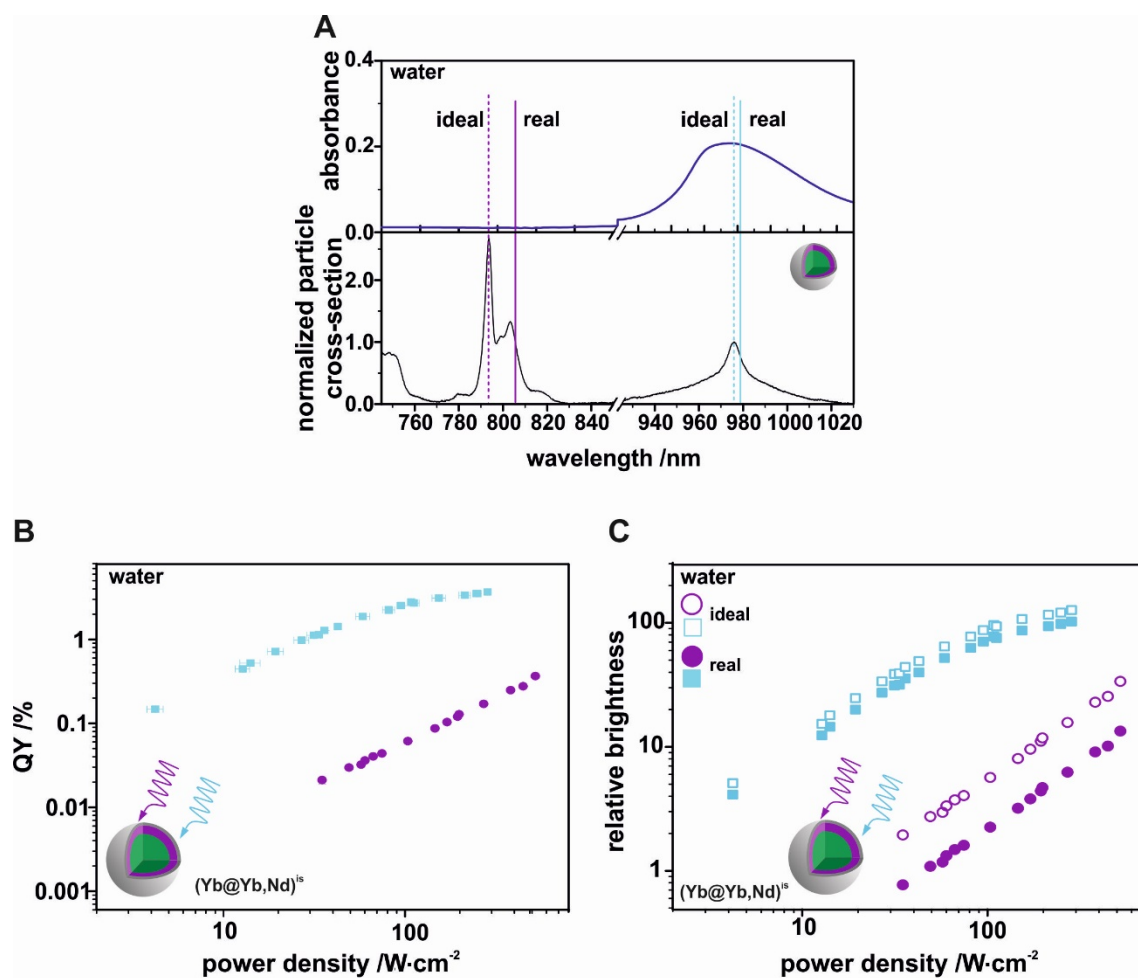


Figure 5.11 | (A) Absorbance spectra of water (top) and normalized absorbance spectra of NaYF₄:Yb,Er@NaYF₄:Yb,Nd@NaYF₄ ((Yb@Yb,Nd)^{is}) particles (bottom). The dashed lines show the wavelengths which are ideal for excitation, while the lines present the wavelengths which are commonly used for excitation. (B) Power density dependent quantum yield of (Yb@Yb,Nd)^{is} particles dispersed in water at Nd- (purple) and Yb- (turquoise) excitation. (C) Relative brightness in dependence of laser power of (Yb@Yb,Nd)^{is} particles excited by 805 nm (purple) and 978 nm (turquoise) system in aqueous solution calculated with the ideal and the real excitation.

Upconversion Quantum Yields. When comparing Φ_{UC} data it must be kept in mind that these values equal the number of emitted photons per number of absorbed photons and provide an overall measure for emitter performance. Φ_{UC} is affected by the distribution of and distance between the active Ln³⁺ ions, and thus by the crystal lattice of the host and dopant ion concentrations, as well as by surface and lattice defects, the presence of quenchers, P , and temperature. The number of absorbers in a (Yb@Yb,Nd)^{is} particle and the corresponding absorption cross-sections are, however, not considered by Φ_{UC} values on an individual basis.

This implies that differences in the actual number of Yb³⁺ and Nd³⁺ sensitizer ions of 34,500 Yb³⁺ ions and about 13,200 Nd³⁺ per particle are not reflected by Φ_{UC} data.

Figure 5.11B shows the P -dependent Φ_{UC} values ($\Phi_{UC}(P)$) obtained for (Yb@Yb,Nd)^{is} in water at both sensitizer excitation wavelengths for P varied from 4 to 520 W·cm⁻². Apparently, Yb-excitation leads to higher Φ_{UC} values. In addition, the slopes of the decay of the Er³⁺ emission at 540 nm (²H_{11/2} → ⁴I_{15/2}) resulting for Nd- and Yb-excitation are different. This indicates different population dynamics of Er³⁺. A possible explanation is the higher local density of excited Yb³⁺ ions at 978 nm as the core, where the ET from Yb³⁺ to Er³⁺ occurs, has an Yb³⁺ doping concentration of 20% compared to the active shell containing only 10% Nd³⁺. The Yb³⁺ ions in the core are directly excited at 978 nm and can then transfer the excitation energy directly to the Er³⁺ ions. The lower Φ_{UC} values and different P dependence found for 805 nm excitation of the Nd³⁺ ions in the shell region of (Yb@Yb,Nd)^{is} are attributed to the lower absorber concentration in combination with several ET steps.

Brightness Values. The B_{UC}^{rel} values were calculated from the Φ_{UC} values measured at 805 nm and 978 nm excitation (real) and for excitation conditions at the respective absorption maxima (ideal) as displayed in Figure 5.11C. The particle brightness (B_{UC}) of an UC system is defined as the product of the total number of Ln³⁺ absorbers per nanoparticle (N_{Ln}) times the absorption cross-section ($\sigma_{Ln}(\lambda_{Ex})$ [cm²]) of one absorbing Ln³⁺ ion at the chosen excitation wavelength λ_{Ex} times the absolute quantum yield (Φ_{UC}) (equation 4).

$$B_{UC,Ln}(\lambda_{Ex}) = N_{Ln} \times \sigma_{Ln}(\lambda_{Ex}) \times \Phi_{UC}(P_{Ex}) = \sigma_{UCNP}(\lambda_{Ex}) \times \Phi_{UC}(P_{Ex}) \quad (4)$$

Since the determination of σ_{UCNP} , which is controlled by the (average) particle size and (average) number of absorbing Ln³⁺ ions and their molar absorption coefficient, which is highly sensitive to the measurement conditions and varies in literature especially for the Nd ion (Table 5.2), we decided to calculate the relative brightness B_{UC}^{rel} instead by replacing $\sigma_{UCNP}(\lambda_{Ex})$ in (equation 4) by a relative particle cross section σ_{UCNP}^{rel} as defined in (equation 5) below. The sample absorbance and particle cross section are related by $A = N \cdot \sigma_{UCNP}$, A being the absorbance, N being the total particle number present in the sample, and σ_{UCNP} being the single particle cross-section as defined in (equation 2), so the ratio of the absorbances equals the ratio of the particle cross sections at the respective wavelengths. We choose to calculate σ_{UCNP}^{rel} from the high resolution normalized absorbance spectrum of the (Yb@Yb,Nd)^{is} system (Fig. 5.11A) by taking the ratio of the measured absorbance values at the laser excitation

wavelength λ_{Ex} and at maximum Yb absorbance (975.9 nm, the ideal Yb excitation wavelength).

$$\sigma_{UCNP}^{rel}(\lambda_{Ex}) = \frac{\sigma_{UCNP}(\lambda_{Ex})}{\sigma_{UCNP}(\lambda_{Ex,Yb}^{ideal})} \quad (5)$$

The N_{Ln} in (equation 4) was calculated by taking the number of ions per hexagonal unit cell ($N_{unit, Ln}$) depending on the doping concentration (c_{Ln}) and the calculation of the number of unit cells per NP (n_{cells}) using the ratio of NP volume (V_{NP}) to unit cell volume (V_{cell}) (calculated using a method reported by Mackenzie *et al.* [61]), leading to the numbers presented in Table 5.4.

Table 5.3. The calculated volume values of a hexagonal unit cell, of the core, the shell, and the calculated numbers of unit cells in the core, in the shell, and the number of ions per unit cell are listed.

term	number
$V_{cell, hexagonal}$	$1.06778 \cdot 10^{-22} \text{ cm}^3$
$N_{unit, Ln}$ (with f is doping rate of Ln: Yb, Er, Nd)	$1.5 \cdot f(Ln)$
$V_{NP, core}$	$7.238229 \cdot 10^{-18} \text{ cm}^3$
$n_{cells, core}$	$6.7800 \cdot 10^4$
$V_{NP, shell}$	$9.599362 \cdot 10^{-18} \text{ cm}^3$
$n_{cells, shell}$	$8.9900 \cdot 10^4$

Table 5.4 The number of Yb, Er and Nd ions are given for the four particle systems

system	N_{Yb}	N_{Er}	N_{Nd}
(Yb@Yb,Nd) ^{is}	$3.4472 \cdot 10^4$	$1.830 \cdot 10^3$	$1.3215 \cdot 10^4$
(Yb@Yb) ^{is}	$3.4472 \cdot 10^4$	$1.830 \cdot 10^3$	
(Yb@Yb) ^{is2}	$4.8334 \cdot 10^4$	$4.960 \cdot 10^3$	
(Yb@Yb) ^{is5}	$2.094645 \cdot 10^4$	$1.830 \cdot 10^3$	

At P of $103 \text{ W}\cdot\text{cm}^{-2}$, direct Yb-excitation leads to a B_{UC}^{rel} of 73 that exceeds the value observed for Nd-excitation by a factor of 36 (73 @ 978 nm and 2 @ 805 nm) for the $(\text{Yb}@\text{Yb},\text{Nd})^{is}$ particles. By switching from the real ($\lambda = 805 \text{ nm}$) to the ideal excitation wavelength ($\lambda = 794 \text{ nm}$), B_{UC}^{rel} is increased by a factor of around three to a value of six for Nd-excitation at P of $103 \text{ W}\cdot\text{cm}^{-2}$.

5.4.4 Influence of Particle Architecture

For applications *in vivo* and bioimaging at deep tissue penetration, particle size is a crucial parameter. Therefore, we compared the performance of UCNPs of types $(\text{Yb})^{is2}$ and $(\text{Yb})^{is5}$ to that of $(\text{Yb}@\text{Yb},\text{Nd})^{is}$. $(\text{Yb})^{is2}$ and $(\text{Yb})^{is5}$ differ only in the thickness of the inert surface passivation shell. For the $(\text{Yb})^{is5}$ system, the previously studied active shell was replaced by an inert protective shell, whereas for the $(\text{Yb})^{is2}$ system, the active shell was substituted by a shell of similar chemical composition as the core. As revealed by spectroscopic studies done with both types of UCNPs in water, Φ_{UC} of the $(\text{Yb})^{is5}$ system exceeds that of the $(\text{Yb})^{is2}$ particles by a factor of a ~ 10 at P of $100 \text{ W}\cdot\text{cm}^{-2}$. Consequently, the calculation of B_{UC}^{rel} values for Yb-excitation under real conditions (978 nm) also yielded higher values equaling about a twofold enhancement (Figs. 5.12A and 5.12B). Apparently, the inert shell does not efficiently shield the surface of the $(\text{Yb})^{is2}$ UCNPs from water quenching. Moreover, the confirmation that the Nd^{3+} ions do not influence the energy transfer in $(\text{Yb}@\text{Nd},\text{Yb})^{is}$ particles, is presented in Figure 5.12C and D. Here the Φ_{UC} data and B_{UC}^{rel} calculations at Yb excitations of the $(\text{Yb}@\text{Nd},\text{Yb})^{is}$ and $(\text{Yb}@\text{Yb})^{is}$ are compared and nearly no difference of the data is observed.

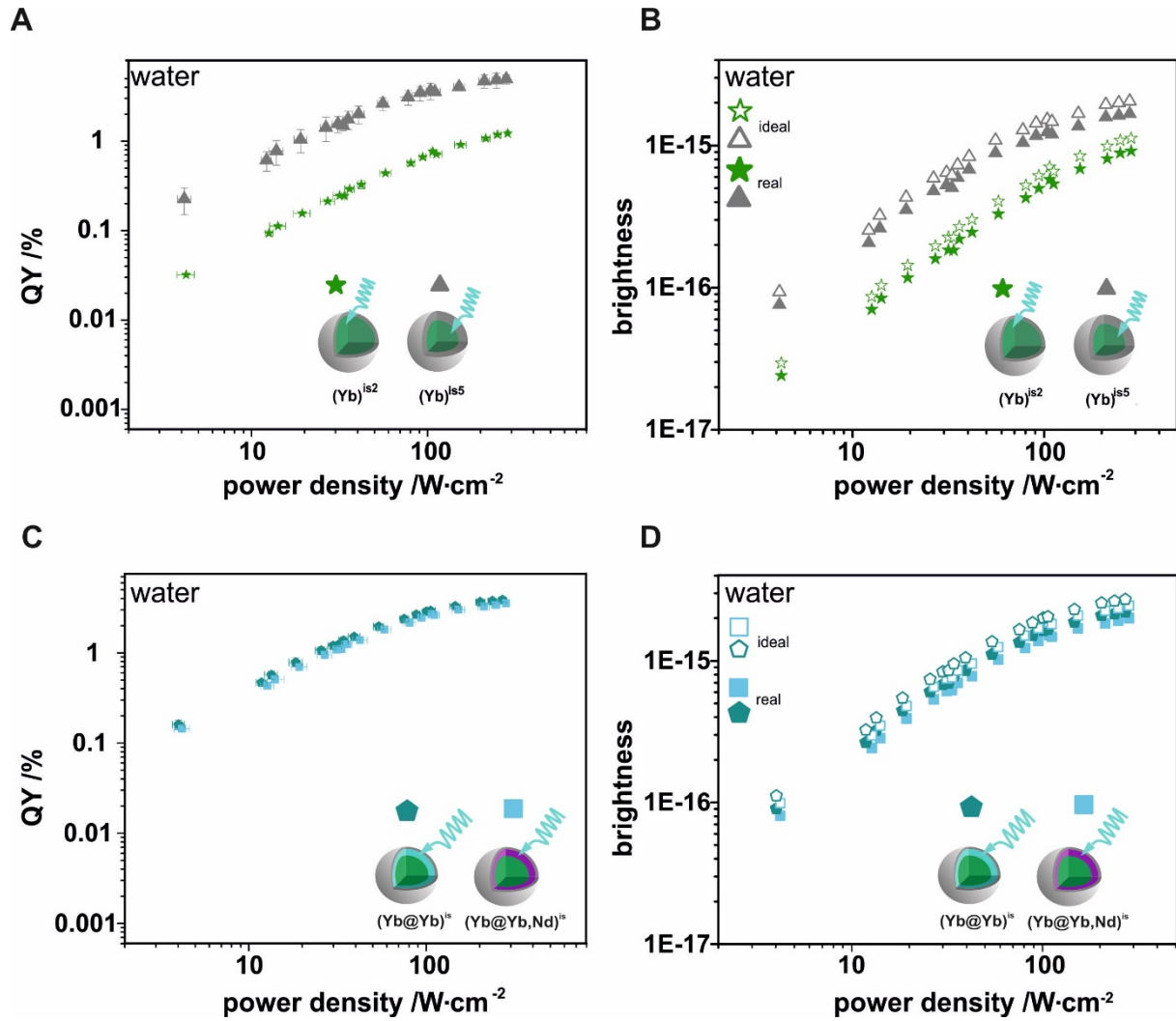


Figure 5.12 | Power density dependent absolute quantum yields of $NaYF_4:Yb,Er@NaYF_4 (Yb)^{is2}$ (green) and $(Yb)^{is5}$ (grey) particles dispersed in water at 978 nm excitation (A). Relative brightness in dependence of laser power of $(Yb)^{is2}$ (green) and $(Yb)^{is5}$ (grey) particles measured by excitation at 978 nm (real) in aqueous solution and calculated for an ideal excitation at 976 nm (B). For the particles $NaYF_4:Yb,Er@NaYF_4:Yb@NaYF_4 (Yb@Yb)^{is}$ and $NaYF_4:Yb,Er@NaYF_4:Yb,Nd@NaYF_4 (Yb@Nd,Yb)^{is}$ dispersed in water also power density dependent absolute quantum yield by excitation at 978 nm (C) and relative brightness measurements (D) in dependence of laser power were performed. For the brightness also the ideal values for an excitation at 976 nm were calculated.

Comparing the performance of the $(Yb)^{is5}$ particles at Yb-excitation and the $(Yb@Yb,Nd)^{is}$ UCNPs at Nd-excitation, a 57 times higher Φ_{UC} is found for the former system. Also, the B_{UC}^{rel} values calculated for ideal excitation of the $(Yb)^{is5}$ particles are 10 times higher (Fig. 5.13).

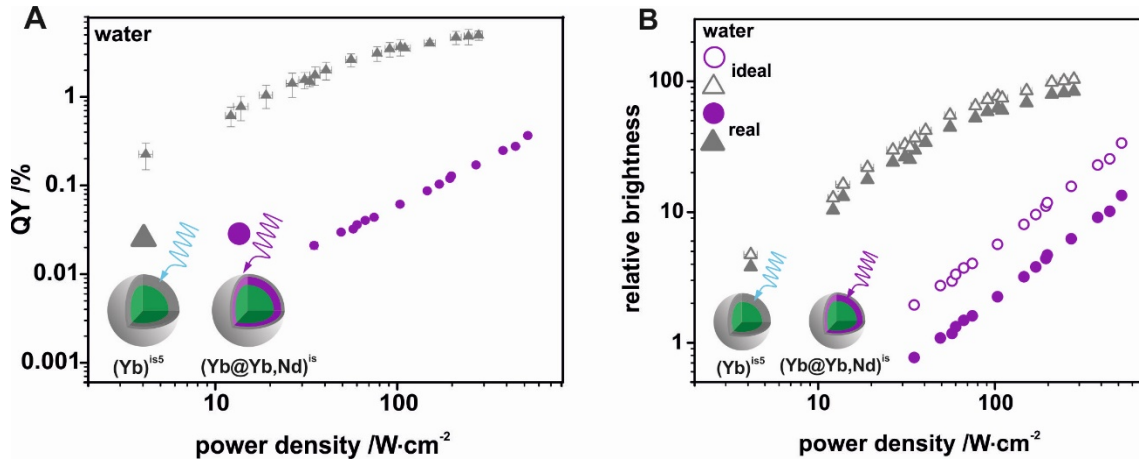


Figure 5.13 | (A) P -dependent Φ_{UC} values of $\text{NaYF}_4:\text{Yb,Er}@ \text{NaYF}_4$ ((Yb)^{is5}) excited at 978 nm (grey) and $\text{NaYF}_4:\text{Yb,Er}@ \text{NaYF}_4:\text{Yb,Nd}@ \text{NaYF}_4$ ((Yb@Yb,Nd)^{is}) excited at 805 nm (purple), both dispersed in water. (B) Relative brightness in dependence of P of (Yb@Yb,Nd)^{is} and (Yb)^{is5} in aqueous solution calculated for the ideal and real excitation conditions.

5.4.5 Penetration Depth in Phantom Tissue

Subsequently, we assessed the influence of the penetration depth x_c on signal size in water, thereby aiming to derive an estimate, at which x_c value the use of Nd^{3+} as sensitizer and excitation at about 808 nm becomes advantageous with respect to brightness. Since water shows higher absorption coefficient values ($\alpha_{\text{H}_2\text{O}}$) at 980 nm compared to 808 nm (Fig. 5.11A), with deeper penetration (x) of excitation light the effective local power density (P_{Ex}) is more strongly decreased for the 980 nm excitation. With lower P_{Ex} the $\Phi_{UC}(P_{Ex})$ is also reduced, which leads to a decrease of the luminescence emission signal ($I_{UC,Ln}$). At a certain penetration depth (x_c) the previously stronger emission of Yb-excited UCNPs shows the same signal as the Nd-excited systems (crossing point). For $x > x_c$ the Nd-excitation will lead to a brighter emission in water than Yb-excitation.

$I_{UC,Ln}$ depends on local P_{Ex} , the number of Ln^{3+} absorbers (N_{Ln}), the absorption cross section (σ_{Ln}) and the Φ_{UC} :

$$I_{UC,Ln}(x) \approx P_{Ex}(x) \times N_{Ln} \times \sigma_{Ln}(\lambda_{Ex}) \times \Phi_{UC}(P_{Ex}(x)) \quad (6)$$

In an absorbing medium the passing light – here excitation light and therefore P_{Ex} – is reduced following the Beer-Lambert law:

$$P_{Ex}(x) \approx P_0 \cdot e^{-\alpha_{\text{H}_2\text{O}}(\lambda_{Ex}) \cdot x}, \quad (7)$$

with $P_0 = P_{Ex}(x=0)$. With $N_{Ln} \cdot \sigma_{Ln} \sim A_{Ln}$ it follows:

$$I_{UC,Ln}(x) \approx P_0 \cdot e^{-\alpha_{\text{H}_2\text{O}}(\lambda_{Ex}) \cdot x} \times A_{Ln} \times \Phi_{UC}(P_{Ex}(x)) \quad (8)$$

In Figure 5.14A the penetration depth x_c , at which the signal intensities for Yb- and Nd-excitation are equal, is plotted for six different initial power densities $P_{Ex} (x = 0) = P_0 = 5, 50, 100, 200, 300$ and $400 \text{ W}\cdot\text{cm}^{-2}$ for both the real and the ideal excitation. $x_c (P_0)$ is estimated from:

$$I_{UC,Yb} (x_c) = I_{UC,Nd} (x_c) \quad (9)$$

For the real laser excitation wavelength, we obtained an x_c of $\sim 9 \text{ cm}$ in water. For ideal excitation conditions, for penetration depths exceeding $\sim 6 \text{ cm}$, Nd-excitation results in higher signals. This underlines that for a high penetration depth and minimal overheating with continuous wave excitation in deep-tissue imaging and theranostic applications of UCNPs with Nd³⁺-sensitization, the exact match of the laser profile and the Nd³⁺ absorption becomes relevant. With increasing P , x_c decreases and the Nd-doped system starts to outperform the efficiency of the Yb-doped particles at shorter penetration depths. To further optimize the triple doped UCNP, a detailed study of the influence of the Nd³⁺-concentration in the active shell and variations in Nd³⁺ and Yb³⁺ ratios are mandatory, thereby also considering other relevant parameters like UCNP size and P . In Figure 5.14B the critical penetration depth x_c varied with Nd doping concentration $c_{Nd} (N_{Nd})$ was calculated for ideal and real excitation at $P_0 = 50 \text{ W}\cdot\text{cm}^{-2}$. Since $I_{UC,Ln}$ scales linearly with N_{Nd} the change in c_{Nd} has a linear effect on $I_{UC,Nd}$. The increase in $I_{UC,Nd}$ with higher c_{Nd} shifts crossing point of signal intensities for Yb- and Nd-excitation to lower depths x_c . For this calculation no influences by cross relaxation due to the shorter ionic distances as well as lattice strain resulting from the different ionic radii of Nd³⁺ and Yb³⁺, which could alter the crystal structure and result in defects at the interface are considered. suggest that a higher Nd³⁺ content in the active shell shifts the crossing point x_c to smaller penetration depths in water. However, this rough estimation does not consider the influence of *e.g.* cross-relaxation favored by the shorter distances of the different Ln³⁺ ions and the lattice strain resulting from the different ionic radii of Nd³⁺ and Y³⁺. The latter could alter the crystal structure and result in defect formation.

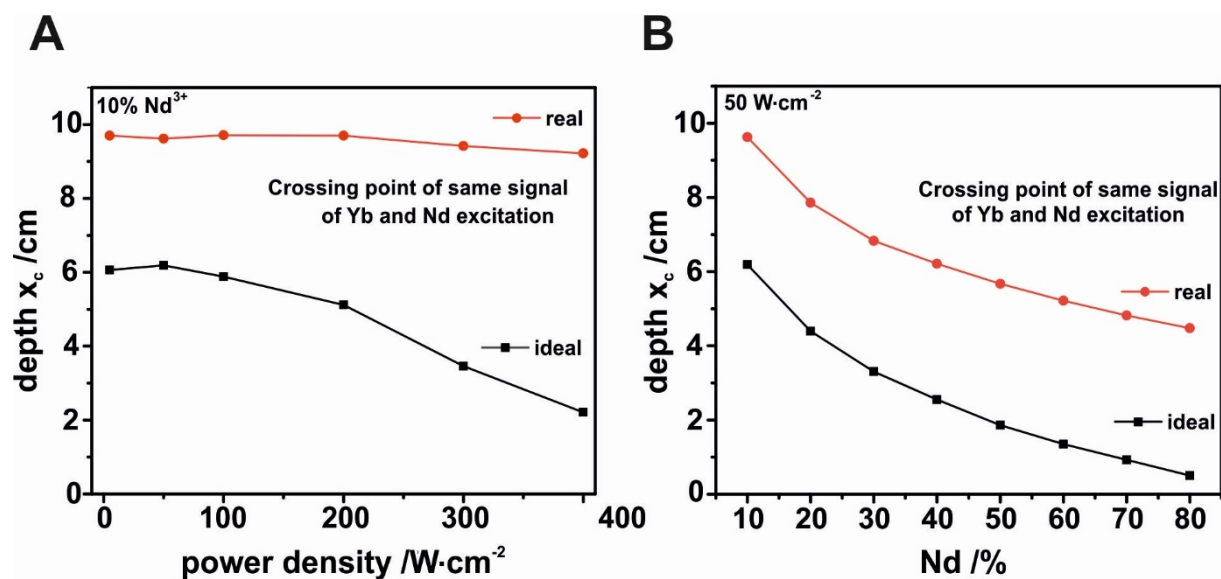


Figure 5.14 | Calculation of the penetration depth x_c in water, at which the signal intensities resulting for Yb- and Nd-excitation are equal (crossing point) for 5 power densities varying from 5 to 400 W·cm⁻² for real and ideal excitation conditions and **(B)** for a change in Nd³⁺ doping concentration in NaYF₄:Yb,Er@NaYF₄:Yb,Nd@NaYF₄ ((Yb@Yb,Nd)[®]) varied from 10% up to theoretically 80% at 50 W·cm⁻².

For a more realistic scenario, we used a tissue-simulating phantom medium, *i.e.* an emulsion of phospholipid micelles of polydisperse nature and water referred to as intralipid. Intralipid is turbid with no significant absorption bands in the VIS and NIR but strongly scattering, like tissue (Fig. 5.15).

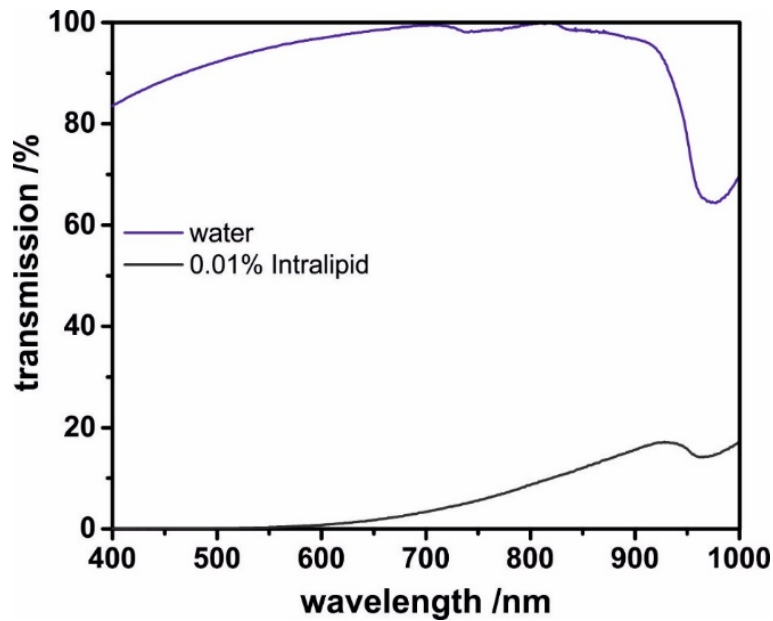


Figure 5.15 | Transmission measurements of water and a 0.01% Intralipid emulsion. Due to large scattering of the intralipid emulsion, a 100-times dilution was used compared to the penetration depth measurements.

At a wavelength of 633 nm scattering is more than 13,000 times more effective than absorbance [62]. (Yb@Yb,Nd)^{is} particles can be homogeneously dispersed in this matrix and remain colloidally stable at a UCNP concentration of 1 mg·mL⁻¹. As this formulation [63] is rather heterogeneous with large batch-to-batch variations, an exact description of its optical features by parameters such as absorption, scattering or total attenuation coefficient is very challenging. We assume that in this matrix or medium, the energy fluence rate becomes the limiting factor for *P*-dependent UCL. The strong scattering of this phantom tissue renders also the accurate determination of *P* values at a certain distance very difficult. Therefore, as an estimate, we determined the decrease of the Nd- and Yb-excitation power upon propagating through an increasing thickness of intralipid. For relatively low *P* (~150 mW, cw), which is recommended for medical applications, the power of the 808 nm laser diode is already reduced to 8% of the initial value at a penetration depth of 5 mm in the phantom tissue. For 980 nm excitation, the loss in power is even more pronounced, reaching a value of 1.6% of the initial signal at this penetration depth (Fig. 5.16).

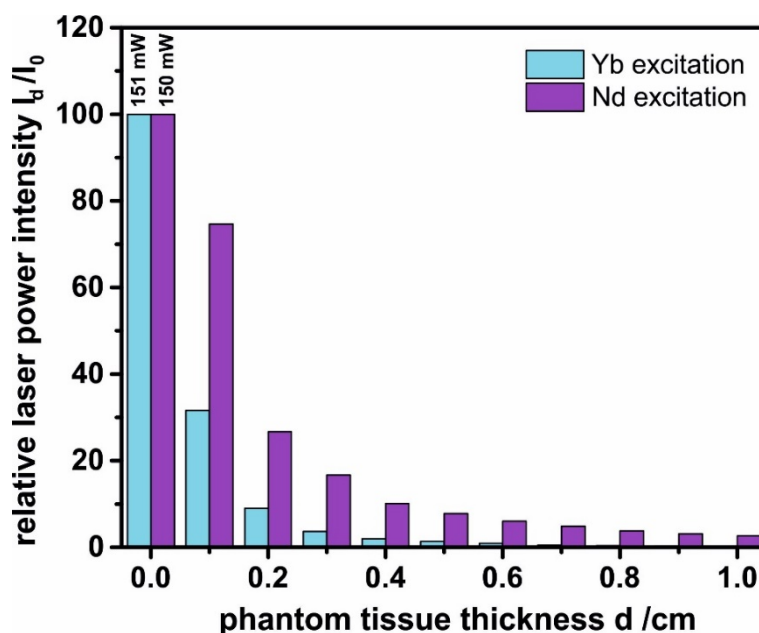


Figure 5.16 | Decrease of the 808 nm laser power presented in purple and the 980 nm laser power presented in turquoise when propagating through an intralipid emulsion (1%) with increasing thickness from 0 - 1 cm.

This becomes obvious when recording the UCL spectra at low excitation power (~ 200 mW, cw). In this case, the intensity of the green Er^{3+} emission of $(\text{Yb}@\text{Yb},\text{Nd})^{is}$ excited at 980 nm is diminished by 92% under these conditions, while it drops only by 66% for excitation at 808 nm (Figs. 5.17C and 5.17D).

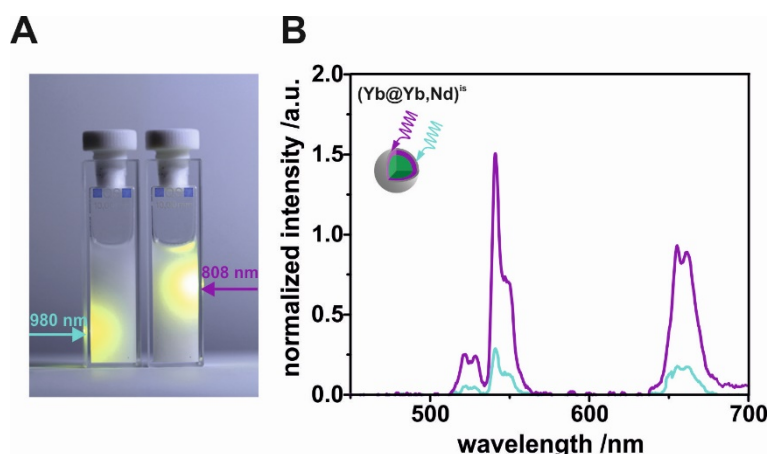


Figure 5.17 | (A) Photos and (B) luminescence spectra of $(\text{Yb}@\text{Yb},\text{Nd})^{is}$ dispersed in phantom tissue ($1 \text{ mg} \cdot \text{mL}^{-1}$). The Nd-excitation (808 nm, 200 mW, cw) is indicated in purple and the Yb-excitation (980 nm, 200 mW, cw) in turquoise.

5.5 Conclusion

In summary, the performance of a set of similarly sized $(\text{Yb}^{3+},\text{Nd}^{3+},\text{Er}^{3+})$ -doped core – shell UCNPs of different particle architecture were spectroscopically examined in water at broadly varied P using 980 nm (Yb-excitation) and 808 nm excitation (Nd-excitation). As a measure

for UCNP performance, the excitation power density (P)-dependent UC quantum yield (Φ_{UC}) and its saturation behavior were used as well as particle brightness (B_{UC}). Our results confirm a higher absorption cross-section and a lower water absorption at excitation wavelengths typical for Nd^{3+} as sensitizer compared to Yb^{3+} as reported by many other groups and underline that these general advantages do not necessarily lead to brighter UCL emission. Moreover, we stress the need to use precisely measured Nd^{3+} - and Yb^{3+} -absorption cross-sections to avoid misleading assumptions about sensitizer efficiencies. To enable the comparison of different sensitizers, we developed an efficient approach to model conditions advantageous for a certain sensitizer and certain measurement conditions like a desired penetration depth or a given P using experimentally determined Φ_{UC} and relative brightness values.

A first proof of concept study in phantom tissue revealed the need for more accurate studies of the influence of tissue on the photophysical properties of UCNPs and signal size. This is especially relevant for conditions where scattering dominates, and the illumination conditions cannot be well controlled. Motivated by our estimation of the effect of Nd^{3+} concentration on signal size, in the future, we will rationally design particle architectures with confined regions of the Nd^{3+} and Yb^{3+} sensitizer ions, varying in concentration and study their optical properties systematically in different matrices.

5.6 References

- [1] Auzel F (2004) Upconversion and anti-stokes processes with f and d ions in solids. *Chem. Rev.* 104(1):139-74.
- [2] Wu X, Chen CY, Shen J, Li Z], Zhang YW, Han G (2015) Upconversion nanoparticles: A versatile solution to multiscale biological imaging. *Bioconjug. Chem.* 26(2):166-75.
- [3] Xu CT, Zhan QQ, Liu HC, Somesfalean G, Qian J, He SL, Andersson-Engels S (2013) Upconverting nanoparticles for pre-clinical diffuse optical imaging, microscopy and sensing: Current trends and future challenges. *Laser & Photonics Rev.* 7(5):663-97
- [4] Wang HQ, Batentschuk M, Osvet A, Pinna L, Brabec CJ (2011) Rare-earth ion doped upconversion materials for photovoltaic applications *Adv. Mater.* 23(22):2675-80.
- [5] Gnach A, Bednarkiewicz A (2012) Lanthanide-doped up-converting nanoparticles: Merits and challenges. *Nano Today* 7(6):532-63.
- [6] Wang F, Liu XC (2009) Recent advances in the chemistry of lanthanide-doped upconversion nanocrystals. *Chem. Soc. Rev.* 38(4):976-89.
- [7] Goldschmidt JC, Fischer S (2015) Upconversion for photovoltaics: A review of materials, devices and concepts for performance enhancement. *Adv. Opt. Mater.* 3(4):510-35.

- [8] Zheng W, Huang P, Tu D, Ma E, Zh H, Chen X (2015) Lanthanide-doped upconversion nano bioprobes: Electronic structures, optical properties, and biodetection. *Chem. Soc. Rev.* 44(6):1379-415.
- [9] Zhou B, Shi B, Jin D, Liu X (2015) Controlling upconversion nanocrystals for emerging applications. *Nat. Nanotechnol.* 10(11):924-36.
- [10] Gorris HH, Wolfbeis OS (2013) Photon-upconverting nanoparticles for optical encoding and multiplexing of cells, biomolecules, and microspheres. *Angew. Chem. Int. Ed.* 52(13):3584-600.
- [11] Kim D, Lee N, Park YI, Hyeon T (2017) Recent advances in onorganic nanoparticle-based NIR Luminescence imaging: Semiconductor nanoparticles and lanthanide Nanoparticles. *Bioconjug. Chem.* 28(1):115-23.
- [12] Gorris HH, Saleh SM, Groegel DBM, Ernst S, Reiner K, Mustroph H, Wolfbeis OS (2011) Long-wavelength absorbing and fluorescent chameleon labels for proteins, peptides, and amines. *Bioconjug. Chem.* 22(7): 1433-37.
- [13] Gorris HH, Resch-Genger U (2017) Perspectives and challenges of photon-upconversion nanoparticles - Part II: Bioanalytical applications. *Anal. and Bioanal. Chem.* 409(25):5875-90.
- [14] Hososhima S, Yuasa H, Ishizuka T Hoque MR, Yamashita T, Yamanaka A, Sugano, E, Tomita H, Yawo H (2015) Near-infrared (NIR) up-conversion optogenetics. *Sci. Rep.* 10(5):16533-43.
- [15] Wu X, Zhang Y, Takle K, Bilsel O, Li Z, Lee H, Zhang Z, Li D, Fan W, Duan C, Chan EM, Lois C, Xiang Y, Han G (2016) Dye-sensitized core-active shell upconversion nanoparticles for optogenetics and bioimaging applications. *ACS Nano* 10(1):1060-6.
- [16] Pliss A, Ohulchanskyy TY, Chen GY, Damasco J, Bass CE Prasad PN (2017) Subcellular optogenetics enacted b targeted nanotransformers of near-infrared light. *ACS Photon.* 2017, 4(4):806-14.
- [17] Chen S, Weitemier AZ, Zeng X, He L, Wang X, Tao Y, Huang AJY, Hashimoto-dani Y, Kano M, Iwasaki H, Parajuli LW, Okabe S, The DBL, Ali AH, Tsutsui-Kimura I, Tanaka, KF, Liu X, McHugh TJ (2018) Near-infrared deep brain stimulation via upconversion nanoparticle-mediated optogenetics. *Science* 359(6376):679-83.
- [18] Feliu N, Neher E, Parak WJ (2018) Toward an optically controlled brain. *Science* 359(6376):633-4.
- [19] Lu YQ, Zhao JB, Zhang R, Liu YJ, Liu DM, Goldys EM, Yang XS, Xi P, Sunna A, Lu, J, Shi Y, Leif RC, Huo YJ, Shen J, Piper JA, Robinson JP, Jin DY (2014) Tunable lifetime multiplexing using luminescent nanocrystals. *Nat. Photon* 8(1):33-7.
- [20] Zheng XL, Zhu XJ, Lu YQ, Zhao JB, Feng W, Jia GH, Wang F, Li FY, Jin DY (2016) High-contrast visualization of upconversion luminescence in mice using time-gating approach. *Anal. Chem.* 88(7):3449-54.
- [21] Resch-Genger U, Gorris HH (2017) Perspectives and challenges of photon-upconversion nanoparticles-Part I: Routes to brighter particles and quantitative spectroscopic studies. *Anal. Bioanal. Chem.* 409(25):5855-74.
- [22] Liu Y, Lu Y, Yang X, Zheng X, Wen S, Wang F, Vidal X, Zhao J, Liu D, Zhou Z, Ma C, Zhou J, Piper JA, Xie P, Jin D (2017) Amplified stimulated emission in upconversion nanoparticles for super-resolution nanoscopy. *Nature* 543(7644):229-45.
- [23] Liu TM, Conde J, Lipiński T, Bednarkiewicz A, Huang CC (2016) Revisiting the classification of NIR-absorbing/emitting nanomaterials for in vivo bioapplications. *NPG Asia Mater.* 8(8):e295.
- [24] Skripka A, Marin R, Benayas A, Canton P, Hemmer E, Vetrone F (2017) Covering the optical spectrum through collective rare-earth doping of NaGdF₄ nanoparticles: 806 and 980 nm excitation routes. *Phys. Chem. Chem. Phys.* 19(19):11825-34.
- [25] Cortelletti P, Skripka A, Facciotti C, Pedroni M, Caputo G, Pinna N, Quintanilla M, Benayas A, Vetrone F, Speghini A (2018) Tuning the sensitivity of lanthanide-activated NIR nanothermometers in the biological windows. *Nanoscale.* 10(5):2568-76.

- [26] Liu G (2015) Advances in the theoretical understanding of photon upconversion in rare-earth activated nanophosphors. *Chem. Soc. Rev.* 44(6):1635-52.
- [27] Lin M, Zhao Y, Liu M, Qiu M, Dong Y, Duan Z, Li YH, Pingguan-Murphy B, Lu TJ, Xu F (2014) Synthesis of upconversion NaYF₄:Yb³⁺,Er³⁺ particles with enhanced luminescent intensity through control of morphology and phase. *J. Mater. Chem. C* 2(19):3671-6.
- [28] Shang Y, Hao S, Liu J, Tan M, Wang N, Yang C, Chen G (2015) Synthesis of upconversion β -NaYF₄: Nd³⁺/Yb³⁺/Er³⁺ particles with enhanced luminescent intensity through control of morphology and phase. *Nanomaterial* 5(1):218-32.
- [29] Hossain MY, Hor A, Luu Q, Smith SJ, May PS, Berry MT (2017) Explaining the nanoscale effect in the upconversion dynamics of β -NaYF₄: Yb³⁺, Er³⁺ core and core-shell nanocrystals. *J. Phys. Chem. C* 121(30):16592-606.
- [30] Kraft M, Würth C, Muhr V, Hirsch T, Resch-Genger U (2018) Particle-size-dependent upconversion luminescence of NaYF₄: Yb,Er nanoparticles in organic solvents and water at different excitation power densities. *Nano Res.* 11(12):6360-74.
- [31] Fischer S, Bronstein ND, Swabeck JK, Chan EM, Alivisatos AP (2016) Precise tuning of surface quenching for luminescence enhancement in core-shell lanthanide-doped nanocrystals. *Nano Lett.* 16(11):7241-7.
- [32] Wang F, Wang J, Liu X (2010) Direct evidence of a surface quenching effect on size-dependent luminescence of upconversion nanoparticles. *Angew. Chem. Int. Ed.* 49(41):7456-60.
- [33] Zhao J, Lu Z, Yin Y, McRae C, Piper JA, Dawes JM, Jin D, Goldys EM (2013) Upconversion luminescence with tunable lifetime in NaYF₄:Yb,Er nanocrystals: Role of nanocrystal size. *Nanoscale* 5(3):944-52.
- [34] Wiesholler LM, Hirsch T (2018) Strategies for the design of bright upconversion nanoparticles for bioanalytical applications. *Opt. Mater.* 80:253-64.
- [35] Yuan D, Tan MC, Riman RE, Chow GM (2013) Comprehensive study on the size effects of the optical properties of NaYF₄: Yb, Er nanocrystals. *J. Phys. Chem. C* 117(25):13297-304.
- [36] Cheng Q, Sui J, Cai W (2012) Enhanced upconversion emission in Yb³⁺ and Er³⁺ codoped NaGdF₄ nanocrystals by introducing Li⁺ ions. *Nanoscale* 4(3):779-84.
- [37] Kim JH, Choi H, Kim EO, Noh HM, Moon BK, Jeong JH (2014) Li doping effects on the upconversion luminescence of Yb³⁺/Er³⁺-doped ABO₄ (A= Ca, Sr; B= W, Mo) phosphors. *Opt. Mater.* 38:113-8.
- [38] Ding M, Ni Y, Song Y, Liu X, Cui T, Chen D, Ji Z, Xu F, Lu C, Xu Z (2015) Li⁺ ions doping core-shell nanostructures: an approach to significantly enhance upconversion luminescence of lanthanide-doped nanocrystals. *J. Alloy. and Comp.* 623:42-8.
- [39] Würth C, Fischer S, Grauel B, Alivisatos AP, Resch-Genger U (2018) Quantum yields, surface quenching, and passivation efficiency for ultrasmall core-shell upconverting nanoparticles. *J. Am. Chem. Soc.* 140(14):4922-8.
- [40] Homann C, Krukewitt L, Frenzel F, Grauel B, Würth C, Resch-Genger U, Haase M (2018) NaYF₄: Yb, Er/NaYF₄ core-shell nanocrystals with high upconversion luminescence quantum yield. *Angew. Chem. Int. Ed.* 57(28):8765-9.
- [41] Wang F, Deng R, Wang J, Wang Q, Han Y, Zhu H, Chen X, Liu X (2011) Tuning upconversion through energy migration in core-shell nanoparticles. *Nat. Mater.* 10(12):968-73.
- [42] Ye S, Chen C, Shao W, Qu J, Prasad PN (2015) Tuning upconversion through a sensitizer/activator-isolated NaYF₄ core-shell structure. *Nanoscale* 7(9):3976-84.
- [43] Würth C, Kaiser M, Wilhelm S, Grauel B, Hirsch T, Resch-Genger U (2017) Excitation power dependent population pathways and absolute quantum yields of upconversion nanoparticles in different solvents. *Nanoscale* 9(12):4283-94.

- [44] Wen S, Zhou J, Zheng K, Bednarkiewicz A, Liu X, Jin D (2018) Advances in highly doped upconversion nanoparticles. *Nature Commun.* 9(1):2415.
- [45] Wang YF, Liu CY, Sun LD, Xiao JW, Zhou JC, Yan CH (2013) Nd³⁺-sensitized upconversion nanophosphors: Efficient in vivo bioimaging probes with minimized heating effect. *ACS Nano.* 7(8):7200-6.
- [46] Estebanez N, Ferrera-González J, Francés-Soriano L, Arenal R, González-Béjar M, Pérez-Prieto J (2018) Breaking the Nd³⁺-sensitized upconversion nanoparticles myth about the need of onion-layered structures. *Nanoscale* 10(26):12297-301.
- [47] Kaiser M, Würth C, Kraft M, Hyppänen I, Soukka T, Resch-Genger U (2017) Power-dependent upconversion quantum yield of NaYF₄: Yb³⁺, Er³⁺ nano- and micrometer-sized particles measurements and simulations. *Nanoscale* 9(28):10051-8.
- [48] Muhr V, Würth C, Kraft M, Buchner M, Baemumner AJ, Resch-Genger U, Hirsch T (2017) Particle-size-dependent Förster resonance energy transfer from upconversion nanoparticles to organic dyes. *Anal. Chem.* 89(9):4868-74.
- [49] Johnson NJ, Korinek A, Dong C, van Veggel FC (2012) Self-focusing by Ostwald ripening: a strategy for layer-by-layer epitaxial growth on upconverting nanocrystals. *J. Am. Chem. Soc.* 134(27):11068-71.
- [50] Wiesholler LM, Genslein C, Schroter A, Hirsch T (2018) Plasmonic enhancement of NIR to UV upconversion by a nanoengineered interface consisting of NaYF₄:Yb,Tm nanoparticles and a gold nanotriangle array for optical detection of vitamin B12 in serum. *Anal. Chem.* 90(24):14247-54.
- [51] Braslavsky SE (2007) Glossary of terms used in photochemistry (IUPAC Recommendations). *Pure Appl. Chem.* 79(3):293-465.
- [52] Ma Z, Zhang M, Yue J, Alcazar C, Zhong Y, Doyle TC, Dai H, Huang NF (2018) Near-infrared IIb fluorescence imaging of vascular regeneration with dynamic tissue perfusion and high spatial resolution. *Adv. Func. Mater.* 28(36):1803417.
- [53] Zhong Y, Tian C, Gu Z, Yang Y, Gu L, Zhao Y, Ma Y, Yao J (2014) Elimination of photon quenching by a transition layer to fabricate a quenching-shield sandwich structure for 800 nm excited upconversion luminescence of Nd³⁺-sensitized nanoparticles. *Adv. Mater.* 26(18):2831.
- [54] Wang F, Liu X (2014) Multicolour tuning of lanthanide-doped nanoparticles by single wavelength excitation. *Acc. Chem. Res.* 47(4):1378-85.
- [55] Bhutta T, Chardon AM, Shepherd DP, Daran E, Serrano C, Munoz-Yague A (2001) Low phonon energy, Nd: LaF₃ channel waveguide lasers fabricated by molecular beam epitaxy. *IEEE J. Quantum Electron.* 37(11):1469-77.
- [56] del Rosal B, Pérez-Delgado A, Carrasco E, Jovanović DJ, Dramićanin MD, Dražić G, de la Fuente ÁJ, Sanz-Rodríguez F, Jaque D (2016) Neodymium-based stoichiometric ultrasmall nanoparticles for multifunctional deep-tissue photothermal therapy. *Adv. Opt. Mater.* 4(5):782-9.
- [57] Lupei V, Lupei A, Ikesue A (2005) Transparent Nd and (Nd, Yb)-doped Sc₂O₃ ceramics as potential new laser materials. *App. Phys. Lett.* 86(11):111118.
- [58] Jaque D, Maestro LM, Del Rosal B, Haro-Gonzalez P, Benayas A, Plaza JL, Rodriguez EM, Solé JC (2014) Nanoparticles for photothermal therapies. *Nanoscale* 6(16):9494-530.
- [59] del Rosal B, Rocha U, Ximendes EC, Rodríguez EM, Jaque D, Solé JC (2017) Nd³⁺ ions in nanomedicine: Perspectives and applications. *Opt. Mater.* 63:185-96.
- [60] Lupei V, Lupei A, Gheorghe C, Ikesue A (2010) A sensitized Yb³⁺ emission in (Nd, Yb):Y₃Al₅O₁₂ transparent ceramics. *J. App. Phys.* 108(12):123112.
- [61] Mackenzie LE, Goode JA, Vakurov A, Nampi PP, Saha S, Jose G, Millner PA (2018) The theoretical molecular weight of NaYF₄: RE upconversion nanoparticles. *Sci. Rep.* 8(1):1106.

- [62] Flock ST, Wilson BC, Patterson MS (1987) Total attenuation coefficients and scattering phase functions of tissues and phantom materials at 633 nm. *Med. Phys.* 14(5):835-41.
- [63] ST Flock, SL Jacques, BC. Wilson, WM Star, MJC van Gemert (1992) Optical properties of intralipid: A phantom medium for light propagation studies. *Lasers Surg. Med.* 12:510-19.

6. Conclusion and Future Perspectives

Upconversion nanoparticles (UCNPs) are a class of promising luminescent probes and reporters in many fields in life science and have attracted massive interest to researchers. The first groundbreaking work dates back to 1959 where Leverenz and Bloembergen described upconversion and anti-stokes processes in solids [1,2]. Nevertheless, after almost 60 years of development and improvements on lanthanide-doped nanocrystals, there still are a lot of open questions starting from ideal composition up to surface functionalization. This chapter presents a critical résumé on the state of the art and gives an outlook for future direction in research on UCNPs.

One of the greatest challenges in designing probes with upconversion capability is the need to boost the efficiency of this process. To fully understand how this can be done, one has to take a close look at the principle of upconversion: Low energy is converted by a sequential absorption of at least two high energy photons, which leads to the emission of light at shorter wavelengths compared to the excitation, also called anti-Stokes emission. The process of photon upconversion can be briefly explained by three general models: energy transfer upconversion (ETU), excited-state absorption (ESA) and photon avalanche (PA) [1]. The simplified schemes, showing absorption, energy transfer and emission processes by the energy levels of one or two involved atoms, are presented in Figure 6.1A [3].

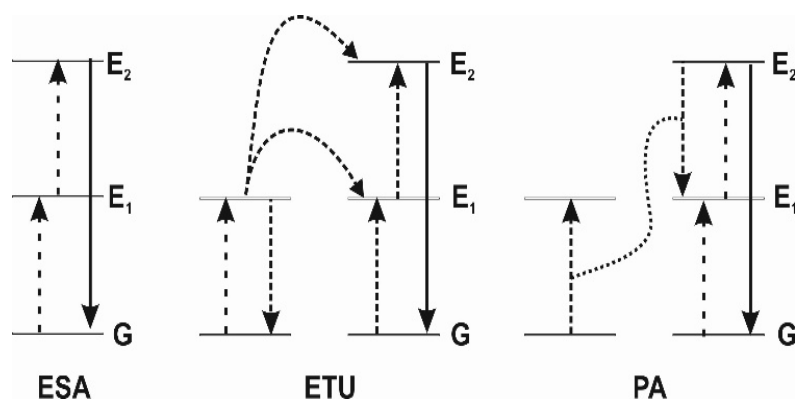


Figure 6.1 | Simplified representations of the three main processes describing the upconversion process in lanthanide-doped nanocrystals: excited state absorption (ESA), energy transfer upconversion (ETU) and photon avalanche (PA). Dashed arrows symbolize photon absorption, full arrows represent photon emission and dotted arrows refer to non-radiative processes between ground states (G) and excited states (E) of one or two atoms.

All these processes deal with the absorption of two or more photons [4]. However, the most efficient UC process with a probability of $\eta = 10^{-3}$ is ETU, which is 100 times more likely to occur than the second-best process ESA [5]. In detail, first the so-called sensitizer ion is responsible for the resonant photon absorption of low energy to get excited. This sensitizer needs to be in close proximity to the so-called activator to effectively transfer the energy *via* a non-radiative transfer. This process is then repeated for one or several more times, leading to the population of higher excited states of the activator. Such a cascade is mainly enabled due to the long-lasting excited states and the high number of energy levels of lanthanide ions [6-8] (Fig. 6.2A). Moreover, a lot of processes exist, which interrupt the upconversion process like the Stokes-emission, non-radiative deactivation and cross-relaxation. When coming to the real world, one has to realize that these ideal models are encountered by some drawbacks. First to mention is the activator ion. In essence only ytterbium can be used as activator, which can absorb NIR light at 976 nm. In all other cases the situation is more complicated due to many energy levels and in case of cerium, which has also only one excited state, the excitation wavelength is in the 4 μm region. Second, lanthanide ions are known for their generally low absorption coefficients, often less than $1 \text{ M}^{-1}\cdot\text{cm}^{-1}$, due to the f-f transitions being forbidden according to Laporte's parity rule [9]. Especially the huge number and the complexity of possible deactivation steps during the ETU process of lanthanide ions in a host material, as theoretically describes by the workgroup of Emory Chan [10] (Fig. 6.2B), impressively underlines the importance of finding the ideal architecture of UCNPs in terms of the right distance of sensitizer and activator ions [10,11].

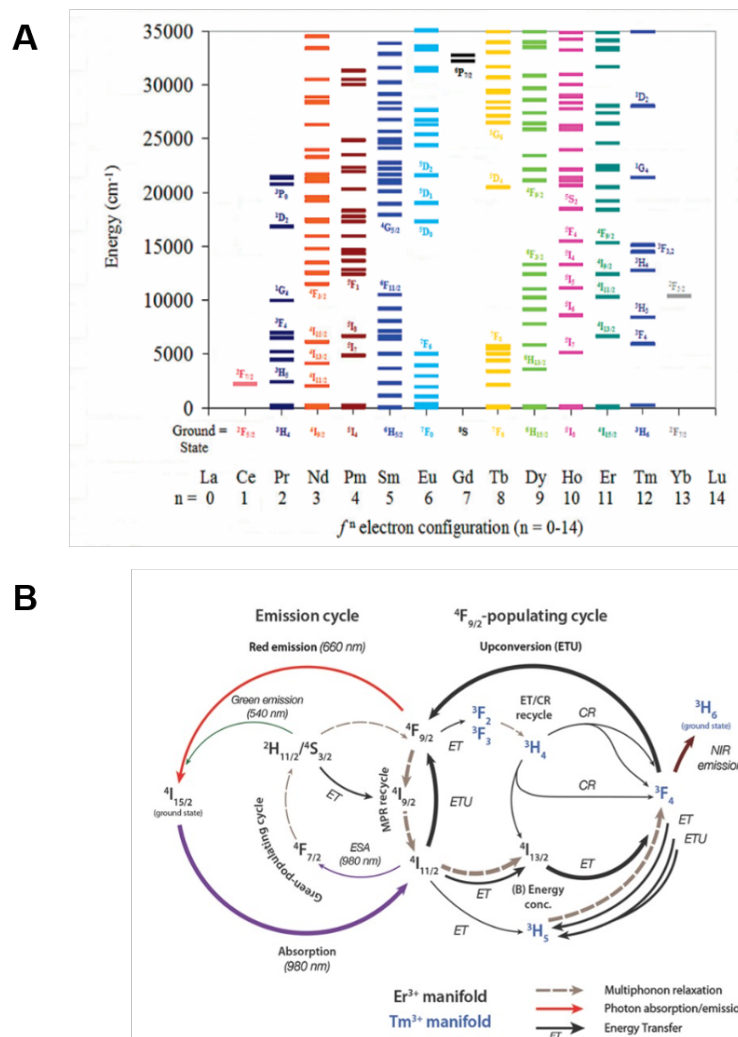


Figure 6.2 | (A) summary of electronic excited state energy levels for the Ln^{3+} ions. Adapted with permission from [7] © 2009 American Chemical Society. (B) Emission, population, and energy recycling pathways of Er^{3+} and Tm^{3+} in NaYF_4 host material. Adapted with permission from [10] © 2012 American Chemical Society.

This can be achieved by the proper choice of doping rates within the crystal. Important is that the absorption of all photons needed for upconversion has to take place in a short time by one sensitizer ions [12]. But also the type of the crystal itself needs to be carefully selected. One can imagine the host material like a bank. In former times a massive building protecting deposits and used for exchange. In case of upconversion materials the host has a similar function, it conserves the energy in excited states of sensitizer ions which could be symbolizes as a safe and the activator ions as a counter. And like a bank used for currency exchange, the host enables the exchange of NIR photons to Vis or UV photons. A good bank does not charge a lot of fees for currency exchange, the same for a good host, which should not consume the energy itself. A measure for this is given by the phonon energy, which should be very low. Therefore, the host material of choice for lanthanide ions excitable in the NIR is NaYF_4 [13], with a phonon energy of 305cm^{-1} [4]. Activator ions matching the Yb^{3+} sensitizer are Er^{3+} , Ho^{3+}

(both with predominately green and weak red emissions), and Tm^{3+} (with strong emission in the blue and in the NIR and a weak emission in the UV) [14]. Up to four photons are needed to obtain the desired emission (two NIR photons \rightarrow green (540 nm) and red emission (655 nm); three NIR photons \rightarrow blue emission (475 nm); four photons \rightarrow UV emission (345 & 360 nm). The theoretically best photon exchange rate one can get, according to the model of ETU is 1:3 for green emission and 1:4 for blue emission. In reality, the best exchange rate was realized so far by the group of Markus Haase, designing upconversion nanoparticles converting 980 nm photons to 540 nm photons with a rate of about 1:11. This outstanding value of a quantum yield of up to 9% for nanocrystals of 45 nm diameter was achieved by three principles: a) a total excluding water during synthesis, b) growing of a large inert shell of NaYF_4 of about 10 nm thickness and c) the dispersion of this particles in organic solvents. Unfortunately, they do not transfer these particles into water [15], the far most interesting media for applications of UCNPs. Compared to the state of the art, the $\text{NaYF}_4:\text{Yb},\text{Er}@\text{NaYF}_4$ particles consisting of a 25 nm core and an only 5 nm thick shell reported in Chapter 5 of this work show a quantum yield of 6.3% at comparable excitation power density in cyclohexane, which is of the same quality compared to the smaller size. In water, with poly(acrylic acid) as surface capping, these particles show a remarkable quantum yield of 1.6 %. To the best of my knowledge there are no reports on particles with higher quantum efficiency in water so far. Nevertheless, due to the complexity to measure absolute power-dependent quantum yields, there are not many studies available, which is a general problem in the development of UCNPs. There are many papers reporting on bright particles, but without presenting reliable information allowing a fair comparison. It is suggested to define standards or to offer a reference material which can be easily used by researchers to allow any judgement.

Since about four years the synthesis of these promising luminescent materials got reproducible and controllable by several groups [4,16-20]. Despite this it is still wondering why there is no agreement in the most efficient doping so far. Up to now most research stay with the doping ratio 20% : 2% for the Yb^{3+} and Er^{3+} system, and 25% : 0.3% for the Yb^{3+} and Tm^{3+} system. These doping ratios have been optimized for the bulk material [11]. To my experience with different doping ratios and particle sizes prepared in our group these ratios should be adapted to the particle size as for smaller nanoparticles surface tremendously affect the brightness.

In this work it was shown that plasmonic enhancement from gold arranged in close proximity to Tm -doped UCNPs enables a modulation of the peak ratios of the individual emissions. We

achieved selectively an enhancement of the UV-emission, which was utilized for the first time to design a label-free sensor for vitamin B12 in serum. A comparison of this assay to an identical system with classical Tm-doped particles dispersed in cuvettes but without plasmonic enhancement was not able to detect about 500 nM of the analyte whereas the LOD with plasmonic enhancement was as low as 3 nM. It is expected that also for other UCNPs coupling to plasmonic or photonic materials can lead to tailored spectral properties fitting to a special application.

In a previous study our workgroup in cooperation with the Federal Institute for Material Research and Testing in Berlin investigated the dependence of different surface ligands to the upconversion efficiency [21], and addressed the main mechanism of quenching by the multiphoton deactivation of the Yb^{3+} sensitizer ion caused by the -O-H vibrations at the surface of the nanocrystal [22]. This is also one of the main reasons not to reach a quantum yield of 10% in water, as shown by Markus Haase for UCNPs dispersed in cyclohexane. Since two research groups independently published about a significant enhancement of the upconversion efficiency by using an inert NaYF_4 -shell on $\text{NaYF}_4:\text{Yb},\text{Er}$ particles (Fig. 6.3) preventing surface quenching [23,24], core – shell particles got very attractive. The thickness of the shell has to be optimized equal to the size of the core particles. In 2009, first the workgroup of Capobianco replaced the inert shell by a so-called active shell consisting of $\text{NaYF}_4:\text{Yb}$ for getting more photons absorbed and transferred by energy migration into the core [25,26]. The possibility of doping core and shell with different Ln^{3+} ions and the control of the shell thickness during the synthesis was also part of this thesis. Here this approach was utilized to a) shift the excitation wavelength from 980 nm to 808 nm by additional Nd^{3+} sensitization and b) to enhance the luminescence by growing an additional thin, inert shell. The epitaxial growth concept is a good analogy for explaining the formation of core – multi-shell particles. Due to the different doping in the core as in the shell material leads to a varied lattice constants (heteroepitaxy). The guideline is to minimize the lattice and symmetry mismatches between core and shell material for a successful heteroepitaxy growth [27].

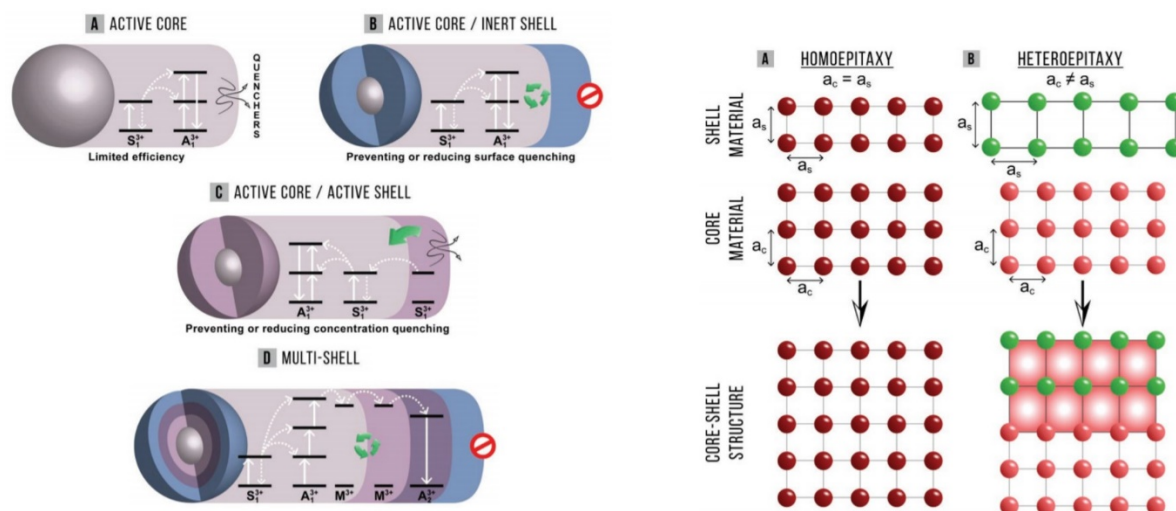


Figure 6.3 | (Left) Energy flux management in lanthanide-doped UCNPs relies on the implementation of basic architectures. (Right) The traditional epitaxial growth concept is either based on homoepitaxy (A) or heteroepitaxy (B). Figure adapted with permission from Ref [27] © 2014 Wiley-VCH GmbH, Weinheim.

This means that not all materials or doping ratios work in the same for the core and the shell as lattice mismatch often prevents a successive shell growth. Due to experimental limits it was also not possible to study the stability of core – shell particle architectures. For Eu^{3+} -doped core – shell particles it was shown that Eu^{3+} got dissolved from the core particle when growing a shell under high temperature conditions [28]. It would be very important to get a better understanding of these processes to optimize the synthesis strategies, but therefore one needs to have access to an electron microscope with high spatial resolution or advanced X-ray technologies to resolve different lanthanide ions in such small dimensions and such low concentrations on individual particles. Nevertheless, the particles with core – multi-shell architectures were stable in their luminescence properties over the entire time of now up to three years. This indicates that at room temperature there is no intermixing between confined regions within the particle. But even when the total elemental composition of the particles always was verified by ICP-OES or ICP-MS control measurements, this is not an evidence that the core and the shell will be completely separated in their elemental composition. In case of a region with a gradient of the dopants between the core and the shell this would additionally reduce the brightness of the particles due to the possibility of cross-relaxations. Therefore, it is expected to even further enhance the luminescence by a proper adjustment of the shell growth conditions, e.g. by using lower temperatures or by variations in heating rates.

Core – multi-shell particles with Nd^{3+} sensitization have been designed in this work to obtain bright particles for a NIR induced photo-switchable drug release. The inert outer shell significantly reduced the surface quenching of the active shell by co-sensitization with Nd^{3+}

prevents the sample heating by shifting the excitation wavelength to 808 nm, where water only shows a very weak absorption. The water absorption at 980 nm is accompanied by several problems in utilizing UCNPs. In a water matrix, the excitation power density gets reduced with the distance, and therefore the brightness and even the peak ratios of the individual upconversion emissions will not stay constant. This is a major drawback in sensor development, as the feature of self-referencing gets lost, but this can be overcome by core – multi-shell particle architecture with Nd^{3+} sensitization. Nevertheless, this leads to another challenge which needs to be overcome in future: For applications in cells or *in vivo*, it is highly desired to have ultra-small particles (<10 nm), which is in contradiction to a core – shell approach. In the last years researchers have focused synthesizing such particles with the aim of a possible clearance from the body. Due to increased surface-to-volume-ratio, the efficiency of such small UCNPs in biologically relevant media gets extremely reduced. All sensitizer ions are too close to the particle surface and therefore are prone for quenching. As these processes have a fast decay time, they are very effective. The workgroup of Bruce E. Cohen has recently published an interesting concept to overcome such limitations by setting the activator concentrations to an unusual high level resulting in enhanced brightness of these particles. The Er^{3+} ions can adopt a second role to enhance the absorption by desaturating the Yb^{3+} ions or by directly absorbing photons. At a laser excitation of $0.1 \text{ W}\cdot\text{cm}^{-2}$ the core – shell ($\text{NaYbF}_4\text{:}80\%\text{Er@NaYF}_4$) particles with a size of only 12 nm were used for imaging in mice [29].

Focusing on biological applications an important point is the deep tissue penetration. For the Nd^{3+} -doped particles the deeper penetration depth in water at same or even higher brightness was confirmed by a systematic study of a set of identical sized particles but different architecture. This study revealed a penetration depth of 6 cm and more at which the 808 nm excitation gets beneficial. This can also be partly revealed in phantom tissue. But here one clearly can see the massive impact of scattering, which does not allow a detailed study as the illumination gets diffuse and therefore it gets challenging to measure the energy flux precisely. Up to now the community of researcher dealing with UCNPs are mostly neglecting this fact and still discussing the deep tissue penetration. Together with the fact that the irradiation power density of the NIR light needs to be lower than $4 \text{ W}\cdot\text{cm}^{-2}$ [30] to prevent tissue and cell damages, there is a lot of more work to do to improve the efficiency of UCNPs. From the actual viewpoint, for deep tissue penetration it might be better to address the second biological window ranging from 1,000 to 1,350 nm by investigating the Stokes emission of lanthanide-doped nanoparticles [31]. Especially for imaging applications also the emissions can be

collected from deep tissue, which is not the case for green or blue emissions in UCNPs. Erbium for instance exhibit a Stokes emission at 1520 nm, excitable at 808 nm by Nd^{3+} , verified on a first measurement with the particles described in Chapter 5 (Fig. 6.4).

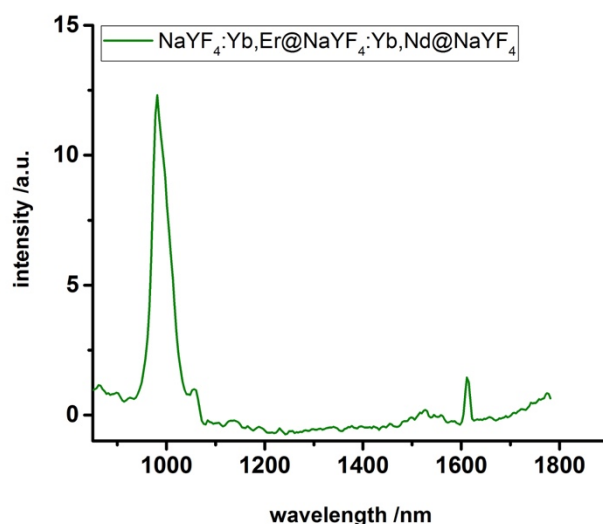


Figure 6.4 | Spectra of $(\text{Nd}^{3+}, \text{Yb}^{3+}, \text{Er}^{3+})$ -doped UCNPs excited at 808 nm showing emissions at 980 nm for Yb^{3+} and 1616 nm (overtone of the 808 nm excitation) as well as a very weak emission at 1520 nm assigned to Er^{3+} -Stokes emission.

Of course, for such particles the doping ratio need to be completely redesigned, as it was optimized to minimize Stokes emission. It is expected that much higher intensities for the Stokes-emission can be achieved and therefore the requirement of a low irradiation dose can be fulfilled. So far, such probes are still in its infancy as there are not so much detectors for emissions in this region available up to now, due to high costs and due to military reasons, which have complicated or even prevented the commercial usage [32].

Nevertheless, the rapidly growing interest of UCNPs in the research community promises interesting biological applications of upconversion nanoparticles in the near future. Recently, a tremendous public interest was triggered by the workgroup of Xue from China, which has developed ocular injectable photoreceptor-binding upconversion nanoparticles as miniaturized NIR light transducers to create NIR light image vision in mice increasing the spectral range of vision beyond 700 nm. This approach was frequently shared on social media and the article was also discussed in German newspaper [33]. In conclusion, there is still a large open field on questions for the development of bright and small UCNPs, which will be addressed by the vivid community to bring this class of material to novel and excited application in biology and clinical applications.

6.1 References

- [1] Bloembergen N (1959) Solid state infrared quantum counters. *Phys. Rev. Lett.* 2(3):84-5.
- [2] Auzel F (2004) Upconversion and anti-stokes processes with f and d ions in solids. *Chem. Rev.* 104(1):139-74.
- [3] Vetrone F, Capobianco JA (2008) Lanthanide-doped fluoride nanoparticles: Luminescence, upconversion, and biological applications. *Int. J. Nanotechn.* 5(9-12):1306-39.
- [4] Haase M, Schäfer H (2011) Upconverting nanoparticles. *Angew. Chem. Int. Ed.* 2011 50(26):5808-29.
- [5] Gamelin DR, Güdel HU (2000) Design of luminescent inorganic materials: New photophysical processes studied by optical spectroscopy. *Acc. Chem. Res.* 33(4):235-42.
- [6] Joubert MF (1999) Photon avalanche upconversion in rare earth laser materials. *Opt. Mater.* 11(2-3):181-203.
- [7] Moore EG, Samuel AP, Raymond KN (2009) From antenna to assay: lessons learned in lanthanide luminescence. *Acc. Chem. Res.* 42(4):542-52.
- [8] Wang F, Liu X (2014) Multicolor tuning of lanthanide-doped nanoparticles by single wavelength excitation. *Acc. Chem. Res.* 47:1378-185.
- [9] Bünzli JCG (2015) On the Design of Highly Luminescent Lanthanide Complexes. *Coord. Chem. Rev.* 293:19-47.
- [10] Chan EM, Levy ES, Cohen BE (2015) Rationally designed energy transfer in upconverting nanoparticles. *Adv. Mater.* 27(38):5753-61.
- [11] Aebischer A, Heer S, Biner D, Krämer K, Haase M, Güdel HU (2005) Visible light emission upon near-infrared excitation in a transparent solution of nanocrystalline β -NaGdF₄:Yb³⁺,Er³⁺. *Chem. Phys. Lett.* 407(1-3):124-8.
- [12] Chen X, Ma E, Liu G (2007) Energy levels and optical spectroscopy of Er³⁺ in Gd₂O₃ nanocrystals. *J. Phys. Chem. C.* 111(28):10404-11.
- [13] Suyver JF, Grimm J, Van Veen MK, Biner D, Krämer KW, Güdel HU (2006) Upconversion spectroscopy and properties of NaYF₄ doped with Er³⁺, Tm³⁺ and/or Yb³⁺. *J. Lumin.* 117(1):1-2.
- [14] Wang G, Peng Q, Li Y (2011) Lanthanide-doped nanocrystals: synthesis, optical-magnetic properties, and applications. *Acc. Chem. Res.* 44(5):322-32.
- [15] Homann C, Krukewitt L, Frenzel F, Grauel B, Würth C, Resch-Genger U, Haase M (2018) NaYF₄: Yb,Er@NaYF₄ core-shell nanocrystals with high upconversion luminescence quantum yield. *Angew. Chem. Int. Ed.* 57(28):8765-9.
- [16] Meruga JM, Baride A, Cross W, Kellar JJ, May PS (2014) Red-green-blue printing using luminescence-upconversion inks. *J. Mater. Chem. C* 2(12):2221-7.
- [17] Wang F, Han Y, Lim CS, Lu Y, Wang J, Xu J, Chen H, Zhang C, Hong M, Liu X (2010) Simultaneous phase and size control of upconversion nanocrystals through lanthanide doping. *Nature* 463(7284):1061-5.
- [18] Gargas DJ, Chan EM, Ostrowski AD, Aloni S, Altoe MV, Barnard ES, Sanii B, Urban JJ, Milliron DJ, Cohen BE, Schuck PJ (2014) Engineering bright sub-10-nm upconverting nanocrystals for single-molecule imaging. *Nature Nanotechn.* 9(4):300-5.
- [19] Hirsh DA, Johnson NJ, van Veggel FC, Schurko RW (2015) Local structure of rare-earth fluorides in bulk and core/shell nanocrystalline materials. *Chem. Mater.* 27(19):6495-507.
- [20] Naccache R, Yu Q, Capobianco JA (2015) The fluoride host: Nucleation, growth, and upconversion of lanthanide-doped nanoparticles. *Adv. Opt. Mater.* 3(4):482-509.

- [21] Wilhelm, S.; Kaiser, M.; Würth, C.; Heiland, J.; Carrillo-Carrion, C.; Muhr, V.; Wolfbeis, O. S.; Parak, W. J.; Resch-Genger, U.; Hirsch, T (2015) Water dispersible upconverting nanoparticles: Effects of Surface Modification on their luminescence and colloidal stability. *Nanoscale* 7:1403–10.
- [22] Arppe R, Hyppänen I, Perälä N, Peltomaa R, Kaiser M, Würth C, Christ S, Resch-Genger U, Schäferling M, Soukka T (2015) Quenching of the upconversion luminescence of NaYF₄: Yb³⁺, Er³⁺ and NaYF₄: Yb³⁺, Tm³⁺ nanophosphors by water: the role of the sensitizer Yb³⁺ in non-radiative relaxation. *Nanoscale* 7(27):11746-57.
- [23] Qian HS, Zhang Y (2008) Synthesis of hexagonal-phase core – shell NaYF₄ nanocrystals with tunable upconversion fluorescence. *Langmuir* 24(21):12123-5.
- [24] Yi GS, Chow GM (2007) Water-soluble NaYF₄: Yb,Er (Tm)-NaYF₄-polymer core-shell-shell nanoparticles with significant enhancement of upconversion fluorescence. *Chem. Mat.* 19(3):341-3.
- [25] Vetrone F, Naccache R, Mahalingam V, Morgan CG, Capobianco JA (2009) The active-core-active-shell approach: A strategy to enhance the upconversion luminescence in lanthanide-doped nanoparticles. *Adv. Func. Mater.* 19(18):2924-9.
- [26] Chen F, Deng R, Wang J, Wang Q, Han Y, Zhu H, Chen X, Liu X (2011) Tuning upconversion through energy migration in core–shell nanoparticles. *Nature Mater.* 10(12):968-73.
- [27] Hudry D, Howard IA, Popescu R, Gerthsen D, Richards BS (2019) Structure property relationships in lanthanide-doped upconverting nanocrystals: Recent advances in understanding core–shell structures. *Adv. Mater.* 1900623-48.
- [28] Voss B, Haase M (2013) Intrinsic focusing of the particle size distribution in colloids containing nanocrystals of two different crystal phases. *ACS Nano.* 7(12):11242-54.
- [29] Tian B, Fernandez-Bravo A, Najafiaghdam H, Torquato NA, Altoe MV, Teitelboim A, Tajon CA, Tian Y, Borys NJ, Barnard ES, Anwar M (2018) Low irradiance multiphoton imaging with alloyed lanthanide nanocrystals. *Nature Commun.* 9(1):3082-90.
- [30] Chen C, Shen J, Ohulchanskyy TY, Patel NJ, Kutikov A, Li Z, Song J, Pandey RK, Ågren H, Prasad PN, Han G (2012) α -NaYbF₄: Tm³⁺-CaF₂ core-shell nanoparticles with efficient near-infrared to near-infrared upconversion for high-contrast deep tissue bioimaging. *ACS Nano.* 6(9):8280-7.
- [31] Xu J, Gulzar A, Yang P, Bi H, Yang D, Gai S, He F, Lin J, Xing B, Jin D (2019) Recent advances in near-infrared emitting lanthanide-doped nanoconstructs: Mechanism, design and application for bioimaging. *Coord. Chem. Rev.* 381:104-34.
- [32] Rogalski A (2012) History of infrared detectors. *Opto-Electronics Review.* 20(3):279-308.
- [33] Retrieved April 8, 2019 from <https://www.sueddeutsche.de/wissen/infrarotsicht-nanopartikel-verleihen-maeusen-superblick-1.4350363>.

Curriculum Vitae

Persönliche Daten

Name	Lisa Marie Wiesholler
Geburtsdatum	07.10.1990
Geburtsort	Gehrden
Familienstand	ledig
Staatsangehörigkeit	deutsch

Hochschulausbildung

Nov 2015 – Mai 2019	Promotionsstudium Chemie an der Universität Regensburg <i>„Upconverting Nanoparticles of small Size and high Brightness for Analytical Application in Aqueous Solutions“</i> , Institut für Analytische Chemie, Chemo- und Biosensorik (Dr. Thomas Hirsch, Prof. Antje J. Bäumner) Abschluss mit <i>summa cum laude</i> am 21. Juni 2019
Okt 2013 – Sept 2015	Masterstudium Chemie an der Universität Regensburg (Note:1,2) Hauptfach: Analytische Chemie, 1. Nebenfach: Anorganische Chemie, 2. Nebenfach: Biochemie Abschlussthema: <i>„Colloidally-stable Upconverting Nanoparticles with Enhanced Luminescence Properties in Aqueous Solutions“</i> , Institut für Analytische Chemie, Chemo- und Biosensorik (Dr. Thomas Hirsch, Prof. Antje J. Bäumner)
Okt 2010 – Juli 2013	Bachelorstudium Chemie an der Universität Regensburg (Note: 2,9) Abschlussthema: <i>„Entwicklung optischer Sensorsysteme für Aldehyde“</i> (Fraunhofer EMFT, Prof. Joachim Wegener)
Sept 1997 – Juli 2010	Allgemeine Hochschulreife am Gymnasium Neubiberg

Weiterbildungen

Februar 2019	Ich, die Führungskraft (Carpe verba, Regensburg)
August 2018	Selbstmarketing im außeruniversitären Bewerbungsprozess (Falkenberg Seminare, Regensburg)
Juli 2018	BWL für Ingenieure (Strategische Partnerschaft Sensorik Regensburg, Regensburg)
Mai 2018	Endspurt für Horizon 2020, EU-Forschungsförderung (Universität Regensburg, Regensburg)
Oktober 2017	Opening the Editor's Black Box: Insider Tips for Successful Submissions (GDCh, München)
April 2017	Spring School on Properties, Design and Applications of Upconversion Nanomaterials in Valencia (COST CM1403, Valencia)
Juni 2017	10th Advanced Study Course on Optical Chemical Sensors (Institut für Photonik und Elektronik, Tschechische Akademie der Wissenschaft, Třešť)
April 2017	Tutorien auf der MRS 2017 in Phoenix, USA: „Essentials on how your work gets published“ und „Women in Materials Science & Engineering“ (MRS Spring Meeting 2017, Phoenix)
Juli 2015	Qualitätsmanagement in der Analytischen Chemie (Universität Regensburg, Regensburg)
Februar 2015	Frühjahrsschule Industrielle Analytische Chemie (Fachgruppe Analytische Chemie der Gesellschaft Deutscher Chemiker, Regensburg)

Stipendien

2018	Reisestipendium von der GDCh (Europt(r)ode XIV, Neapel)
2017	Reisestipendium vom DAAD (SHIFT2017, Teneriffa)
2017	Reisestipendium vom Btha (10th Asc0s2017, Třešť)
2016	Reisestipendium von der GDCh (Europt(r)ode XIII, Graz)

Forschungsaufenthalt

Februar 2016 Aufenthalt für spektroskopische Messungen an der Bundesanstalt für Materialforschung und -prüfung in Berlin (Referenz Dr. Ute Resch-Genger)

Präsentationen

Oral Presentation

2019 – Doktorandenkolloquium ChemPharm, Regensburg, Deutschland

Upconversion Nanoparticle based Neural Stem Cell Differentiation Control

2017 - SHIFT2017, Teneriffa, Spanien

Design, Synthesis, and Theranostic Application of Upconversion Nanoparticles with Tandem Sensitization

Poster Presentation

2018 - 2nd Upcon 2018, Valencia, Spanien

Plasmonic Enhancement of Upconversion Luminescence for Label-free Detection of Vitamin B12 in Serum

2018 - Europt(r)ode XIV, Neapel, Italien

Plasmonic Enhancement of Upconversion Luminescence for Label-free Detection of Vitamin B12 in Serum

2017 - MRS Spring Meeting, Phoenix (AZ), USA

Core – Shell Nd³⁺-doped Upconversion Nanoparticles with Enhanced Luminescence Properties in Aqueous Solutions for Bioanalytical Applications

2016 - Europt(r)ode XIII, Graz, Österreich

Colloidally-stable Upconverting Nanoparticles with Enhanced Luminescence Properties in Aqueous Solutions

2016 - 10. Interdisziplinäres Doktorandenseminar, Berlin, Deutschland

Colloidally-stable Upconverting Nanoparticles with Enhanced Luminescence Properties in Aqueous Solutions

2015 - 11th International Workshop on Biosensors and Bioanalytical Microtechniques for Environmental, Food and Clinical Analysis, Regensburg, Germany

Colloidally-stable Upconverting Nanoparticles with Enhanced Luminescence Properties in Aqueous Solutions

Veröffentlichungen

6. **L. M. Wiesholler**, F. Frenzel, B. Grauel, C. Würth, U. Resch-Genger and T. Hirsch, Yb,Nd,Er-Doped Upconversion Nanoparticles for Deep Tissue Applications: 980 nm versus 808 nm Excitation, *published in Nanoscale*, July 1th, **2019**, doi:10.1039/C9NR03127H
5. Y. Zhang, **L. M. Wiesholler**, P. Jiang, J. Lai, H. Rabie, T. Hirsch, K. Lee, NIR-mediated Spatiotemporal Control of Stem Cell Fate Using Multifunctional Upconversion Nanoparticles, *submitted to Nature Nanotechnology* at July 4th, **2019**
4. E. S. Tsai, S. F. Himmelstoß, **L. M. Wiesholler**, T. Hirsch, E. A.H. Hall, Upconversion Nanoparticles for Sensing pH, *submitted to Analyst* **2019**, *in revision*
3. **L. M. Wiesholler**, C. Genslein, A. Schroter, T Hirsch, Plasmonic Enhancement of NIR to UV Upconversion by a Nanoengineered Interface Consisting of NaYF₄: Yb, Tm Nanoparticles and a Gold Nanotriangle Array for Optical Detection of Vitamin B12 in Serum. *Analytical Chemistry* **2018**; 90(24):14247-54, doi: 10.1021/acs.analchem.8b03279
2. **L. M. Wiesholler**, T Hirsch, Strategies for the design of bright upconversion nanoparticles for bioanalytical applications. *Optical Materials* **2018**; 80:253-64, doi: 10.1016/j.optmat.2018.04.015
1. S. F. Himmelstoß, **L. M Wiesholler**, M. Buchner, V Muhr, S Märkl, A. J. Baeumner, T. Hirsch, 980 nm and 808 nm excitable upconversion nanoparticles for the detection of enzyme related reactions, *SPIE BiOS. International Society for Optics and Photonics*, **2017**; 10077p-100770L, doi: 10.1117/12.2252381

Eidesstattliche Erklärung

Ich erkläre hiermit an Eides statt, dass ich die vorliegende Arbeit ohne unzulässige Hilfe Dritter und ohne Benutzung anderer als der angegebenen Hilfsmittel angefertigt habe; die aus anderen Quellen direkt oder indirekt übernommenen Daten und Konzepte sind unter Angabe des Literaturzitats gekennzeichnet.

Weitere Personen waren an der inhaltlich-materiellen Herstellung der vorliegenden Arbeit nicht beteiligt. Insbesondere habe ich hierfür nicht die entgeltliche Hilfe eines Promotionsberaters oder anderer Personen in Anspruch genommen. Niemand hat von mir weder unmittelbar noch mittelbar geldwerte Leistungen für Arbeiten erhalten, die im Zusammenhang mit dem Inhalt der vorgelegten Dissertation stehen.

Die Arbeit wurde bisher weder im In- noch im Ausland in gleicher oder ähnlicher Form einer anderen Prüfungsbehörde vorgelegt.

Ort, Datum

Unterschrift